

Novel Applications of Grid-Forming Converters in Offshore Wind Farms

A thesis presented for the degree of Doctor of Philosophy

Rui Alves

Power Electronics, Drives and Energy Conversion Electronic and Electrical Engineering University of Strathclyde, Glasgow, United Kingdom

January 2025

To my family.

This thesis is the result of the author's original research. It has been

composed by the author and has not been previously submitted for

examination which has led to the award of a degree.

The copyright of this thesis belongs to the author under the terms of

the United Kingdom Copyright Acts as qualified by University of

Strathclyde Regulation 3.50. Due acknowledgement must always be

made of the use of any material contained in, or derived from, this

thesis.

Signed:

Date:

ii

Abstract

The global shift from fossil fuel-based generation to renewable energy sources is transforming the operation and stability of electrical grids. Offshore wind power plants are central to this transition, but their integration through long high voltage alternating current transmission systems presents significant stability challenges. As conventional synchronous machines are phased out, new approaches are required to provide essential services such as inertia, frequency regulation, and reactive power support.

This thesis develops and evaluates a control and compensation framework to address these challenges. Several transmission system topologies were studied, combining different shunt reactor placements with either grid-forming or grid-following converter control. Steady-state, small-signal, and electromagnetic transient analyses show that the best-performing configuration is the one using grid-forming control with shunt reactors placed at both ends and at a mid-point of the transmission cable. This arrangement achieves the highest stability, particularly for long cable lengths and weak grids, increases the maximum stable transmission distance, and remains robust under variations in short-circuit ratio, avoiding the instability observed with grid-following control in similar conditions.

The research also examines the ability of alternating current-connected offshore wind power plants to provide power system restoration. Results show that a balanced mix of grid-forming and grid-following control can meet all technical requirements for restoration. For top-up restoration scenarios, 40% to 60% grid-

Chapter 0. Abstract

forming penetration delivers the highest stability, while for anchor restoration scenarios, 20% to 40% is optimal. The addition of an external frequency supervisory controller reduces frequency dips during restoration and enables recovery without synchronous generation, allowing reliable self-start of the plant.

Through comprehensive simulations and analysis, this work demonstrates that offshore wind power plants equipped with the proposed control and compensation framework can provide both enhanced steady-state stability and dependable power system restoration capability, offering a practical pathway for replacing conventional synchronous plants in future low-carbon grids.

A	bstra	act			iii
Li	st of	Figur	es		X
Li	st of	Table	s		χv
\mathbf{A}	bbre	viation	ıs	XV	viii
\mathbf{A}	ckno	wledge	ements		ХХ
1	Inti	roduct	ion		2
	1.1	Objec	tives and Summary Of Work		5
	1.2	Thesis	s Outline		6
	1.3	Scient	sific Contributions		8
	1.4	List C	Of Publications		9
2	Tec	hnolog	gies and Challenges in Renewable Energy Systems		10
	2.1	Renev	vable Energy Penetration Challenges		11
		2.1.1	System Strength and Stability Concerns		12
		2.1.2	Inertia and Frequency Control		13
		2.1.3	Fault Ride-Through Response		15
		2.1.4	Adverse System Interactions and Protection Systems		16
	2.2	Offsho	ore Wind Power Plants and Transmission Challenges		17
		2.2.1	Cost Comparison and Maturity		17

		2.2.2	System stability and Reactive Power Compensation	18
		2.2.3	The Role of GFM Controllers in HVAC Transmission	18
		2.2.4	Competitiveness of HVAC with GFM and Reactive Power	
			Compensation	19
		2.2.5	Addressing Gaps in Existing Research	20
	2.3	Power	System Restoration from Offshore Wind Power Plants	22
		2.3.1	Overview of Power System Restoration from Offshore Wind	
			Power Plants	22
		2.3.2	Challenges and Requirements	24
		2.3.3	PSR from OWPPs – Process Overview	25
		2.3.4	Conclusion	28
	2.4	Grid-I	Following Controllers	28
		2.4.1	Operational Principles of the GFL Controller	28
		2.4.2	Challenges and Limitations of the Grid-Following Controller	31
	2.5	Grid-I	Forming Control	32
		2.5.1	Operational Principles Of The GFM Controller	33
		2.5.2	Droop Control	36
		2.5.3	Power Synchronization Control	39
		2.5.4	Direct Power Control	39
		2.5.5	Virtual Oscillator Control	40
		2.5.6	Virtual Synchronous Machine	40
		2.5.7	Conclusion	44
	2.6	Self-St	tart Wind Turbine Generators	44
		2.6.1	Patents On Self-Starting Wind Turbines	45
		2.6.2	Academic Research On Self-Starting Wind Turbines	47
3	Nov	el Mo	delling and Analysis Framework for an Offshore Wind	
	Pow	ver Pla	unt	53
	3.1	Introd	luction	53

	3.2	Design	n Of Offshore Wind Power Plant - Grid	55
		3.2.1	Aggregated Offshore Wind Power Plant	55
		3.2.2	Export cable	57
		3.2.3	Shunt reactors	61
		3.2.4	The Electrical Grid	62
		3.2.5	Offshore Transformer	64
		3.2.6	Onshore Loads	64
		3.2.7	Final Designs	65
		3.2.8	Cost Comparison of the Final Designs	69
	3.3	Steady	y-State Analysis	71
		3.3.1	Offshore Wind Power Plant Capabilities And Limitations .	71
		3.3.2	Impact of reactive power shunt compensation	77
		3.3.3	Voltage Profile	80
1	Ma	4:6.4	Conventor Control Approach to Improve System Sta	
4			Converter Control Approach to Improve System Sta-	
4	bilit	ty		84
4	bilit	t y Introd	uction	84
4	bilit	t y Introd Grid I	Sollowing Converter Control	84 84 85
4	bilit	Introd Grid I 4.2.1	Following Converter Control	84 84 85 85
4	bilit	Introd Grid I 4.2.1 4.2.2	Pollowing Converter Control	84 84 85 85 86
4	bilit 4.1 4.2	Introd Grid I 4.2.1 4.2.2 4.2.3	Phase Locked Loop	84 84 85 85 86 87
4	bilit	Introd Grid I 4.2.1 4.2.2 4.2.3 Grid I	Phase Locked Loop	84 84 85 85 86 87
4	bilit 4.1 4.2	Introd Grid I 4.2.1 4.2.2 4.2.3 Grid I 4.3.1	Phase Locked Loop	84 84 85 85 86 87 89
4	bilit 4.1 4.2 4.3	Introd Grid I 4.2.1 4.2.2 4.2.3 Grid I 4.3.1 4.3.2	Phase Locked Loop Inner Loop Current Controller Outer Loop Controller Forming Converter Control VSM VSM With Virtual Impedance	84 84 85 85 86 87 89 91
4	bilit 4.1 4.2	Introd Grid I 4.2.1 4.2.2 4.2.3 Grid I 4.3.1 4.3.2 Stabil	Following Converter Control Phase Locked Loop Inner Loop Current Controller Outer Loop Controller Forming Converter Control VSM VSM With Virtual Impedance ity Assessment and Comparison Between Controllers	844 845 856 866 877 899 91
4	bilit 4.1 4.2 4.3	Introd Grid I 4.2.1 4.2.2 4.2.3 Grid I 4.3.1 4.3.2 Stabil: 4.4.1	Phase Locked Loop Inner Loop Current Controller Outer Loop Controller Forming Converter Control VSM VSM With Virtual Impedance ity Assessment and Comparison Between Controllers GFL Small Signal Model	84 84 85 85 86 87 89 91 92
4	bilit 4.1 4.2 4.3	Introd Grid I 4.2.1 4.2.2 4.2.3 Grid I 4.3.1 4.3.2 Stabil	Following Converter Control Phase Locked Loop Inner Loop Current Controller Outer Loop Controller Forming Converter Control VSM VSM With Virtual Impedance ity Assessment and Comparison Between Controllers	844 845 856 866 877 899 91

5	Goi	ing Further Offshore With Grid Forming Converters	101
	5.1	Introduction	101
	5.2	System Under Study And Small Signal Model	103
	5.3	Stability Assessment For Smaller HVAC Cable	106
	5.4	Extending Cable Length	110
	5.5	Concerning Weaker Networks	115
	5.6	Discussion	119
	5.7	Chapter conclusions	121
6	Nov	vel Approach to Power System Restoration Using Offshore	е
	Wii	nd Power Plants	123
	6.1	Scenarios to energize OWPP	125
	6.2	Steady State Analysis	130
		6.2.1 Local network loads	131
		6.2.2 Case studies	133
	6.3	Availability Study	135
		6.3.1 OWPP Case 1	139
		6.3.2 OWPP Case 2	142
	6.4	Chapter conclusions	144
7	Nov	vel Grid-Forming Control Strategy for Enhanced Power Sys	-
	tem	n Restoration	146
	7.1	Introduction	146
	7.2	EMT Analysis	147
		7.2.1 Energisation sequence	149
		7.2.2 Results	151
		7.2.3 Discussion	162
	7.3	SSM Analysis	165
		7.3.1 Model linearisation	165

		7.3.2	Small signal model validation	167
		7.3.3	Stability analysis	167
	7.4	Chapt	er Conclusions	171
8	Con	clusio	ns	174
	8.1	Genera	al Conclusions	174
	8.2	Future	e Work	178
\mathbf{A}	Refe	erence	frames	206
	A.1	Clarke	e transformation	206
		A.1.1	From abc to $\alpha\beta0$	206
		A.1.2	Clarke transformation instantaneous power theory	207
	A.2	Park t	ransformation	209
		A.2.1	From abc to $qd0$	209
		A.2.2	Park transformation instantaneous power theory	210
В	Syst	tem A	nd Controller Parameters	211
	B.1	System	n parameters	211
	B.2	Conve	rter controller parameters	212
	B.3	Design	ning shunt compensations	212
\mathbf{C}	Stat	e-Spac	ce Matrices For The Power System	214
D	Para	ametei	rs for PSR Studies	216
	D.1	Appen	ndix D.1	218
${f E}$	Sta	te Spa	ace Matrices for Controller Models	223
	E.1	Filters	s, Park and Park Inverse Transformations	223
		E.1.1	Low Pass Filter	223
		E.1.2	Park Transformation	224
		E.1.3	Inverse Park Transformation	225

	E.2	Grid-I	Following Controller	226
		E.2.1	Phase Locked Loop	226
		E.2.2	Outer Loop Controller	226
	E.3	Grid-I	Forming Controller	230
		E.3.1	Power loop	230
		E.3.2	Voltage loop	231
		E.3.3	Power and Voltage Calculations	232
\mathbf{F}	Wir	nd Sne	ed and Power Curves	234
-		-		
	F.1	OWPI	P Case 1	234
		F.1.1	Wind Speed	234
		F.1.2	Power Curve For the NNG Wind Turbines	235
	F.2	OWPI	P Case 2	236
		F.2.1	Wind Speed	236

2.1	Synthetic inertia emulation after frequency drop	15
2.2	Possible power system restoration from OWPP	26
2.3	Power system restoration from OWPP-anchor vs. top-up solutions	27
2.4	GFL converter controller working principle	29
2.5	GFL controller with power and voltage outer loops connected to a	
	one-line power system	30
2.6	GFM converter controller working principle	34
2.7	GFM converter acting as a voltage source	35
2.8	Droop characteristics for P/f and Q/V	36
2.9	Droop control diagram with droop loop, voltage outer loop and	
	current inner loop	38
2.10	GFM controller connected to one-line system	43
3.1	Scheme of the OWPP connected to a power system	55
3.2	Equivalent electrical diagram of a VSC converter connected to a	
	three-phase power transmission system and grid	58
3.3	One-line $\pi\text{-model}$ representation of an HVAC cable section $\ .\ .\ .$	60
3.4	Final equivalent one-line $\pi\text{-model}$ representation of an HVAC cable	
	section	60
3.5	Distributed model of the one-line π -model representation	61
3.6	Distributed model of the one-line π -model representation	62

3.7	One-line diagram of the Thevenin equivalent grid	63
3.8	Scheme of the one-line onshore RL loads	65
3.9	System configurations (A1, A2, and A3) of shunt reactors distri-	
	bution for the transmission system	67
3.10	One-line diagram of an OWPP connected to a load	69
3.11	Illustrative capital cost comparison of A1, A2, and A3	71
3.12	OWPP and network one-line impedance base model	72
3.13	Voltage magnitude when varying P and Q as function of the power	
	factor, $cos(\phi)$	75
3.14	PV curves for different power factors	75
3.15	Voltage stability limits for different HVAC export cable lengths $$.	76
3.16	Voltage stability curve on the PQ plane for transmission line with	
	and without shunt compensation	78
3.17	Converter operation area in the PQ plane	79
3.18	Voltage profile for an 80 km HVAC export cable for A0 (no com-	
	pensation), A1, A2 and A3	81
3.19	Impact of varying SCR and $\rm X/R$ in the voltage profile for an 80	
	km HVAC export cable	82
4.1	GFL controller with active and reactive power as inputs of the	
	outer loop	89
4.2	GFM controller connected to one-line system	90
4.3	GFM controller connected to one-line system, with virtual impedance	92
4.4	Scheme of linearised system (SSM) for the GFL converter controller	95
4.5	Scheme of linearized system (SSM) for the GFM converter controller	97
5.1	One-line diagram of an OWPP connected via an HVAC transmis-	
	sion system to the electrical grid	104

5.2	Validation of SSM against EMT results for a 0.01 pu active power
	jump
5.3	Step response for both SVCC and VSM for power and voltage
	operating points
5.4	Disk margins for GFL and GFM for active power and voltage op-
	erating points
5.5	Disk margins for active power operating points and for both $\operatorname{GFM}/\operatorname{GFL}$
	controllers and different system arrangements for a cable of $80~\mathrm{km}$ 111
5.6	Disk margins for active power operating points and for both $\operatorname{GFM}/\operatorname{GFL}$
	controllers and different system arrangements for a cable of 120 km 112 $$
5.7	Disk margins for active power operating points and for both $\operatorname{GFM}/\operatorname{GFL}$
	controllers and different system arrangements for a cable of 150 km 112 $$
5.8	Gain and phase disk margins across the frequency spectrum 113
5.9	Disk margins for different SCR and X/R for a cable of 80 km 116 $$
5.10	Disk margins for different SCR and X/R for cables of 120 km and
	150 km
5.11	Gain and phase disk margins across the frequency spectrum for
	SCR and X/R variation
6.1	One-line diagram of studied system with the different APS located
	onshore, offshore, and inside WT (self-start scenario) 127
6.2	One-line diagram of Scenario S1, with the APS located on shore $$. $$
6.3	One-line diagram of scenario 2, with self-start capable WTs 128
6.4	One-line diagram of scenario 3, with the APS located offhore 129
6.5	Energisation steps for three different local network demands, Cases,
	1, 2 and 3
6.6	OWPP and local network (P,Q) OP: Case 1 $\dots \dots 136$
6.7	OWPP and local network (P,Q) OP: Case 2 $\dots \dots 136$
6.8	OWPP and local network (P,Q) OP: Case 3

6.9	Sketch of methodology used to study power and energy availability	
	of an OWPP $\ \ldots \ \ldots \ \ldots \ \ldots \ \ldots \ \ldots$	138
6.10	Active power average daily production	140
6.11	Active power average daily production	143
7.1	One-line diagram of the EMT model analysed	148
7.2	Offshore transformer energisation without any inrush current mit-	
	igation technique $\ldots \ldots \ldots \ldots \ldots \ldots$	153
7.3	Offshore transformer energisation with POW for a GFM penetra-	
	tion of 20%	154
7.4	Inrush currents after transformer energisation for different GFM	
	penetration percentages	154
7.5	Cable and shunt reactors compensation for a GFM penetration of	
	40%	156
7.6	Inrush currents after cable and shunt compensation energisation	
	for different GFM penetration percentages	157
7.7	Active power at the load and converter control action (GFM and	
	GFL) for an 80% GFM penetration during block loading for the	
	top-up scenario	158
7.8	Voltage and frequency at the PCC during block loading for the dif-	
	ferent GFM penetrations (from 0% to 100%) for the top-up scenario	o159
7.9	Frequency drop to compare GFM and GFL behaviour	161
7.10	Sketch of the supervisory frequency support controller	162
7.11	Voltage and frequency at the PCC during block loading for the	
	different GFM penetrations (from 0% to 100%) without frequency	
	control for the anchor scenario	163
7.12	Voltage and frequency at the PCC during block loading for the	
	different GFM penetrations (from 0% to 100%) with frequency	
	control for the anchor scenario	164

7.13	GFM and GFL converters forming the aggregated wind farms and	
	power system for SSM analysis	166
7.14	Scheme of the linearised system (SSM) with both GFM and GFL	
	aggregated wind farms and controllers and power system \dots	167
7.15	SSM validation for both GFL (left) and GFM (right) converter	
	controllers: Active power reference, $P_{ref,GFL}$ and $P_{ref,GFM}$, PCC	
	active power from EMT model, $P_{cc2,EMT}$ and $P_{cc1,EMT}$, and PCC	
	active power from SSM, $P_{cc2,SSM}$ and $P_{cc1,SSM}$	168
7.16	DM results for the top-up scenario	169
7.17	DM results for the anchor scenario	170
F.1	Weibull distribution for OWPP Case 1 and monthly average wind	
	speed	235
F.2	OWPP Case 1 wind turbine computed power curve	236
F.3	Weibull distribution for OWPP Case 2 and monthly average wind	
	speed	237
F.4	BwB OWPP wind turbine computed power curve	238

List of Tables

2.1	Comparison of Patents on Self-Starting Wind Turbines	48
2.2	Comparison of Self-Starting Wind Turbine Papers	52
3.1	Illustrative capital cost comparison	70
3.2	Shunt compensation for different cable lengths	77
3.3	Arrangements of shunt compensation analysed	80
3.4	Power factor for three cable lengths, and for the case of no com-	
	pensation (A0) and for the three different arrangements	83
4.1	State-space, LTI, matrices for filters and transformations used	94
4.2	State-space, LTI, matrices for the GFL controller	95
4.3	State-space, LTI, matrices for the GFM controller	98
5.1	GFL controller parameters for preliminary study	107
5.2	GFM controller parameters for preliminary study	107
5.3	OS and ST for voltage operating points	107
5.4	OS and ST for voltage operating points	108
5.5	Advantages and disadvantages of GFL and GFM control strategies	
	based on the paper findings	119
6.1	Scenarios for WT-OWPP energisation	126
6.2	Wind speed, converter voltage angle and magnitude for the differ-	
	ent study cases	135

List of Tables

6.3	Average daily active power and energy production for OWPP Case 113	} 9
6.4	OWPP Case 1 P90 values for different months	11
6.5	Energy and Power Data for Different Wind Scenarios 14	12
6.6	Power and Energy Properties of the OWPP Case 2	12
6.7	OWPP Case 2 P90 values for different months	13
6.8	Energy and Power Data for Different Wind Scenarios 14	14
7.1	Technical requirements analysed via EMT simulations	17
7.2	Energisation sequence of PSR	51
7.3	Top-up generation - Results of EMT simulations for different GFM $$	
	penetrations	34
7.4	Anchor generation - Results of EMT simulations for different GFM $$	
	penetrations	j5
B.1	System parameters	1
B.2	GFM converter parameters for A2, 80 km	2
В.3	GFL converter parameters for A2, 80 km	2
B.4	Reactive power measured and shunt reactors values in (H) for the	
	three cable lengths, for $SCR = 3$ and $X/R = 5 \dots 21$	13
D.1	Power system parameters	16
D.2	(P,Q) pairs, R_{LD} and C_{LD} for local network studies	17
D.3	Offshore transformer parameters	17
D.4	Grid forming converter controller parameters	17
D.5	Grid following converter controller parameters	8
F.1	Wind Turbine Properties for OWPP Case 1	35
F.2	Wind Turbine Properties for OWPP Case 2	38

Abbreviations

The following abbreviations are used in this manuscript:

APS Auxiliary Power Supply

BESS Battery Energy Storage System

BS Black Start

BSU Black Start Unit
DG Diesel Generator

DES Distributed Energy Resources

DM Disk Margin

EMT Electromagnetic Transient

FFR Fast Frequency Response

FLL Frequency-Locked Loop

GFL Grid-Following

GFM Grid-Forming

GWEC Global Wind Energy Council

IBPS Inverter-Based Power Source

LTI Linear Time-Invariant

HVAC High Voltage Alternating Current

HVDC High Voltage Direct Current

MIMO Multi-Input, Multi-Output

NBSU Non Black Start Unit

Chapter 0. Abbreviations

OWPP Offshore Wind Power Plant

OS Overshoot

PCC Point of Common Coupling

PIR Pre-Insertion Resistor

PLL Phase-Locked Loop

POW Point On Wave

PSR Power System Restoration

PT Power Transmission

PV Photovoltaics

RES Renewable Energy Sources

SCR Short Circuit Ratio

SG Synchronous Generators

SISO Single-Input, Single-Output

SIF Strategic Innovation Fund

SO System Operator

ST Settling Time

TSO Transmission System Operator

VSC Voltage Source Converter

VSM Virtual Synchronous Machine

WT Wind Turbine

Acknowledgements

I would like to express my gratitude to those who have supported and contributed to the completion of my PhD. Firstly, I wish to extend my thanks to my supervisor, Agustí Egea-Alvarez, for the great moments shared, guidance, expertise, and encouragement throughout this research. Our incredible trips together, especially to Qatar, countless coffees, lunches, dinners and walks, and even the time spent at some rather questionable coffee spots like the Spitfire, have made this journey not only rewarding but also unforgettable. I am also grateful to my supervisor at Siemens Gamesa Renewable Energy, Thyge Kneuppel, for the support throughout the PhD. Special thanks to my PhD colleagues whose assistance with technical advice and software tools have been crucial to the completion of this thesis. I would like to acknowledge the support of the Wind & Marine Energy Systems & Structures Centre for Doctoral Training (EP/S023801/1) and the Power Electronics, Drives and Energy Conversion department for providing the necessary resources and facilities that have been essential for this research. I also extend my sincere thanks to all the individuals involved in the SIF Blade Project. Their collaboration and contributions have significantly supported and enriched my research. My heartfelt appreciation goes to my family and friends for their unwavering support, patience, and understanding throughout this challenging journey. Their encouragement has been a source of strength and motivation. Thank you all for your support and encouragement.

Chapter 0. Acknowledgements

Chapter 1

Introduction

In recent years, the global energy landscape has undergone a profound transformation, driven by the dual imperatives of combating climate change and addressing the depletion of fossil fuel reserves. As the effects of climate change become increasingly evident, manifesting in more frequent and severe weather events, rising sea levels, and shifting ecosystems [1,2], the urgency to reduce greenhouse gas emissions has never been greater. This urgency has catalyzed a worldwide shift towards renewable energy sources (RES), which are not only environmentally sustainable but also becoming more economically viable [3].

Central to these efforts is the Paris Agreement [4], an international treaty adopted in 2015. It has set the goal of limiting global temperature rise to well below 2°C above pre-industrial levels, with aspirations to cap it at 1.5°C. A significant increase in the share of RES in the global energy mix is required to achieve this target. Consequently, several countries worldwide are implementing policies and initiatives to accelerate the adoption of renewable energy technologies [5,6].

The global capacity of RES has been growing steadily over the years, with RES now accounting for 20.52% of primary energy consumption in the United Kingdom (UK) and 17.93% across Europe (EU) [7]. In 2010, these figures stood at just 3.67% for the UK and 10.06% for the EU, highlighting the significant

growth over time [8].

Offshore wind power plants (OWPPs) play an increasingly important role in this transition [9,10]. OWPPs are recognised as one of the most secure, clean, and reliable forms of renewable energy [11]. As of 2023, global offshore wind capacity reached 72.7 GW [12]. China leads the market with 31.5 GW in operation and 6.3 GW under construction, followed by the UK, which has 14.7 GW in operation and approximately 4 GW under construction [13]. The UK is projected to surpass 40 GW by 2030 [14]. The Global Wind Energy Council (GWEC) Market Intelligence forecasts that over 380 GW of new offshore wind capacity will be added between 2023 and 2032, bringing total capacity to 447 GW by the end of the decade [15].

While the global increase in the adoption of RES marks a significant achievement in the fight against climate change, it also introduces new challenges to the stability and reliability of the power grid. One of the most pressing concerns is the weakening of the grid network, primarily due to the decommissioning of conventional fossil fuel-based power plants in favour of RES [16,17]. Traditional power plants, particularly those using synchronous generators, have played a crucial role in maintaining grid stability due to their inherent physical characteristics.

Synchronous generators, which are typically found in fossil fuel power plants, possess a substantial amount of rotational inertia because of their large, heavy spinning masses. This inertia acts as a buffer against sudden changes in power demand or supply, helping to maintain a stable frequency within the electrical grid. However, as these conventional generators are increasingly being replaced by RES, such as wind and solar power, which do not rely on heavy rotating machinery, the overall system inertia decreases. This reduction in inertia can lead to a more fragile electrical system, making it more susceptible to frequency fluctuations and, consequently, less resilient to disturbances [18, 19].

In addition to this complex inertia challenge, the integration of RES introduces other complexities related to the inherent characteristics of these energy sources.

Unlike traditional power plants, RES are variable, unpredictable, and intermittent by nature. Wind and solar power generation depend on weather conditions, which can change rapidly and are often difficult to predict accurately. This variability can lead to significant fluctuations in power output, complicating the task of balancing supply and demand in real time. Furthermore, the intermittency of RES, where power generation can start and stop unexpectedly, poses additional challenges for grid operators who must ensure a continuous and reliable power supply.

These factors combined, reduced inertia, variability, unpredictability, and intermittency, contribute to an increased vulnerability of the electrical grid, presenting new challenges for maintaining grid reliability. Addressing these challenges requires a thorough understanding of grid dynamics and the development of advanced control strategies to ensure that the increasing penetration of RES does not compromise the reliability of the power system.

In addition to the challenges previously mentioned, there are further complexities specific to OWPPs. As OWPPs are being commissioned further from shore to harness stronger wind resources and deploy larger turbines, new technical hurdles emerge. One significant area of focus is the transmission of power from OWPPs commissioned far from shore, using long HVAC export cables. Another area of focus is the role of OWPPs in power system restoration (PSR), a service traditionally provided by synchronous generators.

To fully exploit the potential of OWPPs, it is necessary to address these gaps in academic research, particularly in making OWPPs more resilient and reliable within the grid system. This includes treating OWPPs similarly to synchronous machines, allowing them to provide inertia and support grid stability effectively.

Additionally, as offshore projects aim to export increasing amounts of power, providing increased technology readiness and competitiveness is crucial. To achieve this, OWPPs must be elevated to the same level as conventional power stations in

terms of reliability and cost-effectiveness, ensuring their viability as a cornerstone of future energy systems.

1.1 Objectives and Summary Of Work

This thesis focuses on two of these key challenges. The first challenge relates to the stability of a power system connected to an OWPP via a long HVAC export cable. This design introduces several complexities, primarily due to the length of the cable. Long HVAC cables generate significant amounts of capacitive reactive power, which must be managed using additional equipment, such as shunt reactors and converter control strategies. This thesis investigates various system configurations and compares two converter control strategies: grid-following (GFL) and grid-forming (GFM).

The second challenge examines the ability of OWPPs to provide PSR. The study analyses whether OWPPs can meet the technical requirements for PSR and whether the system remains stable during block loading, especially for different levels of GFM penetration.

The objectives of this thesis are as follows:

- Analyse the impact of HVAC cables and shunt reactors on the stable and reliable transmission of power from an OWPP
- Evaluate the impact of converter control strategies (GFM and GFL) on system stability and identify which provides enhanced stability
- Determine whether GFM controllers allow for an increase in HVAC cable length while maintaining stable operation
- Study the technical requirements for PSR from an OWPP
- Assess whether an OWPP can provide PSR while meeting technical requirements

• Investigate the optimal GFM penetration level for enhanced stability during PSR

1.2 Thesis Outline

This thesis comprises seven additional chapters. Chapter 2 provides an overview of technologies and challenges in renewable energy systems. It discusses the grid-following and grid-forming converter controllers, including an introduction to various grid-forming control strategies, their operating principles, and associated challenges. The concept of self-starting wind turbines is also introduced, highlighting their capability to initiate operation and inject power into the electrical grid without relying on an external power supply. Furthermore, the chapter outlines the broader challenges associated with renewable energy integration, focusing specifically on the key topics addressed in this thesis: the operation and stability of offshore wind power plants, the transmission challenges associated with these systems, and the role of offshore wind power plants in power system restoration.

In Chapter 3, the designed test systems connecting the OWPP to the onshore grid or loads are introduced. The components used in the studies are presented, including the OWPP aggregated model, the transmission system comprising the HVAC cable and shunt reactors, the offshore transformer for PSR purposes, the grid model (Thevenin equivalent), and the resistive-inductive (RL) loads. Additionally, a steady-state analysis is conducted to evaluate the capabilities and limitations of the OWPP in delivering active and reactive power to the grid. A second steady-state study focuses on the voltage profile along the HVAC export cable and the impact of the shunt reactors in maintaining the power factor and voltage within acceptable limits of operation. This chapter also introduces the linearised state-space matrices used for small-signal analysis.

Chapter 4 introduces the converter controllers used in the studies, covering both GFM and GFL approaches. The GFL controller is based on the standard vector current controller, while the GFM controller is an adaptation of the virtual synchronous machine. The chapter provides a detailed explanation of the dynamic equations governing both controllers.

Additionally, this chapter outlines the linearisation approach employed for the small signal stability studies and explains the methods used to assess stability, with a particular focus on disk margins. This discussion establishes the foundation for the analysis presented in Chapter 5.

In Chapter 5 it is presented a study which aims to evaluate the ability of the GFM and GFL controllers to maintain stability with longer HVAC cables and various system configurations. Initially, a shorter cable with a standard compensation approach was analysed. Then, the study was extended to include multiple cable lengths and different system configurations. Additionally, besides assessing the performance of both controllers across a range of cable lengths and system arrangements, the controllers are further compared for scenarios with lower short-circuit ratios (SCR) and X/R ratios as to test the capabilities of both units in weaker grids.

Chapter 6 explores the topic of PSR from OWPPs. It presents a series of scenarios based on the location of the auxiliary power supply for cranking the OWPP, as well as the necessity of GFM wind turbines. GFM wind turbines are required only in the case of self-start wind turbines; otherwise, standard GFL wind turbines may be sufficient. A steady-state analysis is performed to demonstrate that the OWPP can create a range of active and reactive power (P, Q) operating points, capable of meeting the requirements of a network provider. Furthermore, an availability study is performed in order to analyse the capabilities of the OWPP to provide active power taking into consideration wind availability of specific offshore wind farm sites.

Chapter 7 presents an electromagnetic transient (EMT) and small-signal model (SSM) stability analysis comparing the performance of the OWPP during PSR for varying levels of GFM converter penetration. The EMT analysis assesses whether several key requirements—such as voltage and frequency control, block loading, and reactive power at zero crossing—are met for each level of GFM penetration. Challenges related to the energization of the onshore transformer, HVAC cables, and shunt reactors are also addressed. The small-signal stability analysis investigates whether a certain percentage of GFM converters enhances stability for different operating points, varying by active and reactive power at the load.

Finally, Chapter 8 presents the conclusions of this work and outlines future research directions. Appendices are included to provide explanations of reference frames, the parameters used throughout the studies, and the state-space matrices for the small-signal model analysis.

1.3 Scientific Contributions

The following contributions are presented in this thesis:

- Comparative evaluation of grid-forming and grid-following converter control strategies for offshore wind power plants connected through long high voltage alternating current cables.
- Investigation of the influence of shunt reactor placement on system stability for extended submarine cable transmission.
- Analysis of control strategy performance under varying transmission distances, grid strengths, short-circuit ratios, and X/R ratios.
- Development of a control and compensation framework combining optimal shunt reactor placement with advanced converter control.

- Assessment of offshore wind power plants' capability to provide power system restoration using different control strategy mixes.
- Identification of optimal grid-forming penetration ranges for distinct restoration scenarios.
- Design of an external frequency supervisory controller to enhance frequency stability during restoration events.

1.4 List Of Publications

The following conference works have been published as a result of this thesis:

- R. Alves, A. Egea-Àlvarez, and T. Knuppel, "Capabilities and limitations of black start operation for system restoration from offshore wind farms," 2024 4th International Conference on Smart Grid and Renewable Energy, pp. 1–6, 2024.
- R. Alves, A. Egea-Àlvarez, and T. Knuppel, "Grid forming and grid following comparison for an offshore wind farm connected via a HVAC cable,"
 21st Wind and Solar Integration Workshop (WIW 2022), pp. 9–16, 2022.

This thesis has resulted in the following journal publications:

- Alves, Rui, Ning Yang, Lie Xu, and Agustí Egea-Àlvarez. 2025. "Enabling Power System Restoration from Offshore Wind Power Plants in the UK" Energies 18, no. 2: 436. https://doi.org/10.3390/en18020436
- Alves, Rui, Thyge Knuppel, and Agustí Egea-Àlvarez. 2025. "Grid-Forming:
 A Control Approach to Go Further Offshore?" Electricity 6, no. 1: 4.
 https://doi.org/10.3390/electricity6010004

Chapter 2

Technologies and Challenges in Renewable Energy Systems

This chapter provides an in-depth review of the primary topics relevant to this research. It begins with the broader issues associated with the growing penetration of RES into the electrical grid, identifying and analysing six principal challenges associated with this shift:

- System strength and stability concerns
- Inertia and frequency control
- Fault ride-through response
- Adverse system interactions and protection systems
- OWPP and transmission challenges
- PSR from OWPP

For the first four challenges, a concise overview is provided to give context to the issues faced by modern power systems as RES integration increases. However, the final two challenges—Offshore Wind Power Plants and Transmission challenges, and Power System Restoration from Offshore Wind Power Plants—are particularly important to this thesis. Dedicated sections examine these topics in greater depth, thoroughly discussing their impact on power system stability, control, and restoration.

Then, an examination of power converter controllers used in RES, specifically distinguishing between GFL and GFM configurations, is introduced. Traditionally, GFL controllers have been the standard choice in RES applications. However, as the electrical power system transitions towards a more inverter-dominated landscape, GFM controllers are increasingly regarded as a viable solution to address emerging stability and operational challenges.

Subsequently, a section is devoted to introducing the concept of self-starting wind turbines, a topic that will be examined further in the context of power system restoration studies. These turbines have the unique capability to initiate operation without reliance on external power sources, positioning them as a promising solution for enabling power system restoration from OWPPs.

2.1 Renewable Energy Penetration Challenges

The global shift towards renewable energy, particularly the widespread integration of inverter-based power sources (IBPS) such as onshore and offshore wind, as well as solar photovoltaic (PV) systems, introduces significant technical challenges to maintaining the stability and reliability of the electrical grid. As the penetration of renewable energy increases, power systems are subjected to increasingly complex dynamic behaviours, reduced system strength, diminishing inertia, and difficulties in frequency regulation. Addressing these issues requires the development of innovative strategies and technologies to ensure the grid remains both secure and resilient. This section outlines some of the key challenges from the perspective of system operators, challenges that are expected to intensify as IBPS penetration levels continue to rise [20, 21].

Power system restoration and challenges from OWPP transmission systems are addressed separately, as they are the main topics of this research.

2.1.1 System Strength and Stability Concerns

A primary issue arising from the increasing penetration of IBPS is the deterioration of system strength, particularly in power systems where synchronous generators (SGs) are progressively displaced.

According to [22], system strength can be defined in terms of impedance, which includes contributions from generators, transformers, transmission lines, and loads, or through the mechanical rotating inertia. High impedance corresponds to weaker system strength, leading to undesirable effects such as voltage variations. The mechanical rotating inertia, on the other hand, determines the ability of a system to maintain frequency stability in the short term and also influences its capacity to stabilise variations in voltage angle [23].

Traditionally, system strength is quantified by the short-circuit ratio (SCR) at various nodes within the grid [24]. High SCR values typically denote a more robust system, yet as IBPS replace SGs, system strength diminishes due to a reduction in available fault current [25].

In regions with high IBPS penetration, such as Ireland, Great Britain, and South Australia, system operators (SOs) have had to install synchronous condensers (SCs) to offset this loss in strength. However, while this approach provides some mitigation, it introduces new operational constraints and increased costs [26].

Presently, GFL IBPS are designed to function stably down to a minimum system strength. However, when system strength falls below this threshold—whether due to disconnections of key network components or reduced SG capacity—GFL inverters may lose stability, triggering their automatic disconnection or forcing a significant power runback. In contrast, GFM IBPS can act as voltage sources,

inherently contributing to system strength even in low SCR environments. This makes GFM technology appealing for grids with a high proportion of IBPS, where the ability to maintain voltage and frequency stability is vital to overall system reliability [26,27].

2.1.2 Inertia and Frequency Control

In a power grid, inertia is provided by synchronised generators, which rotate in unison at the same frequency. During normal operation, the system frequency remains stable, as demand is balanced with generation. However, if a fault occurs or generation is lost, an imbalance is created. In such cases, the stored energy in large rotating synchronous generators is released to compensate for the loss, providing the system with a few crucial seconds for the mechanical system to respond to the imbalance. Inertia, traditionally supplied by synchronous generators, plays a vital role in damping the rate of change of frequency (RoCoF) following significant disturbances [28].

However, as renewable energy penetration increases, the synchronous inertia stored in the grid diminishes, creating challenges in maintaining frequency stability [29]. This is particularly concerning in isolated systems or grids with limited interconnections, such as those in Great Britain, Ireland, and Tasmania, where a minimum level of synchronous inertia is critical to prevent cascading failures after significant generation or load disconnections [26].

In low-inertia systems, fast frequency response (FFR) from GFL IBPS can only partially substitute the missing inertia, and even then, precise coordination with remaining SGs is required to maintain stability. The rapid dynamic response of IBPS, while advantageous in some circumstances, can destabilise the system if not correctly managed. Studies conducted by National Grid and EirGrid have demonstrated that as IBPS penetration exceeds 65%, the system becomes increasingly sensitive to frequency deviations, and traditional primary frequency

Chapter 2. Technologies and Challenges in Renewable Energy Systems

response mechanisms fail to provide adequate control [30].

To address this, GFM power converters have been proposed as a source of synthetic inertia [31–33]. Using advanced control strategies, these converters can mimic the inertial response of traditional SGs, helping to slow the rate of frequency change and stabilise the grid. Despite the promise of GFM technology, it is still in its early stages, and its widespread deployment faces both technical and economic challenges, particularly in the context of large-scale renewable integration [27].

An example of synthetic (or virtual) inertia is illustrated in Figure 2.1, case studied for a full back-to-back (full-scale converter) Type 4 wind turbine generator. In the study conducted in [34], a multi-rotor wind turbine demonstrated the capability to provide inertia emulation. In this particular scenario, the system experiences a frequency drop from 50 Hz to 49 Hz. At this point, the kinetic energy stored in the rotating mass of the wind turbine is used to emulate inertia through the implemented controller. Specifically, as the frequency decreases, the current reference is adjusted to increase power injection into the grid. This, in turn, causes the rotational speed of the wind turbine to decrease as energy is extracted from its stored inertia.

Subsequently, at t=10 s, the turbine returns to normal operation, which is followed by a temporary power reduction due to the inertia of the wind turbine and its associated rotational speed dynamics. This response is governed by an inertia emulation controller, which continuously compares the system frequency with its natural reference. Based on the detected frequency deviation, the controller adjusts the active current injected into the converter, thereby helping restore the system frequency to its nominal value.

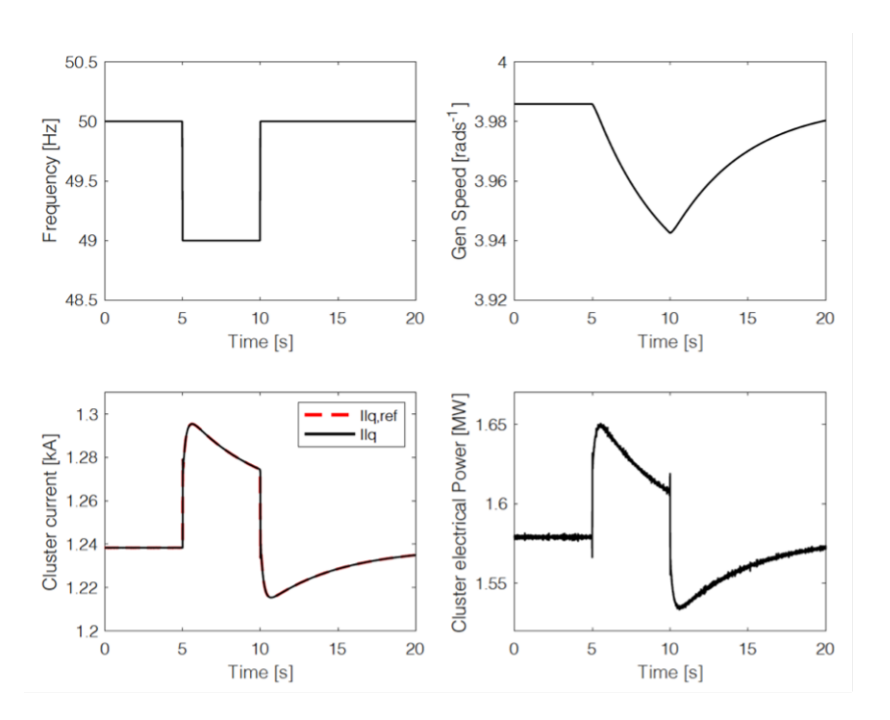


Figure 2.1: Synthetic inertia emulation after frequency drop

2.1.3 Fault Ride-Through Response

In IBPS, particularly for offshore wind power plants, maintaining connection to the grid during voltage disturbances is essential. These systems must provide active and reactive current injections to support system recovery [35]. While fast active power recovery is less critical in well-connected grids, it becomes vital in islanded or weakly interconnected networks. However, GFL IBPSs may face limitations in simultaneously delivering high levels of active and reactive current, especially without significant overcurrent capacity [20,36]. Additionally, in weak grid conditions, GFL systems may need to slow down their current injection to maintain stability, although modern GFL control strategies help address this challenge. In contrast, GFM IBPSs are more resilient, providing stable responses regardless of grid strength, and can inject current quickly without risking system instability [26,27].

Another concern is the impact of sudden changes in the voltage phase an-

gle, which can disrupt the control systems of GFL IBPSs [37]. The severity of these disruptions depends not only on the depth of voltage dip but also on the suddenness of the phase shift. Therefore, it is important to consider a variety of fault scenarios rather than just focusing on severe, close-in faults. GFM IBPSs, however, are better suited to handle such disturbances, as they can prevent rapid angular changes and improve overall system stability during significant disturbances.

2.1.4 Adverse System Interactions and Protection Systems

The large-scale integration of IBPS also introduces risks of adverse system interactions, including phenomena such as subsynchronous resonance and torsional interactions, which were historically confined to systems dominated by synchronous machines [20,38,39]. These interactions have become more difficult to predict and manage with the introduction of numerous IBPS, particularly in weak grids where oscillatory instabilities can occur across a broad frequency range [30].

Protection systems designed for grids dominated by SGs face challenges as IBPS penetration increases. Fault current availability is diminished in IBPS-dominated grids, as are the sequence components required by traditional protection schemes [40, 41]. Consequently, protection systems may fail to accurately detect and isolate faults, especially in cases where IBPS do not provide sufficient negative-sequence current. In response, jurisdictions such as Germany have updated grid codes to require negative-sequence current injection from IBPS to address these concerns [30].

2.2 Offshore Wind Power Plants and Transmission Challenges

OWPPs, increasingly located further from shore, hold the potential to provide services to SOs. Through advanced GFM or GFL converter controls, OWPPs can contribute significantly to critical grid functions, including inertia, frequency regulation, grid stability during disturbances, and PSR. However, one of the main challenge lies in maintaining the stability of the power system when OWPPs are connected via long HVAC transmission cables.

While HVAC technology is typically preferred over HVDC due to its lower cost and technological maturity, long HVAC cables introduce operational challenges that must be managed to ensure stable system operation. Over longer distances, HVAC cables suffer from increased power losses caused by capacitive effects, which lead to reactive power imbalances and variations in voltage levels along the transmission line. To mitigate these reactive power issues, shunt reactors are often employed to provide compensation, ensuring that voltage levels remain within acceptable limits [42–44]. Without such compensation, voltage instability could jeopardise both the performance of the offshore wind farm and the stability of the onshore grid. Although HVDC cables offer advantages such as lower losses and the elimination of the need for reactive power compensation, HVAC remains the preferred option for many OWPP projects due to its economic benefits and the simplicity of the technology [45].

2.2.1 Cost Comparison and Maturity

Cost is a primary consideration when comparing HVAC and HVDC transmission systems. Research demonstrates that HVDC becomes more economical over very long distances, typically beyond 600–800 km for overhead lines and approximately 50 km for submarine cables, due to its lower transmission losses. How-

ever, the high initial cost of HVDC converter stations makes it less attractive for shorter distances [45, 46]. HVAC, on the other hand, remains cost-effective for distances typically encountered in offshore wind projects, as the lower upfront infrastructure costs outweigh the potential savings from reduced line losses in HVDC systems [45,47]. For many offshore wind farms located within 50–100 km from shore, HVAC remains the most economically viable solution due to its lower capital costs and the well-established nature of the technology [45,46].

2.2.2 System stability and Reactive Power Compensation

One of the most significant technical challenges associated with HVAC transmission systems is the capacitive charging current generated over long distances, which can result in small-signal voltage instability and reduction of power factor. This is particularly problematic in OWPPs located far from shore, where the longer transmission distances exacerbate reactive power imbalances [45, 47]. To address this issue, shunt reactors are employed to absorb excess reactive power, maintain small-signal stability and keep the voltage level along the transmission line within acceptable pre-determined transmission system operator voltage levels. The placement of these reactors, both at the shore and mid-cable, is crucial for ensuring the reliable operation of HVAC transmission systems [44, 48]. Effective reactive power compensation not only ensures stable voltage levels but also mitigates harmonic distortions and resonance, which can lead to system instability [49].

2.2.3 The Role of GFM Controllers in HVAC Transmission

GFM controllers may play a critical role in managing the stability challenges posed by long HVAC cables. In contrast to GFL converters, which as previously

mentioned, rely on PLLs or FLLs to synchronise with the grid and require a strong grid connection, GFM converters actively regulate both voltage and frequency. This makes them well-suited for OWPPs connected via long HVAC cables, where grid strength is reduced, and SCR are lower [20, 22, 50]. GFM controllers may provide virtual inertia and enhance grid stability by mitigating voltage dips and phase angle variations that occur as a result of reactive power generation from long transmission lines [46, 47].

The ability of GFM controllers to stabilise voltage and regulate frequency across long HVAC cables significantly reduces the risk of system instability. By providing GFM capabilities, these controllers ensure continuous power delivery even in weaker grids, making them essential for the reliable operation of OWPPs. Furthermore, GFM technology helps mitigate large disturbances, such as faults or the loss of generation, by actively controlling the power flow and supporting the grid during recovery [49,50].

2.2.4 Competitiveness of HVAC with GFM and Reactive Power Compensation

When combined with advanced GFM controllers and effective reactive power compensation techniques, HVAC transmission systems remain competitive with HVDC, particularly for offshore wind farms within moderate distances. GFM controllers enable stable voltage and phase angle regulation even under varying power conditions, reducing the need for disconnections or significant power runbacks [45,46]. The combination of GFM technology and optimally placed shunt reactors extends the feasible range for HVAC transmission, allowing it to remain a viable and cost-effective solution for many offshore wind projects [48].

2.2.5 Addressing Gaps in Existing Research

This thesis focuses on the challenges associated with using GFM and GFL converters in OWPPs connected via long HVAC cables, particularly under varying active power operating points. The research explores how these converters perform under different wind conditions and in weaker network environments where SCRs and X/R ratios are lower. These conditions increase the vulnerability of offshore grids to stability issues, making the choice of converter and system configuration critical to maintaining stable grid operation. Existing research often overlooks the specific challenges posed by long HVAC cables, reactive power compensation, and weaker grid conditions, leaving gaps in the literature.

By analysing the performance of GFM and GFL converters under these conditions, this thesis aims to provide a detailed analysis into optimal converter configurations and strategies for maintaining grid stability even in scenarios with lower SCRs and higher reactive power demands.

With the intention of harnessing steadier and stronger winds, and due to new technologies and improvements in offshore infrastructures, OWPP are being commissioned further away from shore. This increase in distance leads to the need for longer submarine export cables. These may be either High Voltage Alternate Current (HVAC) or High Voltage Direct Current (HVDC).

HVAC connections are preferred due to their maturity and reliability. However, as the distance from OWPP to the onshore transmission system increases, it is suggested that HVDC connections become cost competitive [51], with a break-even-distance that is considered to be between 80-100 km [46, 52, 53].

Several considerations are being given to ways in which HVAC technology can be used for longer, yet reliable and robust export cables [51,54–58]. XLPE cables have a high inherent capacitance which is dependent on the cable length, insulation and construction materials. This capacitance causes a leading power factor, and therefore a leading reactive power. To maintain the power quality and

Chapter 2. Technologies and Challenges in Renewable Energy Systems

the voltage stability of the system, reactive power needs to be balanced, which is achieved with shunt reactive power compensation devices. With the addition of lagging reactive power components in the system, the power factor can be adjusted closer to unity, reducing losses and enhancing transmission efficiency and stability [59,60].

Several projects consisting of long HVAC export cables with shunt reactive compensations have already been commissioned. An inter-connector was installed between Malta and Sicily with a voltage of 245 kV, an overall cable length of 117.6 km and two asymmetrical shunt reactor compensations in both ends of the cable [61,62]. East Anglia 1 OWF commissioned a 420 kV - 100 km HVAC export cable which exports 714 MW [63]. West of Adlergrudnd involves a 90 km long HVAC export cable with a nominal voltage of 245 kV, exporting 250 MW [64].

Shunt compensation close to the connection point between sea and land cables were installed in the Horns Rev B OWPP, which exports 210 MW at a nominal voltage of 150 kV. In [65] it was seen that the shunt compensation commissioned led to a reduction of the cable loading, a reduction of yearly losses of 23 %. Further, the voltage was kept between the acceptable limits established by the Danish transmission system operator (TSO). The overall cable length was slightly over 100 km. However, the undersea export cable considered is only 42 km.

It is also analysed in several studies ways that the shunt reactors can be optimized, as well as its location. A multi-objective optimization function was utilized in [47] to determine the optimal location and value for shunt reactive compensations. This was performed taking into account the reduction of power losses, the minimization of the cost of such compensations and improvement in the voltage profile. It was seen from the study that the employment of these compensations depends on the voltage level of the overall system and the cable length - for lower voltages and shorter distances two reactors would suffice; however, for longer distances, the configuration with three reactors provides lower losses and

Chapter 2. Technologies and Challenges in Renewable Energy Systems cost.

Following the previous study, Dakic et al. developed a study comparing HVAC transmission with shunt compensations, varying their location, and VSC-HVDC technology [48]. It was concluded that the most cost-effective transmission system is the HVAC topology with three shunt reactors, including one located offshore at the mid-point of the cable. This solution is reported to be suitable for high OWPP rated power and transmission distances between 70 km and 150 km. Among all voltage levels analysed, 220 kV was identified as the most favourable. However, while this configuration may appear cost-effective in a theoretical analysis, its practical implementation could be questionable. In particular, installing a mid-cable shunt reactor would likely require an offshore substation, which introduces substantial logistical and economic challenges. From a practical engineering perspective, such a requirement could significantly affect the overall feasibility of the solution due to the high costs and complexity associated with offshore substation infrastructure.

The aim of this study was to analyse the stability of the proposed configuration by comparing the performance of the OWPP when operating under two different converter control modes, GFM and GFL, in order to assess whether the choice of control strategy has a significant impact on system stability.

2.3 Power System Restoration from Offshore Wind Power Plants

2.3.1 Overview of Power System Restoration from Offshore Wind Power Plants

Offshore wind power plants, like other renewable energy sources, are increasingly recognised as key players in power system restoration, traditionally a role per-

Chapter 2. Technologies and Challenges in Renewable Energy Systems

formed by synchronous generators. PSR, or black start, refers to re-energising the grid after a full or partial blackout. Historically, this has been the responsibility of synchronous machines, but as these generators are decommissioned in favour of renewable sources, OWPPs are poised to take on this role.

OWPPs equipped with grid-forming control strategies have the potential to autonomously establish grid voltage and frequency. This capability has been explored in projects such as SIF Blade in the UK, which aims to demonstrate the feasibility of OWPPs providing black start services. However, several technical challenges remain, particularly around the ability to supply consistent active and reactive power during restoration while maintaining grid stability [26, 30].

One key challenge is that wind turbines, unlike conventional generators, cannot self-start without external power. Auxiliary power, essential for starting the turbines, can be provided by small diesel generator units, battery energy storage systems, or self-starting turbines, though the latter are not yet commercially viable. Ensuring reliable auxiliary power and managing it effectively during PSR events is crucial for OWPPs to play a major role in system restoration.

The intermittent nature of wind energy introduces further complexities. Variable wind speeds may limit the steady power output required for grid re-energisation and block loading. To overcome these issues, reliable auxiliary power and sufficient reactive power capability are essential for OWPPs to contribute to both the anchor and top-up stages of PSR.

Despite the potential of OWPPs, several technical hurdles need to be addressed, including the development of self-starting turbines, optimisation of auxiliary power systems, and adapting black start standards and requirements to reflect the capabilities of converter-based technologies. Future research and technological advancements will be vital to unlocking the full potential of OWPPs in providing black start and other grid restoration services.

2.3.2 Challenges and Requirements

The European Network of Transmission System Operators (ENTSO-E) includes black start and island operation as optional requirements for AC and HVDC-connected OWPPs. However, specific PSR requirements for OWPPs are not yet in place [66]. Transmission system operators (TSOs) such as Elia in Belgium and National Grid ESO (NGESO) in the UK have proposed various requirements for OWPPs [67–69]. This section outlines the key requirements, which are further explored in the EMT studies in Chapter 7. Some challenges specific to PSR from OWPPs are also discussed. For further details on all requirements, consult references [66–70].

Self-start capability

A black start unit (BSU) must be able to self-start without external power within a specified time, as required by the TSO. Traditional wind turbines (WTs) cannot self-start as they are grid-following (GFL) units, which depend on an external voltage reference. However, GFM units, combined with an auxiliary power supply (APS) such as a BESS or external APS, can establish a voltage reference, enabling them to self-start.

Block loading capability

Block loading refers to a BSU's ability to accept an instantaneous load. This value is determined by the TSO, with typical ranges between 35 and 50 MW for systems at 400/275 kV and 123 kV, while lower voltage systems may handle smaller loads [68]. During block loading, the BSU must maintain voltage and frequency within acceptable limits.

Frequency and voltage control

Maintaining frequency and voltage within acceptable limits is critical during block loading. According to NGESO, the frequency should remain between 47.5 Hz and 52 Hz, and voltage deviations should not exceed $\pm 10\%$ [66]. Elia specifies voltage limits depending on block loading conditions.

Reactive power capability

NGESO requires wind farms to have a reactive power capability of at least 50 MVAr, while conventional generators are required to provide 100 MVAr. In Belgium, Elia sets different reactive power requirements for various black start zones, typically ranging from 30 to 50 MVAr [66,70]. Shunt reactors can assist in managing reactive power needs, particularly to mitigate the capacitive reactive power generated by long cables under low load conditions. OWPPs must also manage magnetic inrush and transient voltages during network energisation.

2.3.3 PSR from OWPPs – Process Overview

PSR is a complex process, although it is a low-probability, high-impact event [71]. This section provides an overview of the PSR process and its challenges identified by academia and industry. The general PSR process is typically divided into three stages: black start, network reconfiguration, and load restoration [72–74].

The black start (BS) stage involves providing cranking power from a BSU to non-black start units (NBSU), allowing the energisation of units that cannot self-start [74]. This phase requires identifying critical system components, the status of circuit breakers, and the availability of BSUs [75–77]. The TSO then selects BSUs based on cost, restoration time, and system conditions. In the case of OWPPs, if multiple units can serve as BSUs and wind forecasts are favourable, the system can be divided into generating islands that are later synchronised [74,

Chapter 2. Technologies and Challenges in Renewable Energy Systems 78,79].

Network reconfiguration follows once BSUs have supplied cranking power to NBSUs, increasing generation capacity and energising additional generators and key substations. This phase must follow an optimised restoration plan to minimise system collapse risk. This stage also allows the restoration of critical loads. Load restoration, the final phase, focuses on restoring the rest of the system loads as quickly as possible [77,80].

Incorporating OWPPs into PSR follows the same basic principles but presents unique challenges due to their inverter-based technology. OWPPs can facilitate PSR by using external auxiliary power sources to crank wind turbines or through GFM wind turbines that can establish a power island independently of the grid [81]. Once an initial power island is established, the OWPP can progressively energise larger sections of the grid through block loading. Throughout this process, OWPPs must maintain voltage and frequency control to ensure stability [66,70]. Synchronisation of the OWPP with other energised sections of the grid is crucial to prevent overloading and ensure seamless integration.

Figure 2.2 displays a possible timeline of PSR using an OWPP, utilising the traditional system approach mentioned previously of black start, network reconfiguration and load restoration.

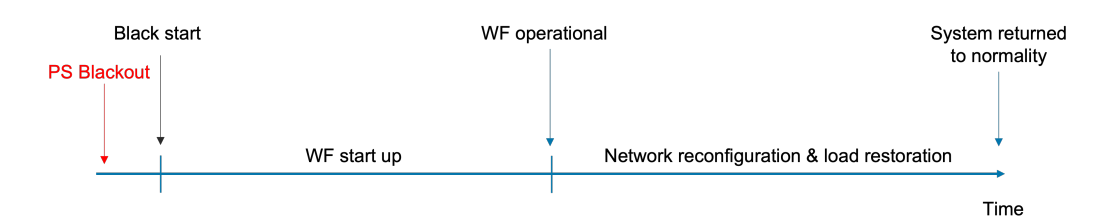


Figure 2.2: Possible power system restoration from OWPP

After a power system blackout, the restoration process begins with the startup of the OWPP. Once the wind farm is operational, the network is reconfigured, and loads are gradually restored, ultimately returning the system to normal op-

Chapter 2. Technologies and Challenges in Renewable Energy Systems

eration. Figure 2.3 highlights the distinction between the roles of top-up and anchor generation, both of which the OWPP can fulfil.

In the event of a blackout, an OWPP can be utilised to provide either an anchor or a top-up service, depending on whether the network is already partially energised. If the network is de-energised, the OWPP may take on the role of reenergising it, thereby establishing a skeletal network and delivering an anchor service. Conversely, if a skeletal network is already in place, the OWPP provides a top-up service by supplementing existing generation.

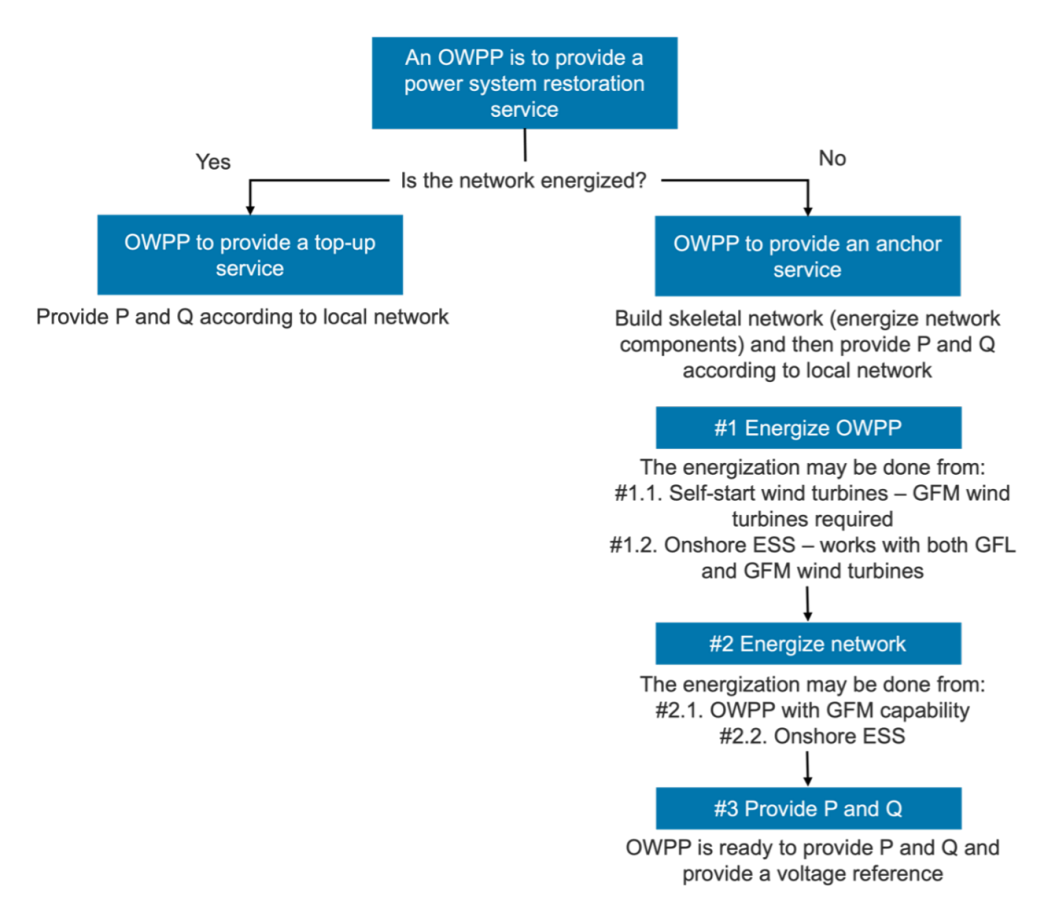


Figure 2.3: Power system restoration from OWPP-anchor vs. top-up solutions

2.3.4 Conclusion

OWPPs have the potential to play a significant role in PSR, but several technical and operational challenges must be addressed. These include developing self-starting turbines, optimising auxiliary power systems, and adapting black start standards to better align with renewable energy sources. OWPPs also need to meet specific reactive power, block loading, and frequency control criteria. With further research and development, OWPPs could become key contributors to renewable-based grid restoration services.

2.4 Grid-Following Controllers

2.4.1 Operational Principles of the GFL Controller

This section provides a detailed overview of the operation of a standard GFL converter control unit. It describes each control loop, including the inner, outer, and synchronisation loops. However, the equations governing the behaviour of this controller are presented later in Section 4.2, where the specific GFL controller utilised throughout this thesis is thoroughly explained.

A GFL converter controller can be represented as a current source in parallel with a high impedance, Z_c , as illustrated in Figure 2.4. This approximation is based on the way the controller operates with respect to the electrical grid. Such controllers regulate the output current to follow a reference, often synchronising with the grid voltage and frequency through a dedicated module within the controller to inject the desired current based on the grid voltage. Consequently, the controller does not impose a voltage; instead, it responds passively to the grid voltage, thus behaving like a current source. The output impedance Z_c is intentionally kept high to prevent interference with the voltage waveform. This high impedance enables the GFL inverter to adapt its current output according

Chapter 2. Technologies and Challenges in Renewable Energy Systems

to fluctuations in the grid voltage without attempting to control or stabilise the voltage directly, which would otherwise conflict with its grid-following function.

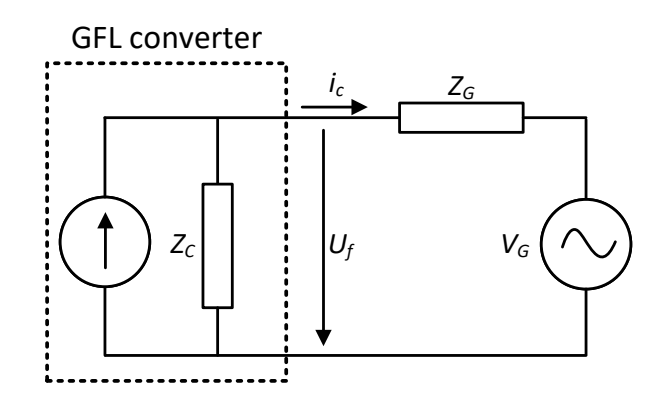


Figure 2.4: GFL converter controller working principle

The GFL controllers comprise three primary submodules: the network inner loop, the outer loop controller, and the synchronisation loop. Figure 2.5 presents a schematic diagram of this configuration, showing the network side of an inverter connected to an LC filter with parameters R_c , L_c , and C_f . The current flowing from the converter to the network, i_c , and the voltage at the PCC terminal, U_f , serve as inputs to the GFL controller. These parameters are modelled in the standard abc reference frame; however, as the controller operates in the qd0 reference frame, a Park transformation is applied to convert the current and voltage from the abc format to qd0, and subsequently back to abc to provide feedback to the converter. Further details on the Park and inverse Park transforms can be found in Appendix A.

Each of these modules performs a distinct function. The synchronisation loop, labelled as PLL in the figure, is responsible for grid synchronisation. In this case, the phase-locked loop (PLL) extracts the estimated voltage angle and magnitude at the PCC, aligning the inverter-based resource with the electrical grid. The outer loop generates reference values for the network inner loop in the

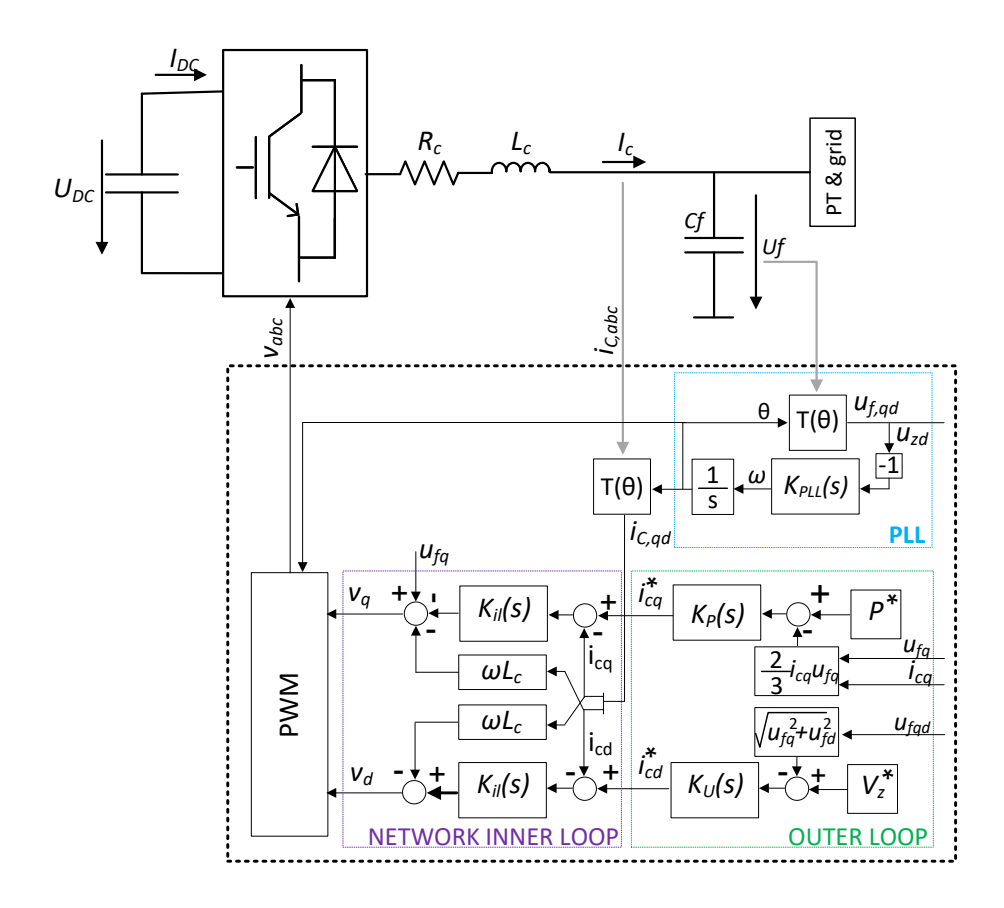


Figure 2.5: GFL controller with power and voltage outer loops connected to a one-line power system

qd0 frame, regulating active power on the q-axis and voltage on the d-axis. As will be discussed in Section 5.5, the d-axis component may alternatively receive reactive power as an input instead of the voltage signal at the PCC. The network inner loop is tasked with fast regulation of the output current, providing the converter with feedback on voltage signals in both the q and d axes. The inverse Park transformation is then used to feed back the voltage V_{abc} to the converter.

2.4.2 Challenges and Limitations of the Grid-Following Controller

GFL converter controllers are widely employed in RES due to their ability to synchronise with the grid voltage. These controllers rely on a phase-locked loop (PLL) or frequency-locked loop (FLL) to track and follow the grid voltage angle and frequency, ensuring that the converter remains synchronised with the external grid [82].

GFL converters provide several services, such as voltage and primary frequency support based on droop, inertia response, and fault ride-through capabilities. However, these controllers lose effectiveness in weak power grids. As discussed in [83], GFL converters face several issues which can be categorised into three groups: stability challenges related to voltage and frequency, PLL and synchronisation difficulties, and limitations in providing grid support services such as fault ride-through, transient stability, and frequency response. Recent advancements in research have focused on enhancing GFL controllers to enable more active participation in essential services such as primary frequency and inertia response [84]. These enhancements are achieved through the implementation of external control loops, including PQ control, droop control, and current-controlled virtual synchronous generators [85].

Frequency and inertia support, for example, are realised through inertia emulation, where power output is determined based on the rate of change of frequency, enabling the controller to deliver a rapid frequency response [86, 87]. However, there is a trade-off between the speed and the overall magnitude of the response [32]. Other approaches, such as using energy stored from the DC link capacitors of HVDC systems, have also been proposed to provide inertia, although these methods are limited by the amount of energy available in the DC link [88,89].

Chapter 2. Technologies and Challenges in Renewable Energy Systems

Despite their role in maintaining frequency stability, GFL controllers encounter challenges related to voltage stability and system strength, particularly in weak grids [90]. These issues stem from their current-source behaviour and reliance on PLLs or FLLs for synchronisation [91]. While some studies suggest that GFL controllers can be tuned to provide fast voltage control, the effectiveness of this tuning is highly dependent on the overall system configuration [92,93]. In weaker grids, the PLL may fail to synchronise, preventing the realisation of the potential benefits of rapid voltage control. In stronger grids, improper tuning could lead to instabilities at non-fundamental frequencies, potentially causing interactions with system capacitance [94].

2.5 Grid-Forming Control

The rapid growth of RES, particularly OWPPs, has introduced new challenges for integrating these sources into the electrical grid. At the heart of this integration are power converters which use switches such as IGBTs, that play a fundamental role in the operation of wind turbines and other RES. As mentioned in the previous section, currently, the standard approach for controlling wind turbines, and thus, their converters, is through GFL controllers, which depend on the electrical grid to set frequency and voltage reference points. While effective in modern power systems, as it will be seen in section 2.1, these controllers face limitations as renewable energy penetration increases, especially in scenarios where grid strength is compromised or more dynamic interactions are required.

An alternative to the GFL controller is the GFM unit, which aim to address issues found in GFL units by autonomously regulating voltage and frequency. However, while GFL controllers are standardised, GFM controllers are not, resulting in the existence of various GFM units.

This section begins by explaining the operational principles of GFM con-

Chapter 2. Technologies and Challenges in Renewable Energy Systems

trollers and examining their inherent limitations. Following this, various types of GFM converter controllers are introduced. However, the primary focus of this thesis is on the virtual synchronous machine (VSM), a GFM controller unit that emulates the behaviour of traditional synchronous generators, offering potential advantages for enhancing system stability and resilience.

As power systems increasingly shift from conventional synchronous machines to converter-based renewable energy sources, GFM converters are critical for maintaining stability. As it was previously stated, unlike GFL converter controllers, which synchronise with existing grid voltage and frequency and regulate injected current, GFM converters actively establish grid conditions. They function as voltage sources with a low series impedance, regulating both voltage and frequency, which makes them particularly suitable for low-inertia power systems. This section presents an overview of various GFM control methods and their operational principles. Then, it delves into the virtual synchronous machine controller that was used throughout the different studies presented in this document.

2.5.1 Operational Principles Of The GFM Controller

As previously mentioned, GFL converters behave as controlled current sources with high parallel impedance, regulating active and reactive power by adjusting the injected current into the grid. The fundamental difference between GFL and GFM control strategies lies in their response to grid disturbances and their performance in terms of small-signal stability under varying grid conditions [95,96]. A GFM converter controller can be represented as a voltage source in series with a low impedance, Z_C , as shown in Figure 2.6. This representation aligns with the operational principles of GFM controllers, which actively establish and regulate the voltage and frequency at their terminals. Unlike GFL controllers, GFM controllers are not dependent on the grid voltage for synchronisation. Instead, they provide the reference voltage waveform and adapt their current output to meet

Chapter 2. Technologies and Challenges in Renewable Energy Systems

the power demands of the connected load or grid. The low output impedance ensures that the controller can effectively control the terminal voltage and respond to variations in system conditions, such as changes in load or disturbances in the grid. By doing so, the GFM controller enhances system stability and supports functionalities such as power system restoration capability and the integration of renewable energy sources in weak grids.

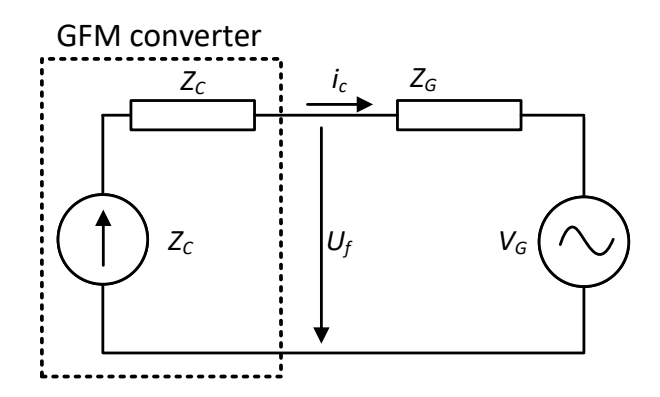


Figure 2.6: GFM converter controller working principle

Figure 2.7 displays the voltage source behaviour of a GFM converter controller. By controlling the voltage E and angular frequency ω , the active and reactive power, P and Q, respectively, are exported to the electrical grid, by means of the inductance X_L [97]. Assuming that the PCC has a phase displacement of δ_E , such that the voltage at the PCC is represented by E/δ_E , and the grid voltage is given by V/δ_V , the control design complexity can be reduced by decoupling the apparent power into its real and imaginary components. This simplification leads to the fundamental equations governing the GFM converter, which are as follows:

$$\delta_p = \delta_E - \delta_V \tag{2.1}$$

Chapter 2. Technologies and Challenges in Renewable Energy Systems

$$P = \frac{EV sin\delta_P}{X_L} \tag{2.2}$$

$$Q = \frac{E^2 - EV cos\delta_p}{X_L} \tag{2.3}$$

Where δ_p is the angle difference between generation and grid.

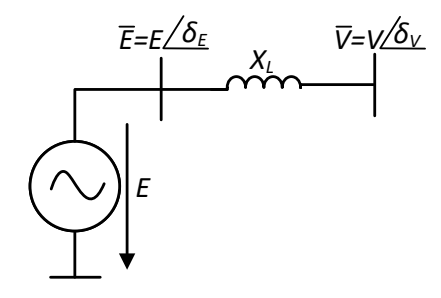


Figure 2.7: GFM converter acting as a voltage source

The concept of GFM converter controllers is not officially standardised, and there is ongoing debate in both academia and industry regarding its precise definition. Consequently, several GFM control structures have been proposed, each tailored to different operational requirements [98,99]. GFM converters are particularly advantageous in systems with a high penetration of renewable energy, where traditional sources of inertia are lacking, providing grid services such as frequency regulation and voltage support, ensuring system stability even under weak grid conditions [100,101]. The remainder of this section provides a brief description of several GFM control structures. These include droop control in Section 2.5.2, power synchronization control in Section 2.5.3, direct power control in Section 2.5.4, the virtual synchronous oscillator in 2.5.5, and finally, the virtual synchronous machine, which is the method used in this thesis, in Section 2.5.6.

2.5.2 Droop Control

Droop control is the most widely used GFM control strategy. Its principles are based on the droop characteristics of rotational synchronous generators, and it is designed to mimic their behaviour by adjusting the system frequency according to active power deviations and the system voltage based on reactive power deviations [98, 102, 103].

In this method, and assuming an inductive grid [104], where the inductive component of the transmission line is typically much greater than the resistive component, an increase in active power output is achieved by decreasing the internal frequency reference of the GFM unit, following a predefined droop characteristic. Similarly, an increase in reactive power consumption results in a reduction in the internal voltage reference. This local response mimics the behaviour of synchronous machines and is illustrated in Figure 2.8.

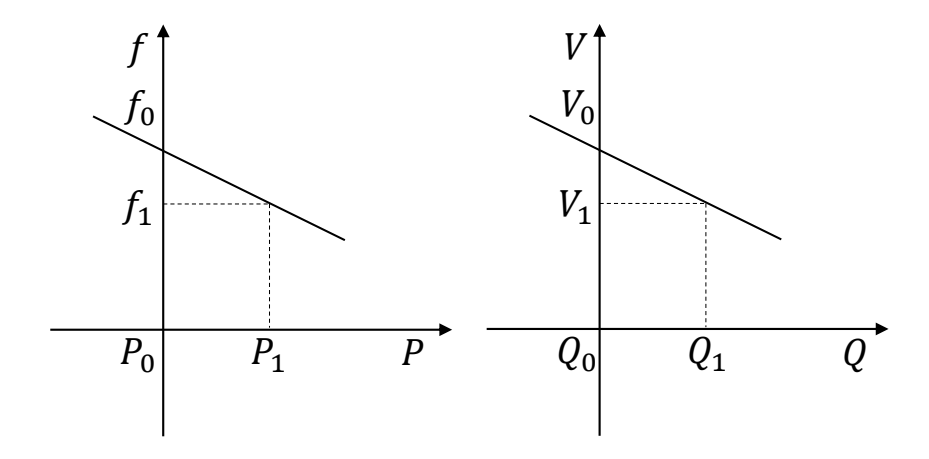


Figure 2.8: Droop characteristics for P/f and Q/V

From the figure, the droop characteristic expressions for the active power/frequency (P/f) loop and reactive power/voltage (Q/V) loop can be defined as follows:

$$\Delta f = -k_p \Delta P \tag{2.4}$$

$$\Delta V = -k_q \Delta Q \tag{2.5}$$

In these equations, Δf represents the frequency variation, defined as $f_1 - f_0$, corresponding to an active power deviation of $P_1 - P_0$. Similarly, ΔV denotes the voltage variation $V_1 - V_0$ for a reactive power change of $Q_1 - Q_0$. The slopes of the characteristic curves shown in the figure represent the gains, denoted as k_p and k_q . It is evident that the controller adjusts its injection of active and reactive power depending on the grid frequency and voltage.

As can be observed, the operation of the droop controller is quite straightforward. However, while it is simple and robust under steady-state conditions, it is noted in [105,106] that it may struggle with dynamic responses, particularly during large disturbances, as well as with voltage regulation and transient response times, which may be slower compared to that of more advanced controllers.

Various improvements to droop control have been proposed, such as the inclusion of AC voltage and reactive power control loops with a cascaded inner-outer loop design [107].

Based on the discussion of droop characteristics in this section, Figure 2.9 presents a possible implementation of a droop controller incorporating the described characteristics. The controller consists of three main components: the droop control, the voltage control loop, and the current control loop, each working in a cascaded structure to ensure stable operation of the grid-forming inverter.

The droop control block establishes the reference signals for the system frequency and voltage magnitude based on the active and reactive power deviations, respectively. The frequency reference is derived from the active power deviation using a proportional droop coefficient, while the voltage reference is adjusted according to the reactive power deviation. These references determine the output voltage and frequency of the inverter, mimicking the behavior of a synchronous generator.

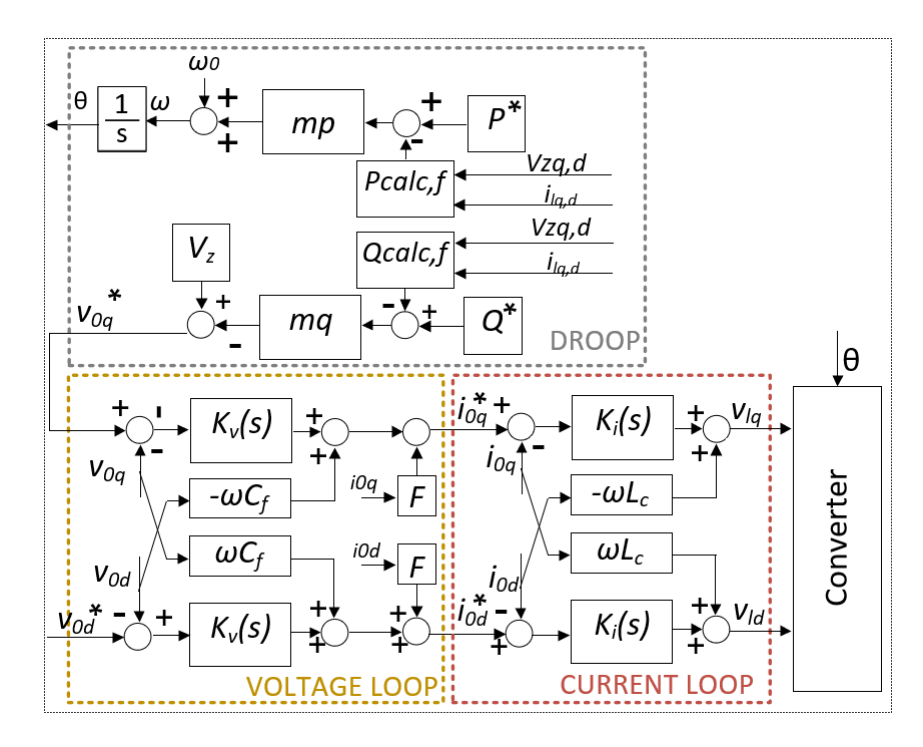


Figure 2.9: Droop control diagram with droop loop, voltage outer loop and current inner loop

The voltage control loop, shown within the yellow-dashed region, regulates the inverter's terminal voltage by generating the reference current components i_{od}^* and i_{oq}^* . The voltage controller $K_v(s)$ processes the voltage deviation and produces the required current references. Additionally, capacitor current feedforward terms $\omega C_f V_{od}$ and $\omega C_f V_{oq}$ are incorporated to improve the dynamic response.

The inner current control loop, outlined in red, ensures accurate tracking of the reference currents i_{od}^* and i_{oq}^* . The current controllers $K_i(s)$ process the current errors and generate the appropriate voltage commands V_{od} and V_{oq} . Inductor voltage feedforward terms $\omega L_c i_{od}$ and $-\omega L_c i_{oq}$ are used to enhance system stability and response speed.

This cascaded control structure allows the inverter to dynamically adjust its output in response to grid variations, ensuring proper voltage and frequency regulation while maintaining power-sharing capability. The combination of droop control with inner voltage and current loops provides a robust and effective apChapter 2. Technologies and Challenges in Renewable Energy Systems proach for GFM inverters in modern power systems.

2.5.3 Power Synchronization Control

The power synchronization control (PSC) loop is inspired by the synchronization process between two synchronous machines in an AC system, and its primary objective is to eliminate the need for a phase-locked loop (PLL). Unlike other controllers, the PSC does not require a vector-current controller, as the current reference is not predetermined.

The active power output of the PSC is determined directly by the power synchronization loop, making it similar to the previously introduced droop controller. However, an additional damping coefficient allows the converter to contribute to inertia support for the electrical grid [106]. Reactive power is regulated by adjusting the voltage magnitude using a proportional voltage controller, with the option to include an outer reactive power controller [103].

According to [108], a current controller is only required during system faults, where it serves to prevent potential over-currents. In [106] it is further high-lighted several advancements and characteristics of the PSC controller, including its robust small-signal performance in weak networks. Additionally, the integration of virtual impedance with the PSC was also tested, and it was seen that it reduces circulating currents between parallel converters, thus improving power quality [109].

2.5.4 Direct Power Control

Direct power control is characterised by its ability to regulate active and reactive power output directly without the need for traditional current control loops. It is derived from AC motor direct torque control [106], where the active and reactive power are managed by tracking the error between the actual power and their

Chapter 2. Technologies and Challenges in Renewable Energy Systems respective reference values.

A look-up switching table is employed to select between switching signals. The hysteresis regulator is used, and the output is generated by selecting the optimal voltage vector. This vector is chosen based on the instantaneous errors in active and reactive power, along with the phase angle of the converter terminal voltage [110,111].

2.5.5 Virtual Oscillator Control

The virtual oscillator control (VOC) differs from the other strategies presented, as it does not rely on phasor representations of the inverter voltages. Instead, this controller operates in the time domain and emulates the behaviour of a nonlinear oscillator circuit. It was initially proposed using the Van der Pol oscillator [112], where the voltage at the terminals of the oscillator and the current are generated by the circuit [113,114].

This method creates a voltage signal by emulating the dynamics of a nonlinear oscillator and does not require additional control loops for its operation [115]. Furthermore, the VOC does not rely on voltage or frequency measurements, which, according to [101], makes it faster for synchronization and power sharing.

However, the original structure of the VOC does not regulate output power, requiring the integration of additional control loops to achieve this. In [116], the VOC was compared to the droop controller, and it was observed that both strategies exhibit similar characteristics.

2.5.6 Virtual Synchronous Machine

Virtual Synchronous Machine (VSM) control represents a significant advancement over traditional droop control by emulating the inertia and damping characteristics of conventional synchronous machines. VSM controllers implement the swing

Chapter 2. Technologies and Challenges in Renewable Energy Systems

equation, which describes the dynamics of synchronous machine rotors, thereby providing synthetic inertia to the grid. This capability allows the converter to respond dynamically to frequency changes in a manner similar to a physical synchronous generator, significantly improving grid frequency stability, particularly during disturbances or sudden load changes [95]. The provision of both inertia and damping by VSM control enhances the stability of the power system and supports grid frequency regulation during grid events [96, 100].

The first VSM algorithm referred to as VISMA, was introduced in [99,117]. This controller captures both the static and dynamic characteristics of a synchronous generator, enabling bidirectional control of active and reactive power. This makes it particularly suitable for energy storage applications [118]. However, several challenges have been identified with VISMA, including a lack of voltage quality during no-load operation in islanded mode and an absence of reactive power control. Additionally, the synchronous generator behaviour may not be replicated if the current tracking error of the hysteresis controller becomes too large. Instability has also been reported due to the numerical data involved. VISMA can be computationally intensive, requiring real-time solutions to the swing equation. Increased control loop delays can also impact transient performance [118,119].

A new VSM algorithm, known as the synchroconverter, was introduced in [98,120]. Simplified implementations, such as the synchronverter, have been developed to reduce the computational burden while retaining the essential grid-support functions of synchronous machines. The synchronverter offers the same dynamics as a synchronous generator from a grid perspective. It balances computational efficiency with the ability to provide inertia and reactive power support, making it a practical solution for many applications. The synchroconverter is modelled as a round rotor machine, but certain generator effects, such as dampers, eddy currents, and iron core losses, are neglected to simplify the model [118].

Chapter 2. Technologies and Challenges in Renewable Energy Systems

Due to its droop controllers, which include frequency and voltage control loops, the synchroconverter enables the parallel operation of multiple units. It is also noted that, unlike VISMA, the synchroconverter includes a dedicated controller for reactive power.

There are other models based on the virtual synchronous machine, such as the ISE Lab VSM [121] and the synchronous voltage controller [122]. The ISE Lab VSM is a simplified version of the virtual synchronous machine, considering only the swing equation that characterises the VSM. It employs a voltage-mode control where the angle and magnitude of the converter are modulated to regulate the active and reactive power outputs.

The synchronous voltage controller differs from other virtual synchronous machine controllers as it synchronises with the grid through the voltage loop rather than the power loop. This approach uses an outer current loop and an inner voltage loop, reversing the conventional order of control loops.

In [123], a VSM is introduced, which serves as the model used in this work. It emulates a synchronous generator by utilising a variation of the swing equation to form the active power loop and employs an automatic voltage regulator for the voltage controller. This system is illustrated in Figure 4.2, where a converter is connected to the power transmission system and grid through an LC filter. Two key quantities are utilised in the converter: the current flowing from the converter and the voltage at the point of common coupling (PCC).

The controller consists of two loops, as previously mentioned: the power loop and the voltage loop. The power loop is based on the following swing equation:

$$J\frac{d^2\theta}{dt^2} + D\frac{d\theta}{dt} = \Delta(P_m - P_e)$$
 (2.6)

where P_m represents the mechanical power, P_e the electrical power of the synchronous machine, J the moment of inertia, D the damping factor, and θ the output angle. The power loop PI controller, shown in Figure 4.2, is inspired by

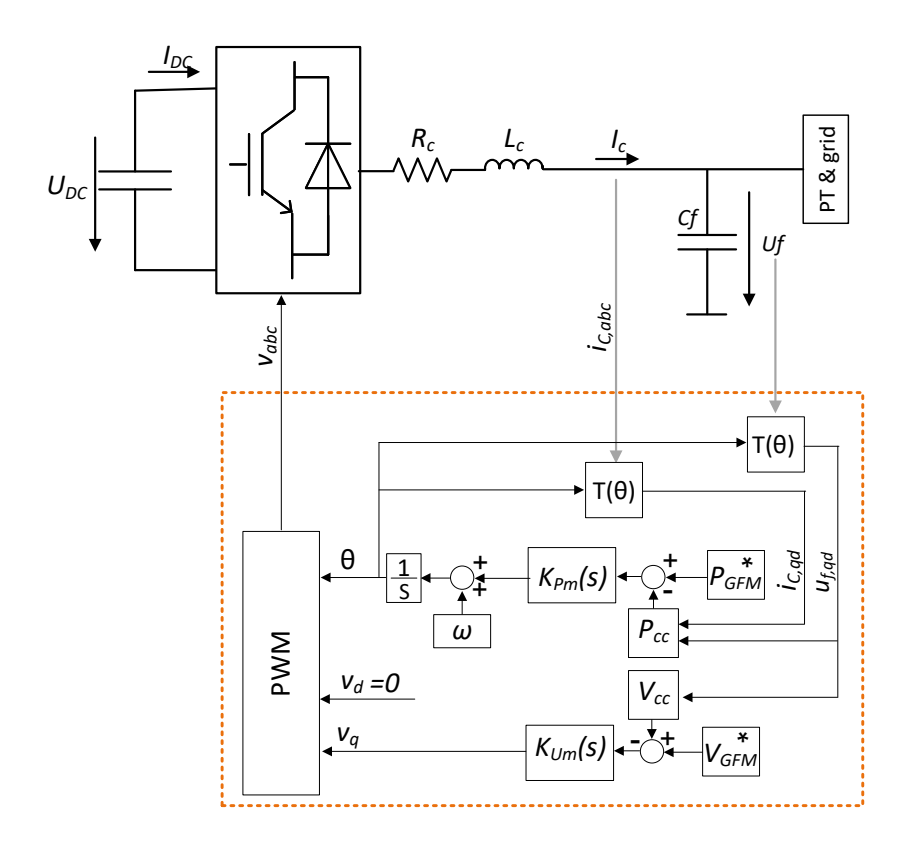


Figure 2.10: GFM controller connected to one-line system

Equation 2.6; the proportional term, k_p , accounts for the damping, D, while the integral term, k_i , represents the inertia, J.

The voltage loop, which determines the voltage at the converter terminals, is modelled after the voltage regulator of a synchronous machine.

The tuning of the power controller was carried out by considering the natural frequency, apparent power, and inertia of the synchronous machine, as outlined in [94]:

$$k_i = \frac{\omega}{2HS_r} \tag{2.7}$$

Chapter 2. Technologies and Challenges in Renewable Energy Systems

$$k_p = \frac{Dk_i}{k_m} \tag{2.8}$$

where H represents the inertia constant, S_r is the rated apparent power, and k_m is a constant dependent on the natural frequency and the integral gain given by

$$k_m = \frac{\omega^2}{k_i} \tag{2.9}$$

2.5.7 Conclusion

GFM converter controllers are essential for ensuring the stability of future power systems dominated by renewable energy. Each of the control methods discussed—droop control, VSM control, PSC, DPC, and VOC—offers distinct advantages depending on the specific application and grid conditions. While droop control remains the most widely used method due to its simplicity, more advanced strategies such as VSM and PSC provide enhanced stability and dynamic performance, particularly in weak grid scenarios. As renewable energy penetration continues to grow, the development and refinement of these control strategies will be critical for ensuring the stable operation of power systems in the future.

2.6 Self-Start Wind Turbine Generators

The global transition to renewable energy has brought significant advancements in wind power technologies, particularly in the development of wind turbines. One critical challenge in this domain is the ability of wind turbines to autonomously start under varying wind conditions, especially in remote or low-wind environments.

Self-starting capabilities are essential for ensuring the efficiency and reliability of wind turbine operations, reducing the need for external intervention or auxil-

Chapter 2. Technologies and Challenges in Renewable Energy Systems

iary systems. This capability becomes even more critical in the context of power system restoration, where wind turbines must play a role by energising the grid without relying on an external power supply.

Despite the growing importance of self-starting capabilities for wind turbines, especially in the context of OWPPs, there has been relatively limited attention given to this topic in academic research. Addressing this challenge has predominantly been the focus of patented innovations, which propose mechanisms and designs to enhance self-starting performance. These include advanced blade profiles, aerodynamic enhancements, and integrated starting systems. In contrast, academic studies on self-starting wind turbines remain sparse, with only a few experimental investigations, computational simulations, and field tests exploring their behaviour and performance under various conditions.

The advancements made through these efforts are particularly relevant for OWPPs, which are increasingly expected to provide grid services traditionally delivered by synchronous generators, such as frequency regulation and support during power system restoration. This highlights the need for further academic exploration and innovation to close existing knowledge gaps and fully realise the potential of self-starting wind turbines in modern power systems.

This section provides a comprehensive overview of the existing patents and academic studies dedicated to self-starting wind turbines. Each patent and paper is described in detail, highlighting its contributions to the field. Finally, an analysis summarises the key features of these innovations, offering valuable insights into their practical applications and limitations, particularly in the context of black start and power system restoration.

2.6.1 Patents On Self-Starting Wind Turbines

Several innovative approaches to self-starting wind turbines have been patented, addressing the challenges associated with initiating turbine operation during grid

Chapter 2. Technologies and Challenges in Renewable Energy Systems

outages or in remote locations. One invention, as described in [124], leverages internal energy storage systems within the wind turbine, such as capacitors or batteries, to provide the necessary initial power for starting. This design focuses on operational independence by enabling turbines to re-synchronise with the grid autonomously after a failure. Stored energy is strategically directed to essential subsystems, including the pitch system for blade angle adjustments, auxiliary components such as controllers and sensors, and communication modules. Safety mechanisms are integrated into the system to prevent overloading and ensure efficient use of stored energy during the startup process, making it particularly useful in blackout scenarios where external power sources are unavailable.

Another innovative method for self-starting wind turbines, as outlined in [125], involves utilising the pitch system battery to transition the turbine into a self-sustaining operational mode with minimal external input. This method adjusts blade angles to optimise torque generation under low wind conditions, enabling the rotor to achieve sufficient rotational speed. Once operational, the generator engages to produce power, which is then redirected to sustain the subsystems of the wind turbine, creating a self-sustaining loop. Enhancements to the pitch control system enable prioritisation of energy use and extended battery life, particularly during prolonged grid outages. This approach is particularly advantageous for remote and offshore wind turbines, where grid access can be unreliable, ensuring continued operation with minimal external support.

A more advanced self-starting mechanism tailored for offshore wind turbines, as discussed in [126], combines hybrid energy storage systems with predictive control algorithms to optimise startup performance. The hybrid system integrates batteries, which provide sustained power for auxiliary systems, and supercapacitors, which address high-power, short-duration requirements, such as initiating rotor movement. A predictive control algorithm dynamically manages energy flow based on wind speed and turbine operating conditions, ensuring an efficient

Chapter 2. Technologies and Challenges in Renewable Energy Systems

and adaptable startup process. This design also incorporates fault detection and recovery mechanisms to enhance system robustness during startup, minimising downtime and reducing maintenance requirements. The combination of hybrid energy storage and intelligent control not only ensures reliable operation but also improves the operational autonomy of offshore wind turbines, addressing the logistical and financial challenges of maintenance in offshore environments.

Additionally, [127] presents a system integrating energy storage devices, such as batteries, supercapacitors, or flywheels, into wind turbines to enhance their operational flexibility and grid services. While this patent is not explicitly designed for self-starting, its features can be adapted to this context. The energy storage system provides auxiliary power to critical components, including yaw drives, pitch systems, and control electronics, enabling independent operation during grid outages. A bidirectional UPS system facilitates energy flow between the storage, auxiliary loads, and the grid, making it particularly advantageous for restarting operations post-blackout. The system also supports functionalities such as low-voltage ride-through, power smoothing, and inertial response, essential for maintaining operational stability during power system restoration. These features highlight its potential applicability to self-starting wind turbines, especially in offshore environments where maintenance and grid access are challenging.

A comparison of these four patents is summarised in Table 2.1, which highlights the key features, energy storage mechanisms, and targeted applications of each innovation.

2.6.2 Academic Research On Self-Starting Wind Turbines

Self-starting wind turbines represent a promising avenue for addressing the challenges of power system restoration and autonomous operation in remote or offshore locations. Academic research in this area has explored several approaches,

Chapter 2. Technologies and Challenges in Renewable Energy Systems

Table 2.1: Comparison of Patents on Self-Starting Wind Turbines

Patent	Innovation	Energy Storage	Advantages
[124]	Internal energy storage for self-	Batteries or capaci-	Provides independence
	starting using integrated control	tors.	from external power;
	strategies. Powers pitch sys-		facilitates safe, efficient
	tems and auxiliary components		startup.
	autonomously, ensuring grid re-		
	synchronisation during blackouts.		
[125]	Utilisation of pitch system bat-	Pitch system bat-	Ensures continued opera-
	tery for startup. Adjusts blade	tery.	tion during outages; pri-
	angles for optimal torque, cre-		oritises energy use to ex-
	ating a self-sustaining loop that		tend battery life.
	powers turbine subsystems.		
[126]	Hybrid energy storage with pre-	Batteries and su-	Ideal for offshore appli-
	dictive control algorithms. Inte-	percapacitors.	cations; robust startup
	grates batteries and supercapaci-		under varying wind con-
	tors to optimise energy flow and		ditions; reduces mainte-
	fault detection during startup.		nance costs.
[127]	Integration of energy storage sys-	Batteries, super-	Supports low-voltage
	tems with wind turbines to pro-	capacitors, or	ride-through and in-
	vide auxiliary power and enhance	flywheels.	dependent operation
	grid services. While not explic-		during outages; facil-
	itly for self-starting, its features		itates post-blackout
	can be adapted for this purpose.		restarts.

often leveraging advanced control strategies and energy storage systems to enable turbines to start and operate independently of external power sources. This section provides an overview of five key studies, discussing their methodologies, innovations, and implications for the future of self-starting wind turbines.

In [128], it is proposed a coordinated control strategy for Doubly Fed Induction Generator (DFIG)-based wind turbines integrated with a BESS. This approach addresses microgrid frequency regulation while maintaining the Maximum Power Point Tracking (MPPT) operation of the WT.

The study utilises a droop controller in the grid-side converter of the DFIG, with the BESS connected to the DC link via a bidirectional buck-boost converter. This setup allows the BESS to provide active power support during frequency disturbances while ensuring the DC link voltage remains stable. Simulation results demonstrate improved frequency regulation, reduced nadirs, and faster recovery

Chapter 2. Technologies and Challenges in Renewable Energy Systems times under varying wind conditions.

Though primarily focused on frequency regulation, the system architecture has potential applications in self-starting wind turbines. The BESS provides an energy reserve that can power essential subsystems, such as pitch and yaw mechanisms, during startup. This design enables autonomous turbine operation without external grid power, making it valuable for offshore wind turbines and black start scenarios. This work underscores the versatility of integrated BESS systems in enhancing wind turbine independence and operational stability.

The study presented in [129] discusses the use of permanent-magnet synchronous generator (PMSG)-based wind power generation in black start procedures. It outlines how wind turbines can contribute to power system restoration, a traditionally challenging role for renewable energy sources. By employing virtual inertia control strategies, the research proposes enhanced frequency stability during the initial stages of a black start.

While the paper is primarily about black start strategies, its concepts are applicable to self-starting wind turbines. The integration of energy storage systems and advanced control algorithms, such as the virtual inertia approach, aligns with mechanisms that could enable self-starting capabilities. For instance, using stored kinetic energy or additional storage components could initiate turbine operation in the absence of external grid power, similar to self-starting requirements.

In [130] it is proposed the integration of a BESS with a DFIG based WT using a modified Triple Star Bridge Cell (TSBC) converter. This approach is modular, facilitates large-scale energy storage integration, and offers several advantages such as power fluctuation mitigation, fault tolerance, and improved low-voltage ride-through capabilities.

The TSBC converter structure supports multiple battery banks, dividing the energy storage across smaller units and enabling efficient control of power flow between the grid and rotor. A control strategy is presented to partially absorb

Chapter 2. Technologies and Challenges in Renewable Energy Systems

or supply power fluctuations due to wind speed variations.

This technology could potentially support self-starting mechanisms for wind turbines by using the energy from the BESS to provide the required power for auxiliary systems and rotor movement during startup, especially in grid-absent scenarios. The modular design and fault tolerance make it suitable for remote or offshore wind applications.

Another contribution is the work in [131], which introduces an optimised control strategy for a grid-connected DFIG-based WT, integrating a BESS unit at the DC link through a bidirectional DC-DC converter. This approach addresses challenges of wind variability and power quality. A higher-order adaptive control method manages the grid-side converter, ensuring smooth power output, minimal harmonic distortion, and efficient energy transfer.

In the context of self-starting wind turbines, and similar to the work in [128], the integration of a BESS system could provide the energy required during startup by enabling autonomous power delivery to key turbine subsystems. This setup is useful during grid outages or in weak grid conditions, ensuring the turbine can achieve operational speed and synchronise with the grid effectively.

Finally, [132] explores an innovative approach to managing energy storage in wind power systems using a dual-battery energy storage system (DBESS). It focuses on stabilising intermittent wind power while reducing operational costs.

The system alternates between two batteries—one charging when wind power exceeds demand and the other discharging when demand exceeds wind power. This dynamic role-switching maximises the lifespan of the batteries. The proposed DBESS uses predictive control to ensure consistent power dispatch, optimise battery usage, and handle wind power forecast errors.

Although the paper does not directly address self-starting wind turbines, the underlying concepts of energy storage and power management could be applied to self-starting mechanisms. Specifically, the DBESS could provide the required

Chapter 2. Technologies and Challenges in Renewable Energy Systems

initial power for self-starting wind turbines, enhancing their ability to operate autonomously and reconnect to the grid after outages, which align with the principles of reliable and resilient wind energy systems.

These studies collectively highlight the potential of advanced energy storage systems and control strategies to enable self-starting wind turbines. Table 2.2 summarises the key findings, methodologies and technologies proposed, and the relevance to self-starting wind turbines, offering a comparative perspective on their contributions to this evolving field.

Table 2.2: Comparison of Self-Starting Wind Turbine Papers

Paper	Key Focus	Methodology	Relevance
[128]	Proposes a control strategy integrating BESS and MPPT for DFIG-based wind turbines.	Combines real-time battery management with wind turbine controllers to enhance efficiency and reliabil- ity.	Facilitates energy availability dur- ing grid outages, enabling wind tur- bines to self-start and support grid restoration.
[129]	Examines the fea- sibility of using a DC-link-based BESS for DFIG systems.	Utilises an optimised DC-link structure with energy storage for smoother grid integration and fault handling.	Demonstrates potential for sup- porting initial power needs during self-start scenarios.
[130]	Introduces a TSBC topology with integrated BESS for DFIG wind energy systems.	Employs a modular converter design to improve stability and dynamic performance during grid disturbances.	The modular structure and BESS integration make it suitable for self-start applications by ensuring auxiliary power.
[131]	Focuses on optimal MPPT and BES coordination in grid-tied DFIG systems.	Combines advanced MPPT algorithms with BESS control to maximise energy yield and maintain grid stability.	Enhances the capability of wind turbines to operate independently during grid outages, aiding in self-start mechanisms.
[132]	Proposes a dual- battery system for wind power appli- cations.	Uses two batteries with distinct characteristics to handle varying energy demands and improve system resilience.	Provides a robust framework for sup- plying startup en- ergy to wind tur- bines in low wind or grid-failure con- ditions.

Chapter 3

Novel Modelling and Analysis Framework for an Offshore Wind Power Plant

3.1 Introduction

This chapter presents the system models developed for electromagnetic transient (EMT) analysis and small signal stability studies within the scope of this thesis. These models form the foundation for investigating the dynamic behaviour and steady-state performance of an OWPP connected to an onshore electrical grid or onshore loads via a HVAC transmission system.

The models include an aggregated OWPP based on voltage source converter (VSC) technology, designed to represent the overall behaviour of the OWPP. The transmission system is modelled using an HVAC export cable, with shunt reactors included to compensate for the capacitive reactive power generated by the long-distance cable. The electrical grid is represented by a Thevenin equivalent voltage source. Additionally, RL loads are modelled for PSR studies, while an offshore transformer is employed to study transient phenomena, such as inrush currents

during energisation. Therefore, the following components are modelled in this Chapter:

- Aggregated OWPP
- HVAC submarine export cable
- Shunt reactors
- Grid Thevenin equivalent
- Local network loads

This chapter also introduces the mathematical equations describing the full system model, which lay the groundwork for the subsequent formulation of the state-space matrices. These state-space matrices, presented in the reference synchronous frame, are later used for small-signal stability analysis.

In addition, steady-state studies are conducted to examine the capabilities and limitations of the OWPP in providing active and reactive power to the electrical grid and onshore loads. The performance of the transmission system in maintaining voltage profiles along the HVAC transmission cable and power factor within acceptable limits is also evaluated. Special attention is given to the configuration of the HVAC cable and shunt reactors, assessing how different arrangements affect voltage stability and overall system performance.

Figure 3.1 presents the overall system considered in this thesis. While the system undergoes slight modifications from section to section, these changes will be explained in detail within each Chapter. The breakers included in the figure are used for the PSR studies discussed in Chapters 6 and 7.

The figure illustrates an OWPP connected to an offshore transformer, which steps up the voltage for transmission. Although the OWPP is shown with multiple individual turbines, transformers, and array cables, for the purposes of the studies

in this thesis, an aggregated model is used. A static shunt compensator is located between the offshore transformer and the export cable, while a variable shunt compensator is positioned onshore, allowing for reactive power compensation to be adjusted as required. The diagram also includes onshore network loads and a local onshore network.

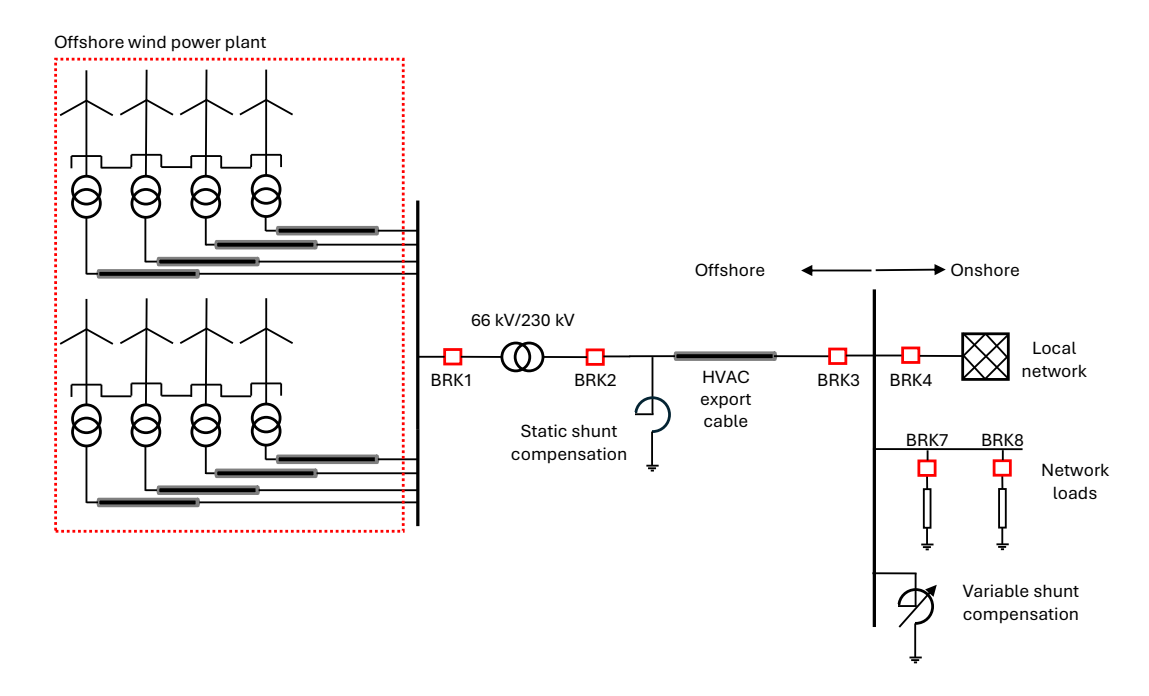


Figure 3.1: Scheme of the OWPP connected to a power system

3.2 Design Of Offshore Wind Power Plant - Grid

3.2.1 Aggregated Offshore Wind Power Plant

RES are interfaced with the grid via inverters. Following industry and academic trends, the inverter used in this study is a three-phase, two-level VSC, which uses insulated-gate bipolar transistor (IGBT) switches. The VSC exchanges power between the generation (DC side, via U_{DC}) with the AC side. The latter exchanges power to the power transmission (PT) system and grid.

An average model of the VSC converter may be used [133], which consists of three controlled voltage sources, one for each phase, where the output of the inverter is the voltage, which is calculated as

$$V_{a,b,c} = \frac{U_{DC}}{2} m_{a,b,c}(t)$$
 (3.1)

where $m_{a,b,c}(t)$ are the modulation functions responsible for modulating the PWM signal used in the converter [134,135]. The VSC average model is connected to an LC filter consisting of a coupling inductor and a PWM filter.

If it is considered that every wind turbine of the OWPP is injecting, on average, the same current to the power system, it is possible to aggregate the OWPP by multiplying the number of wind turbines, N, by the different quantities that characterise the system. Thus, the equivalent impedances of the coupling reactor, Z_c , PWM filter, Z_f , and park transformer, Z_t , which is also factored in this impedance equivalent, are obtained by dividing the impedance for one turbine over the total number of turbines in the OWPP [136], as shown in the next equations:

$$Z_c = Z_t + \frac{Z_{cv}}{N} \tag{3.2}$$

$$Z_f = \frac{Z_{cfv}}{N} \tag{3.3}$$

Figure 3.2 illustrates the process of simplifying an OWPP into a one-line diagram that represents the aggregated system. The impedances of the aggregated model are first calculated, as outlined earlier. It should be noted that, although turbine transformers are represented in the figure, they were not modelled in the studies presented here. Including them would have added unnecessary complexity to the small-signal models. Furthermore, the objective of the analysis was to investigate the dynamics of the overall wind farm and transmission system, rather

Chapter 3. Novel Modelling and Analysis Framework for an Offshore Wind Power Plant

than the interactions between individual wind turbines. However, future studies should consider including turbine transformers to capture their potential impact on local dynamics and interaction effects within the wind farm. The LC filter and offshore transformer are modelled as their equivalent components, leading to the final representation shown in the figure. In this diagram, the voltage V corresponds to the AC-side output of the converter, while the current i_c represents the power injected into the transmission system by the aggregated OWPP. The impedance Z_c , composed of R_c and L_c , represents the coupling filter, while Z_f , consisting of C_f , represents the PWM modulation filter.

3.2.2 Export cable

OWPP are connected to the onshore grid via a transmission system, which consists of submarine high-voltage cables. These cables may be either high-voltage alternating current (HVAC) or high-voltage direct current (HVDC). For the purposes of this study, HVAC cables were utilized. Due to the high capacitance of HVAC cables, they generate excess capacitive reactive power, as previously explained in Section 2.2. To compensate for this and maintain voltage within acceptable limits, shunt reactors are employed to regulate the power factor. This section outlines the modeling approach used for the HVAC submarine cable and the associated shunt reactors.

For the steady-state and small signal analysis conducted in this study, a distributed parameter model was employed to characterize the HVAC cable. This approach allows for the calculation of voltages and currents along the entire length of the transmission line.

The transmission line is defined by four parameters, which are distributed continuously along its length. These parameters include the series resistance, R_{hv} , which accounts for both the stranding and skin effects; the inductance, L_{hv} , representing the flux linkages both within the conductor cross section and the

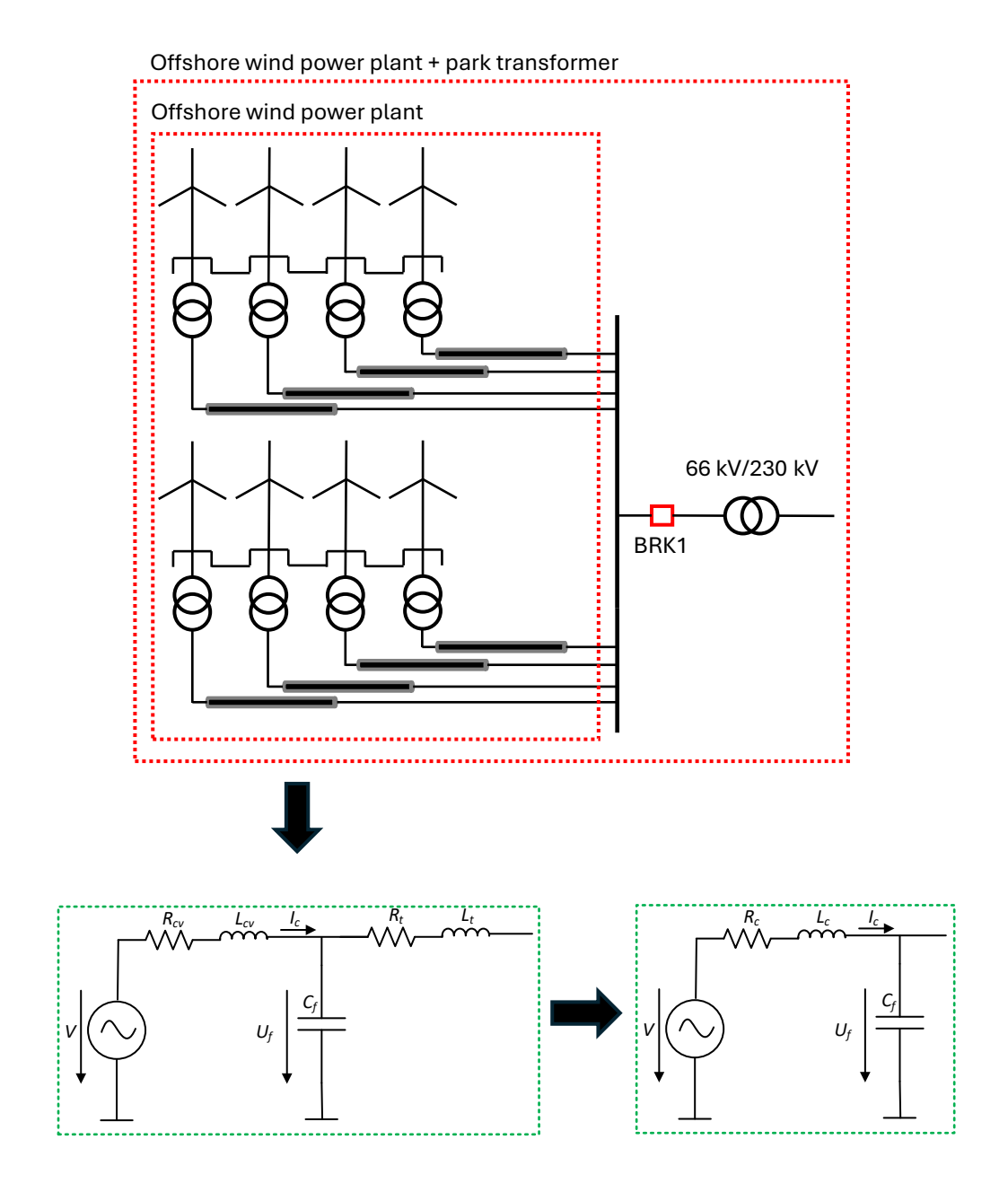


Figure 3.2: Equivalent electrical diagram of a VSC converter connected to a three-phase power transmission system and grid

external flux linkages; the conductance, G_{hv} , which models losses due to leakage currents along the insulator strings and corona effects; and the capacitance, C_{hv} , which describes the difference of potential between conductors [137].

These distributed parameters are represented as shown in Figure 3.3, where the series impedance, z_{hv} , and shunt admittance, y_{hv} , per unit length are considered for the line model.

$$z_{hv} = R_{hv} + j\omega L_{hv}$$

$$y_{hv} = G_{hv} + j\omega C_{hv}$$
(3.4)

The relationship between the sending end and receiving end currents and voltages may be computed according to the characteristic impedance, Z_C and propagation constant, γ , as:

$$\begin{bmatrix} V_S \\ I_S \end{bmatrix} = \begin{bmatrix} \cosh(\gamma l) & Z_C \sinh(\gamma l) \\ \frac{\sinh(\gamma l)}{Z_C} & \cosh(\gamma l) \end{bmatrix} \begin{bmatrix} V_R \\ I_R \end{bmatrix}$$
(3.5)

where

$$Z_C = \sqrt{\frac{R_{hv} + j\omega L_{hv}}{G_{hv} + j\omega C_{hv}}}$$
(3.6)

and the propagation constant, γ is defined as

$$\gamma = \sqrt{(R_{hv} + j\omega L_{hv})(G_{hv} + j\omega C_{hv})} \tag{3.7}$$

However, in power system studies, usually the conductance, G_{hv} , is practically zero, and therefore, the shunt admittance contains only the capacitive component C_{hv} . Therefore the characteristic impedance and propagation constant are as follows:

$$Z_C = \sqrt{\frac{R_{hv} + j\omega L_{hv}}{j\omega C_{hv}}}$$
(3.8)

Chapter 3. Novel Modelling and Analysis Framework for an Offshore Wind Power Plant

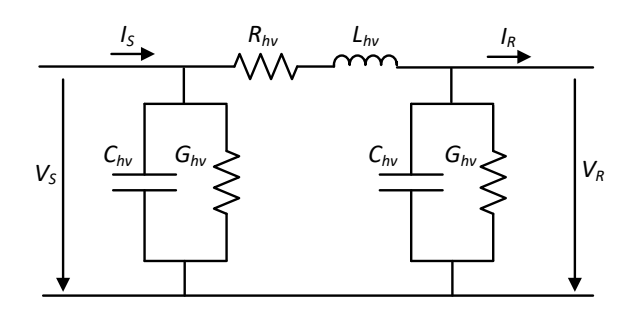


Figure 3.3: One-line π -model representation of an HVAC cable section and the propagation constant, γ is defined as

$$\gamma = \sqrt{(R_{hv} + j\omega L_{hv})(j\omega C_{hv})} \tag{3.9}$$

And for this particular case, which is the one used in this study, Figure 3.4 displays a section of the final equivalent π -cable representation used throughout this study.

Using the π -equivalent displayed in Figure 3.4, a distributed model is obtained by cascading several sections, each one of one kilometer, obtaining thus, the equivalent distributed π -equivalent which may be seen in Figure 3.5.

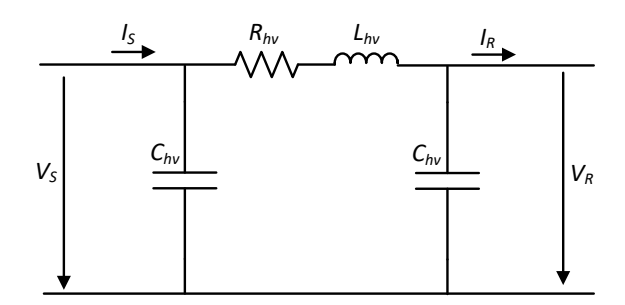


Figure 3.4: Final equivalent one-line π -model representation of an HVAC cable section

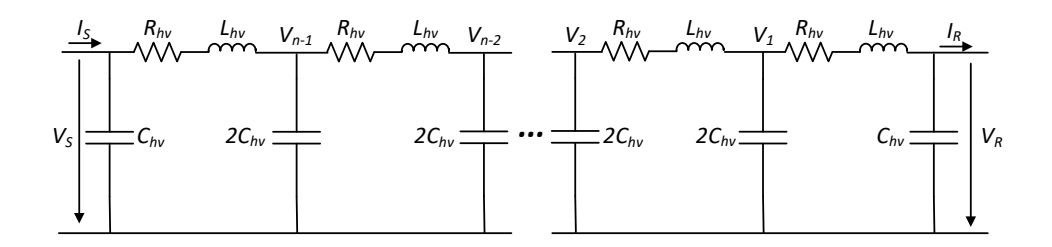


Figure 3.5: Distributed model of the one-line π -model representation

3.2.3 Shunt reactors

The shunt compensations were used to compensate for the reactive power excess due to the high capacitance of the HVAC submarine cable, both onshore, mid-cable, and offshore. After determining exactly how much reactive power needed to be compensated, the inductance per phase was computed as follows.

$$Li, j, k = \frac{U_n^2}{2\pi f Q_{PCC}} \tag{3.10}$$

where U_n is the voltage at the terminals of the offshore (L_i) , mid-cable (L_j) or onshore (L_k) shunt compensations, and Q_{PCC} is the reactive power measured at the offshore PCC.

The reactive power to be compensated was chosen to enable a power factor close to unity, within TSO standards, between -0.95 and 0.95 at the offshore PCC and to maintain a voltage level within the 0.9 pu and 1.1 pu range. Table B.4 displays 60% of the reactive power measured at the PCC, which was the amount chosen to be compensated via shunt reactors, and the values of the shunt reactors chosen were computed as shown in Equation 3.10. If the power factor, presented in Table 3.4, did not fall within the specified range, the shunt reactors were manually adjusted to achieve the desired power factor and voltage levels.

The resistor shown in Figure 3.6 is a damping resistor added owing the inter-

actions between the parallel of shunt reactors and the capacitance of the cable. The damper was computed as follows:

$$R_{i,j,k} = \frac{1}{2} \sqrt{\frac{L_{i,j,k}}{C_{hv}}} \tag{3.11}$$

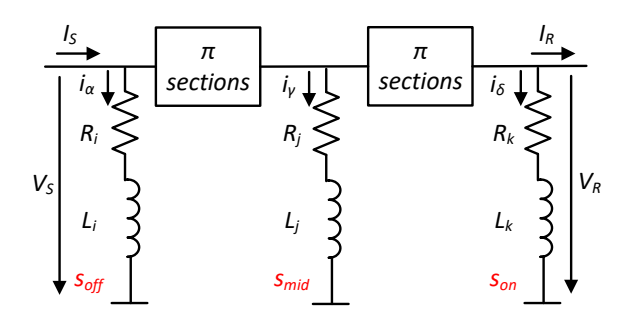


Figure 3.6: Distributed model of the one-line π -model representation

3.2.4 The Electrical Grid

The electrical grid is modeled as an RL Thevenin equivalent [138], characterized by a grid voltage V_g , resistance R_g , and inductance L_g . This system is depicted in Figure 3.7. The frequency is assumed to be 50 Hz, leading to an angular frequency of:

$$\omega_0 = 2\pi 50 \tag{3.12}$$

The nominal voltage is 230 kV. The three-phase grid voltages are described by the following equations:

Chapter 3. Novel Modelling and Analysis Framework for an Offshore Wind Power Plant

$$V_{g,a}(t) = V_g \cos(\omega_0 t)$$

$$V_{g,b}(t) = V_g \cos\left(\omega_0 t - \frac{2\pi}{3}\right)$$

$$V_{g,c}(t) = V_g \cos\left(\omega_0 t + \frac{2\pi}{3}\right)$$
(3.13)

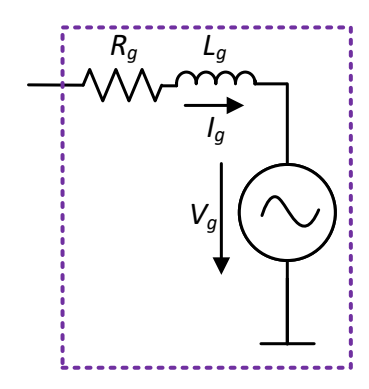


Figure 3.7: One-line diagram of the Thevenin equivalent grid

While the grid is represented here using a simple RL Thevenin equivalent model [138], this is a simplification that does not capture the full complexity of modern power systems with high inverter penetration. In contemporary networks, the dynamic behaviour is increasingly shaped by the presence of power electronic converters, reduced system inertia, and control-driven interactions. However, for the purpose of this analysis, particularly in the context of small-signal modelling, this representation is considered appropriate and provides a tractable framework for assessing system dynamics. Future work should aim to include more detailed grid representations to account for the evolving characteristics of modern power systems and to better reflect their dynamic response under high inverter-based generation scenarios.

3.2.5 Offshore Transformer

An offshore transformer was considered between the OWPP and the offshore shunt reactor, stepping up the voltage from 66 kV to 230 kV. Two offshore transformers were modelled for the studies. One transformer was specifically designed for the PSR studies in Chapters 6 and 7, and was modelled for EMT simulations. The modelling of transformer magnetisation and related characteristics is discussed later in the respective chapters. Furthermore, no top change range was modelled for these studies.

Additionally, a transformer based on an equivalent impedance model was developed, using a resistor and inductor as described in [135], for small signal model analysis. This version was applied in all studies that involved small signal analysis, and the impedance value was factored into the aggregated OWPP impedance, as mentioned in section 3.2.1.

3.2.6 Onshore Loads

For some of the steady-state and PSR studies, resistive-inductive (RL) loads were considered. A scheme of such loads may be seen in figure 3.8. In the figure, it can be seen that four loads are connected. This is for the PSR studies, where the interest was to study energization steps for different active and reactive power injections. Thus, the breakers (BRK1 to BRK4) would be closed at specific time instants.

Considering the the active and reactive power operating points are given, and considering a three-phase balanced system, the resistive and inductive components, R_{LD} and L_{LD} , are computed as follows:

$$R_{LD} = \frac{V_{LD}^2}{P_{LD}} \tag{3.14}$$

Where V_{LD} is the voltage at the load terminals and P_{LD} is the active power

demanded by the load.

$$L_{LD} = \frac{V_{LD}^2}{2\pi f Q_{LD}} \tag{3.15}$$

Where Q_{LD} is the inductive reactive power consumed by the load.

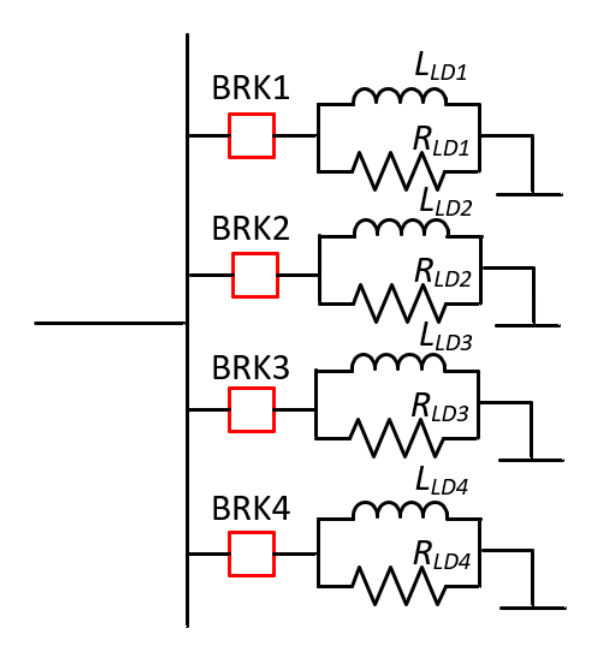


Figure 3.8: Scheme of the one-line onshore RL loads

3.2.7 Final Designs

Figure 3.9 presents three configurations of an OWPP connected to an onshore grid via a transmission system. These configurations, depicted in Figures 3.9a, 3.9b, and 3.9c, represent an aggregated OWPP, modelled as a voltage source with a coupling filter, a PWM filter.

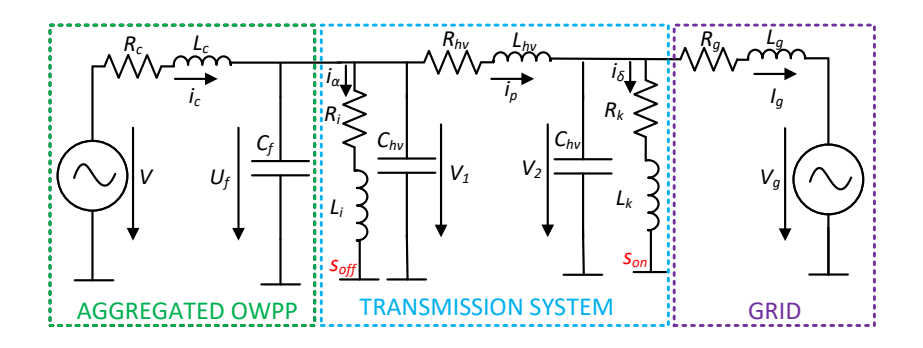
Depending on the configuration, these systems include shunt reactor compensators, labelled as s_{off} , s_{mid} , and s_{on} , depending on the location of the shunt reactor. Additionally, these systems feature an HVAC export cable. It is important to note that, for simplicity, the system is represented by a single π -equivalent model, although, as stated in Section 3.2.2, each cable is modelled as a distributed

line with cascaded sections, each 1 km in length. These diagrams also include a Thevenin equivalent representation of the grid.

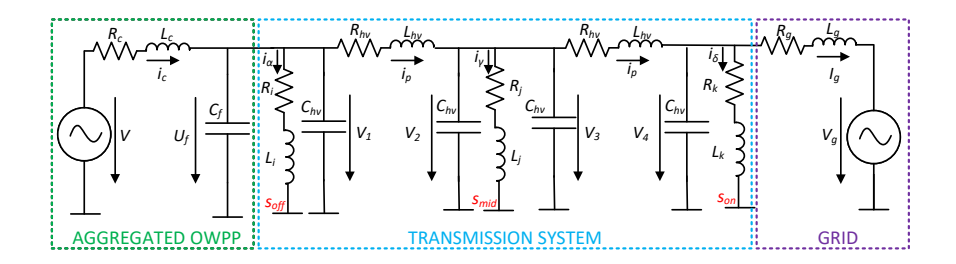
The three configurations illustrated in Figure 3.9 are described as follows:

- A1 The OWPP is connected to the electrical grid via an HVAC transmission system with two shunt reactors: one located at the offshore PCC and one onshore.
- A2 Similar to A1, but with an additional shunt reactor placed at the midpoint of the cable, resulting in three shunt compensation points (offshore, mid-cable, and onshore).
- A3 A simplified configuration with a single shunt reactor installed onshore.

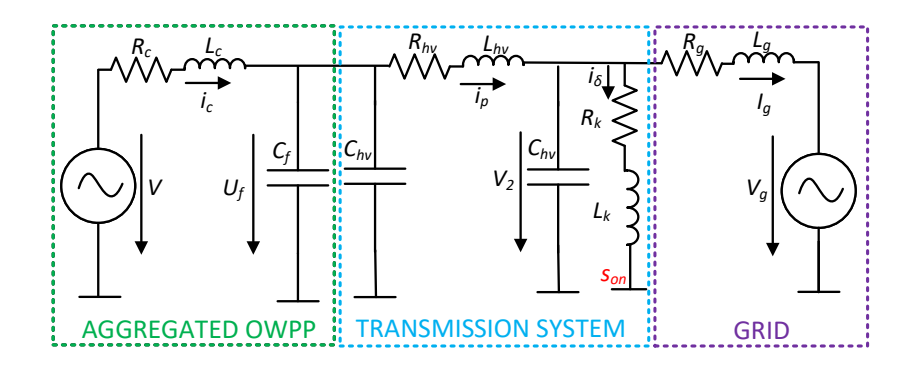
Chapter 3. Novel Modelling and Analysis Framework for an Offshore Wind Power Plant



(a) One-line diagram of configuration A1



(b) One-line diagram of configuration A2



(c) One-line diagram of configuration A3

Figure 3.9: System configurations (A1, A2, and A3) of shunt reactors distribution for the transmission system

All these configurations were used for small signal stability studies and were thus linearised and transformed into a state-space representation. The state-space

model of configuration A1 can be found in Appendix C, where all state-space models are explained in detail. The equations describing the system presented here are given from (3.16) to (3.22). The parameters used in these studies vary, and as such, they are presented in each chapter.

$$\frac{di_c}{dt} = -\frac{1}{L_c} u_f - \frac{R_c}{L_c} i_c + \frac{1}{L_c} V \tag{3.16}$$

$$\frac{du_f}{dt} = -\frac{1}{C_f}(i_c + i_\alpha) \tag{3.17}$$

$$\frac{di_{\alpha}}{dt} = \frac{1}{L_i} V_1 - \frac{R_i}{L_i} i_{\alpha} \tag{3.18}$$

$$\frac{di_p}{dt} = \frac{1}{L_{hv}} V_1 - \frac{R_{hv}}{L_{hv}} i_p - \frac{1}{L_{hv}} V_2 \tag{3.19}$$

$$\frac{i_{\delta}}{dt} = -\frac{R_k}{L_k} i_{\delta} - \frac{1}{L_k} V_2 \tag{3.20}$$

$$\frac{dV_2}{dt} = \frac{1}{C_{hv}} i_p - \frac{1}{C_{hv}} i_\delta - \frac{1}{C_{hv}} i_g \tag{3.21}$$

$$\frac{i_g}{dt} = -\frac{1}{L_g} V_g - \frac{R_g}{L_g} i_g + \frac{1}{L_g} V_2 \tag{3.22}$$

In equations (3.16) to (3.22), i_c is the current flowing to the PCC from the converter, with V representing the converter voltage; u_f is the voltage at the shunt capacitor C_f ; R_c and L_c are the resistance and inductance of the filter, respectively; i_p is the current flowing through the HVAC export cable; R_{hv} , L_{hv} , and C_{hv} are the resistor, inductor, and capacitor components of the export cable; V_1 and V_2 are the voltages across the export cable capacitors; R_g and L_g represent the resistor and inductor of the grid, combined with the voltage source V_g to form the Thevenin equivalent; L_i and L_k are passive reactors used for compensating reactive power in the system, and the resistors R_i and R_k its dampers.

Figure 3.10 provides a simplified one-line diagram of an OWPP connected to an onshore load. This configuration is identical to that shown in Figure 3.9a,

with the exception that the voltage source representing the grid is replaced by a load, Z_{LD} , with a voltage V_{LD} .

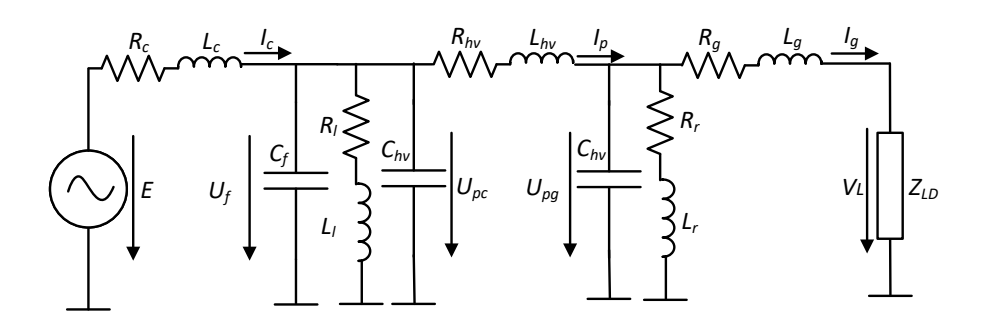


Figure 3.10: One-line diagram of an OWPP connected to a load

3.2.8 Cost Comparison of the Final Designs

This section compares the indicative capital cost of the three compensation arrangements for the export cable: A1 (two shunt reactors at the offshore and onshore substations), A2 (A1 plus a mid-cable shunt reactor on its own offshore site), and A3 (a single onshore shunt reactor). The comparison is illustrative and is intended to establish the order of magnitude of costs rather than provide a project-specific estimate.

For consistency, each reactor is modelled as a 200 MVAr unit. A unit cost of £28,900/MVAr is adopted from the Electricity Transmission Costing Study, which implies £5.786 million per 200 MVAr reactor [139]. This aligns with a National Grid submission that reports about £5.7 million for a 200 MVAr shunt reactor at 400 kV, providing a United Kingdom benchmark for hardware cost [140]. As an international cross-check, a 100 MVAr turnkey variable shunt reactor is publicly reported at \$3.7 million, which supports the same order of magnitude [141].

Integration and installation allowances are applied to reflect site conditions. For an onshore substation bay and associated works, an allowance of £0.5 million

Chapter 3. Novel Modelling and Analysis Framework for an Offshore Wind Power Plant

is used, with £0.2 million for installation and commissioning. For integration at an existing offshore substation, an allowance of £2.0 million for bay modifications and £1.0 million for offshore installation is used to reflect marine access and integration complexity. The defining cost driver for the mid-cable option is the need for a new offshore site. To represent a minimal reactor-only platform, a conservative fraction of an assessed offshore substation platform value is used: 25% of £158 million (that is, £39.5 million), derived from a recent cost assessment, to capture fixed marine, structural, switchgear, termination, access, and commissioning costs even for a reduced scope [142]. Broader guide values for offshore substation scope and installation (for example, £240,000/MW and £43,400/MW) corroborate that even stripped-down platforms fall in the tens of millions due to fixed costs [143].

Under these assumptions, the cost comparison is summarised in Table 3.1. The corresponding bar chart in Figure 3.11 visualises the relative magnitude of each arrangement.

Table 3.1: Illustrative capital cost comparison

	A1	A2	A3
Number of reactors (200 MVAr each)	2	3	1
Reactor hardware (£m)	11.56	17.34	5.78
Onshore bay $+$ installation (£m)	0.70	0.70	0.70
Offshore bay $+$ installation (£m)	3.00	3.00	0.00
Mid-cable platform $(£m)$	0.00	39.50	0.00
Illustrative capital expenditure total (£m)		60.54	6.48

On a cost basis alone, the arrangement requiring a new mid-cable offshore site (A2) is materially higher due to the additional platform. The two-ended arrangement using existing offshore and onshore substations (A1) is typically mid-cost. A single onshore reactor (A3) is usually lowest cost, provided it satisfies technical limits for voltage and reactive control.

Chapter 3. Novel Modelling and Analysis Framework for an Offshore Wind Power Plant

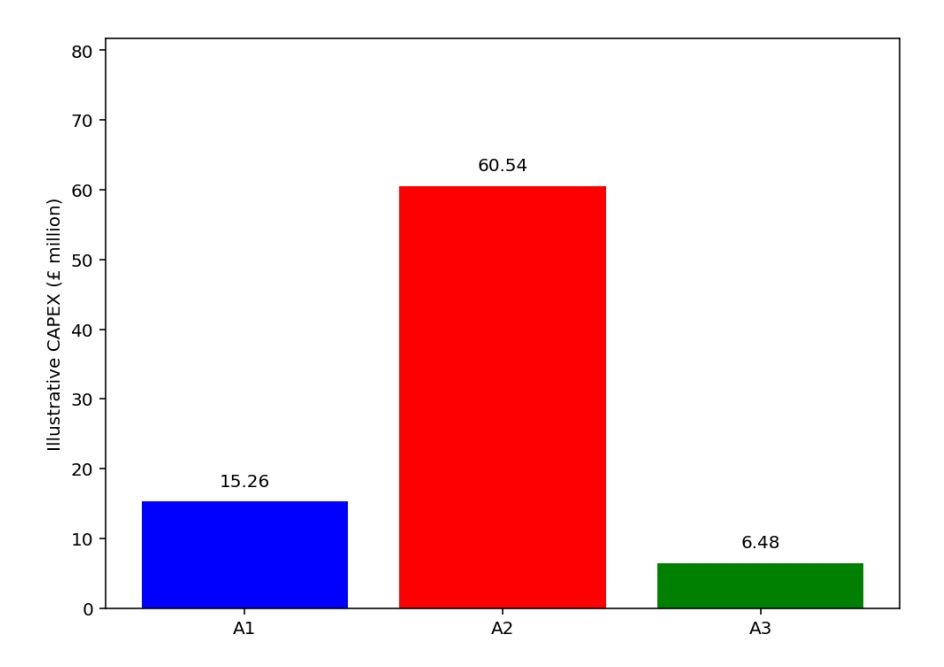


Figure 3.11: Illustrative capital cost comparison of A1, A2, and A3

3.3 Steady-State Analysis

Two steady-state analysis were conducted throughout this study. The first one concerns the capabilities and limitations of the OWPP in injecting active and reactive power into the electrical grid (or onshore loads). The second study was about the voltage profile—the impact of shunt compensation and cable length on the voltage.

3.3.1 Offshore Wind Power Plant Capabilities And Limitations

The model used for this study was that of Figure 3.10. In the figure, an aggregated offshore wind farm is represented with a voltage source E and its LC filter via R_c and L_c . The model also includes offshore shunt compensation with L_i and R_i , and onshore shunt compensation with L_j and R_j . As previously detailed, the export cable is modelled as a π cable with parameters C_{hv} , R_{hv} , and L_{hv} . Additionally,

the grid line is represented with parameters R_g and L_g and is connected to a load, Z_{LD} .

The system represented in Figure 3.10 was further simplified in impedance as seen in Figure 3.12. This way, the entire system was encapsulated, only considering a voltage source with varying magnitude, \overline{E} , and angle, α , an equivalent impedance, representing all the system components and the load. This way, it was possible to vary the impedance depending on the system parameters such as OWPP nominal power output, local network demand and wind speed and analyse the impacts on the load, which here represents the local network demand, as will be explained in the next section.

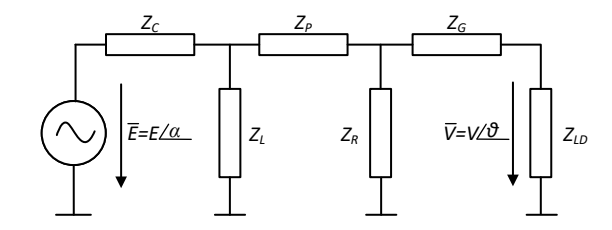


Figure 3.12: OWPP and network one-line impedance base model

From Figure 3.12, all impedances are combined, and the final Thevenin voltage and impedance are given by

$$V_{th} = \overline{E} \cdot \frac{Z_C \cdot (Z_L + Z_P + Z_R)}{Z_L \cdot (Z_P + Z_R) + 2Z_C \cdot (Z_L + Z_P + Z_R)}$$
(3.23)

$$Z_{th} = \frac{Z_C Z_L Z_R + Z_P Z_R}{Z_C Z_L + Z_P (Z_C + Z_L) + Z_R} + Z_g$$
(3.24)

Where V_{th} is the Thévenin voltage and Z_{th} the Thévenin impedance. Such impedance will be later used having its real part, R, and imaginary one, X, separated.

Considering the Thevenin equivalent described by equations 3.23 and 3.24, the current flowing through the converter is

$$\overline{I} = \frac{\overline{E} - \overline{V_{th}}}{Z_{th}} \tag{3.25}$$

The apparent power, S, at the converter terminals, is

$$S_c = \overline{V_{th}} \overline{I}^* = \overline{V_{th}} \left(\frac{\overline{E_s} - \overline{V_{th}}}{Z_{th}} \right)^* \tag{3.26}$$

By developing this equation and separating the real and imaginary parts, the active and reactive power flow equations for the power converter are achieved.

$$P_{c} = \frac{R\overline{VE}cos(\alpha) - \overline{EV}Xsin(\alpha) - \overline{V^{2}}R}{R^{2} + X^{2}}$$
(3.27)

$$Q_c = \frac{X\overline{VE}cos(\alpha) - \overline{EV}Rsin(\alpha) - \overline{V^2}X}{R^2 + X^2}$$
(3.28)

Following [144], by removing the resistive component—and consequently the transmission resistance—from Equations 3.27 and 3.28, the following expressions are derived:

$$P_c = -\frac{\overline{EV}\sin(\alpha)}{X} \tag{3.29}$$

$$Q_c = \frac{\overline{VE}\cos(\alpha) - \overline{V^2}}{X} \tag{3.30}$$

From the previous equations, 3.27, 3.28, and 3.29, 3.30, it is evident that the active and reactive power are calculated based on the voltage magnitude and phase angle. These values represent the operating points of active and reactive power for the converter in this specific system. By eliminating the phase angle dependency through mathematical transformations and assuming a lossless system under a given power factor, the voltage limit of the system for maximum power points is expressed as:

$$V = \sqrt{\frac{\overline{E_s^2}}{2} - QX \pm \sqrt{\frac{\overline{E_s^4}}{4} - X^2 P^2 - X \overline{E_s^2} Q}}$$
 (3.31)

For a given P_c , the reactive power that forces the system to operate under these conditions is:

$$Q = -\frac{P^2X}{\overline{E^2}} + \frac{\overline{E^2}}{4X} \tag{3.32}$$

To study the hardware limitations in terms of export cable length and the use of shunt compensation, the voltage stability limits were plotted in the PQ plane, taking into account Equations 3.31 and 3.32. For this purpose, the active power at the converter terminals, P_c , was varied between -1.5 and 1.5 pu, and the corresponding reactive power, Q_c , was computed. The negative values of active power are included for illustrative purposes only, as in this case the OWPP is assumed to be operating as a generator and therefore only supplies active power.

Figure 3.13 defines a three-dimensional plane which is the solution to Equation 3.31. In this plot, the variation of active and reactive power for different power factor angles and their impact on voltage can be observed.

The PV plane in the figure provides the curves of load voltage as a function of active power for various power factors, as shown in Figure 3.14.

The projection onto the PQ plane is used to understand the system's limitations in terms of active and reactive power. This type of plot was utilised in this study and in the power system restoration study detailed in Chapter 6, Section 6.2.

Impact of HVAC export cable length

This study aimed to analyse the impact of cable length on voltage stability and its operational region, focusing on the overall voltage stability of the system and its active and reactive power capabilities. As shown in Section 3.2.7, Figure 3.10, the

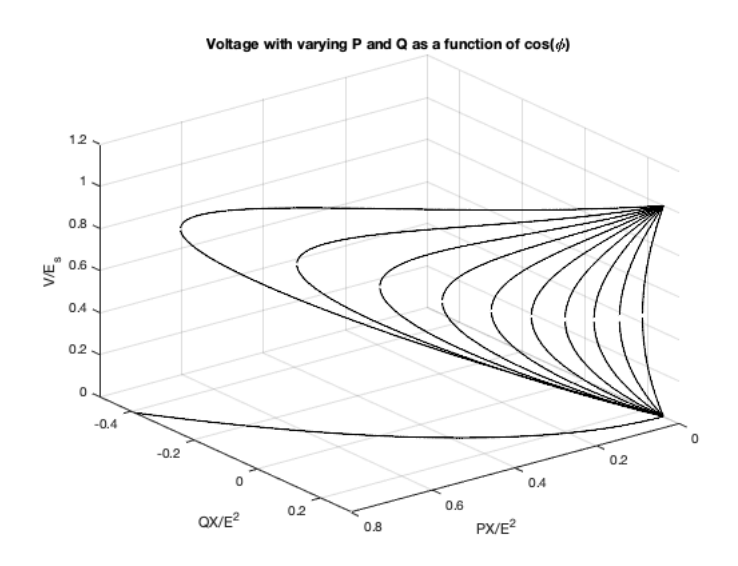


Figure 3.13: Voltage magnitude when varying P and Q as function of the power factor, $cos(\phi)$

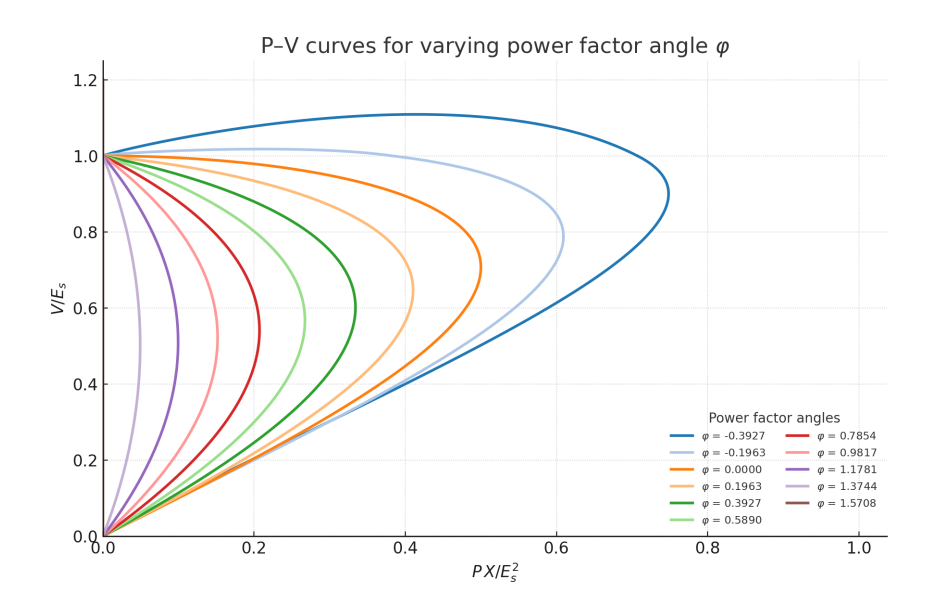


Figure 3.14: PV curves for different power factors

transmission system includes a long HVAC export cable and two shunt reactive power compensations. Three export cable lengths were compared: 50, 100, and 150 km.

Using the PQ plane as previously described, along with the equations for voltage limits and active and reactive power, Figure 3.15 displays the voltage stability limits as a function of the PQ characteristics for the three different export cable lengths. The unity circle of operation, as seen by the electrical grid, is also plotted.

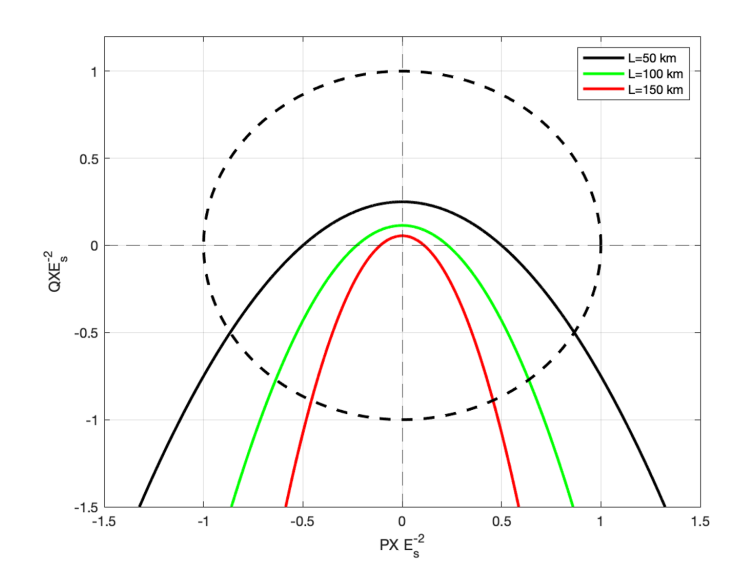


Figure 3.15: Voltage stability limits for different HVAC export cable lengths

The reduction in voltage stability in the PQ plane with increasing transmission system length is associated with a decrease in the permissible operational region. As cable length increases, the impedance and capacitive reactance of the transmission line also increase. Consequently, the electrical network's ability to maintain voltage within acceptable limits under varying load conditions diminishes. Therefore, voltage control and compensation mechanisms are needed to expand the operational envelope and maintain grid reliability over extended transmission distances.

Chapter 3. Novel Modelling and Analysis Framework for an Offshore Wind Power Plant

Moreover, it can be observed from Figure 3.15 that unitary active power can only be injected for the shortest cable (black line). For the 100 km and 150 km cases, the maximum power transferable to the grid is significantly lower than desired. As such, it is necessary to oversize the power converter or include reactive power compensation to address this issue and enable the provision of more active power, which will be discussed in Section 3.3.2.

3.3.2 Impact of reactive power shunt compensation

In Section 3.3.1, it was demonstrated how the length of the HVAC export cable limits the voltage operational stability region. However, this region can be expanded by employing reactive power shunt compensation within the power system. To analyse this scenario, reactive power was fully compensated (1 pu) in the 150 km export cable. One shunt reactor was deployed at the offshore PCC, compensating for 40% of Q, while the second shunt reactor, compensating for the remaining 60%, was installed onshore.

The reactors were sized based on the reactive power compensation percentage, as detailed in Section 3.2.3. The inductance values are shown in Table 3.2 for the three different cable lengths.

Table 3.2: Shunt compensation for different cable lengths

Length (km)	L_{sl} (H)	L_{sr} (H)
50	0.3368	0.5052
100	0.1347	0.2021
150	0.0842	0.1263

Using Equations 3.31 and 3.32, the voltage stability region for a 150 km HVAC cable, both with and without shunt compensation, is plotted in Figure 3.16.

The stable voltage region significantly increases with shunt compensation (black line) compared to the original uncompensated 150 km line (red line). This

Chapter 3. Novel Modelling and Analysis Framework for an Offshore Wind Power Plant

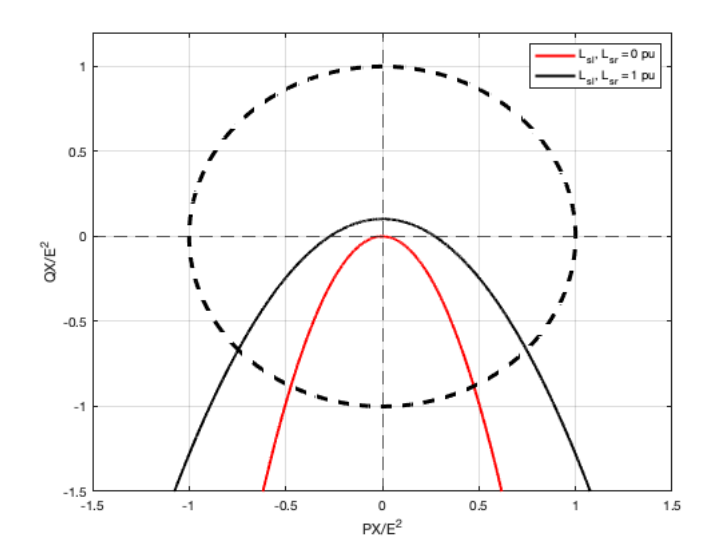


Figure 3.16: Voltage stability curve on the PQ plane for transmission line with and without shunt compensation

increase enables more active power to be delivered from the offshore wind farm to the electrical power system. Additionally, with shunt compensation, the system benefits from improved voltage regulation and enhanced reactive power management, as the flow of reactive power is actively controlled. This allows the system voltage to be maintained within the acceptable limits specified by transmission system operators, significantly expanding the stable operational voltage region. Moreover, deploying shunt compensation improves the power factor, bringing it closer to unity, as will be discussed in Section 3.3.3.

Power converter limitations

In this section, the impact of power system voltage stability on the operation of the power converter was analysed. The power converter output in terms of active and reactive power was previously described using Equations 3.27 and 3.28. From these equations, it is evident that voltage and power factor play a critical role in determining the magnitude of these quantities. Therefore, in this study, the converter voltage was varied between 0.8 pu and 1.2 pu, while the power factor

angles were varied between -45 and 45. Furthermore, this analysis was conducted for the power system both with and without reactive power shunt compensation, for an export cable of 150 km in length.

Figures 3.17a and 3.17b present the results of this analysis. The voltage stability curve in the PQ plane is plotted for the electrical grid with an export cable of 150 km and shunt compensation applied at the PCC. Below this area, the active and reactive power operating points for the specified voltage magnitude and power factor are displayed. Examining Figure 3.17a first, it can be observed that the maximum active power achievable is approximately 0.6 pu, whereas if the system is fully compensated, as shown in Figure 3.17b, the maximum active power exceeds 1 pu.

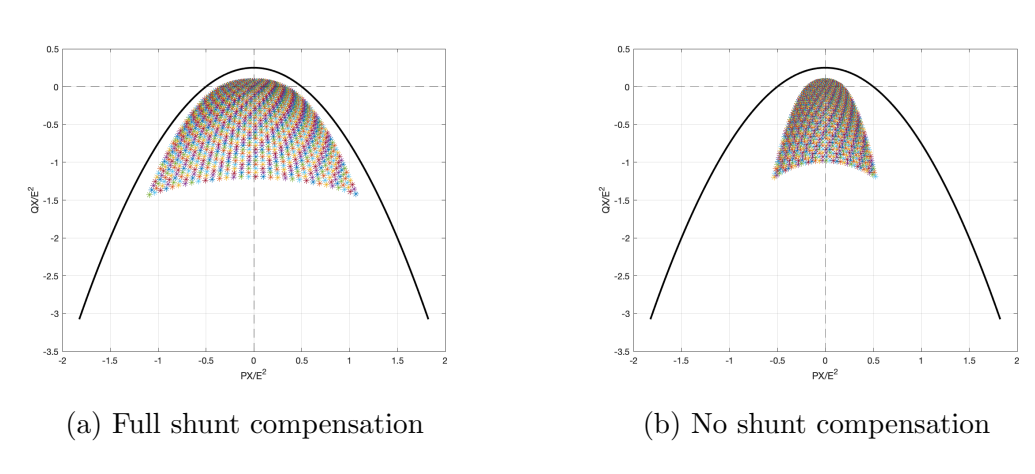


Figure 3.17: Converter operation area in the PQ plane

The operational area in the power system, particularly in the PQ plane, influences the feasibility of providing a stable power flow in steady-state conditions, as well as for black start services. For such capabilities, the ability to re-energise the grid during a blackout or complete shutdown is crucial. It requires generators to start and synchronise with the grid without any external power supply. The operational area shown in the PQ plane directly relates to the capabilities of power converters and their potential to provide essential grid support services. For offshore wind power plants (OWPP) to contribute effectively to black start

operations, their converters must be able to swiftly and reliably re-energise the grid without external support.

Expanding the operational area in the PQ plane by employing reactive power compensation and enhancing the capability of power converters may increase the potential for these renewable sources to participate in power system restoration (PSR) services. A broader operational region signifies greater flexibility and capacity for these sources to manage reactive power, maintain stability, and provide the necessary grid support during critical system restoration.

3.3.3 Voltage Profile

As presented in Section 3.2.7, several system configurations for export cables with shunt compensation were examined, focusing on the different numbers and locations of the shunt reactors. This section describes how these setups affect the voltage profiles for various cable lengths, of 80, 120 and 150 km, as well as the power factor. The shunt compensation can be placed in three locations: at the sending end of the cable immediate after the OWPP (s_{off}) , in the middle of the cable (s_{mid}) , or at the receiving end, onshore (s_{on}) .

The three different arrangements identified are listed in Table 3.3. In arrangement A1, shunt compensations are placed at both the offshore PCC and onshore PCC. Arrangement A2 involved shunt reactors located offshore, mid-cable, and onshore. In arrangement A3, a single shunt reactor was positioned onshore. The final values for the different arrangements, A1, A2 and A3, and for the different cable lengths (80, 120 and 150 km) are shown in Table B.4.

Arrangement	Location reactors
A1	$s_{off} + s_{on}$
A2	$s_{off} + s_{mid} + s_{on}$
A3	s_{on}

Table 3.3: Arrangements of shunt compensation analysed

Shunt reactors were installed to comply with the standard requirements set by most TSO. The main objective was to maintain the voltage within acceptable limits, specifically between 0.9 pu and 1.1 pu, and to ensure that the power factor remained within the range of 0.95 leading to 0.95 lagging at the PCC. The voltage profile results for an 80 km export cable, considering the various compensation arrangements, are shown in Figure 3.18. In this Figure, A0 represents a scenario without shunt compensation. Voltage measurements were taken at the sending and receiving ends of the cable, as well as at 10 km intervals along its length. The results indicate that, without appropriate reactive power compensation, the voltage exceeds the specified TSO limits. By contrast, the three compensated arrangements, A1, A2, and A3, successfully maintained the voltage within the required limits.

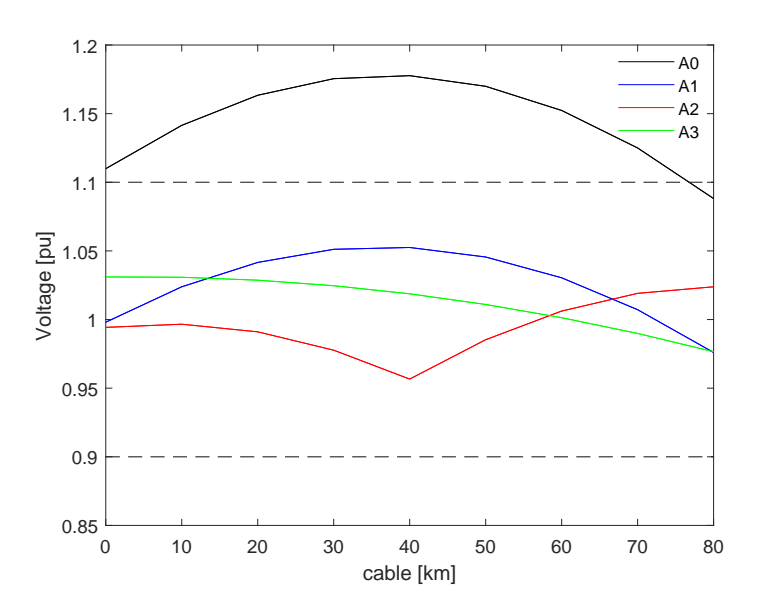


Figure 3.18: Voltage profile for an 80 km HVAC export cable for A0 (no compensation), A1, A2 and A3

The analysis of shunt reactor placement and sizing revealed that both the location and degree of compensation (as distributed among the reactors) influenced the voltage profile. The corresponding power factor results are presented in Table 3.4, demonstrating that the implemented shunt compensations maintained both

the voltage and power factors within the specified ranges. This analysis was conducted under a SCR of 3, which, while indicating a weak grid, is not excessively so.

The power factor and voltage profile were also heavily influenced by the strength of the electrical grid, as illustrated in Figure 3.19. This Figure shows an 80 km cable with no shunt compensation under two SCR conditions (1.5 and 3) and for X/R ratios of 1.5, 5, and 10.

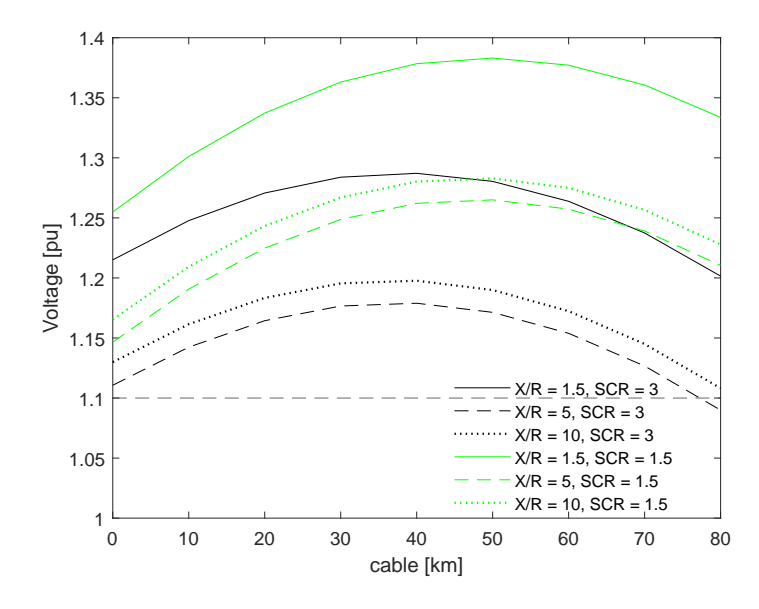


Figure 3.19: Impact of varying SCR and X/R in the voltage profile for an 80 km HVAC export cable

The results demonstrate that the ability to transfer power and maintain voltage within specified limits is directly related to both SCR and X/R ratios. Consequently, the control and tuning of shunt reactors must be adjusted based on the grid strength. This interdependence means that the overall stability of the power system is closely tied to the strength of the grid: the weaker the grid (indicated by lower SCR and lower X/R ratios), the more shunt compensation is required, which, as will be further discussed in Chapter 5, will impact system stability.

Changing both X/R and SCR will change the impedance of the overall system, which aligned with the shunt compensations, and the cable length will cause

Chapter 3. Novel Modelling and Analysis Framework for an Offshore Wind Power Plant

the impedance to vary significantly depending on the arrangement, X/R, SCR and cable length. This impedance will influence the power factor and voltage profile; hence, shunt reactor compensation will need to be computed accordingly to maintain the PF above 0.95 and a voltage between 0.9 and 1.1 pu.

	Cable length (km)		
Power factor	80	120	150
A0	0.7748	0.7071	0.6637
A1	0.9814	0.9752	0.9928
A2	0.9882	0.9973	0.9992
A3	0.9912	0.9873	0.9830

Table 3.4: Power factor for three cable lengths, and for the case of no compensation (A0) and for the three different arrangements

Chapter 4

Modified Converter Control Approach to Improve System Stability

4.1 Introduction

The chapter begins by explaining the standard GFL controller in Section 4.2. Section 4.3 introduces the GFM controller that is used throughout these studies, which is the VSM. In Section 4.4, the process of assessing small signal stability is discussed, focusing on how both GFM and GFL units are modelled and linearised for small signal stability analysis. Additionally, the chapter details the method used to study the stability of multi-input, multi-output (MIMO) systems through disk margins, a technique that measures robust stability.

Both the GFL and GFM controllers are mathematically modelled using dynamic equations, which are linearised to facilitate small signal stability analysis. The chapter explains the development of the small signal models and state-space representations for both control strategies, enabling a deeper understanding of how these controllers respond to system disturbances. Stability is evaluated using

Chapter 4. Modified Converter Control Approach to Improve System Stability disk margins, a robust measure that indicates how close a system is to instability, providing valuable insights into controller performance under varying conditions.

4.2 Grid Following Converter Control

A common implementation of GFL control is the standard vector current controller (SVCC). This controller regulates active and reactive power in the synchronous reference frame by decoupling the q and d components of the converter current. In this scheme, the q-axis controls active power, while the d-axis manages reactive power.

Most GFL controllers include an inner current control loop and an outer power control loop, in addition to the synchronisation loop. The inner loop is responsible for fast current regulation, whereas the outer loop ensures stable power flow control. In this section, these control loops, along with their respective equations, will be described in detail.

The GFL converter utilised in this work is shown in Figure 2.5. A second configuration, with a modified outer loop controller, is illustrated in Figure 4.1. Both configurations are based on the standard vector current controller (SVCC) described in [145]. In the first configuration, the outer loop controls active power and voltage magnitude, while in the second configuration, the outer loop regulates active power and reactive power instead of voltage. While these solutions are standardised, as previously mentioned, additional external control loops may be incorporated to enable frequency and inertia support.

4.2.1 Phase Locked Loop

The PLL is the submodule of the GFL controller responsible for synchronising the plant with the electrical grid, and consists of a feedback loop having as an input the synchronous reference frame d component of the voltage, u_f , measured at

Chapter 4. Modified Converter Control Approach to Improve System Stability

the PCC, filtered by a PI controller. The output of this controller is the angular velocity which, integrating, results in the electrical grid angle, as expressed in Equation 4.1.

$$\theta = -\frac{1}{s} u_{f,d} K_{PLL} \tag{4.1}$$

where θ is the determined grid angle, $u_{f,d}$ is the d component of the voltage at the PCC and K_{PLL} is a PI controller defined as

$$K_{PLL} = k_{p,PLL} + \frac{k_{i,PLL}}{s} \tag{4.2}$$

with proportional gain $k_{p,PLL}$ and the integral gain $k_{i,PLL}$, which were tuned following the method outlined in [145]. This approach primarily considers the damping ratio and electrical angular frequency of the system [146].

4.2.2 Inner Loop Current Controller

The inner loop is the lower-level control of the SVCC. It regulates the current through the inductance of the inductive filter between the VSC and the network. It also allows the independent control of both q and d components due to its decoupling terms. The output of this controller is the voltage which is fed back to the converter as shown in equations (4.3)-(4.4).

$$v_q = u_{f,q} - i_{cd} L_c \omega - K_{il} (i_{cq}^* - i_{cq})$$
(4.3)

$$v_d = i_{cq} L_c \omega - K_{il} (i_{cd}^* - i_c d)$$
 (4.4)

Where v_q and v_d are the output voltages for the VSC, $u_{f,q}$ is the q component of the voltage at the PCC; i_{cd} and i_{cq} are the currents at the PCC which are previously regulated via outer loop; K_{il} represents the PI controller with gains

Chapter 4. Modified Converter Control Approach to Improve System Stability $k_{i,il}$ and $k_{p,il}$ as shown in equation (4.5)

$$K_{il} = k_{p,il} + \frac{k_{i,il}}{s} \tag{4.5}$$

The PI controller K_{il} was tuned via internal model control, with the tuning constant α , which is the desired loop time constant [145, 147]. The constant α is chosen to be five to ten times slower than the power converter switching frequency.

$$k_{p,il} = \frac{L_c}{\alpha} \tag{4.6}$$

$$k_{i,il} = \frac{R_c}{\alpha} \tag{4.7}$$

4.2.3 Outer Loop Controller

As previously mentioned, two distinct outer loops modules were designed and were tuned following [145]. The first one considers that the external reference inputs are the desired active power and the voltage magnitude. The second case considers that the input references are the active and reactive power. Nevertheless, the goal of this module is the same for both cases, and that is the computation of the current references in the synchronous frame, i_{cq}^* and i_{cd}^* .

Figure 2.5, previously introduced in Section 2.4, illustrates the first approach, which considers the active power reference and voltage magnitude as reference signals. In this approach, the output of the module is determined as shown in Equations (4.8)–(4.9), providing the current references in the synchronous reference frame.

$$i_{cq}^* = K_P(P^* - P) (4.8)$$

Chapter 4. Modified Converter Control Approach to Improve System Stability

$$i_{cd}^* = K_U(U^* - U) (4.9)$$

Here, i_{cq}^* and i_{cd}^* represent the current references, P^* denotes the active power reference, and P is the active power measured at the PCC. Similarly, U^* is the voltage reference, while U is the voltage computed in the synchronous reference frame. Finally, K_P and K_U are the PI controllers responsible for regulating the power and voltage loops, as shown in Equations 4.10 and 4.11.

$$K_P = k_{p,PC} + \frac{k_{i,PC}}{s}$$
 (4.10)

$$K_V = k_{p,VC} + \frac{k_{i,VC}}{s} (4.11)$$

Figure 4.1 displays a diagram of the second outer loop option considered. In this case, the input reference signals are the active and reactive power references. In this scenario, the current references i_{cq}^* and i_{cd}^* are computed as follows:

$$i_{ca}^* = K_P(P^* - P) (4.12)$$

$$i_{cd}^* = K_Q(Q^* - Q)$$
 (4.13)

where K_Q is the PI controller refereeing to the reactive power loop and is defined as:

$$K_Q = k_{p,QC} + \frac{k_{i,QC}}{s} \tag{4.14}$$

The active power (P), reactive power (Q), and voltage magnitude (U) utilised in the equations for the outer loop controllers are calculated in the synchronous reference frame. These quantities are determined using the current, $i_{c,qd}$, at the converter terminals and the voltage, $u_{f,qd}$, at the PCC. The detailed calculations

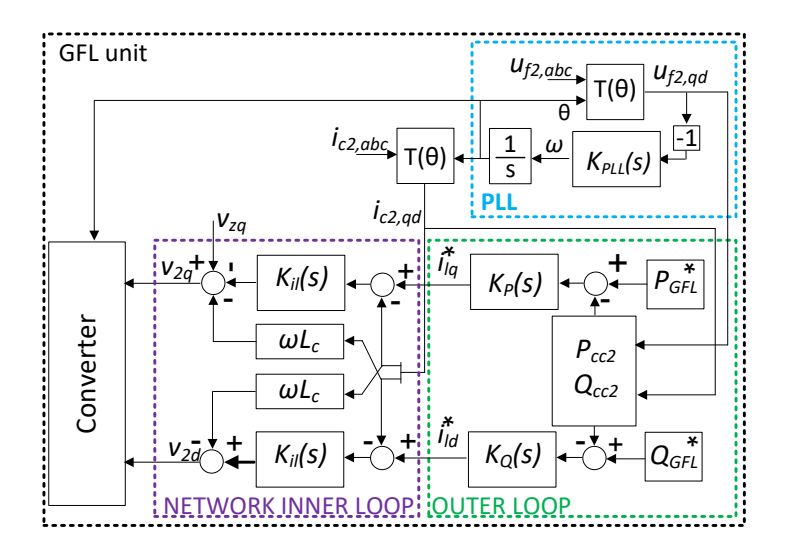


Figure 4.1: GFL controller with active and reactive power as inputs of the outer loop

can be found in Appendix E.1.2.

4.3 Grid Forming Converter Control

4.3.1 VSM

As previously mentioned, the GFM controller used in this study is based on a virtual synchronous machine. This section outlines the controller and the equations that define its behaviour. Two controllers were designed. The first consists of two main loops: a power loop and a voltage loop. The second controller is identical to the first but further includes an additional virtual impedance.

Figure 4.2 illustrates the first design, which includes the power and voltage loops. The power loop calculates the angle at the PCC, while the voltage loop computes the q-axis component of the voltage to be modulated, with the d-axis component set to zero. From the figure, it can be seen that the controller utilises the current from the converter, i_c , and the voltage at the PCC, u_f . These values

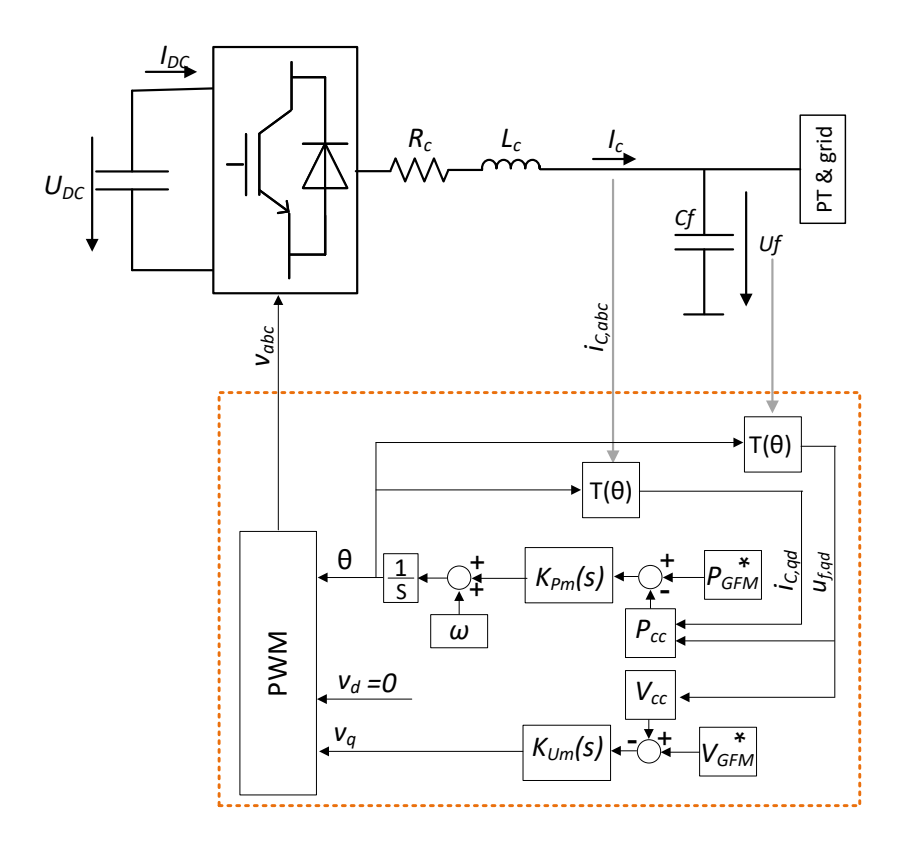


Figure 4.2: GFM controller connected to one-line system

are transformed from the ABC frame to the $\alpha\beta0$ frame. No Park transformation is required, as the d-axis voltage component is zero.

However, for the second GFM design, shown in Figure 4.3, which includes the virtual synchronous machine, the controller requires the synchronous transformation, as both the q and d components are modulated and fed back into the converter.

The power and voltage loops mentioned, which computed the angle and voltage expressions for this controller may be seen in Equations (4.15)-(4.17).

$$\theta = \frac{1}{s} \left((P^* - \frac{2}{3} i_q v_q) K_{Pm} + f \right)$$
 (4.15)

Chapter 4. Modified Converter Control Approach to Improve System Stability

$$v_q = \left(V^* - \sqrt{(v_q^2 + v_d^2)}\right) K_{Um} \tag{4.16}$$

$$v_d = 0 (4.17)$$

In equation (4.15), P^* is the active power reference, i_q is the q component of the current at the PCC, v_q is the q component of the voltage at the PCC, f is the reference frequency and K_{Pm} is the PI controller related to the power loop defined as

$$K_{Pm} = m_p + \frac{m_i}{s} \tag{4.18}$$

In equation (4.16), v_q is the desired voltage to feed the converter, V^* is the voltage reference, v_q and v_d are the q and d components of the voltage at the point of common coupling; finally, K_{Um} is the PI controller of the voltage loop defined as

$$K_{Um} = k_{p,VCC} + \frac{k_{i,VCC}}{s} \tag{4.19}$$

4.3.2 VSM With Virtual Impedance

This controller may be seen in Figure 4.3. The virtual impedance was added to this controller for the power system restoration studies. Several studies were analyzed with regards to virtual impedance implementation [97, 148–152] and eventually the approach described by Rodriguez-Cabero et. all described in [151] was followed, as well as the tuning strategy. The virtual impedance is located after the PI voltage controller. Thus, the q component of the voltage which is fed back to the converter, v_{lq} , is given by

$$v_{lq} = (V_Z^* - u_{f1,q}) \left(k_{p,VCC} + \frac{k_{i,VCC}}{s} \right) - i_{c1,q} R_v - i_{c1,d} L_v \omega$$
 (4.20)

Where V_Z^* is the voltage reference of the controller, $u_{f1,q}$ is the q component

Chapter 4. Modified Converter Control Approach to Improve System Stability of the voltage at the PCC of the grid forming converter and $i_{c1,q}$ and $i_{c1,d}$ are the synchronous reference frame components of the current measured at the converter terminals. For the d component of the voltage at the converter terminals, v_{ld} is given by

$$v_{ld} = -i_{c1,d}R_v + i_{c1,q}L_v\omega (4.21)$$

In both equations 4.20 and 4.21, R_v and L_v are the virtual resistance and inductance and ω is the frequency measured at the PCC.

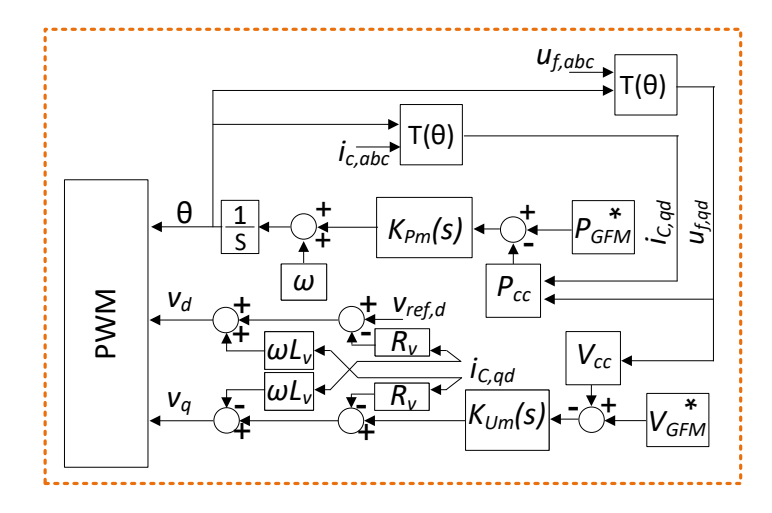


Figure 4.3: GFM controller connected to one-line system, with virtual impedance

4.4 Stability Assessment and Comparison Between Controllers

Throughout this study, system stability is analysed using small-signal models (SSM). The SSM encapsulates the dynamics of the various control loops, which are connected through their inputs and outputs, from the OWPP, through the

Chapter 4. Modified Converter Control Approach to Improve System Stability transmission network, to the electrical grid. This model is formulated as a state-space representation, as shown in Equations 4.22 and 4.23.

$$\Delta \dot{x} = A\Delta x + B\Delta u \tag{4.22}$$

$$\Delta y = C\Delta x + D\Delta u \tag{4.23}$$

In these equations, x represents the state variables, y denotes the system outputs, and u corresponds to the inputs. The matrices A, B, C, and D are the system, input, output, and feedthrough matrices, respectively. By applying this SSM, the non-linear electromagnetic transient (EMT) model is linearised around specific operating points. These operating points, derived from the time-domain EMT simulations, are subsequently used to populate the state-space, linear time-invariant (LTI) matrices, enabling stability analysis of the system.

Once the controllers are linearised, the first step is to integrate them with the state-space matrices defined in Chapter 3, Section 3.2.7, which represent the power system, electrical grid, and loads. This ensures that the entire model is linearised and prepared for small signal stability analysis.

Following the development of the state-space models, the next step involves validating their accuracy by comparing them with the electromagnetic transient (EMT) model. For this validation, a power step of 0.01 pu was applied to both the EMT and SSM simulations, for both GFM and GFL controllers. Stability is then assessed using disk margins, which is the technique employed throughout this study. The linearisation of the GFL unit is explained in Section 4.4.1, the linearisation of the GFM unit in Section 4.4.2, and the stability assessment method used to evaluate stability and robustness is described in Section 4.4.3.

Table 4.1: State-space, LTI, matrices for filters and transformations used

Loop	State-space
LPF	E.1.1
T(heta)	E.1.2
$T^{-1}(\overset{\cdot}{ heta})$	E.1.3

4.4.1 GFL Small Signal Model

Figure 4.4 presents a schematic of the GFL linearised control system. As shown, all control loops are interconnected through their respective inputs and outputs. In the figure:

- OL Outer Loop
- LPF Low Pass Filter
- $T(\theta)$ Park Transformation
- $T(\theta)^{-1}$ Inverse Park Transformation
- PLL Phase Locked Loop
- IL Inner Loop

The system has two primary inputs: the active and reactive power references, or alternatively, the active power and voltage magnitude references. In the figure, only the former is depicted, as it is used in the power system restoration studies discussed in Chapters 6 and 7. However, the latter reference is employed in the studies presented in Chapter 5.

To derive the small signal model, all the equations outlined in Section 4.2 have been linearised and expressed in state-space form within the synchronous reference frame. The full set of equations and state-space models are available in Appendix E.2 and Table 4.2 displays where the different control loops (referring

Chapter 4. Modified Converter Control Approach to Improve System Stability also to both outer loop controllers described in 4.2.3) may be found within the appendix.

However, as an example, the reader may find below the linearisation process, and state-space model, of the inner loop current controller.

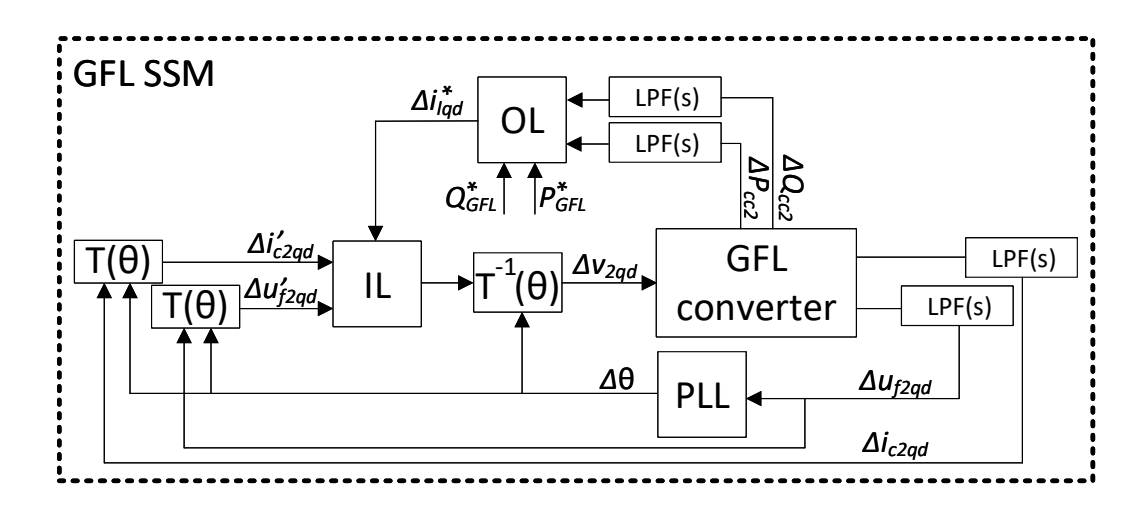


Figure 4.4: Scheme of linearised system (SSM) for the GFL converter controller

Table 4.2: State-space, LTI, matrices for the GFL controller

Loop	State-space
PLL	E.2.1
OL, case 1	E.2.2
OL, case 2	E.2.2

Inner Loop Current Controller State-Space

The equations that describe the inner loop controller may be seen in section 4.2.2. Following these equations and Figure 4.4, the state-space model that characterises this controller is the following.

Chapter 4. Modified Converter Control Approach to Improve System Stability

$$\dot{x}_{cc} = A_{cc}x_{cc} + B_{cc}u_{cc} \tag{4.24}$$

$$y_{cc} = C_{cc}x_{cc} + D_{cc}u_{cc} (4.25)$$

Where the state-space matrices are defined as:

$$A_{cc} = 0$$

$$B_{cc} = \begin{bmatrix} -1 & 0 & 1 & 0 & 0 & 0 \\ 0 & -1 & 0 & 1 & 0 & 0 \end{bmatrix}$$

$$C_{cc} = \begin{bmatrix} k_{i,cc} & 0\\ 0 & k_{i,cc} \end{bmatrix}$$

$$D_{cc} = \begin{bmatrix} -k_{p,cc} & 0 & k_{p,cc} & -\omega L_c & 1 & 0 \\ 0 & -k_{p,cc} & \omega L_c & k_{p,cc} & 0 & 0 \end{bmatrix}$$

The inputs, u_{cc} and outputs, y_{cc} of the inner loop current controller are the following:

$$u_{cc} = \begin{bmatrix} i_{c,qr} & i_{c,dr} & i_{c,qp} & i_{c,dp} & u_{f,q} & u_{f,d} \end{bmatrix}$$
(4.26)

$$y_{cc} = \begin{bmatrix} v_{qp} & v_{dp} \end{bmatrix} \tag{4.27}$$

4.4.2 GFM Small Signal Model

A sketch of the linear time-invariant (LTI) system for the GFM unit is shown in Figure 4.5. It illustrates two external inputs: the active power, P_{GFM}^* , and the voltage magnitude, V_{GFM}^* . In the figure:

• PL - Power Loop

Chapter 4. Modified Converter Control Approach to Improve System Stability

- VL Voltage Loop
- VI Virtual Impedance
- P&V calc Power and Voltage calculations

The power loop (from the power reference to the measured power) and the voltage loop (from the voltage reference to the voltage magnitude) are used to evaluate stability using the disk margin method, which is explained in the next section. Therefore, the MIMO system considered here is a two-input, two-output system. Figure 4.5 shows how all the loops are interconnected through their inputs and outputs. The final state-space LTI matrices are provided in Appendix E.3, and Table 4.3 specifies the corresponding sections within the appendix that detail each loop.

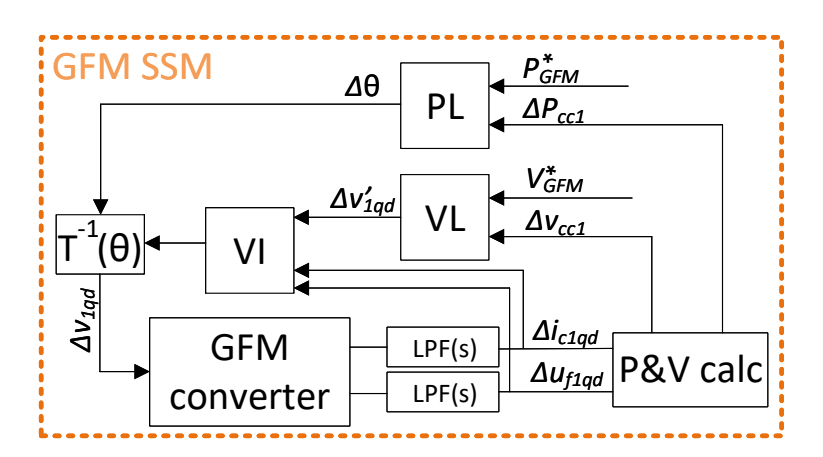


Figure 4.5: Scheme of linearized system (SSM) for the GFM converter controller

Loop	State-space
PL	E.3.1

E.3.2

E.3.3

Table 4.3: State-space, LTI, matrices for the GFM controller

4.4.3 Stability Assessment Methods

VL+VI

P & V calc.

Small signal stability was evaluated using disk margins (DM). Although this section provides a brief overview of disk margins, they have been employed in numerous studies [153–157]. DMs quantify the stability and robustness of a closed-loop system by multiplying the open-loop system "L" by a factor "f", yielding a perturbed loop $L_f = fL$. "f" is a multiplicative, complex, factor which accounts for both gain and phase simultaneously. This factor is nominally 1 and its maximum deviation from f = 1 quantifies the amount of gain and phase variation.

There are two types of DM analysis: the "loop-at-a-time" approach, which introduces a perturbation "f" in a single channel (input or output) while keeping the other channels fixed, and the multi-loop DM analysis. The former, though useful, can be overly optimistic as it may not account for the effects of simultaneous perturbations. Therefore, this study focused on the more comprehensive multi-loop DM analysis, which applies different perturbations across various channels, represented by a matrix of perturbations "F", defined as:

$$F = \begin{bmatrix} f_{1,1} & 0 & \cdots & 0 \\ 0 & f_{2,2} & \cdots & 0 \\ \vdots & \vdots & \ddots & \vdots \\ 0 & 0 & \cdots & f_{n,n} \end{bmatrix}$$
(4.28)

Each element $f_{i,j}$ represents the multiplicative factor applied to the open-loop

Chapter 4. Modified Converter Control Approach to Improve System Stability system L in the channel (i, j). The perturbation factor $f_{i,j}$ is given by:

$$f_{i,j} = \frac{1 + \alpha \left(\frac{(1-\sigma)}{2}\right) \delta}{1 - \alpha \left(\frac{(1+\sigma)}{2}\right) \delta}$$
(4.29)

where δ is the normalised uncertainty, an arbitrary complex value constrained within the unit disk ($|\delta| < 1$).

The parameter α determines the extent of gain and phase variation modelled by F. For a fixed σ , α controls the size of the disk of uncertainty. When $\alpha =$ 0, the perturbation factor $f_{i,j} = 1$, meaning the perturbed system is identical to the nominal open-loop system $(L_s = L)$. In this case, the Nyquist plot of L(s) intersects the critical point -1, and the system operates at the boundary of stability, with no tolerance for uncertainty. This condition is referred to as marginal stability.

Conversely, larger values of α increase the size of the uncertainty disk, allowing for greater gain and phase variations while maintaining stability. This corresponds to a larger disk margin and enhanced robustness. Thus, for $\alpha > 0$, the Nyquist plot of the perturbed system $f_{i,j}L(s)$ remains clear of the -1 point, ensuring stability, while for $\alpha = 0$, the Nyquist plot intersects -1, resulting in marginal stability, where the system cannot accommodate any perturbations.

In this analysis, the multi-loop input/output disk margin is quantified by a single parameter, α , representing the largest disk of perturbations for which the closed-loop system remains stable [156]. Applying factors across all channels simultaneously provides a worst-case scenario for achieving system stability. Therefore, the parameter α was used to assess the stability and robustness of the studied systems. An α value of 0 indicates no tolerance for uncertainty, while values further from 0 indicate greater system stability.

Throughout this thesis, the MIMO DM analysis was employed. The results highlighted the worst-case stability scenarios across the various studies. In Chap-

Chapter 4. Modified Converter Control Approach to Improve System Stability ter 5, this analysis is conducted for different system configurations, varying cable lengths, and both GFM and GFL controllers. In Chapter 7, the DM analysis is used to assess the stability of the power system during block loading following a PSR event.

The small-signal stability analysis throughout this thesis was conducted by evaluating the disk margin across a range of active power operating points, from P=0 pu to P=1 pu. This approach allowed a clear understanding of how active power injection influences system stability under different conditions. By systematically varying the operating point and computing the disk margin, it was possible to identify stability trends and critical points in the system response. This method was applied to all controller types (GFM and GFL) and system configurations investigated in the thesis. In the power system restoration study in Chapter 7, the same approach was used to assess how block loading impacts system stability at different levels of active power injection. Presenting the results in this way provided a clear and intuitive visual representation of stability margins, which is especially useful for power system engineers when comparing controller behaviours and identifying secure operating ranges under varying conditions.

Chapter 5

Going Further Offshore With Grid Forming Converters

5.1 Introduction

It was seen in Section 2.2 how important it is to improve system stability and reliability, especially for OWPP connected via long HVAC cables. This may be achieved via system modifications, such as adding shunt reactor equipment to compensate for capacitive reactive power, or by using advanced converter control strategies. The objectives are to improve the power factor, maintain voltage within acceptable limits across the transmission system, and ensure system stability.

Various considerations have been given to how HVAC technology can be employed for longer, yet reliable and robust, export cables. XLPE cables possess a high inherent capacitance, which is influenced by cable length, insulation, and construction materials. This capacitance results in a leading power factor, consequently producing leading reactive power. To maintain power quality and voltage stability within the system, reactive power must be balanced, which is accomplished through the use of shunt reactive power compensation devices. By intro-

ducing lagging reactive power components into the system, the power factor can be adjusted closer to unity, thereby reducing losses and enhancing transmission efficiency and stability.

At present, most grid-connected inverters operate using GFL converter controllers, which manage the injected current by displacing the phase from the grid voltage at the PCC. GFM control, however, does not require prior knowledge of system frequency, as both the magnitude and phase of voltage are controlled [91, 158]. GFM controllers also increase grid resilience and enable the wind farm to operate autonomously, either in island mode or by supplying power to local loads in the absence of a stable onshore electrical grid. This can be advantageous during grid disturbances or in a black start scenario [159].

From an academic perspective, research indicates that GFM controllers are preferred for voltage-source converter (VSC) HVDC solutions due to their enhanced stability, improved resilience, and better integration with RES [103, 158, 160–162]. However, a gap remains in the literature regarding the stability of OWPPs employing GFM control when connected to long HVAC transmission systems.

Building on the findings of studies [47] and [48], which demonstrated that HVAC export cables combined with distributed shunt compensation reduce power system losses, minimize costs, and improve the voltage profile, this research investigates the benefits of shunt compensation applied at various locations within HVAC transmission system in terms of small-signal stability. Additionally, it examines the application of two distinct converter control methods—grid-forming and grid-following controllers—across different cable lengths. This research aims to address the following questions:

- Can the length of an HVAC export cable be extended when employing a GFM controller?
- Is the stability and robustness of the overall system enhanced with a GFM

Chapter 5. Going Further Offshore With Grid Forming Converters

controller?

• What system configuration (i.e., location of shunt compensations) better enhances stability?

To investigate these questions, an initial study was conducted for a shorter cable of 50 km, using a conventional approach for shunt reactor placement: one reactor onshore and the other at the offshore PCC. This study serves as an introduction to examine the impact of GFM and GFL controllers with shorter cables. Additionally, it is employed to explain the method used to analyse stability in subsequent studies.

Subsequently, a comparative analysis of three different system arrangements was performed, each varying the location of shunt compensation. Moreover, three cable lengths—80 km, 120 km, and 150 km—were evaluated. GFM and GFL controllers were compared using a small signal model, with active power injections ranging from 0 pu to 1 pu. A further study was conducted for varying SCR and X/R ratios to assess stability under weaker grid conditions. Stability was assessed using disk margins to determine the robustness of each configuration.

The remainder of this chapter is structured as follows: Section 5.2 outlines the system configurations defined for the study. Section 5.4 presents the stability analysis for different active power operating points, ranging from 0 pu to 1 pu, at a nominal system voltage of 230 kV. Section 5.5 conducts a similar analysis to Section 5.4, but focuses on a parameter sweep of the short circuit ratio and X/R ratio to assess the impact of control strategies and system arrangements on weaker grids. Then finally, Section 5.7 presents the chapter conclusions.

5.2 System Under Study And Small Signal Model

The system under consideration is illustrated in Figure 5.1. It consists of an OWPP connected to a transformer that steps up the voltage to 230 kV. The

transmission system includes an HVAC submarine cable and shunt reactive power compensation components distributed along the line. These shunt components are varied across the different configurations studied in this work. The system is then connected to an onshore local network. For this specific study, an aggregated wind farm model is used, encapsulating both the OWPP and the offshore transformer.

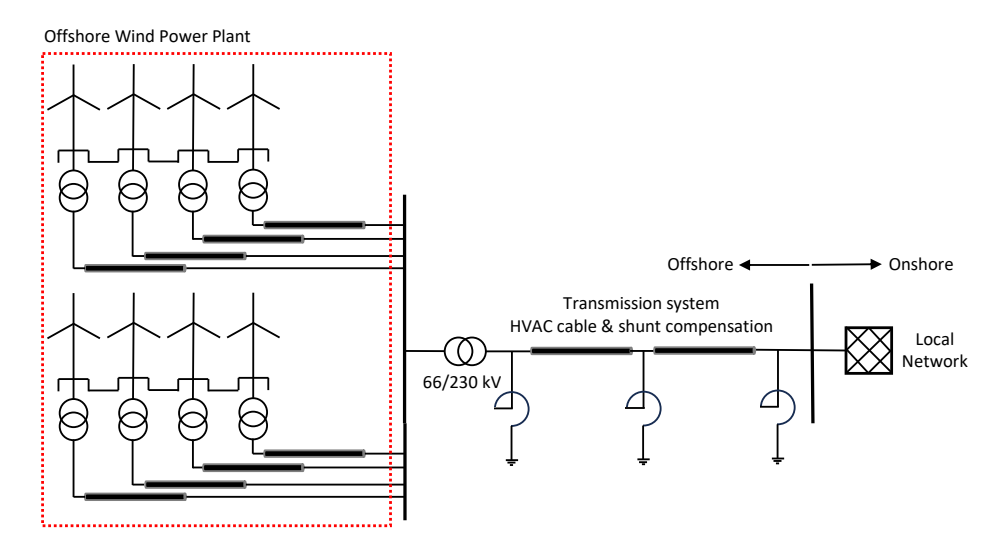


Figure 5.1: One-line diagram of an OWPP connected via an HVAC transmission system to the electrical grid

The detailed modelling approach for the system is shown in Figure 3.9. As previously mentioned, it includes an aggregated OWPP modeled as a voltage source with voltage V and an LC filter with parameters R_c and L_c . The transmission system consists of an HVAC submarine cable and shunt compensations. The electrical grid is represented by a Thevenin equivalent with voltage V_g and the parameters R_g and L_g .

The export cable was modeled using a π -equivalent circuit with parameters R_{hv} , L_{hv} , and C_{hv} . For simplicity and because this study focuses on small signal analysis, the shunt compensations are modeled as reactors, with their values calculated based on the amount of reactive power to be compensated. The parameters used in this study may be seen in Table B.1 of appendix B.

The controllers used in this study are the ones described in Chapter 4. The GFL controller is that of Figure 2.5 and the GFM unit is the one sketched in Figure 4.2. The SSM used for the small signal stability analysis is the one introduced in Section 4.4.

After developing the SSM, the initial step involved validating its accuracy by comparing it with the developed EMT model. For this validation, a single power step of 0.01 pu was applied to both EMT and SSM system representations. Figure 5.2 displays the results for both the GFL and GFM converter controllers for a cable length of 80 km and configuration A2. The same process was followed for the other two arrangements. The close alignment between the SSM and EMT responses in these Figures confirms that the SSM accurately replicates the EMT behavior, demonstrating its reliability for further analysis.

A further comparison between the EMT and small signal models is presented in Figure 7.15. To reflect the use of the controller in a grid restoration scenario, where the system operates across a wide active power range, the small signal model was validated against several operating points. This broader validation supports the accuracy of the small signal model under varying power injection conditions relevant to the study.

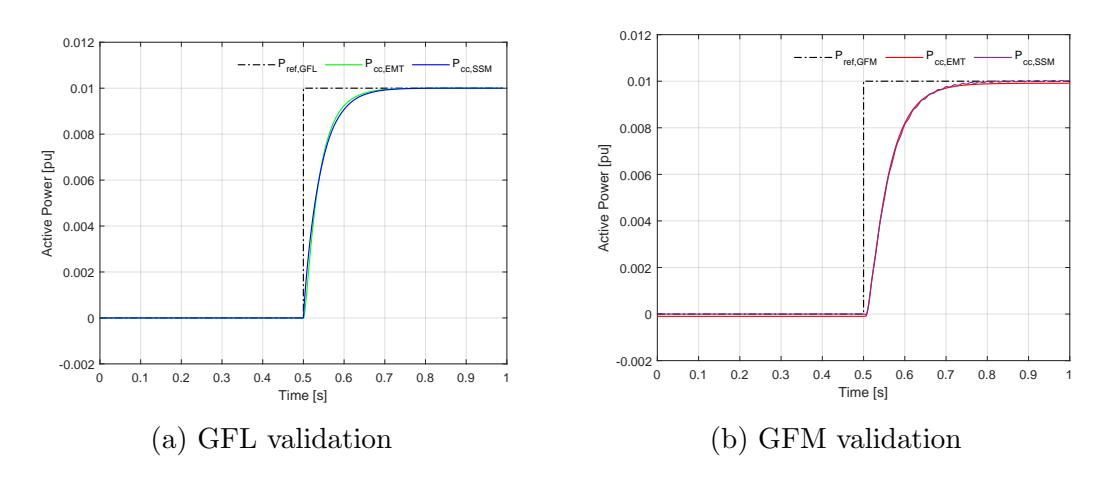


Figure 5.2: Validation of SSM against EMT results for a 0.01 pu active power jump

5.3 Stability Assessment For Smaller HVAC Cable

The aim of the preliminary study was to compare grid-forming and grid-following converter controllers for an offshore wind power plant connected to the grid. A shorter cable of 50 km was used for the initial analysis. The first step was to evaluate whether the control tuning was effective, focusing on overshoot and settling time. Following this, stability was assessed across a range of active power and voltage operating points. The active power was varied from 0 to 1 pu in increments of 0.2 pu, while the voltage was adjusted between 0.9, 1, and 1.1 pu. Lastly, the small signal stability results were compared using disk margins. This comparison establishes a baseline for the subsequent study, where both the cable length is increased and alternative system configurations are employed.

To ensure a fair comparison of the SVCC and VSM controllers it was necessary to take into account their performance which can be specified by requirements on the closed-loop stability margins (such as gain or phase), time-delay margins or time domain specifications such as overshoot and settling time [163]. Two minimum requirements for dynamic performance were chosen, which were the settling time (ST) and overshoot (OS). These requirements were chosen based on [164] and are a settling time lower than 0.5 s and an overshoot below 15%. The tuning was performed for P = 1 p.u. and V = 1 p.u., and this study was performed with a SCR of 5 and an X/R ratio of 10.

The final gains for the SVCC and VSM are presented in Tables 5.1 and 5.2, respectively. After tuning the controllers for the specified active power and voltage operating points, as previously mentioned, several additional operating points were tested. The results, concerning overshoot and settling time, can be found in Tables 5.3, for a power range between P = 0 p.u. and P = 1 p.u., and 5.4, for a voltage range between V = 0.9 p.u. and V = 1.1 p.u.

Table 5.1: GFL controller parameters for preliminary study

Gain	Value	Gain	Value
$\overline{k_{p,cc}}$	3.207	$k_{p,PC}$	3.22×10^{-6}
$k_{i,cc}$	50.38	$k_{i,PC}$	1.04×10^{-4}
$k_{p,PLL}$	2.4×10^{-3}	$k_{p,VC}$	0.013
$k_{i,PLL}$	0.526	$k_{i,VC}$	0.454

Table 5.2: GFM controller parameters for preliminary study

Gain	Value
$\overline{m_p}$	1.609×10^{-8}
m_i	1×10^{-8}
$k_{p,vc}$	0.013
$k_{i,vc}$	27.03

Figure 5.3 illustrates the power and voltage steps applied at the different operating points, from which the overshoot and settling time were measured.

The small signal studies focus on the response of the system when the power injected into the grid and the voltage reference level are varied. In this section, the small signal stability and robustness of the system are analysed when subjected to different power and voltage operating points. Stability was assessed for a range of active power operating points, from P = 0 p.u. to P = 1 p.u., and for voltage operating points between V = 0.9 p.u. and V = 1.1 p.u..

Figure 5.4 presents the results in terms of disk margins (gain and phase) for the different power and voltage operating points. From the figure, it can be

Table 5.3: OS and ST for voltage operating points

	GFL		GFM	
P(p.u)	OS (%)	ST (s)	OS (%)	ST (s)
0	0	0.2243	1.6002	0.1975
0.2	0	0.2259	1.4408	0.2013
0.4	0	0.2279	1.3729	0.2112
0.6	0	0.2314	1.3348	0.2129
0.8	0	0.2385	1.3064	0.2134
1	0.8622	0.2519	1.2826	0.2125

Table 5.4: OS and ST for voltage operating points

	GFL		GFM	
V(p.u)	OS (%)	ST (s)	OS (%)	ST (s)
0.9	0.8847	0.0867	0.6276	0.1562
1	0	0.0998	0.6269	0.1495
1.1	0	0.2260	0.6431	0.1441

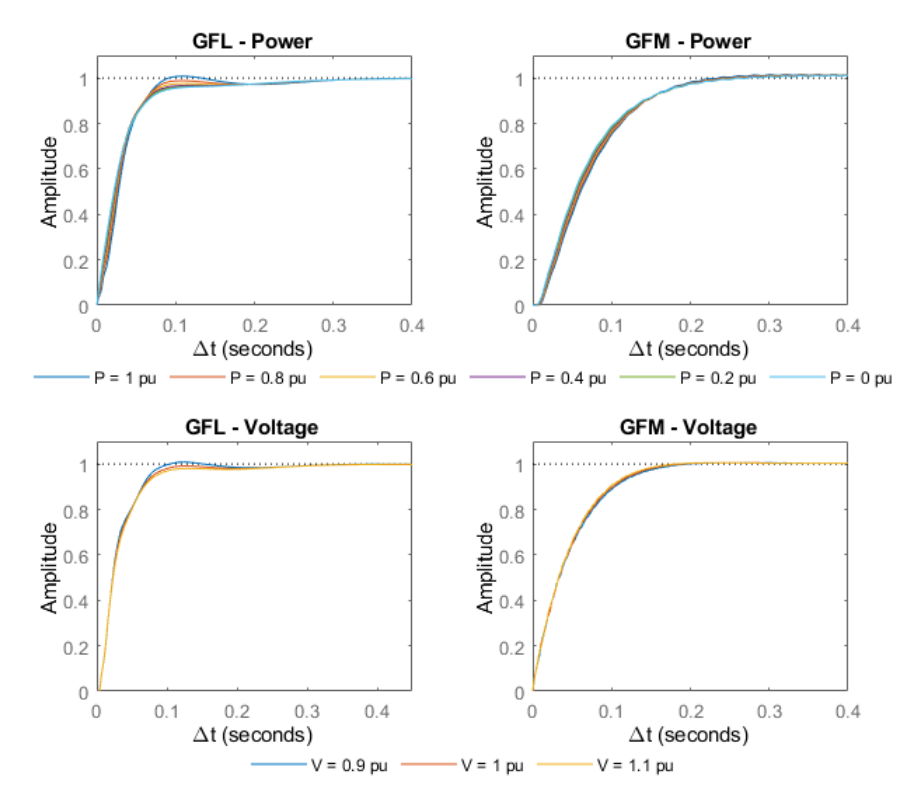


Figure 5.3: Step response for both SVCC and VSM for power and voltage operating points

observed that the frequencies at which the GFL (SVCC) and GFM (VSM) are more sensitive differ: the GFL controller shows the lowest gain margins at around 630 rad/s, whereas the GFM controller exhibits this at the natural frequency, of approximately 314 rad/s. This indicates that GFM and GFL controllers have distinct dynamic responses in terms of control speed. The variation in frequency response is due to the interaction of each controller with the electrical grid.

Specifically, in the GFL scenario, the current controller is a major contributor to the behaviour of the system at these lower frequencies [94]. In the figure, each line represents a power or voltage operating point. In the GFL-power scenario, the lines are spread further apart, indicating that the power injected into the grid has a significant effect on system stability and robustness margins. In contrast, for the GFM case, the power operating points are closely grouped in terms of both gain and phase margins.

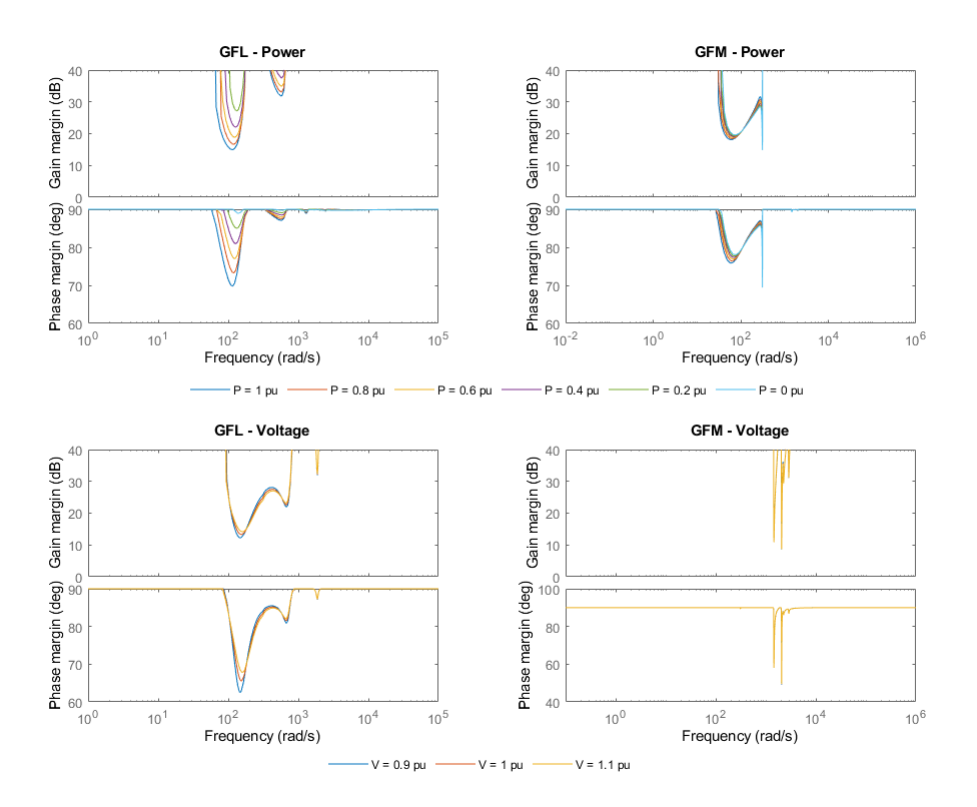


Figure 5.4: Disk margins for GFL and GFM for active power and voltage operating points

A similar pattern is observed for the voltage disk margins. For the GFM scenario, the lines representing different operating points remain closely aligned for both gain and phase. However, in the GFL scenario, these lines are more widely spaced, demonstrating the GFL converter controller has higher sensitivity to variations in power and voltage operating points. Additionally, it is evident

that the SVCC shows the lowest margins when the injected power increases and the voltage level decreases.

Overall, the GFL controller exhibits lower disk margins for both voltage and active power operating points compared to the GFM controller. This study was conducted with a short circuit ratio (SCR) of 5 and an X/R ratio of 10, meaning that the GFL controller still performs well in terms of small signal stability. However, the GFM scenario is superior for the following reasons: stability remains consistent across all operating points, both for active power and voltage; gain and phase disk margins are higher, providing greater tolerance for uncertainty and disturbances.

5.4 Extending Cable Length

This section focuses on the stability analysis, primarily comparing two converter control strategies: GFM and GFL. Additionally, the analysis examines three distinct system configurations, which vary based on the placement of shunt reactor compensations along an HVAC submarine cable. The study also considers three different cable lengths—80 km, 120 km, and 150 km—to evaluate the performance of the converter controllers across various scenarios. The objective is to determine which converter control strategy and system arrangement optimize stability, potentially allowing for longer HVAC cables. Furthermore, the analysis aims to identify the optimal placement of shunt reactors for enhanced stability.

Given the variability in wind speed and the availability of energy from OWPP, it was essential to analyse the stability of the different case studies under various operating points. The stability analysis was conducted over a range of power operating conditions. Specifically, the active power was varied from 0 pu to 1 pu in steps of 0.20 pu at nominal voltage. The stability analysis was performed using disk margins, as explained in Chapter 3.

The disk margin analysis was conducted to assess the stability of the two converter control strategies, grid following and grid forming, across three distinct cable lengths: 80 km, 120 km, and 150 km. This assessment considered three specific system arrangements, A1, A2, and A3, as previously defined in Section 3.2.7. For clarity, A1 includes shunt reactors located onshore and offshore; A2 includes shunt reactors onshore, offshore, and at the mid-cable point; and A3 includes only onshore compensation. Results of the disk margin analysis are shown in Figure 5.5 for 80 km, Figure 5.6 for 120 km, and Figure 5.7 for the longest cable length of 150 km.

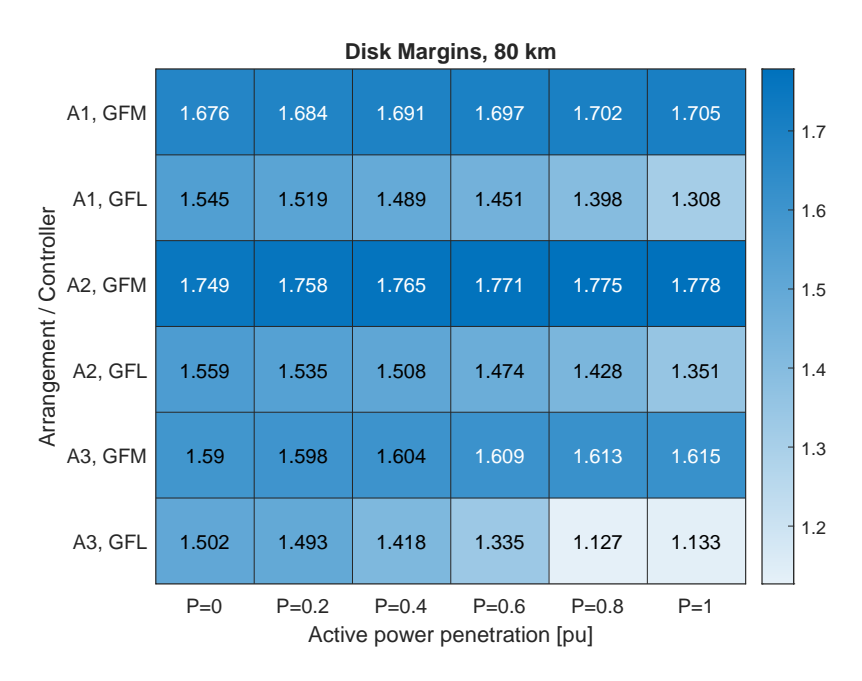


Figure 5.5: Disk margins for active power operating points and for both GFM/GFL controllers and different system arrangements for a cable of 80 km

Among these configurations, the GFM converter controller exhibited the largest disk margins, particularly in the A2 arrangement, followed closely by the A1 arrangement. This suggests that the GFM control strategy is more robust in maintaining stability compared to the GFL approach. It also suggests that distributing the shunt reactors along the export cable (A1 and 2), rather than having just the one shunt compensation onshore (A3) further enhances stability.

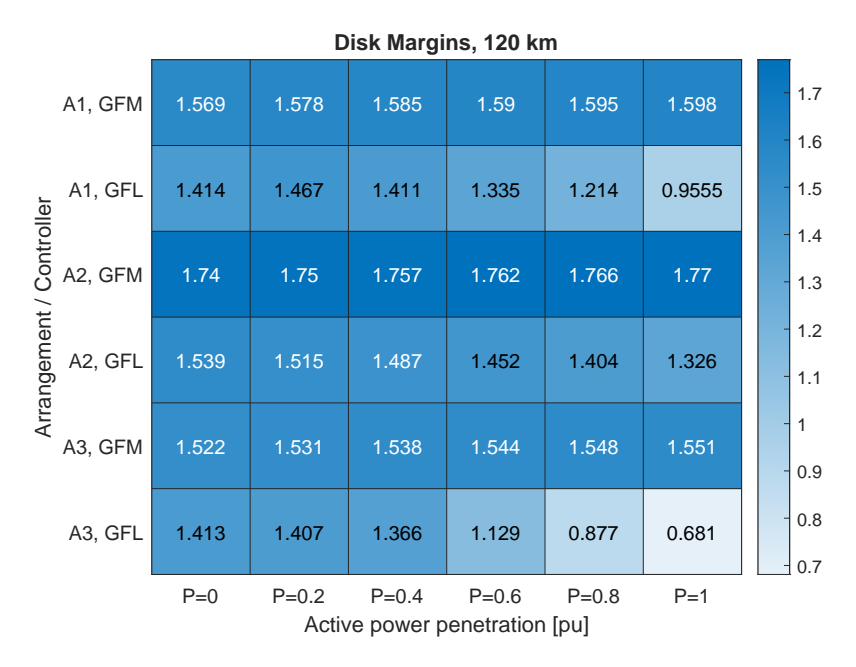


Figure 5.6: Disk margins for active power operating points and for both GFM/GFL controllers and different system arrangements for a cable of 120 km

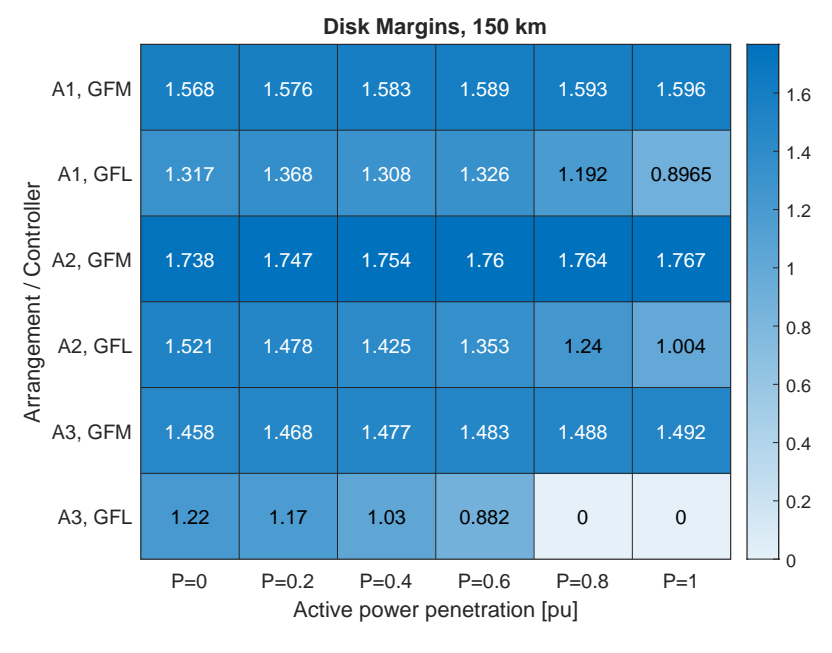


Figure 5.7: Disk margins for active power operating points and for both GFM/GFL controllers and different system arrangements for a cable of 150 km

The disk margins for the GFM controller remained consistent across all operating points, indicating a reliable performance independent of active power variations. In contrast, the disk margins for the GFL controller demonstrated significant variability as the active power level increased from 0 to 1, with the lowest margins belonging to higher active power penetration. Additionally, it was seen that an increase in cable length resulted in a decrease in disk margins, highlighting the influence of transmission distance, hence increased line impedance, on system stability.

Figure 5.8 presents the gain and phase margins across a frequency spectrum where these margins are observed to be at their lowest. This analysis includes both GFL and GFM scenarios. The plots highlight the variation in disk margins for the three different arrangements, specifically for a cable length of 80 km. Although only the 80 km case is depicted, similar trends are observed for cable lengths of 120 km and 150 km.

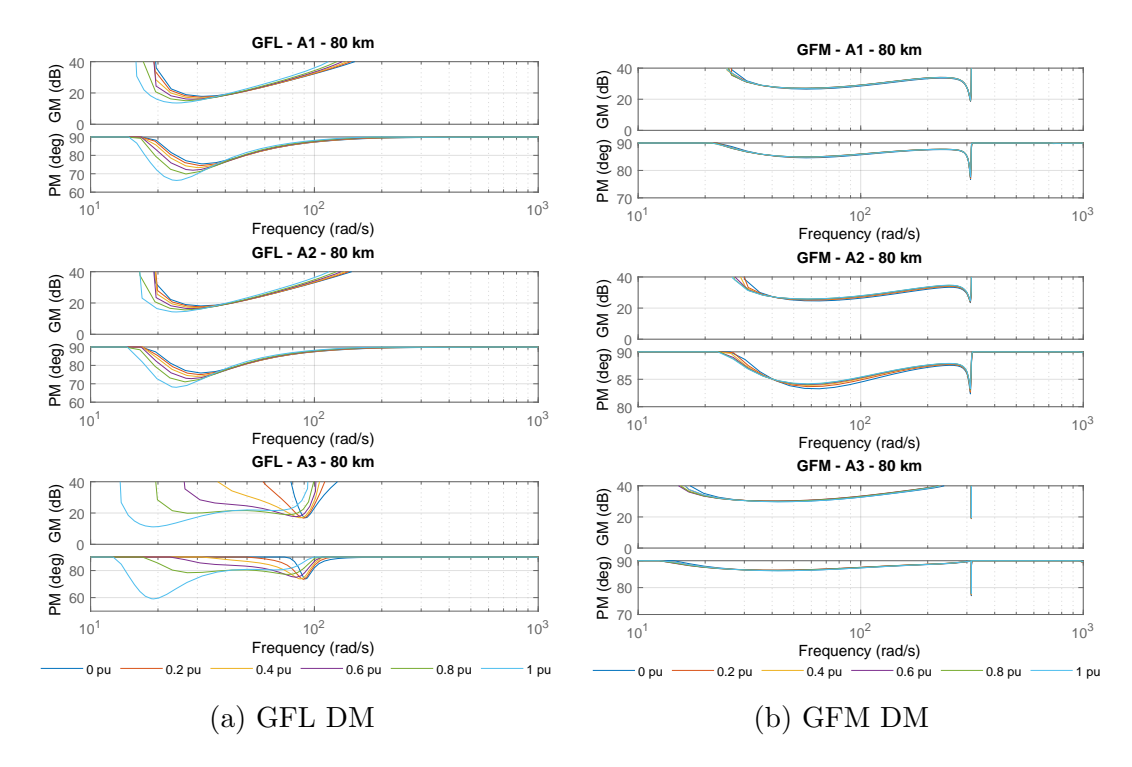


Figure 5.8: Gain and phase disk margins across the frequency spectrum.

The plots reveal that in the GFL scenario, the active power operating points significantly influence both the gain and phase margins. For configurations A1 and A2 within the GFL scenario, the lowest gain and phase margins, and consequently the lowest disk margins, are found at very low frequencies, specifically around 20 to 30 rad/s. These low frequency disk margins are characterized for interactions between the GFL converter controller and the power system, especially due to the use of a PLL for grid synchronization and the inner current controller. In contrast, for configuration A3, there is a notable dip in both gain and phase margins at frequencies below 20 rad/s, with an additional significant low point around 90 rad/s.

In the GFM controller scenario, the gain and phase margins remain consistent across different operating points, corroborating previous observations. This consistency results in similar margin values across the entire frequency range. However, the lowest gain and phase margins for all three configurations occur at the natural frequency of the power system, likely due to interactions between the controller and the electrical grid. The 50Hz peak can be further reduced by adjusting the values of the virtual impedance, specifically R_v and L_v . However, this approach may lead to reduced margins at lower frequencies. Therefore, future work should focus on optimizing the tuning of the virtual impedance to achieve greater mitigation of gain and phase dips while preserving acceptable margins across the frequency spectrum.

The plots also highlight the influence of system arrangements on gain and phase margins. The way the controller interacts with the power system varies depending on the configuration, which plays a critical role in determining the overall stability of the system.

From this section, it can be concluded that the GFM controller demonstrates superior stability. It remains stable and robust across all cable lengths and configurations. Additionally, the stability of the overall system is not critically affected

by active power injection, which is important given that the power injected by OWPP will vary considerably with wind conditions and resource availability.

In contrast, the stability of the GFL-connected converter is influenced by the injected active power, with lower stability margins observed at higher power levels. Its stability is also affected by the transmission line impedance, leading to reduced stability and significantly lower margins with increased cable lengths.

Regarding system configurations, arrangement A2 proved to be the most effective, followed by A1. This suggests that distributed shunt reactors across the transmission system enhance stability, allowing for the use of longer cables.

It is important to note that this study was conducted for a weak grid with a SCR of 3. Further research should explore stronger networks, as the system might benefit from GFL controllers in scenarios with a stronger grid, where a robust voltage reference signal could enhance the GFL controller performance. However, since this study focuses on weaker grids, the next section will examine even weaker grids by varying the SCR and X/R ratio.

5.5 Concerning Weaker Networks

The integration of RES into electrical power systems leads to significant changes in grid dynamics. One of the challenges associated with this transition is the reduction in system strength, which is often quantified using the SCR and X/R. These quantities reflect the ability of the grid to absorb disturbances and power delivery performance.

Section 5.4 focused on the stability of the two controllers, different arrangements and the three cable lengths in a grid with a SCR of 3 and a X/R of 10 (X_g/R_g) . While this SCR value is already indicative of a relatively weak grid, further analysis is necessary to understand the performance and robustness of these controllers under even more challenging conditions. HVAC transmission

introduces additional impedance, as well as the shunt reactors, and it was seen from the previous section that the different arrangements shall benefit from different margins of stability. This effect becomes more noticeable in systems with lower SCR and X/R values.

A similar analysis to the one in section 5.4 was conducted. However, instead of varying the active power injection, the SCR at the offshore PCC (1.5 and 3) and X/R ratio (1.5, 5, and 10) were varied, at an active power operating point of 1 pu. This specific operating point was chosen as it previously showed lower stability margins in the GFL case, making it a critical point of interest.

Figure 5.9 displays the disk margins for different configurations, A1, A2, and A3, under both controllers, with an HVAC transmission length of 80 km. The results confirm the findings from Section 5.4—GFM control improves stability and robustness in weaker grids. Lower X/R and SCR values do not significantly affect the disk margins of this controller.



Figure 5.9: Disk margins for different SCR and X/R for a cable of 80 km

The same conclusion can also be observed in Figure 5.10, which shows that,

for the GFM converter controller, the disk margins maintain consistent gain and phase across all X/R and SCR values for greater cable lengths.

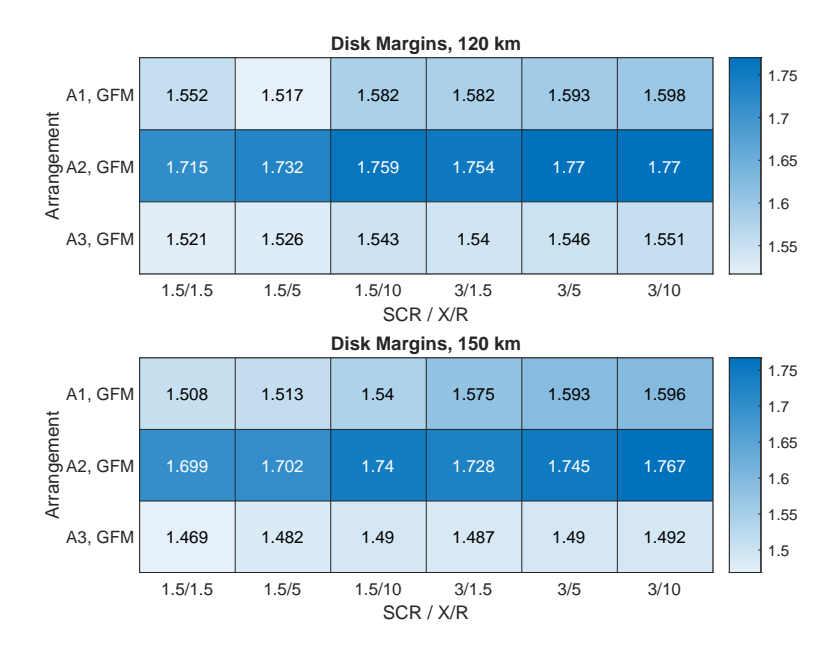


Figure 5.10: Disk margins for different SCR and X/R for cables of 120 km and 150 km

The pole-zero maps in Figure 5.11 further illustrate these effects, where it can be seen that for the GFM unit, in Figure 5.11b, the system remains stable, with no poles on the right-half plane. The pole-zero map was here used as it was necessary to display the instabilities of the GFL scenario, which may be seen in Figure 5.11a, where even for an 80 km transmission with arrangement A2, which performs best, the system becomes unstable.

As seen in Figure 5.11a, the system is unstable at X/R = 1.5 and SCR = 1.5, and nearly unstable at SCR = 3 and X/R = 1.5, with a pole close to the origin. The pole-zero maps clearly demonstrate how X/R and SCR impact stability, with poles shifting to the right as SCR and X/R decrease.

The findings in Figure 5.9 show that nearly all disk margins are unstable for the GFL controller under these conditions, even for the shorter cable length of 80 km of transmission. Therefore, GFM converter units are essential for longer

HVAC transmissions, especially in weaker grids with higher impedances.

The GFM-connected controller has shown consistent performance across different X/R and SCR values, even with longer cables of 120 km and 150 km, as seen in Figure 5.10. The results also indicate that arrangement A2 is the most effective, supporting the conclusion from the previous section that distributing shunt reactors along the line significantly improves stability.

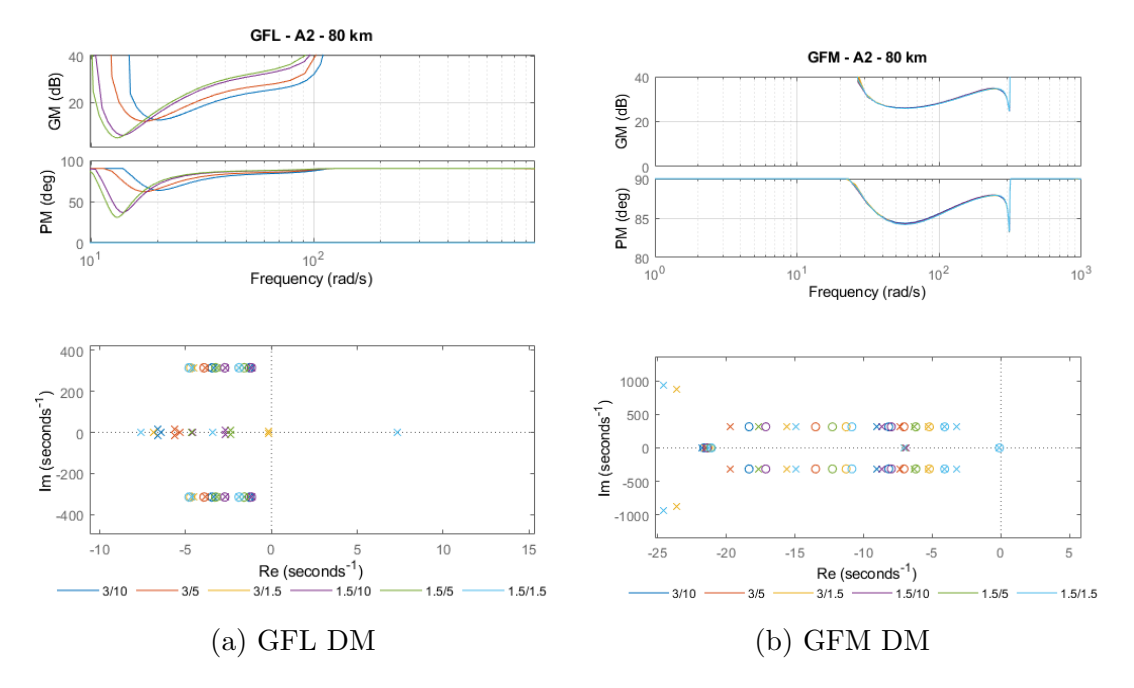


Figure 5.11: Gain and phase disk margins across the frequency spectrum for SCR and X/R variation.

In conclusion, GFM is necessary for longer export cables, particularly in weaker grids with lower X/R and SCR. Arrangement A2 is recommended for enhanced stability, although arrangement A1 has also proven to be robust across all GFM operating points.

5.6 Discussion

The results presented in Sections 5.4 and 5.5 illustrate the comparative performance of GFL and GFM controllers for OWPPs connected via HVAC export cables. Table 5.5 summarises the advantages and disadvantages of both strategies, providing an overview of their characteristics based on the findings.

Table 5.5: Advantages and disadvantages of GFL and GFM control strategies based on the paper findings.

Criteria	Grid-Following	Grid-Forming
Advantages	- Simple and widely adopted	- Superior stability and
	in current OWPP systems.	robustness across all cable
		lengths.
	- Effective in strong grids with	- Performs well in weak grids
	higher short-circuit ratios.	(low SCR and X/R ratios).
	- Easier to implement with	- Stability is independent of
	conventional systems.	active power injection levels.
		- Supports operation in island
		mode and black-start scenar-
		ios.
Disadvantages	- Stability is highly sensitive	- Requires more complex con-
	to active power injection.	trol and tuning processes.
	- Poor performance with weak	- Not yet widely deployed in
	grids and longer HVAC ca-	OWPP systems.
	bles.	
	- Low disk margins at high	- Slightly higher computa-
	power levels and weaker SCR	tional demands due to VSM
	values.	approach.
	- Requires strong voltage ref-	- Needs further research for
	erence for synchronisation.	industrial adoption.

GFM controllers demonstrate superior stability and robustness across all system configurations and cable lengths. This is evident in figures 5.5, 5.5, and 5.5, which show that the GFM control strategy consistently achieves higher α values for all three cable lengths, maintaining stability across all active power operating points analysed.

In contrast, the GFL controller exhibits a significant loss of stability as cable

lengths increase. For the 150 km cable, some operating points already display a disk margin of zero, indicating no tolerance for uncertainty. In such cases, the factor f equals 1, meaning that even a small uncertainty or disturbance would result in instability.

The disk margin analysis also highlights the consistent performance of GFM under weak grid conditions with low SCR and varying X/R ratios. This robustness can be attributed to the independence of GFM control from grid synchronisation, allowing it to maintain stability even under significant active power variations. Conversely, GFL controllers show pronounced stability limitations, particularly as active power injection increases. These limitations are exacerbated by weaker grid conditions and increased cable lengths. Figures 5.9 and 5.10 further emphasise the superiority of GFM, particularly for weaker systems. Even with a shorter 80 km cable, the GFL controller demonstrates zero α values across all configurations and active power penetration levels, underscoring its inability to maintain stability in such conditions.

While GFL remains simpler to implement and is widely adopted in current systems, its performance is heavily reliant on grid strength and a robust voltage reference. These limitations are reflected in the reduced disk margins observed at higher power levels and weaker grid conditions. In contrast, GFM provides a reliable solution for OWPP applications requiring extended HVAC export cables, effectively mitigating stability challenges associated with line impedance and reactive power imbalance.

Despite its superior performance, the adoption of GFM controllers remains limited due to the need for further research and development. Future work should focus on addressing these challenges to accelerate the integration of GFM controllers in offshore wind applications, thereby enhancing grid stability and enabling reliable operation under increasingly demanding conditions.

5.7 Chapter conclusions

This chapter has examined the evolving dynamics of power systems as synchronous generators are phased out in favour of renewable energy sources. The study focused on the integration of OWPP and the challenges associated with increasing transmission distances.

• Key insights:

- OWPPs are being deployed further offshore, which requires the use of HVAC cables with reactive power compensation.
- Shunt reactors play a crucial role in mitigating capacitive effects and ensuring the stability of the system.

• Comparative analysis:

- The study evaluated three HVAC cable lengths (80 km, 120 km, and 150 km) and three shunt reactor configurations (A1, A2, and A3).
- The impact of different control strategies—Grid-Following and Grid-Forming—was assessed using small-signal stability analysis.

• Findings:

- The most robust configuration was A2 (offshore, onshore, and midcable reactors) with GFM control.
- GFM control exhibited superior stability across all operational conditions compared to GFL control.
- The stability of GFL units was highly sensitive to active power injection levels.

• Implications for weaker grids:

- Weaker grids, characterised by lower SCR and X/R values, further highlighted the advantages of GFM control.
- GFM maintained stability across all SCR and X/R conditions, whereas
 GFL controllers failed at even moderate distances.

• Concluding remarks:

- GFM control is recommended for OWPPs, particularly those situated further offshore.
- Incorporating offshore and mid-cable shunt reactors enhances stability and reliability.
- The study underscores the limitations of GFL control in weak-grid conditions, reinforcing the necessity for transitioning towards GFMbased OWPP integration.

Chapter 6

Novel Approach to Power System Restoration Using Offshore Wind Power Plants

With the increasing integration of converter-connected RES into power grids, it is essential to ensure the resilience of power systems in the event of partial or total blackouts. Traditionally, the responsibility for restoring power, known as PSR or BS, has rested with a few large, transmission-connected synchronous generating power stations. However, as these stations are phased out, the task of providing restoration services must also transition accordingly, thus RES such as OWPP, photovoltaics (PV), and battery energy storage systems (BESS) should also be considered as black start units (BSUs) [75, 165].

BSUs are generation assets capable of restarting without support from the electrical grid. In particular, PSR using wind power has not previously been seen as a priority, but due to the high number of planned OWPP, as it was mentioned in Chapter 1, of 40 GW by 2030 [166], it is a matter of energy security to consider this option for the future of PSR in the UK.

Having this in mind, several projects emerged in the UK aiming research

Chapter 6. Novel Approach to Power System Restoration Using Offshore Wind Power Plants

involving both industry and academia, in which it was investigated if RES can potentially contribute to UK's PSR in case of a blackout. An example of such is project PROMOTioN, a project in meshed HVDC offshore transmission networks, which investigated OWPP/WT control for self-start and BS [167, 168]; another is Distributed ReStart which explored how distributed energy resources (DER) such as solar, wind and hydro, may be used for PSR [68].

Following this trend, the project SIF BLADE [169] was launched, aiming to explore and demonstrate how innovative, cost-effective, low-carbon technologies can enable OWPP to restore the onshore grid following a blackout. Validating this concept will facilitate the accelerated deployment of OWPP to replace existing fossil fuel generators, while mitigating any potential resilience challenges that may arise. This paper aims to present the key topics discussed and analysed during the initial stages of the SIF BLADE project: the Discovery Phase and the Alpha Phase. Below, the studies conducted during these phases are detailed, along with the sections where each topic is discussed.

Section 6.1 explores potential scenarios regarding the location of the auxiliary power supply (APS) unit, which is responsible for initiating the start-up of the OWPP; it is also explored the requirement for self-starting grid-forming wind turbines. This is a critical consideration, as a black start units, in this case an OWPP, require an external source capable of supplying a small amount of energy to initiate its operation.

Section 6.2 investigates whether the designed OWPP and power system can meet the local network demand in steady state, in terms of active and reactive power operating points, using data provided by a project partner. The OWPP considered here is the one introduced in Chapter 3. A similar analysis to that conducted in Section 3.3 was performed, this time with the aim of determining whether the OWPP could encapsulate the onshore local network active and reactive power (P,Q) data points.

Following this, an availability study was conducted in Section 6.3. The objective of this study was to assess the active power that could be exported from two different OWPP sites, based on wind speed data specific to each location. Due to data protection restrictions, the specific OWPPs considered will not be named and are referred to as OWPP Case 1 and OWPP Case 2. This allowed for an evaluation of the amount of energy that could be exported from the OWPP, and whether the energy targets set by NGESO for the first 24 and 72 hours following a blackout could be met.

6.1 Scenarios to energize OWPP

In this section, different scenarios for energising an OWPP are discussed. A BSU needs to self-energise and contribute to network reconfiguration. Traditionally, such a unit uses a small cranking generator, such as a DG, for this purpose. For an OWPP, an APS, such as a synchronous DG or a BESS, can be used to start the wind turbines. Alternatively, GFM WTs can self-start. The size of the cranking unit must provide sufficient energy to start key components that enable power generation. These include the wind turbine controllers and communications, heating and cooling loads, water and oil pumps, and motors, such as those for pitch and yaw. According to [170], the auxiliary power needed to self-start a wind turbine is less than 5% of its rated power.

The SIF Blade project explored four energisation solutions, with two selected for further study. These solutions vary based on the APS location and the requirement for GFM WTs. An APS, whether located onshore or offshore, can provide a stable voltage reference, eliminating the need for GFM WTs, as all GFL WTs will synchronise with the APS voltage. Self-starting wind turbines must be GFM-capable. The four scenarios considered in this study to energise the OWPP are shown in Table 6.1. The table presents four scenarios, S1, S2,

S3, and S4. Grid-forming wind turbines are only required for Scenario S2, which involves self-starting wind turbines. Self-starting WTs must be equipped with a small auxiliary power supply, such as an uninterruptible power supply, capable of providing sufficient power to initiate the start-up of the turbine. In the other scenarios, it is assumed that the external APS can maintain stable voltage and frequency signals throughout the energisation of the OWPP.

Table 6.1: Scenarios for WT-OWPP energisation

Scenario	APS location	GFM WT required?
S1	Onshore	No
S2	Self-start WT	Yes
S3	Offshore	No
S4	Hybrid	No

Figure 6.1 graphically illustrates the locations of S1, S2, and S3; S4 is a combination of these APS. In the figure, S1 is situated in the onshore substation, along with several loads, the local network, and a variable shunt compensation. S2 represents an APS located inside a WT, indicating a self-starting WT. S3 is positioned in the offshore substation, following the offshore transformer and static shunt reactive compensation, but before the HVAC export submarine cable.

Scenario 1 (S1) is sketched in Figure 6.2 and involves placing the APS at an onshore substation. The APS would need to energize all equipment from the substation to the OWPP, including the substation itself, reactive power shunt compensations, offshore submarine HVAC export cable, OWPP array cables, and finally the wind turbines. Although this process requires significant energy, the onshore location of the APS allows for larger units due to the absence of space constraints, unlike offshore substations or wind turbines. Additionally, APS units are typically already available at or near onshore substations. Scenario 1 is thus an attractive solution due to its simplicity and technology readiness. Located onshore, the APS is easier to install, operate, and maintain, with no space lim-

Chapter 6. Novel Approach to Power System Restoration Using Offshore Wind Power Plants

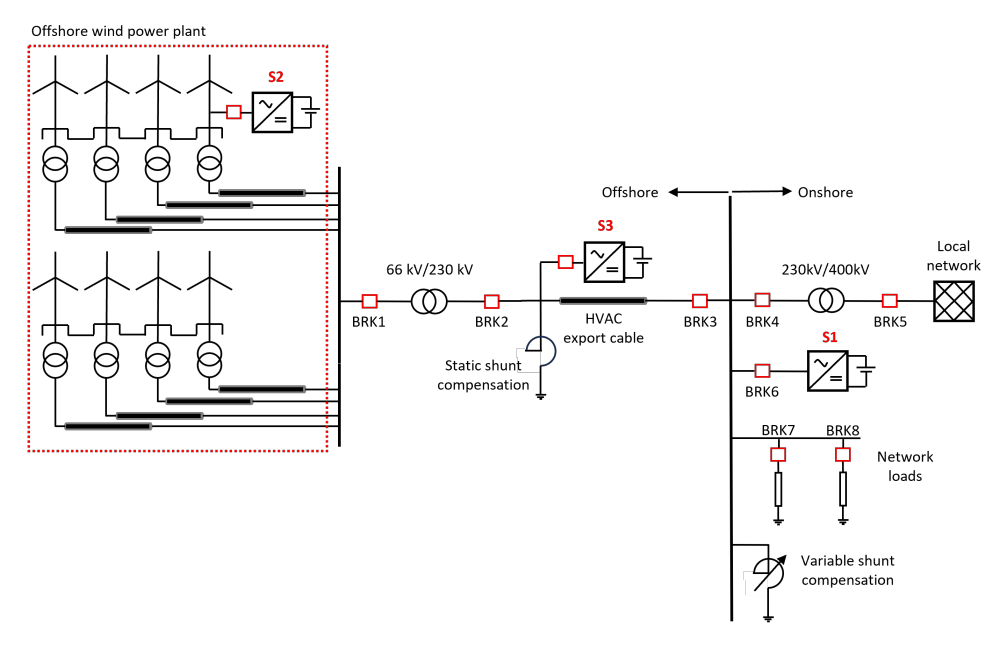


Figure 6.1: One-line diagram of studied system with the different APS located onshore, offshore, and inside WT (self-start scenario)

itations. It can keep a stable voltage reference signal, eliminating the need for GFM wind turbines, that is, assuming the GFL wind turbines maintain stability in such a weak system.

Scenario 2 (S2), which may be seen in Figure 6.3, considers self-starting wind turbines which have the capability to energize themselves. This is done via an uninterruptible power supply (UPS), a small BESS or diesel generator inside a wind turbine. Such wind turbine would need to be equipped with grid forming converter control technology as to be able to keep a constant and reliable voltage source reference signal. Once one, or several self-start, GFM, wind turbines are energised, these units would be responsible for providing enough energy to energise the OWPP array cables and the GFL wind turbines, which would then synchronise with the GFM units.

Previous studies have explored the concept of self-start wind turbines for OWPP. In [171], a method is proposed where wind turbines start using their internal energy storage without external generators. In [172] it is discussed an au-

Chapter 6. Novel Approach to Power System Restoration Using Offshore Wind Power Plants

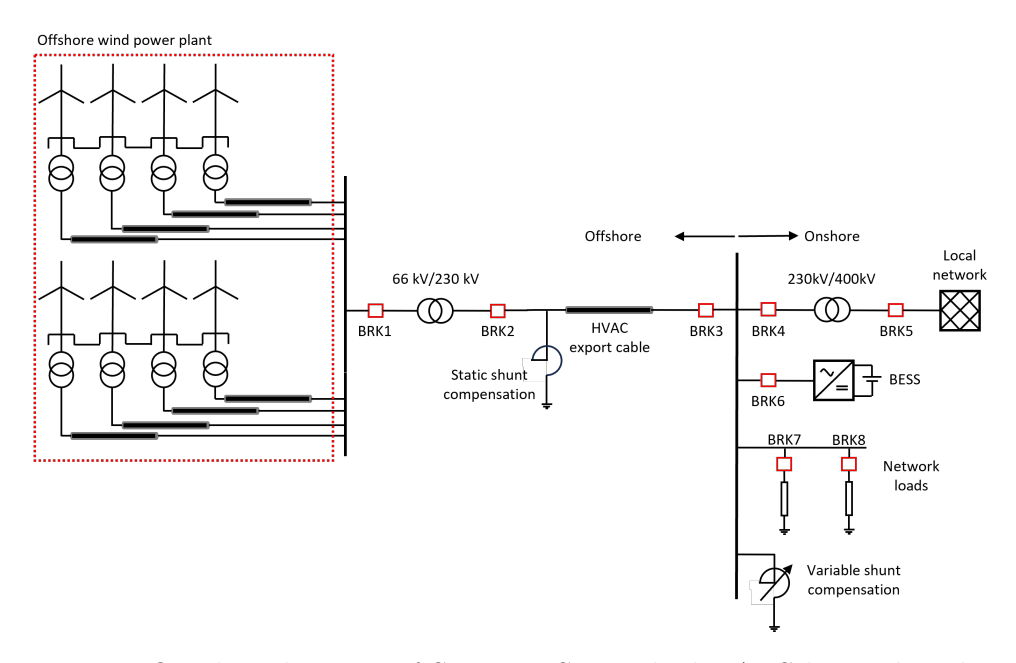


Figure 6.2: One-line diagram of Scenario S1, with the APS located onshore

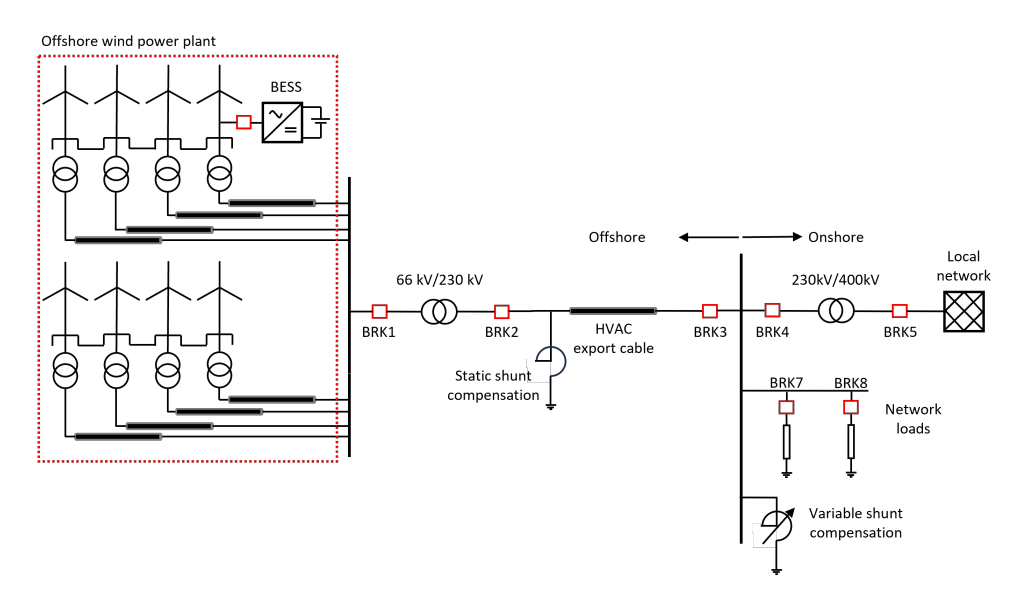


Figure 6.3: One-line diagram of scenario 2, with self-start capable WTs

tonomous startup and synchronization using the wind turbine APS to sequentially energize turbines. Additionally, in [173] is introduced a wind turbine equipped with a DG that can generate power during a blackout, replicating the electricity network and supporting auxiliary devices.

In Scenario 3 (S3), an APS is located in the offshore substation, as may be seen in figure 6.4. Firstly the offshore transformer and substation equipment are energized and then the OWPP itself, reducing energization time compared to an onshore APS. The offshore industry, particularly the oil and gas sector, is familiar with APS in offshore substations, and battery energy storage systems are a topic of interest for such platforms [174–178]. However, limited space in offshore substations makes it challenging to include a BESS unit solely for black-start purposes if the OWPP is already constructed. Scenario 3 is the most expensive due to higher installation and maintenance costs and limited accessibility. Although GFM wind turbines are recommended, they are not necessary as the APS can generate frequency and voltage. Some offshore substations may already have an APS capable of cranking the first wind turbine, providing an alternative for auxiliary power.

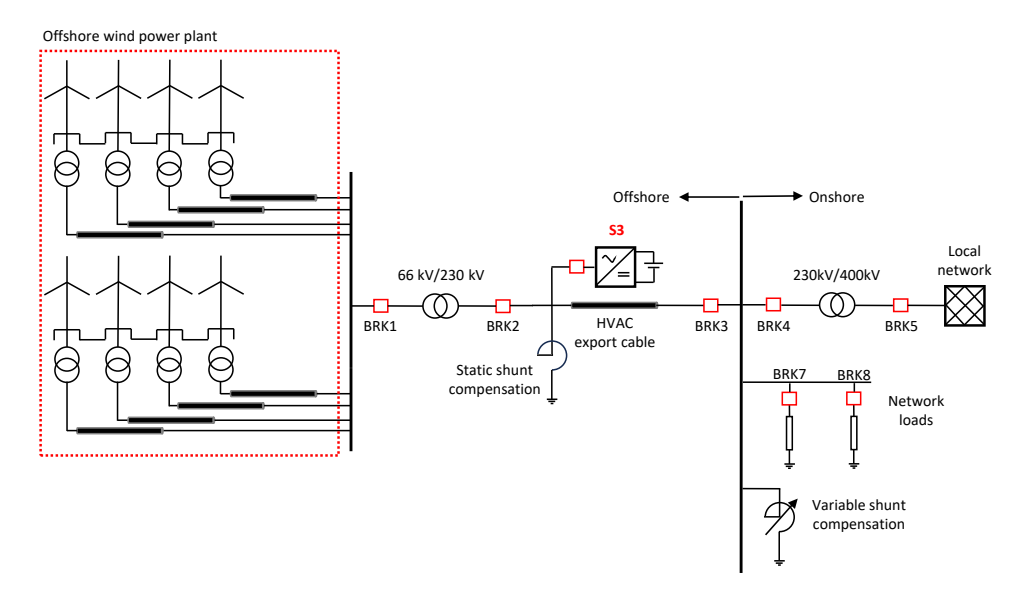


Figure 6.4: One-line diagram of scenario 3, with the APS located offhore

Scenario 4 (S4) proposes a hybrid solution combining onshore and offshore auxiliary power supplies. For example, an onshore BESS could work alongside GFM self-start wind turbines or an additional offshore BESS. This approach reduces costs and improves accessibility compared to other scenarios, while also increasing available energy and redundancy. Some studies already mention this alternative [179–181]. This hybrid configuration leverages the advantages of both onshore and offshore setups, ensuring a more flexible energization process for the OWPP.

For this project, Scenarios S1 and S2 were selected based on their specific advantages. Scenario S1 was chosen primarily due to the technological readiness of the solution, its potential for broader applications such as energy storage for market participation, and the availability of onshore APS units that can be used for future testing. An onshore APS not only facilitates the energization of the OWPP but also provides additional benefits such as voltage and frequency regulation if necessary. Further, since this unit is bigger, it might be able to sustain a voltage reference signal for longer. Scenario S2 was selected due to the high level of expertise and the interest from various partners in utilizing self-starting, GFM wind turbines. This scenario is cost-effective and offers a shorter restoration time, making it a practical choice for efficient and rapid energization. In the following chapter, Chapter 7, both EMT and SSM analyses are conducted, focusing solely on Scenario S2. However, the next phase of the SIF Blade project will involve developing similar studies for Scenario S1, after which a comparison between the two scenarios will be made.

6.2 Steady State Analysis

The aim of this study was to assess if the offshore wind power plant connected to the power system introduced before could generate, in steady state, an envelope

of active and reactive power (P,Q) operating points that would encapsulate the local network (P,Q) needs, thereby matching local network demand. The network demand was provided in terms of (P,Q) operating points, for different wind speeds, demands and paths in the UK.

To examine the steady-state operating conditions, a power flow analysis was conducted. Firstly, the hardware model described in section 3, Figure 3.10, was simplified to achieve an impedance model as shown in Figure 3.12, facilitating the utilization of a Thevenin equivalent for the purpose. Subsequently, the local network demand data was assessed. Once this step was completed, the voltage magnitude and angle of the OWPP were varied to delineate its operational envelope and understand if it effectively encapsulated the operation points of the local network. This iterative process was carried out under various conditions, altering wind speed and local network demand. A selection of the results is presented and explained in this document.

6.2.1 Local network loads

As stipulated in the UK grid codes concerning power system restoration, dispatched providers must collectively be capable of restoring 60% of network demand within the first 24 hours and 100% within 72 hours. This energisation is carried out in incremental steps of active and reactive power. Depending on various factors, such as the number of available generators, demand, and wind speed conditions, black start generators are selected to participate in the energisation process, whether for network reconfiguration or block loading.

The data considered in this study, which assesses the ability of an OWPP to meet local network demand during power system restoration, is based on simulated data provided by a transmission network operator involved in the SIF Blade project. This data defines the active and reactive power requirements at a specific substation during a block loading sequence, representing the incremen-

Chapter 6. Novel Approach to Power System Restoration Using Offshore Wind Power Plants

tal energisation of network components and associated demand. The operating points reflect the power levels that the OWPP would be expected to supply at various stages of the restoration process. While the full simulation includes a comprehensive set of power steps, this study focuses on a subset of the most critical operating points that represent key stages in the energisation sequence. This targeted selection ensures that the stability and performance of the OWPP under the most demanding and representative conditions are thoroughly evaluated. This energisation process is illustrated in Figure 6.5, which shows three different scenarios provided by the TSO. These scenarios are based on simulated system conditions, each representing a different energisation path and load demand sequence. In each case, the active and reactive power requirements are plotted incrementally as the network is restored step by step.

The three scenarios (Cases 1, 2, and 3) differ in two key aspects: the energisation path (i.e., which parts of the network are energised and in what order) and the assumed wind speed at the OWPP location. Wind speed directly influences the level of power that the OWPP can contribute during restoration. For instance, Case 3, which shows the lowest active power levels, corresponds to a scenario with lower wind speed and therefore lower OWPP availability. In contrast, Cases 1 and 2 involve higher wind conditions and greater OWPP participation in the block loading process.

These curves illustrate how the required reactive power increases in steps alongside active power, but with variations across scenarios due to differences in load composition and energisation sequence. Understanding these trends is crucial, as they provide insight into how OWPPs might be expected to respond under varying system conditions and resource availability during power system restoration.

Chapter 6. Novel Approach to Power System Restoration Using Offshore Wind Power Plants

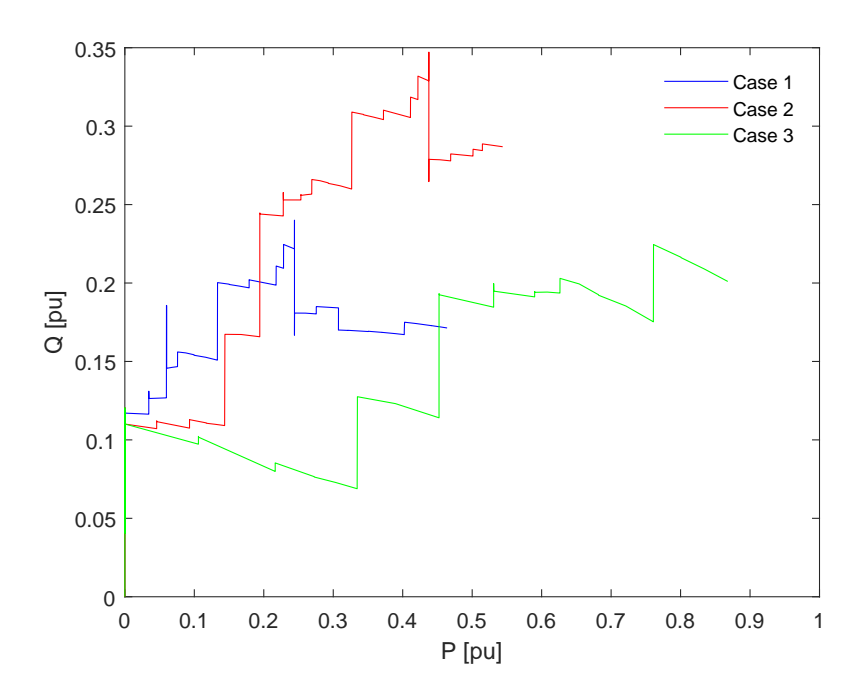


Figure 6.5: Energisation steps for three different local network demands, Cases, 1, 2 and 3

6.2.2 Case studies

In a controlled OWPP, the voltage magnitude and angle output are regulated by the action of the converter controller. However, in this case where the interest was to compute operating points via power flow, the model shown in Section 3.3 was utilized and the operating points of the system computed using the previous equations 3.27 and 3.28.

For each case introduced previously in section 6.2.1, the output voltage and angle at the terminals of the converter were varied to create the operating region of the OWPP. The wind speed used in this analysis was given by a SIF Blade project party. This quantity was varied between 0 and 1, where 1 would mean rated wind speed and 0 no active power production. Hence, to compute the active and reactive power available, the apparent power was multiplied by the wind speed ratio.

Table 6.2 displays the wind speed used for each case, as well as the con-

Chapter 6. Novel Approach to Power System Restoration Using Offshore Wind Power Plants

verter terminal voltage magnitude and phase angle that were used to generate the OWPP operating envelope. The availability of each wind turbine generator (WTG) to deliver active and reactive power depends primarily on the wind resource and the converter limits. In this analysis, wind speed was represented as a per-unit ratio from 0 to 1, with 1 corresponding to rated wind speed. For each case, the total apparent power of the OWPP was scaled by this wind speed ratio to reflect the reduction in available active power due to limited mechanical input.

Although the active power capability of the OWPP decreases with lower wind speed, reactive power can still be supplied within the thermal and voltage constraints of the converter. Therefore, even at lower wind speeds (e.g., Case 1), the OWPP retains the ability to provide reactive power support to the local network. Figures 6.6, 6.7, and 6.8 show the (P,Q) operating envelopes for the three scenarios, where the black markers represent the OWPP capability and the coloured markers correspond to the local substation demand for each case. The coloured operating points were derived from the TSO simulated block loading data, shown previously in Figure 6.5.

Each scenario corresponds to a different energisation path and wind condition, affecting both the network demand and the OWPP ability to meet it. The plots demonstrate that, despite varying wind availability, the OWPP was able to cover the required operating points of the local network in each scenario. This confirms that the OWPP, through appropriate control of the converter terminal voltage magnitude and angle, can provide the necessary active and reactive power support under realistic restoration conditions.

Chapter 6. Novel Approach to Power System Restoration Using Offshore Wind Power Plants

Table 6.2: Wind speed, converter voltage angle and magnitude for the different study cases

Case	Wind (%)	<u>/δ°</u>	$\overline{E_s}$ (pu)
1	0.15	-5 to 2	0.95 to 1.02
2	0.6	-10 to 3	0.91 to 1.01
3	0.35	-8 to 2	0.93 to 1.02

This was achieved without varying any parameter in the impedance model. Thus, there is margin to vary even further the converter terminal voltage magnitude and angle to accommodate local network demand, as well as potentially increase or decrease the shunt compensation that exists in the model. Further, the study here presented was performed for a cable length of 30 km, hence the impact of the capacitance of the HVAC cable did not play a major role in active power losses nor reactive power needs. If such issue arises, and as it was was previously observed in [182], these components significantly impact the voltage stability of the system in steady state as well as the (P,Q) operation envelope which the OWPP may provide to the local network, this study may be carried varying the shunt impedance to analyse how much reactive power would need to be compensated.

6.3 Availability Study

The availability study aims to illustrate the active power and energy production achievable from an OWPP in case of PSR, having in mind wind speed data. Once these amounts are known, it may be seen if extra energy is needed from an energy system storage to match the local network demand. The document [183] outlines the essential technical prerequisites for an OWPP to function as a black start provider. According to the stipulations in this document, the OWPP must have the capability to restore 60% of the necessary local network within the initial 24

Chapter 6. Novel Approach to Power System Restoration Using Offshore Wind Power Plants

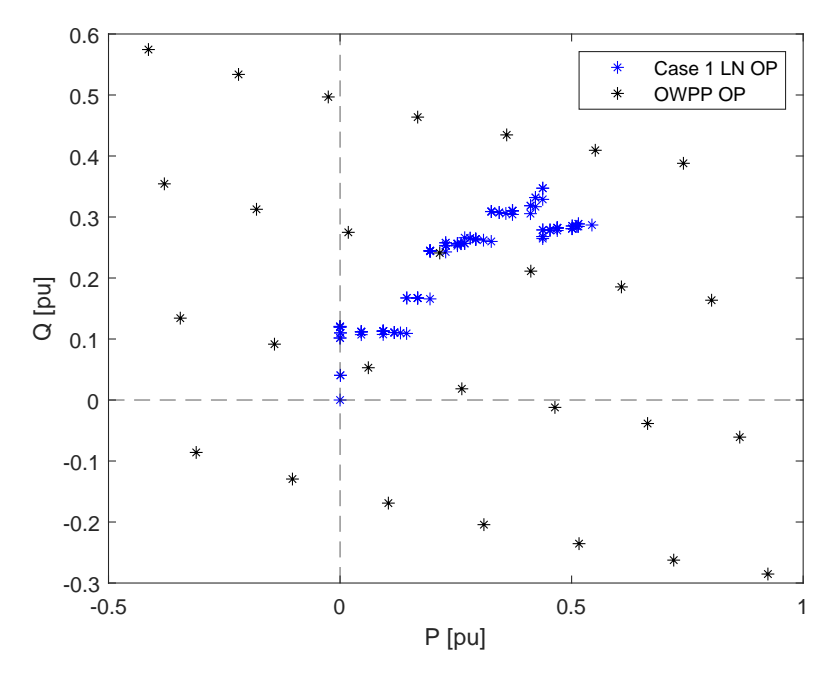


Figure 6.6: OWPP and local network (P,Q) OP: Case 1

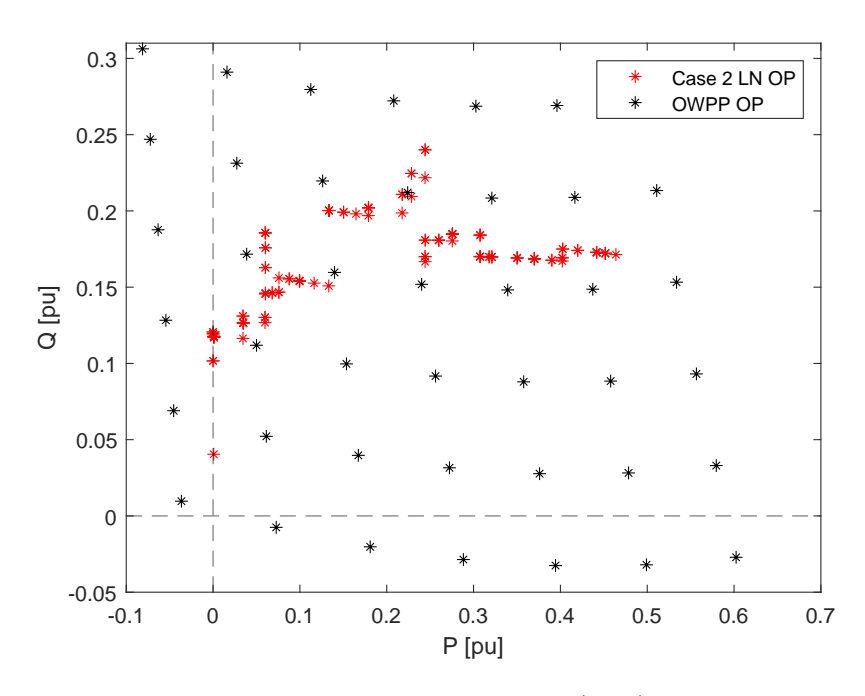


Figure 6.7: OWPP and local network (P,Q) OP: Case 2

hours following a blackout. Furthermore, it is mandated that within 120 hours, the entire system must be fully restored.

Chapter 6. Novel Approach to Power System Restoration Using Offshore Wind Power Plants

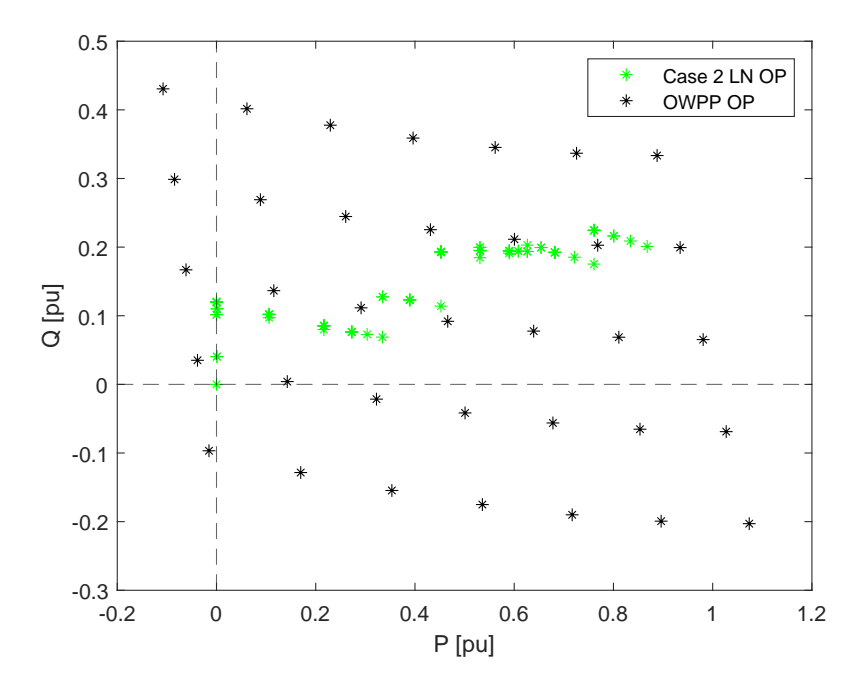


Figure 6.8: OWPP and local network (P,Q) OP: Case 3

Having access to the wind speed at a designated OWPP site along with details about the wind farm and wind turbines employed, it becomes feasible to compute the active power that can be harnessed. Once this power is determined, it can be estimated if extra energy is required from external auxiliary power sources, such as BESS, to fulfil SO requirements.

The availability study was conducted for two OWPP. However, this novel methodology may be adapted for various offshore wind farms by adjusting specific parameters related to the wind speed, wind farm and wind turbines.

The first OWPP encompass 54 wind turbines, each with a capacity of 8 MW, resulting in an aggregate power output of approximately 450 MW. The second OWPP is still on its early stages, and thus there is no available information with regards to the wind turbines that will be employed. Nevertheless, it is known that the expected output power is of 4.1 GW, from which 2.3 GW will be connected to one onshore substation, and it is up to 307 offshore wind turbines.

The methodology used to analyse the power and energy availability of these

wind farms may be seen in Figure 6.9.

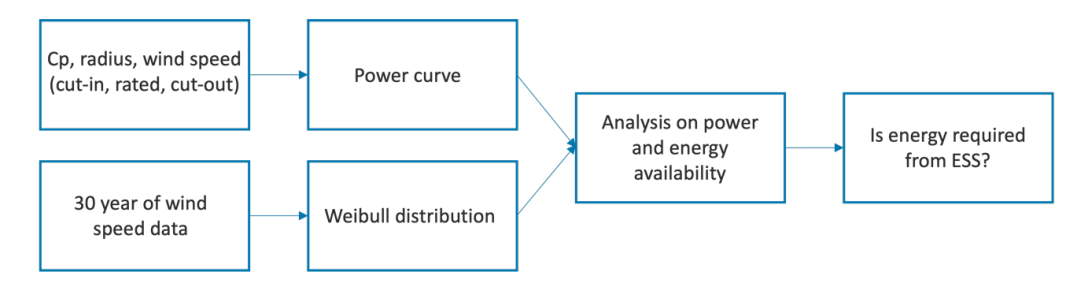


Figure 6.9: Sketch of methodology used to study power and energy availability of an OWPP

Firstly, it was necessary to analyse the wind speed on the OWPP sites. For this purpose, wind speed data sourced from [184] was used. These datasets comprise wind speed information recorded at a height of 100 meters over a span of 30 years, starting from January first, 1990. A series of computations were performed to determine the Weibull distribution for each OWPP site. Further, the wind speed data was used to compute the average monthly wind speed.

Then, it was necessary to compute the power curve of the wind turbines of both OWPP. With this information, and with the wind speed data, it was possible to compute the power and energy production over several time frames, i.e. a day, week, month, or even an averaged year of power production. For these power curves, information of the power coefficient, wind turbine radius and cut-in, cut-out and rated wind speed were needed.

To explore the active power and energy that can be extracted by both wind farms with regards to the available wind speed, the average daily power that can be extracted was computed. Furthermore, it was seen that wind speed varies significantly over a year and thus, a monthly analysis was performed, and active power and energy computations were done for a day and week period in terms of average power and P90.

Furthermore, data available of the local network demand was provided for this analysis. With this information, several scenarios of low wind and a scenario

of rated wind speed were analysed. This way, it was possible to see how much energy was needed from an external auxiliary power supply to match demand in case of low wind speeds.

It should be mentioned that the direction of the wind speed or the wake effect were not considered, and hence it was assumed that, at any time, all the wind turbines of the OWPP were producing the same aerodynamic active power.

This section is divided into two sections, each dedicated to a distinct OWPP. Section 6.3.1 delves into the specifics of OWPP Case 1, while Section 6.3.2 focuses on OWPP Case 2. In both instances, the analysis begins with an examination of wind speeds, demonstrating their variations across the spectrum through Weibull distributions. Then, the study focuses on the power curves of the wind turbines for both wind farms and finally, the power and energy production for each OWPP are computed.

6.3.1 OWPP Case 1

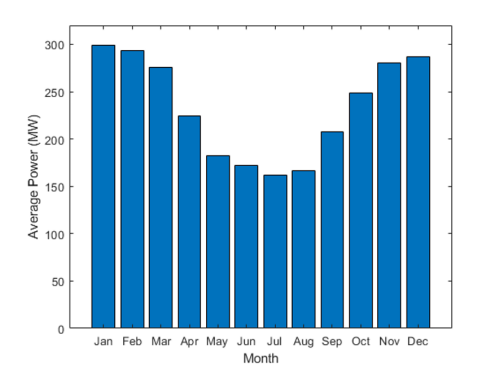
Power and Energy Production

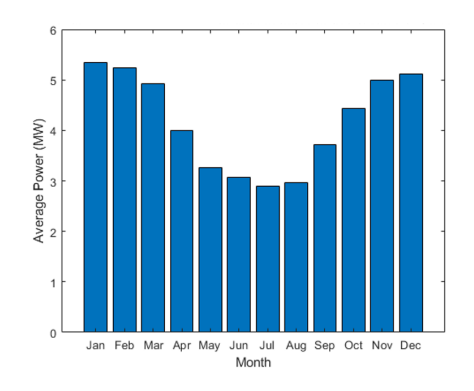
The initial step involved computing the average power output of the OWPP by factoring in the previously computed wind speed distributions and power curve. Values of wind speed and the computer curve used are described in Section F.1. Since the wind speed data available consists of the average wind speed every hour, the active power and energy were computed hourly using the 30-year data available and the average power and energy produced may be seen in Table 6.3.

Table 6.3: Average daily active power and energy production for OWPP Case 1

Property	Value	
Power, one wind turbine [MW]	4.05	
Power, OWPP [MW]	218.80	
Energy, OWPP [GWh]	5.25	

Chapter 6. Novel Approach to Power System Restoration Using Offshore Wind Power Plants





- (a) Average daily production for OWPP Case 1 monthly study
- (b) Average daily production for a wind turbine from OWPP Case 1- monthly study

Figure 6.10: Active power average daily production

Figure F.1b illustrates the considerable variability in wind speed across various months, notably indicating that the average wind speed during winter months is significantly higher than in other seasons. This disparity suggests that the power production during these winter months is likely to be notably higher due to the increased wind speeds, potentially resulting in elevated energy output during this period. Consequently, a detailed monthly analysis was conducted to assess power and energy production for both daily and weekly intervals. Initially, the average power production for each month over a single day was computed, presented in Figure 6.10a for the OWPP and Figure 6.10b for an individual wind turbine.

Subsequently, calculations were made for the P90 power, P90 daily energy production, and P90 weekly energy production. The results are summarized in Table 6.4, showcasing the expected variations in power and energy production throughout the year. It is evident that the colder months tend to yield higher amounts of power, making them potentially significant periods for power restoration scenarios. This highlights the capacity of the OWPP to function effectively as either an anchor or top-up generation source.

Understanding the potential power output is crucial for effectively planning the utilisation of a battery energy storage system. This insight provides a reliable

basis for estimating the energy required from the storage system to meet demand, regulate frequency, and stabilise voltage levels within the grid.

Table 6.4: OWPP Case 1 P90 values for different months

Month	Jan	Feb	Mar	Apr	May	Jun	Jul	Aug	Sep	Oct	Nov	Dez
P90 (MW)	353.02	361.51	350.00	356.00	328.80	327.86	321.29	325.97	352.03	370.12	364.04	365.05
P90, daily (GWh)	8.47	8.68	8.59	8.54	7.89	7.87	7.71	7.82	8.45	8.88	8.74	8.76
P90, weekly (GWh)	42.36	43.38	42.96	42.72	39.46	39.34	38.56	39.12	42.24	44.42	43.68	43.80

Matching Demand

In Section 6.2, it was demonstrated how the operating points provided by a project partner were used to align the active and reactive power requirements of the OWPP. In this section, a similar approach is taken to evaluate power availability, focusing on the active power requirements of 60% within 24 hours and 100% within 120 hours.

The scenario under consideration involved the highest demand, with a maximum active power requirement of approximately 1.2 GW. The 60% threshold for local demand equates to 672 MW.

Given the active power requirements, along with the daily and weekly energy demands, it is possible to assess, based on wind speed, the average power that can be generated by the OWPP and whether additional energy is needed to meet the local grid requirements. Table 6.5 presents an analysis of this scenario. The study considers several low wind speed conditions, as well as the rated wind speed, which produces nominal power. The table shows the average power generated for each wind speed, and for both the 24-hour and 120-hour periods, it calculates the available energy for each wind speed. Using these energy values, and comparing them with the local network demand, the energy storage required for both time frames was determined. The energy storage values presented are indicative only, representing the amount of energy that would be required to fully supply the remaining network if the OWPP output were insufficient. At present, an energy

storage system capable of delivering such high power levels is not available. However, in a future scenario where multiple islands are interconnected, these energy requirements could potentially be met with the support of suitably sized energy storage systems.

Table 6.5: Energy and Power Data for Different Wind Scenarios

Wind scenario (m/s)	Average Power (MW)	Energy, 2	4h (GWh)	Energy, 120h (GWh)		
wind seemans (m/s)	Tiverage I ever (III)	OWPP	ESS	OWPP	ESS	
4	16.00	0.38	15.75	1.92	132.5	
6	53.98	1.30	14.84	6.48	127.96	
8	127.97	3.07	13.06	15.36	119.08	
10	249.94	6.00	10.13	30.00	104.44	
Rated	432	10.37	5.76	51.84	82.60	

6.3.2 OWPP Case 2

Power and Energy Production

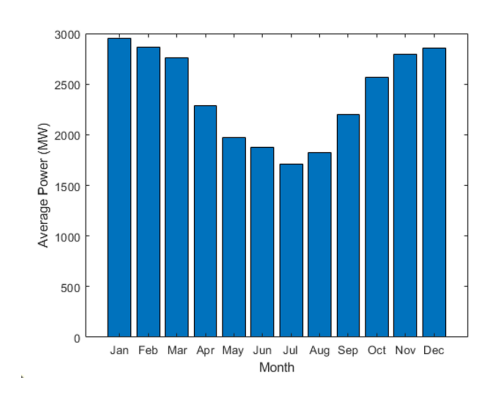
The study that was conducted for OWPP Case 1 wind farm was also conducted for the OWPP Case 2. Values of wind speed and the computer curve used are described in Section F.2. Hence, in this section, the daily average power production was firstly computed for the 30-year data for a year and afterwards, the monthly study was also conducted. Table 6.6 contains the average active power for one wind turbine, the wind farm and the average daily energy.

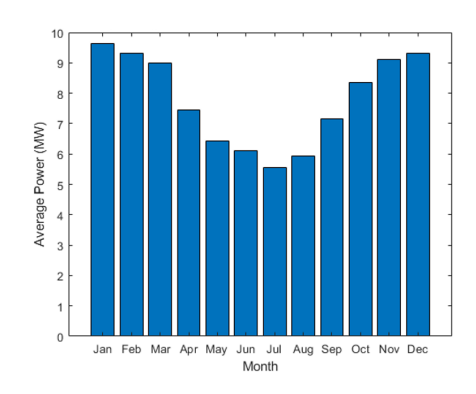
Table 6.6: Power and Energy Properties of the OWPP Case 2

Property	Value
Power, one wind turbine [MW] Power, OWPP [MW] Energy, OWPP [GWh]	7.94 2437.97 58.51

Figure F.3a and Figure F.3b display the results for the average active power production for each month, for the OWPP Case 2 and one offshore wind turbine, respectively. The power P90, the P90 weekly energy and P90 daily energy

productions may be seen in Table 6.7.





- (a) BwB wind speed Weibull distribution
- (b) Monthly average wind speed for BwB

Figure 6.11: Active power average daily production

Table 6.7: OWPP Case 2 P90 values for different months

Month	Jan	Feb	Mar	Apr	May	Jun	$_{ m Jul}$	Aug	\mathbf{Sep}	Oct	Nov	\mathbf{Dez}
P90 (GW)	3.14	3.19	3.37	3.42	3.30	3.32	3.13	3.25	3.25	3.44	3.20	3.30
P90, daily (GWh)	75.27	76.46	80.89	82.02	79.32	79.76	75.16	78.00	77.99	82.47	76.89	79.32
P90, weekly (GWh)	376.35	382.29	404.43	410.09	396.59	398.82	375.81	389.94	389.94	412.37	384.47	396.56

Matching demand

The same local demand considered for OWPP Case 1 was applied to OWPP Case 2. However, for this case, the OWPP output power was set to 2.3 GW, as this is the active power to be connected to the onshore substation. Therefore, instead of considering all 307 wind turbines in the OWPP, only 177 were included, which collectively produce approximately 2.3 GW when operating at rated wind speed and generating nominal active power. As before, low wind speed scenarios (4, 6, 8, 10, and 12 m/s) and the rated wind speed scenario were assessed.

Table 6.8 illustrates the average power and energy output of the wind farm across several low wind speed scenarios and the rated wind speed scenario. It also shows whether additional energy from an auxiliary power supply is needed to meet local network demand. In some wind scenarios, the required energy is "negative," indicating that no energy is needed from the APS due to an energy

surplus. This excess energy can be used for various purposes, such as charging the energy storage system.

Table 6.8: Energy and Power Data for Different Wind Scenarios

Wind scenario (m/s)	Average Power (MW)	Energy, 2	4h (GWh)	Energy, 120h (GWh)		
	Tiverage Fower (Wiv)	OWPP	ESS	OWPP	ESS	
4	43.3	1.04	15.1	5.2	129	
6	146.2	3.51	12.6	17.55	116.8	
8	346.6	8.31	7.80	41.59	92.85	
10	676.9	16.25	-0.11	81.23	53.20	
12	1170	28.07	-1.19	140.37	-5.93	
Rated	2301	55.22	-3.91	276.12	-142	

6.4 Chapter conclusions

This chapter presented four distinct scenarios, each differing in terms of the location of the auxiliary power supply unit required to initiate the offshore wind power plant and the necessity for grid-forming wind turbines. The SIF Blade project was introduced, with two of these scenarios, specifically scenario 1 and scenario 2, selected for further analysis within the project framework.

A comprehensive steady-state analysis was conducted, employing a model of the OWPP based on partner specifications. The results demonstrated that the OWPP could establish an operational envelope capable of meeting the active and reactive power demands of the local network. These demand data points, provided by a project partner, confirmed that the OWPP is technically capable of supporting steady-state operations in a restoration scenario. Moreover, this analysis shows significant potential for future studies on wind farms, as it can be readily adapted and applied to a variety of different cases.

An availability study was also undertaken, highlighting the significant impact of wind speed on the average active power generated by the OWPP. It was observed that during periods of low wind speeds, and even at rated wind speed, external power sources, such as other OWPPs or alternative black start units,

Chapter 6. Novel Approach to Power System Restoration Using Offshore Wind Power Plants

may be necessary to energise 70% of the grid within 24 hours and achieve full energisation within 72 hours. This underlined the importance of effective coordination between different black start units. However, in OWPP Case 2, sufficient power was generated at wind speeds exceeding 8 m/s, enabling the energisation of the specific path examined in this study. These findings emphasise the considerable potential of OWPPs to contribute to power system restoration efforts under appropriate conditions

Chapter 7

Novel Grid-Forming Control Strategy for Enhanced Power System Restoration

7.1 Introduction

This chapter is mainly composed of two studies where it is examined the need for, and benefits of, including GFM converter controllers in the PSR process. These studies were done for both anchor and top-up generation possibilities. These two terms have been added to the Grid Code legal text (GC0156) to clarify the roles of different parties involved in restoration services, based on how actively they participate in the restoration process [69]. The anchor generation assumes the role of system energisation, effectively having an active role in rebuilding the skeleton network and block loading whereas the top-up generation scenario only accounts for its block loading capabilities, hence just providing active and reactive power as required.

Section 7.2 delves into EMT simulations, while Section 7.3 focuses on linear time-invariant (LTI) studies, via SSM. The EMT studies aimed to analyse if

OWPPs with varying percentages of GFM converter controller were able to meet transmission system operator (TSO) requirements, mitigate potential challenges, and maintain stable operation during PSR. The novelty of this research lies in the LTI studies, which involved a stability analysis via SSM — a study not yet performed in the context of PSR. This study aimed to determine the best percentage of GFM penetration for enhanced stability and robustness of the power system in scenarios involving anchor and top-up generation during block loading.

7.2 EMT Analysis

This section presents the EMT studies conducted to analyse the time domain performance in the PSR process. The aim was to determine if different levels of GFM penetration would meet some of the technical requirements set by the TSO. The requirements examined are described in table 7.1 and were previously mentioned in Chapter 2. In this study, the GFM penetration was varied between 0% to 100% in steps of 20%.

Table 7.1: Technical requirements analysed via EMT simulations

No.	Technical requirement	Range
1	Block loading capability	35 to 50 MW
2	Frequency control (while block loading)	47.5 to 52 Hz
3	Voltage control (while block loading)	0.9 to 1.1 pu $(\pm 10\%)$
4	Ability to withstand inrush currents and transient voltages	Analysed during network energisation
5	Reactive range to energise immediate network	50 MVAr

Figure 7.1 displays a one-line diagram of the model used for the time domain

studies and appendix D contains the parameters that were used in this study. To analyze the optimal GFM penetration, the aggregated wind farm was split into two parts, each with a controlled voltage source converter (with voltages V_1 and V_2) and their LC filters (parameters R_c and L_c), representing both GFM and GFL converter penetrations. This setup allowed for varying the percentage of GFM penetration.

The model further includes an offshore transformer that steps up the voltage from 66 kV to 230 kV. An HVAC export cable is represented using a π equivalent model with parameters R_{hc} , L_{hc} , and C_{hc} . This cable has a length of 50 km. Due to the high capacitance of submarine cables, two shunt reactive power compensations were included: one fixed offshore (L_l and R_l) and one variable onshore (L_r and R_r). Four RL loads were connected to simulate the block loading capabilities. The active and reactive power steps and respective values of R_{LD} and L_{LD} may be seen in table D.2 of appendix D.

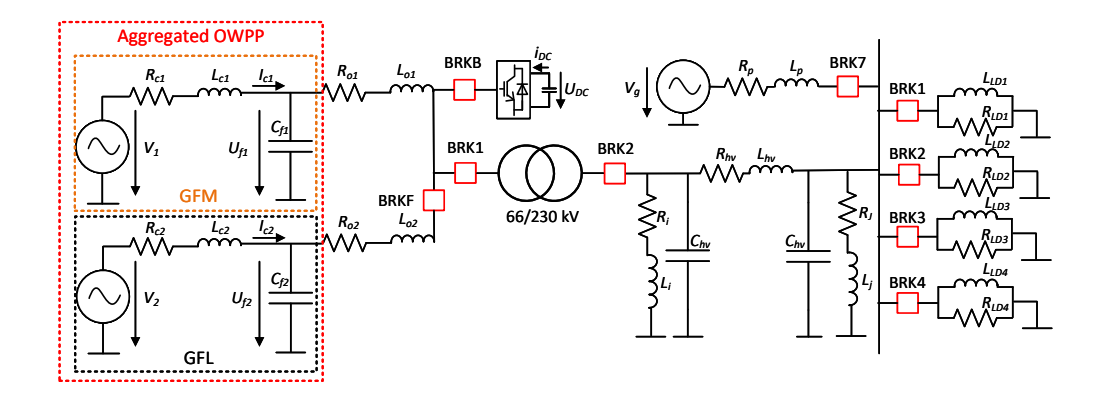


Figure 7.1: One-line diagram of the EMT model analysed

Additionally, the scenario tested here is Scenario 2, involving self-starting wind turbines, with a BESS connected via breaker BRKB to the upper branch of the OWPP. Although the BESS may have several purposes, in this study, it was only used for wind farm energisation. It should also be noted that an aggregated

Chapter 7. Novel Grid-Forming Control Strategy for Enhanced Power System Restoration

wind farm model was used in this study, so array cables of the wind farm and wind turbine transformers were not considered, but study is considered as future work. Furthermore, only the offshore transmission system was considered as no onshore cables were modelled for this study. Furthermore, both top-up and anchor generation scenarios were used. In case of the top-up scenario, as an external grid is present during the energisation process, breaker BRK7 is closed. In case of anchor generation, BRK7 was open through all the simulations and hence, no external grid support was available.

7.2.1 Energisation sequence

The energisation process is detailed in Table 7.2. From the system perspective, it begins by energising one or several self-start-capable GFMs (depending on the percentage of GFM penetration) by closing breaker BRKB. Prior to this, the GFM WTGs are powered through their auxiliary supply (e.g., battery or stored energy system) and operate in a dedicated self-start mode, enabling their converters to synthesise a stable voltage waveform at the machine terminals. When BRKB closes, these units establish the voltage and frequency reference for the de-energised offshore network, charging the cable capacitances and energising any connected transformers. The number of GFMs initially energised is chosen to provide sufficient short-circuit strength and inertia for stable system operation during subsequent energisation steps. In this study, all GFM WTGs are assumed to be self-start capable. Once these units are energised, breaker BRKF is closed to energise the rest of the OWPP, including the GFL units. This step poses synchronisation challenges. Since this study involves an aggregated wind farm model, the resulting transients may not accurately represent the actual events, and this topic will be addressed in future research.

After the OWPP is fully energised and operating in islanded mode, breaker BRK1 is closed to energize the offshore transformer. As mentioned, this step is

Chapter 7. Novel Grid-Forming Control Strategy for Enhanced Power System Restoration

done via the self-start wind turbines energised previously. However, a scenario with a BESS unit as auxiliary power supply would be able to energise the transformer via soft-start. This step presents technical challenges which are addressed in technical requirement number 4, displayed in table 7.1. To address this issue, the point on wave (POW) strategy was employed. Several studies discuss the mitigation of inrush currents [185–188], so this topic will not be fully explored here. However, a brief description of the POW strategy is provided below due to its application in this study.

After energising the offshore transformer, breaker BRK2 is closed to energize the shunt compensations and the HVAC export cable. This step also presents challenges related to transient performance during energisation or de-energisation processes. These transient phenomena can result in inrush currents, high overvoltages, current zero-miss and transient recovery overvoltages in circuit breakers. These phenomena will depend on the length of the cable, power-frequency voltage, system short-circuit power, shunt compensation and switching instant and may be mitigated applying proper shunt compensation, closing a circuit breaker at a specific time or using a pre-insertion resistor [189–193].

Once the path from the OWPP to the onshore network is fully energized, the process of block loading starts. Subsequently, BRK3, is closed, followed by BRK4, BRK5 and BRK6 to energize the for RL loads representing the active and reactive power demand from the local network. These loads, defined in appendix D, were energised every two seconds.

Chapter 7. Novel Grid-Forming Control Strategy for Enhanced Power System Restoration

Table 7.2: Energisation sequence of PSR

Step	Time	Activity
	(s)	
1	0	BRKB is closed and self-start, GFM units, start the energisa-
2	2	tion process BRKF is closed to energize the GFL units, hence fully energising OWPP
3	3.2	BRK1 is closed and offshore transformer is energized
4	5	BRK2 is closed, energising shunt compensations and submarine export cable
5	7	BRK3 is closed to energize first load (P1)
6	9	BRK4 is closed and second load is energized (P2)
7	11	BRK5 is closed and third load is energized (P3)
8	13	BRK6 is closed and fourth load is energized (P4)

7.2.2 Results

This section displays the results of the EMT simulations. For each step of energisation, it was seen if the TSO requirements mentioned in table 7.1 were met. This section is organised as follows: first, it discusses transformer energisation and the associated issues, including the impact of inrush currents. Following this, the focus shifts to the energisation of shunt reactors and cables. Subsequently, results are presented for block loading in both top-up and anchor scenarios. Finally, the section concludes with a summary of the key findings and final conclusions.

Transformer energisation

The energisation of a transformer may results in inrush currents due to the saturation of its core. Several strategies were studied in academia such as the pre-insertion resistor, point on wave (controlled switching) and soft-start. These may require changes in the converter control strategy or even in the transformer hardware. These strategies are detailed in the following studies [194–200].

Due to its simplicity, the classic controlled switching strategy (POW) was

used in this study. This technique relies on closing the breaker of the offshore transformer at an instant at which the residual flux is equal to the prospective flux, that is, at an optimal closing angle α . This may be seen through equation 7.1 where the instantaneous flux is calculated [196].

$$\phi \approx \frac{-L_m V_P cos(\omega t + \alpha)}{\sqrt{R_1^2 + (\omega L_T)^2}} + \left(\phi_r + \frac{L_m V_P cos(\alpha)}{\sqrt{R_1^2 + (\omega L_T)^2}}\right) e^{-\frac{R_1}{L_T}t}$$
(7.1)

where ϕ is the core flux, V_P is the voltage of the energized transformer primary, L_m is the core inductance, L_T is the primary inductance summed with the core inductance, R_1 is the primary resistance, ω is the angular frequency and α is the angle at which the breaker is closed and transformer energized. If the residual flux is equal to the prospective flux, the decaying term in equation 7.1 is eliminated and thus, the inrush currents neutralized.

The prospective flux can be estimated using equation 7.2. This equation shows that the prospective flux is obtained by integrating the voltage applied to the energized (primary) side.

$$\phi_p = \int V_P \sin(\omega t) dt \tag{7.2}$$

For this study, the parameters of the transformer used may be seen in table D.3. Firstly, a simulation was analyzed without any inrush current mitigation strategy, thus, the breaker was closed at a random instant, of t= 3.3 s. Results of such simulation may be seen in figure 7.2. From this figure it is noted that the transformer suffers severe inrush currents, in the order of 10 kA and voltages at both primary and secondary go above and below TSO allowed limits.

Figure 7.3 displays the results of the offshore transformer energisation using the POW energisation strategy for a GFM penetration of 20%. For the residual flux considered (that may be seen in table D.3 of 0.8 pu), the optimum instant of closing the breaker was computed at t = 3.2117 s. In this figure, it may be

Chapter 7. Novel Grid-Forming Control Strategy for Enhanced Power System Restoration

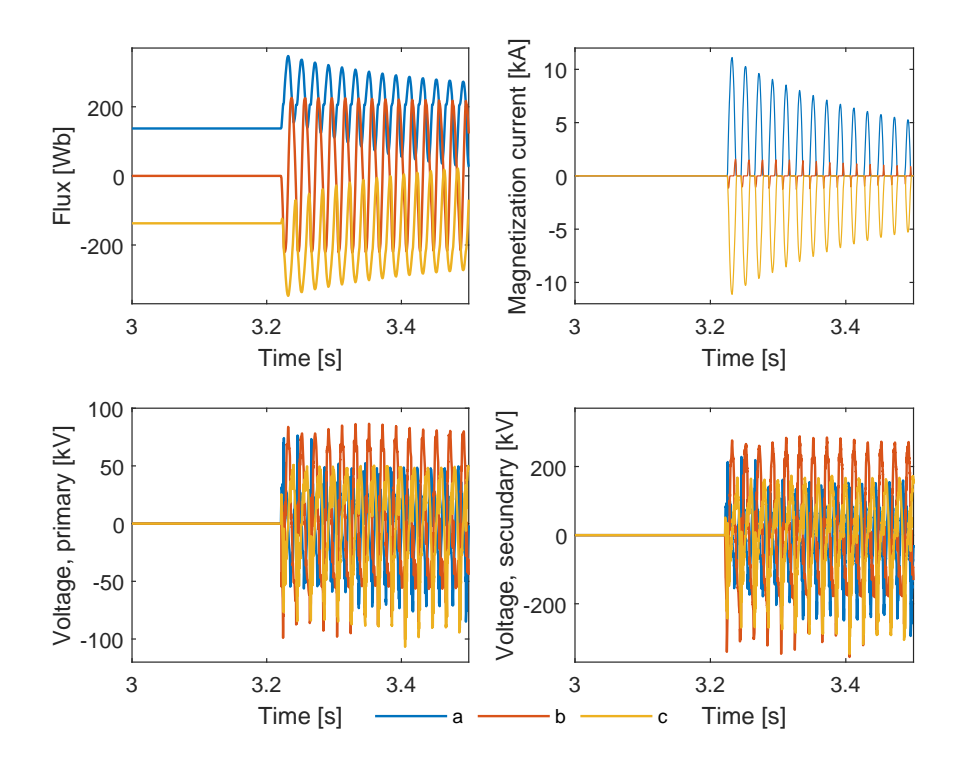


Figure 7.2: Offshore transformer energisation without any inrush current mitigation technique

seen that the inrush currents are mitigated, with the maximum inrush current being of 5 A. Both primary and secondary voltages of the transformer are within acceptable TSO limits.

The POW strategy was applied for various percentages of GFM penetration. This strategy effectively mitigated inrush currents in all cases as may be seen in figure 7.4.

However, the magnitude of the inrush currents varied slightly depending on the GFM penetration. This variation occurs because, at the computed instant when the breaker is closed, the voltage on the primary side of the transformer differs slightly, leading to slight variations in the prospective flux. Since the optimal breaker closing angle is based solely on the residual flux within the transformer core, the prospective flux and residual flux will not be exactly identical, resulting in slight differences in inrush current magnitudes. Additionally, it was seen that

Chapter 7. Novel Grid-Forming Control Strategy for Enhanced Power System Restoration

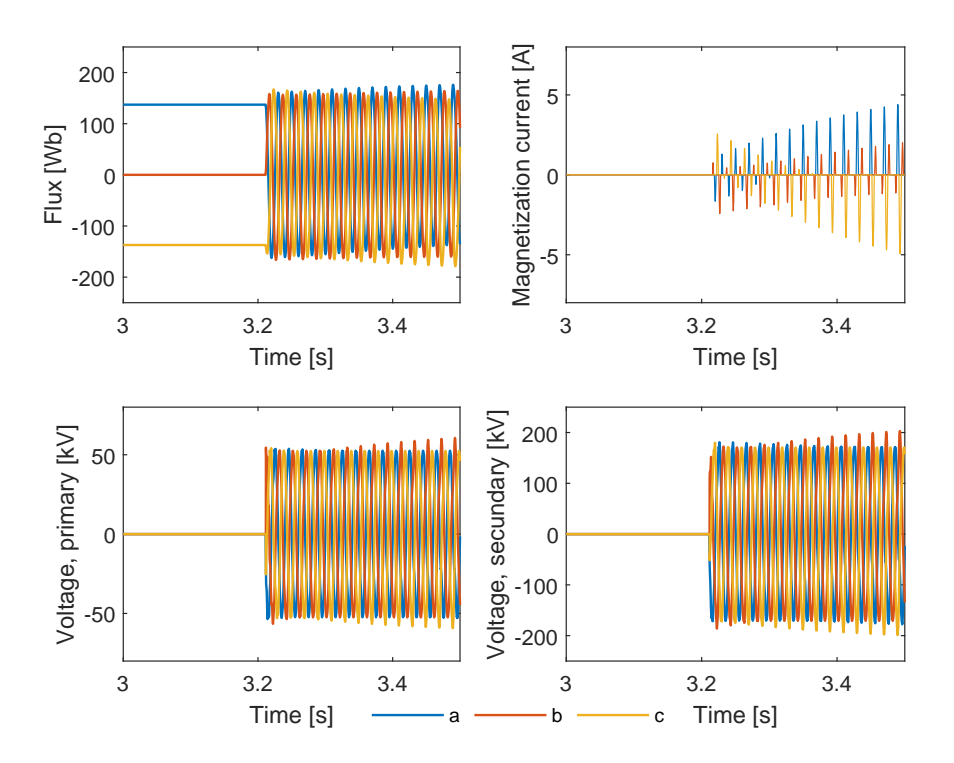


Figure 7.3: Offshore transformer energisation with POW for a GFM penetration of 20%

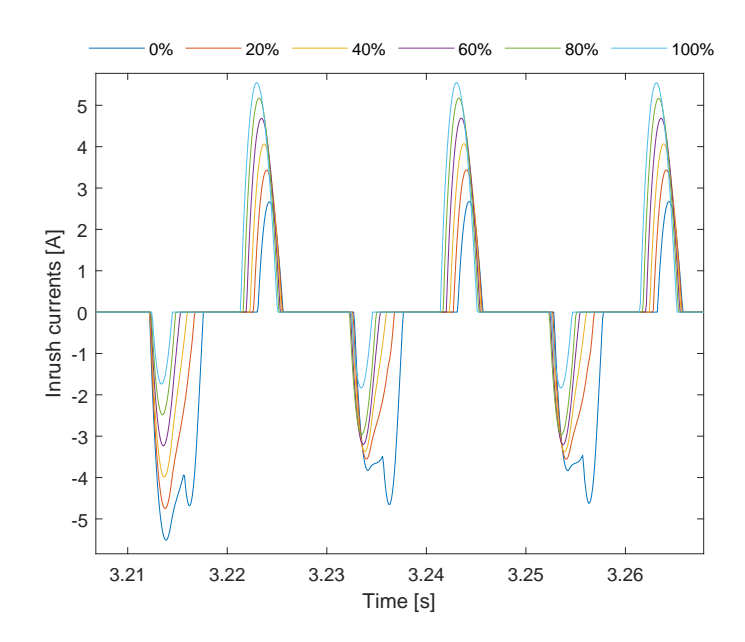


Figure 7.4: Inrush currents after transformer energisation for different GFM penetration percentages

Chapter 7. Novel Grid-Forming Control Strategy for Enhanced Power System Restoration

the offshore transformer is energized only after the GFL units are synchronized with the GFM units and the OWPP is running in islanded mode, which can cause some voltage distortions. Allowing time for the waveform to stabilize and return to its natural sinusoidal form before energising the transformer is necessary; otherwise, undesired inrush currents may occur. Despite these variations, the POW strategy successfully mitigated inrush currents across all levels of GFM penetration, demonstrating its effectiveness regardless of penetration levels.

Shunt reactors and export cable energisation

After energising the offshore transformer, breaker BRK2 was closed to energize the offshore HVAC submarine cable, along with both offshore and onshore shunt compensations. The offshore reactor is static, while the onshore compensation is variable. This means that the onshore compensation value will adjust based on the reactive power requirements, which might differ for normal operation, energisation or de-energisation.

As previously mentioned, the submarine cable is 50 km long and produces significant capacitive reactive power. A load flow analysis was conducted to design the shunt compensations to mitigate this reactive power, ensuring that the cable voltage remains within acceptable TSO limits and the power factor stays close to unity at the PCC. It was concluded that 270 MVAr would be compensated via shunt reactors, and 40% of such quantity would come from the offshore reactor and 60% from the onshore one.

To prevent overvoltages and the zero-missing phenomenon, which occur when reactive power compensation exceeds 60% due to interactions between inductive and capacitive components in both the cable and reactors, a Pre-Insertion Resistor (PIR) was implemented. Additionally, incorporating two shunt compensations, rather than just one onshore, was a critical measure to mitigate these phenomena.

The value of the PIR and the optimal switching time for its connection depend on several factors, including the shunt compensation level and the length of the export submarine cable. The PIR also plays a crucial role in mitigating inrush currents that arise from interactions between the offshore transformer, the export cable, and the shunt components.

For this study, the PIR was designed with a resistance of 30Ω , and the breaker was closed 100 ms after BRK 2. The results are presented in Figure 7.5. This figure shows that the zero-missing phenomenon was eliminated, and no significant overvoltages occurred. Additionally, inrush currents were effectively mitigated.

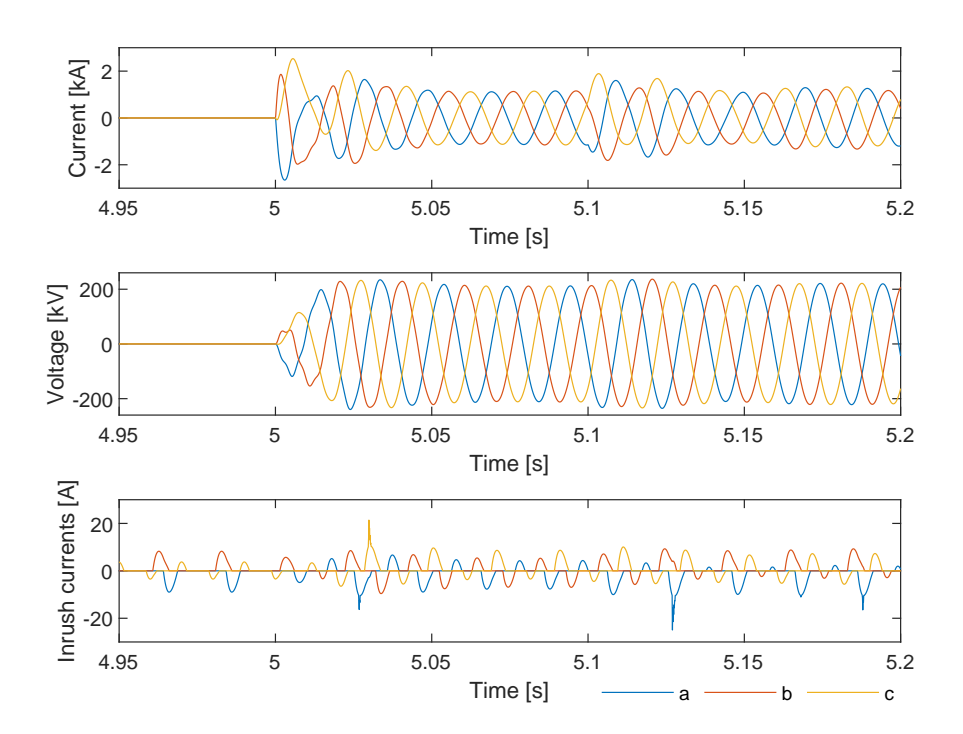


Figure 7.5: Cable and shunt reactors compensation for a GFM penetration of 40%

Figure 7.6 displays the inrush current results for different GFM penetrations. It can be observed that while inrush currents vary slightly depending on the level of GFM penetration, the differences are minimal. Thus, it can be concluded that across all GFM penetrations, the cable and shunt compensations were energized

with minimal impact.

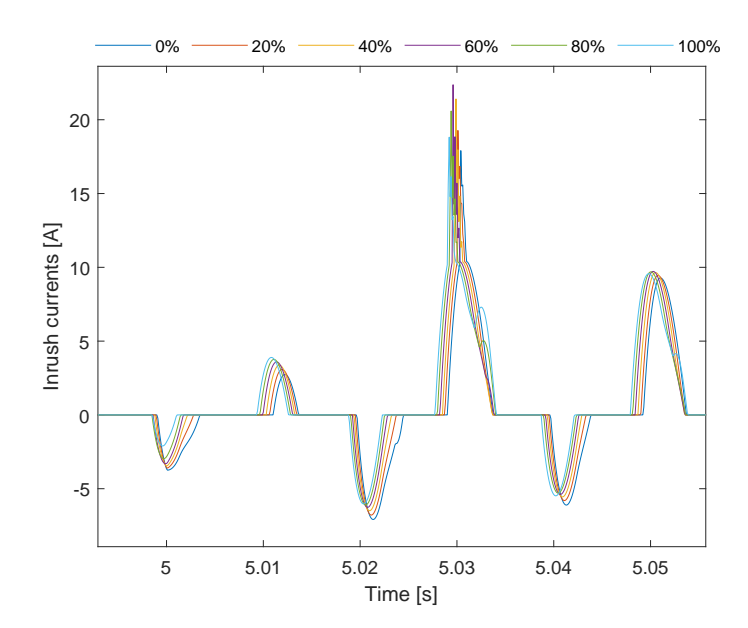


Figure 7.6: Inrush currents after cable and shunt compensation energisation for different GFM penetration percentages

Block loading

Block loading capabilities were analysed for both anchor and top-up generation scenarios. The results depicted in the figure 7.7 illustrate the block loading results for the top-up scenario for an 80% GFM penetration. It can be seen that the active power at the load is well achieved and both GFM and GFL controllers follow its reference as expected.

Figure 7.8 depicts the voltage and frequency responses for the top-up generation scenario under varying levels of GFM penetration, ranging from 0% to 100%. Across all scenarios, the voltage remains well within the TSO acceptable limits of 0.9 to 1.1 pu. This indicates that the integration of OWPP, irrespective of the penetration level of GFM capability, does not adversely affect voltage stability. The system maintains a robust voltage profile, showcasing the efficacy of the external grid's stabilising influence. The model includes only the high-voltage

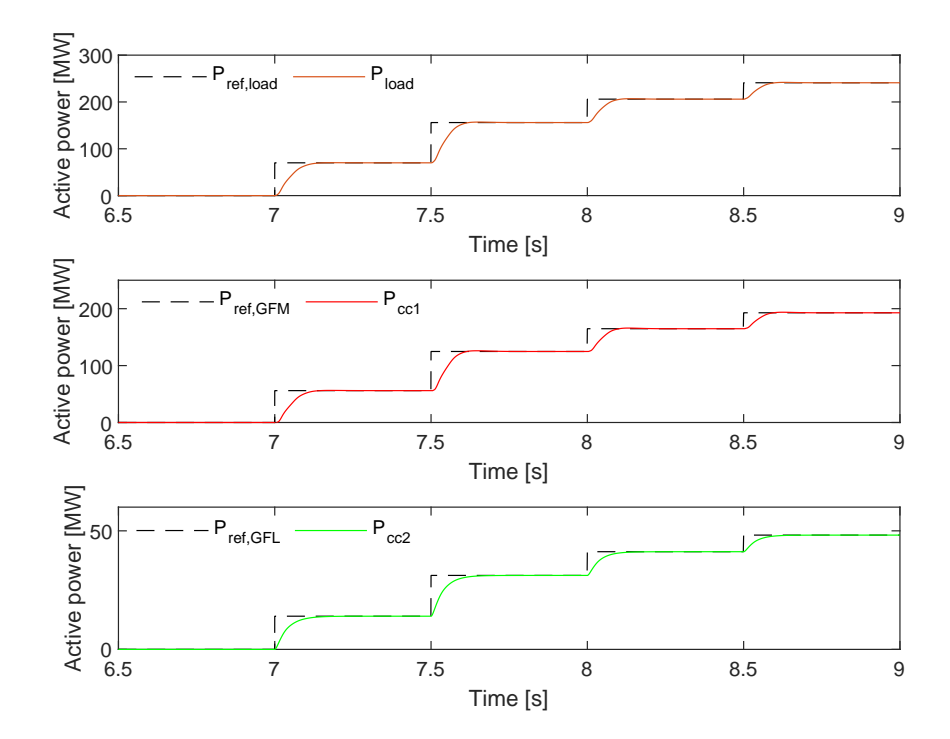


Figure 7.7: Active power at the load and converter control action (GFM and GFL) for an 80% GFM penetration during block loading for the top-up scenario

transformers within the offshore substation; distribution transformers, whose energisation could introduce magnetising inrush currents, are not represented. The impact of such phenomena on system stability could be explored in future work.

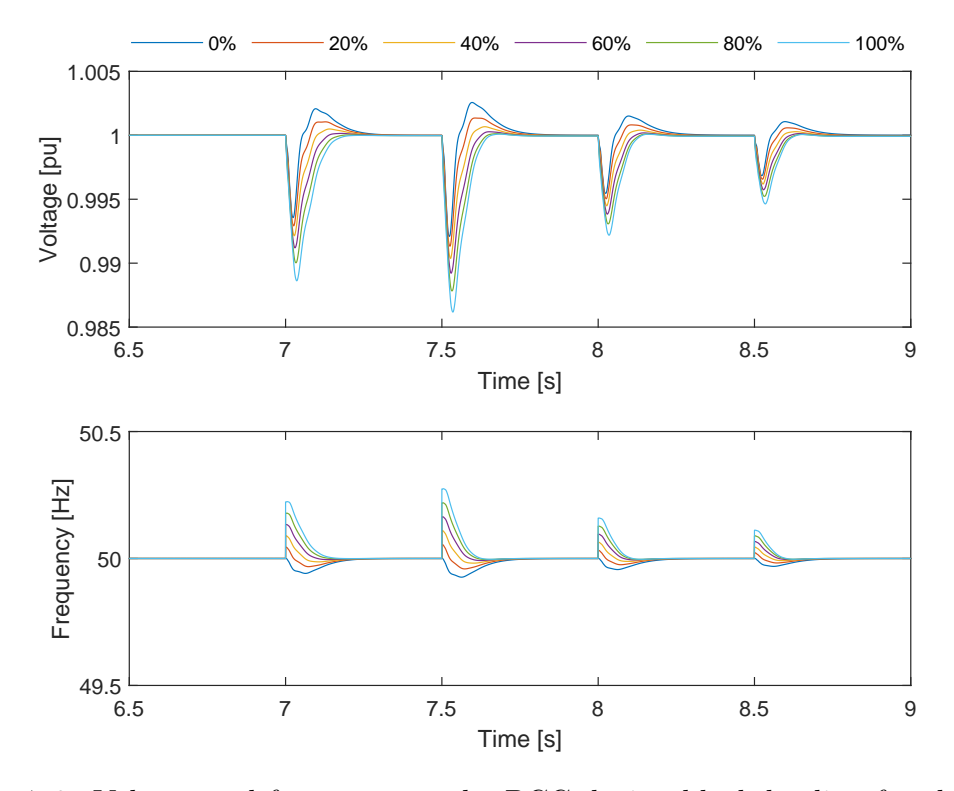


Figure 7.8: Voltage and frequency at the PCC during block loading for the different GFM penetrations (from 0% to 100%) for the top-up scenario

The frequency response similarly remains within the TSO acceptable range of 47.5 to 52 Hz, demonstrating overall stability. However, the data reveal that as the percentage of GFM penetration increases, there are higher frequency peaks. Despite these peaks, the frequency deviations are minimal and transient, quickly returning to the nominal value of 50 Hz. This suggests that while GFM contribute positively to grid stability, their increased penetration introduces minor fluctuations in frequency. This could be due to the more active role these OWPP play in frequency regulation, providing quicker but slightly more variable responses to changes in load. The presence of the external grid (represented as a grid Thevenin equivalent) buffers the system against significant frequency and

Chapter 7. Novel Grid-Forming Control Strategy for Enhanced Power System Restoration

voltage variations, enabling the OWPP to function effectively within the required operational parameters.

Regarding the anchor scenario, the block loading results were similar in that the load received the necessary power. However, the frequency and voltage responses were distinct because no external grid supported the system energisation. The top figure of 7.11 illustrates the frequency and voltage results. While the voltage remains within acceptable TSO limits, the frequency drops significantly, with the worst case occurring at 0% GFM penetration, with the frequency dropping to 42, which is not acceptable as it would trigger under frequency load shedding. Higher GFM penetration results in a smaller frequency drop due to the droop characteristics of the GFM controller.

This is because, as previously discussed in Chapter 3, a grid-following controller does not inherently provide frequency support. A grid-forming controller, however, does, due to its P/f control loop, as the virtual synchronous machine modelled in this work. As illustrated in Figure 4.2, the frequency is determined by the PI controller, which operates based on the error between the active power reference and the power measured at the point of common coupling. In practice, the measured active power depends on the instantaneous wind power available; if the available power is lower than the reference, the sustained positive error causes the PI controller to adjust the frequency until a new equilibrium is reached. If this error increases, the PI controller adjusts the frequency accordingly. This behaviour is depicted in Figure 7.9, where a frequency drop, in ramp mode, from 50 Hz to 49 Hz is shown. The blue line represents the GFL PLL frequency, active power, and voltage magnitude output, while the red line corresponds to the GFM unit.

The controllers used in this study are those outlined in Chapter 4, shown in Figures 4.1 and 4.2. It can be observed that when a frequency deviation occurs, the active power output of the GFM unit adjusts to compensate for the sudden

change, leading to an increase in current injection into the grid. In contrast, the GFL unit follows the current reference provided by its outer control loop, with these references based solely on active and reactive power, rather than frequency. Consequently, the GFL unit does not inject additional current to counterbalance the frequency deviation.

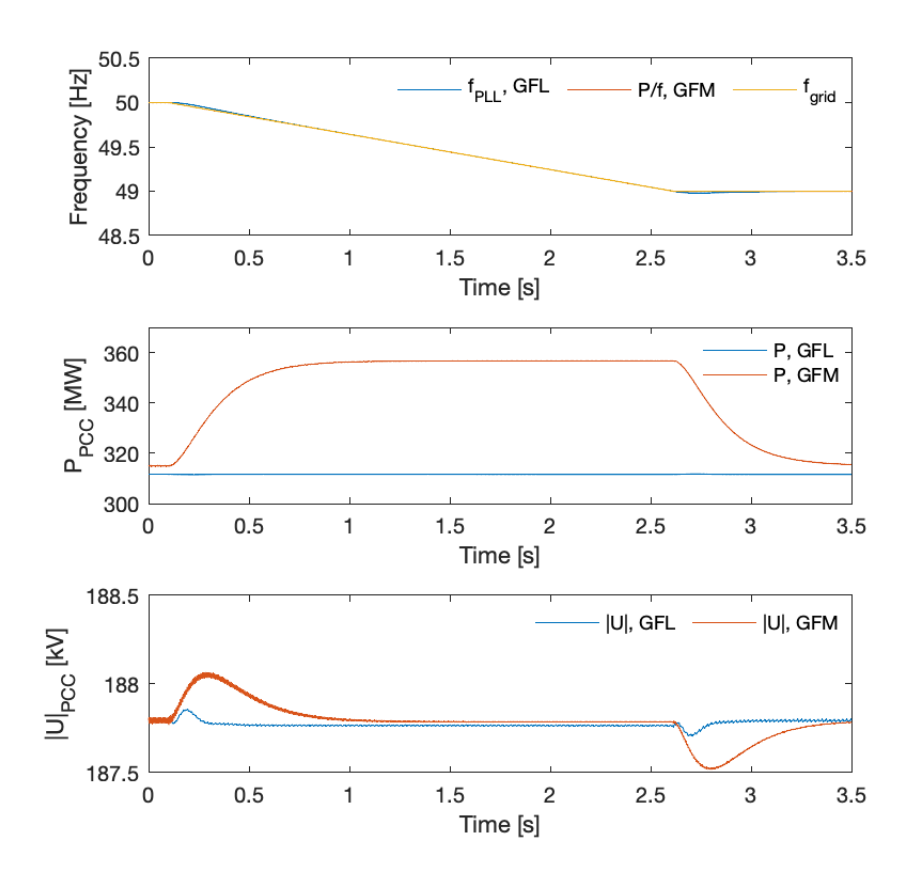


Figure 7.9: Frequency drop to compare GFM and GFL behaviour

Hence, as the results were unsatisfactory, a supervisory frequency support controller was designed which would switched on during the energisation for the anchor scenario.

This external controller provides frequency support, similar to how a governor functions in a synchronous generator. It uses a PI controller integrated with both GFM and GFL loops. The controller adjusts the active power references in both

GFM and GFL systems to keep the frequency within acceptable limits set by the TSO. The power adjustment is shared between the GFM and GFL controllers based on the level of GFM penetration, as shown in Figure 7.10. The controller reacts to frequency deviations $(f^* - f_{PCC})$ by distributing a power increment (x%) and 1 - x% of ΔP between the GFM and GFL controllers.

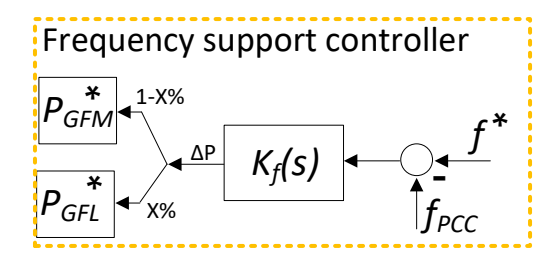


Figure 7.10: Sketch of the supervisory frequency support controller

Results may be seen in figure 7.12. This approach results in an increment in the active power reference for both controllers, ensuring that more power is injected to maintain the desired frequency and facilitate recovery from a dip following load energisation. It may be seen that this strategy mitigated the frequency deviation and the results are satisfactory for all GFM penetrations.

7.2.3 Discussion

Table 7.3 displays the final results with regards to the fulfillment of the requirements for the different GFM penetration percentages. From this table it can be seen that all the requirements were met for all GFM penetrations and for both anchor and top-up generation scenarios. It is important to note that no fault scenarios were considered in this EMT-based analysis of the power system restoration process. The focus was placed on assessing system behaviour under ideal energisation conditions for varying GFM penetration levels. How-

Chapter 7. Novel Grid-Forming Control Strategy for Enhanced Power System Restoration

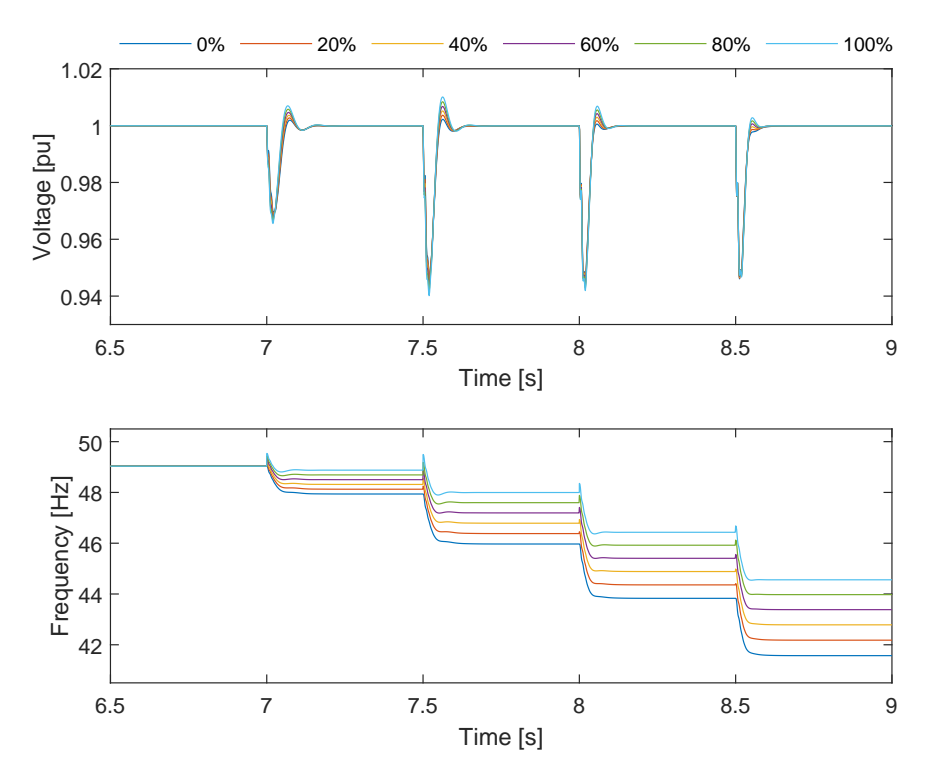


Figure 7.11: Voltage and frequency at the PCC during block loading for the different GFM penetrations (from 0% to 100%) without frequency control for the anchor scenario

ever, in practical restoration sequences, fault events, such as insulation failures or inrush-related issues, may occur and can significantly impact system stability and converter control performance. Investigating the system response under faulted conditions would be a valuable extension of this work. Future studies should consider including fault scenarios to evaluate the robustness of GFM and GFL-based control strategies under more realistic and stressed conditions.

Chapter 7. Novel Grid-Forming Control Strategy for Enhanced Power System Restoration

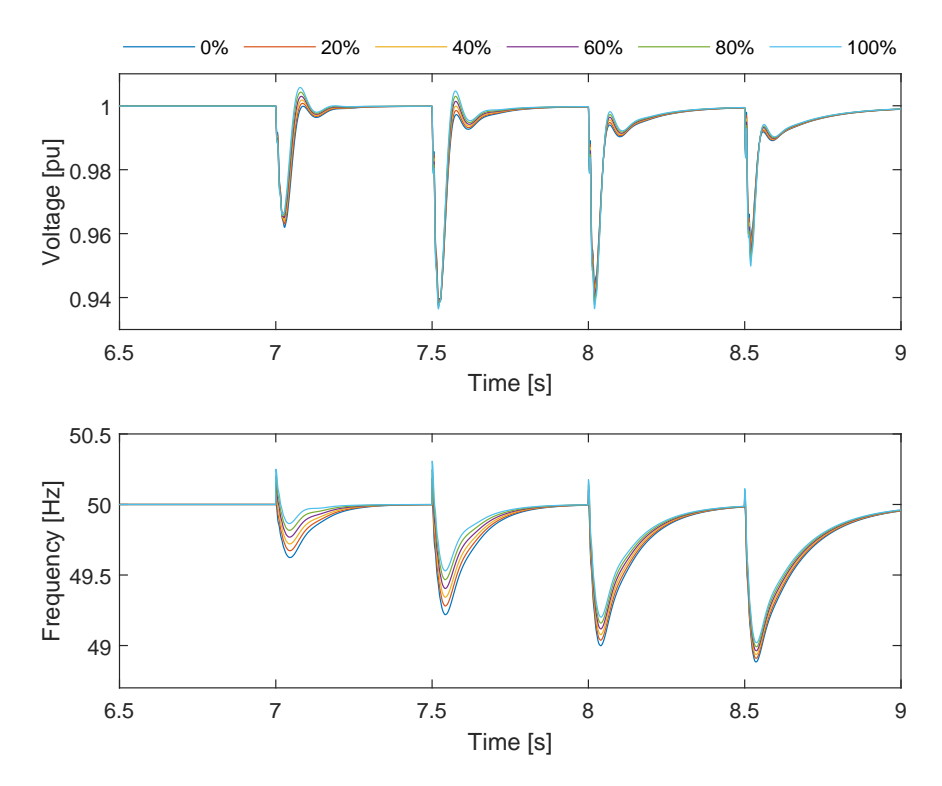


Figure 7.12: Voltage and frequency at the PCC during block loading for the different GFM penetrations (from 0% to 100%) with frequency control for the anchor scenario

Table 7.3: Top-up generation - Results of EMT simulations for different GFM penetrations

No.	0%	20%	40%	60%	80%	100%
1	✓	√	√	√	√	√
$2 f_{max}$	50	50.05	50.11	50.16	50.22	50.27
$2 f_{min}$	49.93	49.96	49.98	49.99	50.00	50.00
$3 V_{max}$	1.00	1.00	1.00	1.00	1.00	1.00
$3 V_{min}$	0.992	0.991	0.990	0.989	0.988	0.987
4	\checkmark	\checkmark	\checkmark	\checkmark	\checkmark	\checkmark
5	\checkmark	\checkmark	\checkmark	\checkmark	\checkmark	\checkmark

Chapter 7. Novel Grid-Forming Control Strategy for Enhanced Power System Restoration

Table 7.4: Anchor generation - Results of EMT simulations for different GFM penetrations

No.	0%	20%	40%	60%	80%	100%
1	√	√	√	✓	√	√
$2 f_{max}$	50	50.06	50.12	50.18	50.25	50.31
$2 f_{min}$	48.88	48.91	48.94	48.96	48.99	49.02
$3 V_{max}$	1.00	1.00	1.00	1.00	1.00	1.00
$3 V_{min}$	0.939	0.938	0.938	0.937	0.937	0.936
4	\checkmark	\checkmark	\checkmark	\checkmark	\checkmark	\checkmark
5	\checkmark	\checkmark	\checkmark	\checkmark	\checkmark	\checkmark

7.3 SSM Analysis

A small signal analysis was performed to analyse the overall stability of the power system, which includes both GFL and GFM aggregated wind farms connected to the power system. The aim of this study was to determine the best percentage of GFM penetration that offers enhanced stability and robustness during the block loading process. This study was performed for both anchor and top-up scenarios.

For this purpose, and just like for the EMT analysis displayed earlier, GFM penetration was varied from 0% to 100% in steps of 20%, and the RL load (R_{ld} and L_{ld}) was adjusted according to the provided active and reactive power values. An explanation on the computation of these parameters is available in Section 3.2.6.

This section explains the linearisation process of the system as well as its validation and then stability results for both anchor and top-up and for the different steps of block loading are expanded in terms of disk margins.

7.3.1 Model linearisation

The one-line diagram seen in figure 7.1 was the baseline utilized for this study. The BESS was only used for WT energisation purposes and thus was removed

and the model utilized for small signal studies may be seen in figure 7.13. This model serves both top-up and anchor generation: for the top-up study, the grid which is here represented as a Thevenin equivalent with R_p , L_p and the voltage source V_g is connected; for the anchor scenario, the Thevenin circuit is removed.

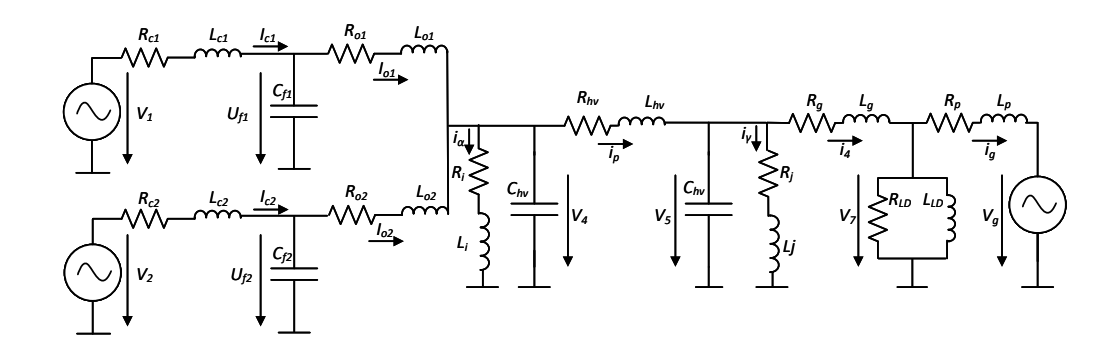


Figure 7.13: GFM and GFL converters forming the aggregated wind farms and power system for SSM analysis

The state-space model, with respect to the aggregated wind farms (considering both GFM and GFL converters), and the rest of the power system, from the offshore PCC to the electrical loads, may be seen in Appendix D.1. The difference between the top-up and anchor state space matrices is that of A_{PS} , B_{PS} , C_{PS} and D_{PS} and the wind farm matrices, represented as A_{WF} , B_{WF} , C_{WF} and D_{WF} remain the same. Essentially, and looking at figure 7.13, for the anchor analysis, the i_g current (represented in the synchronous frame as i_{gq} and i_{gd}) which flows through the grid Thevenin equivalent and the voltage source V_g (represented in the synchronous frame as v_{gq} and v_{gd}) are removed, reducing the overall size of the state space matrices.

The controllers utilized, and represented in Figures 4.1 and 4.2, were linearised the same way as explained in Chapter 4.

Chapter 7. Novel Grid-Forming Control Strategy for Enhanced Power System Restoration

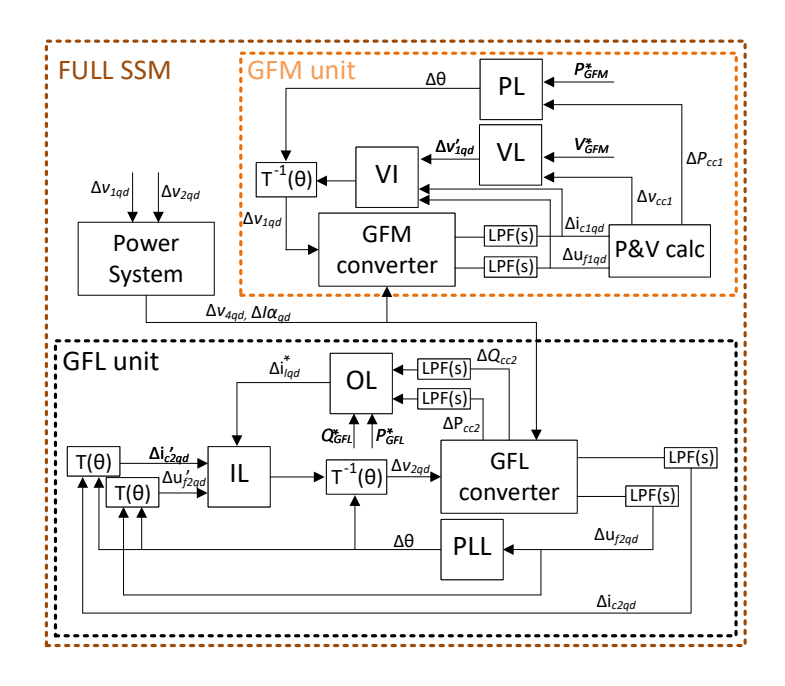


Figure 7.14: Scheme of the linearised system (SSM) with both GFM and GFL aggregated wind farms and controllers and power system

7.3.2 Small signal model validation

After developing the SSM, the first step was to validate this model by matching it against the EMT model. For this purpose, three power steps of 0.01 pu were applied to both the EMT and SSM. This may be seen in Figure 7.15 for both the GFL and GFM converters. From these figures, it is evident that the SSM consistently follows the EMT line, demonstrating that the SSM is an accurate representation of the EMT simulations.

7.3.3 Stability analysis

The small signal stability was analysed once again using disk margins. This analysis was performed for both anchor and top-up scenarios and for different steps of block loading, using the local network demand data previously used for

Chapter 7. Novel Grid-Forming Control Strategy for Enhanced Power System Restoration

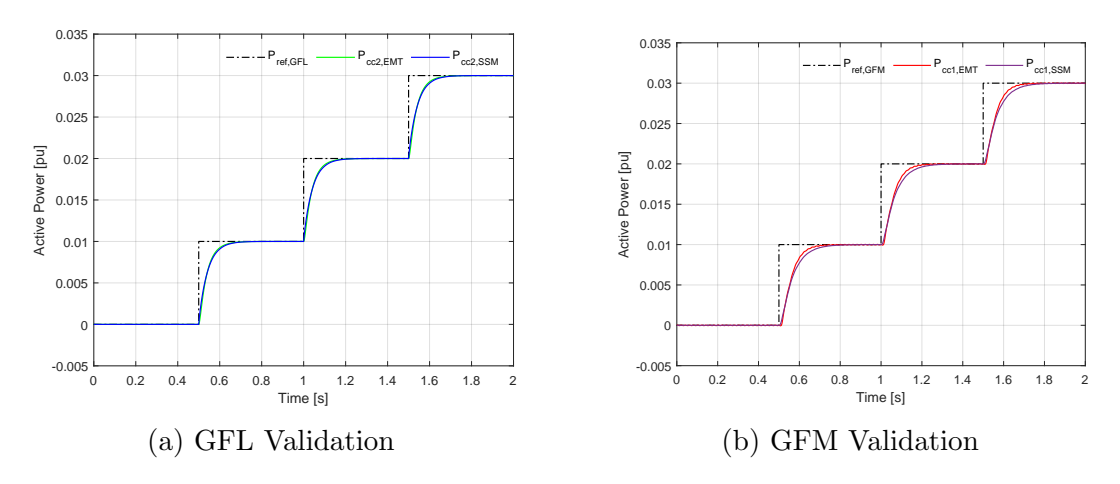


Figure 7.15: SSM validation for both GFL (left) and GFM (right) converter controllers: Active power reference, $P_{ref,GFL}$ and $P_{ref,GFM}$, PCC active power from EMT model, $P_{cc2,EMT}$ and $P_{cc1,EMT}$, and PCC active power from SSM, $P_{cc2,SSM}$ and $P_{cc1,SSM}$

the EMT simulations.

The analysis process was as follows: For both anchor and top-up scenarios, EMT simulations were conducted for different GFM penetrations (from 0% to 100%) and various loads (P1, P2, P3, P4). From these simulations, the initial conditions for the state space models were obtained. Then, the small signal model analysis was performed, retrieving DM, gain, and phase margins for each case. The stability and robustness were compared for each GFM penetration and for both top-up and anchor scenarios based on these results.

Figure 7.16 displays the disk margin results for the top-up generation scenario. In this case, a SCR of 1.5 was considered at the offshore point of common coupling, reflecting the weak grid conditions typically expected during power system restoration. A low SCR value is representative of limited system strength, which is characteristic of early restoration stages when only a small portion of the grid has been energised. The x-axis represents the GFM penetration, and the y-axis represents the active power on the load.

The results indicate that for all GFM penetrations and active power demands,

Chapter 7. Novel Grid-Forming Control Strategy for Enhanced Power System Restoration

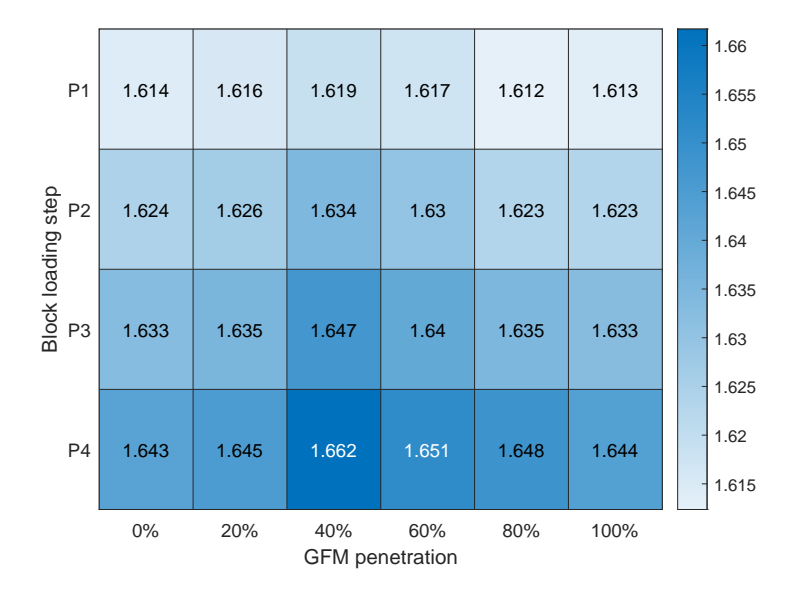


Figure 7.16: DM results for the top-up scenario

the system remains stable (DM > 0). Additionally, from P1 to P4, the DM increases, suggesting that the system becomes more stable with more loads connected. This increased stability occurs because the added loads provide more damping, which reduces the amplitude of oscillations and helps stabilize the system after a disturbance. Additionally, connecting more loads increases the overall inertia of the system, allowing it to withstand and absorb disturbances without experiencing large fluctuations in frequency or voltage.

The highest DM values are observed at 40% and 60% GFM penetration, with robustness decreasing at higher or lower percentages. Although margins differ for each GFM penetration and active power load, the variations are not significant.

The results for the anchor scenario, shown in Figure 7.17, differ from those of the top-up scenario. Firstly, it can be seen that all DM are lower. This is due to the fact that in the top-up scenario, the system is connected to an external grid, which as previously mentioned, is represented as a voltage Thevenin equivalent. The presence of this external grid increases stability margins due to the external grid support, as this source acts as a large stable voltage source, hence

helps in absorbing possible disturbances and reducing the impact of oscillations. Furthermore, this voltage source also offers more inertia and enhanced damping.

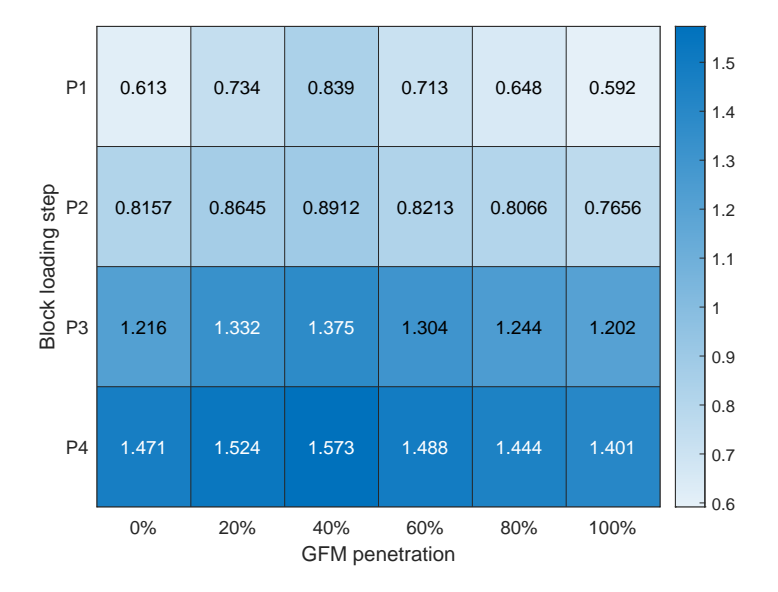


Figure 7.17: DM results for the anchor scenario

Similar to the top-up scenario, increasing connected loads leads to higher DM and greater system robustness. However, this increase is more pronounced in the anchor scenario. There is also a significant difference in margins between different GFM penetration percentages. The highest stability DM occurs at 40% penetration, followed by 20% and then 60%. Without the Thevenin equivalent of an electrical grid connected (network representation), the system has lower overall margins, and a slightly lower percentage of GFM penetration is preferred. In the absence of such external grid, the system needs a sufficient number of GFM converters to provide good robustness and stability. A percentage between 20% and 40% was seen to ensure enough inertia and control to manage the system without overburdening it with too many GFM converters. Above 40% of GFM converters, too many GFM converters can lead to over-compensation, causing control issues and reducing overall stability.

In conclusion, the stability analysis revealed that the margins are larger in the

top-up scenario as the system is connected to an external grid. This connection provides additional support, increased inertia, enhanced damping, and improved voltage and frequency regulation, all of which contribute to greater stability. In the anchor scenario, a preferred percentage of 20% to 40% of GFM converters is required. This range ensures a balance of inertia and control, avoiding over-compensation that could lead to lower stability. Conversely, in the top-up scenario, the preferred percentage of GFM converters is between 40% and 60% due to the additional support from the external grid. This support allows the system to handle a higher percentage of GFM converters, meeting the increased inertia requirement and maintaining stability under various load conditions.

7.4 Chapter Conclusions

This study provided an analysis of the potential for OWPP to contribute to PSR in the UK, particularly in the context of the shift from fossil fuels to inverter-based RES. The findings of the SIF BLADE project demonstrate that OWPP, when equipped with GFM control strategies, can support PSR by meeting technical requirements.

- Given the transition away from fossil fuels, it is necessary to explore the capability of inverter-based RES in providing essential grid services like PSR.
- The SIF BLADE project was initiated to assess the feasibility of PSR from OWPP, conducting a series of comprehensive studies.
- Steady-state analysis:
 - Evaluated OWPP ability to meet local network demands for active and reactive power.

- Confirmed OWPP could fulfill these demands with minimal adjustments, even with variations in reactive power compensation and cable lengths.
- Findings aligned with industry benchmarks and partner data, demonstrating OWPP performance under different steady-state conditions.

• EMT studies:

- Tested various GFM penetration levels (0% to 100% in 20% increments) against NG-ESO technical standards.
- Confirmed all tested levels of GFM penetration met required standards, proving OWPP feasibility under different levels of GFM integration.

• Small signal analysis:

- Determined optimal GFM penetration levels for PSR.
- For top-up generation scenarios, 40% to 60% penetration offered highest stability and robustness.
- For anchor generation scenarios, 20% to 40% penetration was recommended for optimal performance.

• External supervisory controller:

- Integrated with both GFM and GFL loops to mitigate frequency drops during load restoration.
- Adjusted active power references in response to frequency deviations,
 functioning similarly to a governor in synchronous generators.
- Designed to distribute load between GFM and GFL controllers proportionally to the GFM penetration level.

• Limitations and future work:

- Aggregated OWPP model presented challenges in synchronizing GFM and GFL units.
- Future research should develop a wind turbine-specific model to address these limitations.
- Further studies should explore transient effects from array cables and wind turbine transformers, which were not considered in this study.

• Concluding remarks:

- This research provided insights into OWPP's role in PSR as the energy sector transitions to low-carbon technologies.
- Findings demonstrate that OWPP, with optimized GFM and GFL integration, can enhance power system resilience and stability during restoration.
- Future research should refine these strategies and optimize GFM and self-start unit deployment within OWPP to fully realize their potential in providing essential grid services.

Chapter 8

Conclusions

8.1 General Conclusions

This thesis has explored some significant challenges associated with the ongoing energy transition from fossil fuels to RES, with a particular focus on OWPPs. These devices, which are being commissioned at increasing distances from shore to harness stronger winds and employ larger turbines, represent a critical component in achieving the global shift towards cleaner energy. However, this shift introduces technical challenges, particularly in providing services traditionally offered by synchronous machines. One such challenge lies in ensuring system stability, especially for OWPPs connected to the electrical grid via long submarine HVAC transmission systems.

This research has centred on comparing two key converter control strategies, GFL and GFM, to evaluate which approach is best suited to address the emerging technical challenges posed by OWPPs. Through a series of studies, this thesis has investigated the performance of these controllers under various conditions, including differing transmission distances, system configurations, and grid strengths. Moreover, the thesis has explored the potential of OWPPs to contribute to PSR, a critical service that is becoming increasingly necessary as fossil

fuel-based power plants are decommissioned.

The following conclusions can be drawn from the research conducted throughout the thesis:

- The findings demonstrate that GFM converter control generally provides superior stability and robustness compared to GFL control. This has been concluded via small signal stability analysis. The GFM controller showed enhanced capability in maintaining system stability under varying operating conditions, including changes in power output, grid strength, and transmission distance.
- GFL control was found to be more sensitive to changes in system conditions, especially at higher levels of active power injection and in weaker grids with lower SCR and X/R ratios. This sensitivity can lead to instability, particularly when dealing with weaker grids and/or longer transmission cables.
- This thesis has demonstrated that the placement of shunt reactors is critical for ensuring system stability. Various configurations of shunt reactors were analysed, and the most effective configuration was found to be reactors placed at both ends of the cable as well as at a mid-cable point. This configuration, combined with GFM control, proved to be the most robust in ensuring enhanced stability. GFL control, by contrast, was less effective in maintaining stability, particularly over longer transmission distances.
- Beyond cable length and reactive power compensation, the strength of the grid also plays a significant role in system stability. The grid strength, characterised by parameters such as SCR and X/R ratio, was shown to have a major impact on the performance of the control strategies.
- GFM control was far less sensitive to changes in grid strength compared to

GFL control. Even in weak grids with low SCR and X/R values, GFM control maintained stable operation, with no significant degradation in performance. In contrast, GFL control struggled to maintain stability in weaker grids, often becoming unstable in such conditions. This underscores the importance of using GFM control for OWPPs located at greater distances from shore or connected to weaker onshore grids.

- While GFM control offers distinct advantages in terms of stability and robustness, particularly in systems with long transmission distances or weak grids, this thesis has also highlighted the continued importance of GFL control. Specifically, GFL control plays a crucial role in the context of power system restoration (PSR), where a balanced approach involving both GFM and GFL control strategies is necessary.
- A 100% penetration of GFM control does not necessarily result in optimal stability during PSR operations. Instead, the research has shown that a combination of GFM and GFL control strategies is required to ensure reliable system restoration.
- The optimal level of GFM control penetration depends on the specific PSR scenario. For top-up generation scenarios, where additional power is injected into a grid that is already energised but weak, GFM penetration levels between 40% and 60% were found to provide the highest stability. For anchor generation scenarios, where power is restored to a completely de-energised grid, lower GFM penetration levels between 20% and 40% proved to be more effective in maintaining system stability. The GFM control parameters used in this study were tuned to optimise stability for each scenario; however, the impact of using different GFM control strategies or alternative tuning approaches was not investigated. Future studies should explore the role of different GFM controller types and tuning methods, as

these may significantly influence the optimal share of GFM during restoration. These findings emphasise the need for a flexible, adaptive approach to converter control during PSR, with both GFM and GFL controllers playing important roles depending on the specific requirements of the restoration process.

- The research has also demonstrated that OWPPs equipped with both GFM and GFL control strategies are capable of meeting the technical requirements for providing PSR services. The steady-state analysis revealed that OWPPs are able to generate a range of active and reactive power operating points capable of meeting the demands of local networks, indicating that OWPPs have the potential to contribute to grid restoration in accordance with existing technical standards.
- The use of an external frequency supervisory controller, which adjusts active power references in response to frequency deviations, hence injecting more current when required, further enhances the ability of OWPPs to provide reliable black start services. This controller was added due to the inability of the OWPP to recover from frequency dips when there is no grid available (anchor scenario). This shows that additional control loops are sufficient to ensure the reliable operation of the OWPP in case of PSR.

In conclusion, this thesis has demonstrated that GFM control is essential for maintaining stability and robustness, particularly as more renewable energy sources, like OWPPs, are integrated into the electrical system. GFM controllers offer significant advantages when dealing with long transmission distances and weak grids, making them critical for ensuring the future stability of power systems as the share of renewable energy increases. Their ability to provide system inertia and support voltage stability underscores their importance in the transition to a more sustainable energy grid. However, GFL control also remains important,

particularly in the context of PSR, where a combination of GFM and GFL controllers is required to ensure the most effective and reliable system restoration process. The integration of both control strategies is vital to guaranteeing the long-term resilience and stability of OWPPs within HVAC transmission systems.

8.2 Future Work

- While GFM wind turbines have demonstrated superiority for longer distances, the aggregated wind farm model considered either a fully GFM or fully GFL configuration. Future studies should investigate varied percentages of GFM and GFL turbines, as was done for the PSR study, to provide a more comprehensive understanding of mixed configurations.
- The PSR analysis was conducted using virtual synchronous machines as the GFM unit. However, different GFM technologies offer distinct advantages and disadvantages. Therefore, it is important to extend the PSR studies to include other types of GFM units to assess their performance under similar conditions.
- The aggregated wind farm model assumed uniform current injection from all wind turbines. A more detailed analysis should consider individual wind turbines for PSR studies, which would allow for variation in the percentage of GFM turbines across the wind farm, reflecting more realistic scenarios.
- Examining individual wind turbines in the PSR studies would also provide valuable insights into the interactions between converters, including GFM-GFL and GFM-GFM interactions, as well as the effects of transformers, such as sympathetic inrush currents, which are not captured in aggregated models.
- Additionally, the positioning of self-start GFL units within the wind farm

should be studied. Instead of focusing solely on an aggregated wind farm model, future work should explore the optimal placement of self-start units in an array of turbines, considering whether their position—whether closer to the offshore substation or further away—has an impact on restoration performance. This should also include an analysis of how many GFM self-start units are required for optimal system performance.

- [1] "Climate change: Strategies for mitigation and adaptation," The Innovation Geoscience, vol. 1, no. 1, p. 100015, 2023.
- [2] L. A. Attílio, J. R. Faria, and E. C. Silva, "Countervailing impacts of fossil fuel production and exports of electrical goods on energy transitions and climate change," *Journal of Cleaner Production*, vol. 464, no. April, 2024.
- [3] H. Hou, W. Lu, B. Liu, Z. Hassanein, H. Mahmood, and S. Khalid, "Exploring the Role of Fossil Fuels and Renewable Energy in Determining Environmental Sustainability: Evidence from OECD Countries," *Sustainability* (Switzerland), vol. 15, no. 3, 2023.
- [4] J. Delbeke and P. Vis, *Towards a climate-neutral Europe : curbing the trend*. Abingdon; New York : Routledge; Brussels: European Union, 1st editio ed., 2019.
- [5] S. Erdogan, U. K. Pata, and S. A. Solarin, "Towards carbon-neutral world: The effect of renewable energy investments and technologies in G7 countries," *Renewable and Sustainable Energy Reviews*, vol. 186, no. November 2022, p. 113683, 2023.
- [6] N. Alsagr, "Financial efficiency and its impact on renewable energy investment: Empirical evidence from advanced and emerging economies," *Journal* of Cleaner Production, vol. 401, no. October 2022, p. 136738, 2023.

- [7] Q. Hassan, P. Viktor, T. J. Al-Musawi, B. M. Ali, S. Algburi, H. M. Alzoubi, A. K. Al-Jiboory, A. Z. Sameen, H. M. Salman, and M. Jaszczur, "The renewable energy role in the global energy transformations," *Renewable Energy Focus*, vol. 48, 3 2024.
- [8] H. Ritchie and P. Rosado, "Energy mix," Our World in Data, 2020. https://ourworldindata.org/energy-mix.
- [9] S. Molla, O. Farrok, and M. J. Alam, "Electrical energy and the environment: Prospects and upcoming challenges of the world's top leading countries," 3 2024.
- [10] K. Franke, J. F. Garcia, C. Kleinschmitt, and F. Sensfuß, "Assessing world-wide future potentials of renewable electricity generation: Installable capacity, full load hours and costs," *Renewable Energy*, vol. 226, 5 2024.
- [11] H. Díaz and C. Guedes Soares, "Review of the current status, technology and future trends of offshore wind farms," *Ocean Engineering*, vol. 209, p. 107381, aug 2020.
- [12] H. Überseering and H. Taipei, "Global offshore wind report," 4 2024.
- [13] D. for Energy Security Net Zero, "Energy trends june 2024," 6 2024.
- [14] I. Komusanac, G. Brindley, D. Fraile, and L. Ramirez, "Wind energy in Europe 2021 Statistics and the outlook for 2022-2026," Tech. Rep. February, Wind Europe, 2022.
- [15] R. Williams and F. Zhao, "Gwec.net associate sponsors supporting sponsor leading sponsor," 8 2023.
- [16] M. G. Dozein, P. Mancarella, T. K. Saha, and R. Yan, "System strength and weak grids: Fundamentals, challenges, and mitigation strategies," *Aus-*

- tralasian Universities Power Engineering Conference, AUPEC 2018, pp. 1–7, 2018.
- [17] A. Adib, B. Mirafzal, X. Wang, and R. Blaabjerg, "On stability of voltage source inverters in weak grids," *IEEE Access*, vol. 6, pp. 4427–4439, 2017.
- [18] P. Tielens and D. Van Hertem, "The relevance of inertia in power systems," Renewable and Sustainable Energy Reviews, vol. 55, no. 2016, pp. 999–1009, 2016.
- [19] U. Agrawal, J. O'Brien, A. Somani, T. Mosier, and J. Dagle, "A study of the impact of reduced inertia in power systems," *Proceedings of the Annual Hawaii International Conference on System Sciences*, vol. 2020-January, pp. 3010–3017, 2020.
- [20] J. Matevosyan, B. Badrzadeh, T. Prevost, E. Quitmann, D. Ramasubramanian, H. Urdal, S. Achilles, J. Macdowell, S. H. Huang, V. Vital, J. Osullivan, and R. Quint, "Grid-forming inverters: Are they the key for high renewable penetration?," *IEEE Power and Energy Magazine*, vol. 17, no. 6, pp. 89–98, 2019.
- [21] Y. Lin, J. H. Eto, B. B. Johnson, J. D. Flicker, R. H. Lasseter, H. N. V. Pico, G. S. Seo, B. J. Pierre, A. Ellis, J. Miller, and G. Yuan, "Pathways to the next-generation power system with inverter-based resources: Challenges and recommendations," *IEEE Electrification Magazine*, vol. 10, pp. 10–21, 3 2022.
- [22] H. Urdal, R. Ierna, J. Zhu, C. Ivanov, A. Dahresobh, and D. Rostom, "System strength considerations in a converter dominated power system," IET Renewable Power Generation, vol. 9, no. 1, pp. 10–17, 2015.

- [23] H. Gu, S. Member, R. Yan, and T. Saha, "Review of system strength and inertia requirements for the national electricity market of Australia," CSEE Journal of Power and Energy Systems, vol. 5, no. 3, pp. 295–305, 2019.
- [24] R. M. Furlaneto, I. Kocar, A. Grilo-Pavani, U. Karaagac, A. Haddadi, and E. Farantatos, "Short circuit network equivalents of systems with inverterbased resources," *Electric Power Systems Research*, vol. 199, no. November 2020, p. 107314, 2021.
- [25] R. Yin, Y. Sun, S. Wang, and L. Zhang, "Stability Analysis of the Grid-Tied VSC Considering the Influence of Short Circuit Ratio and X/R," IEEE Transactions on Circuits and Systems II: Express Briefs, vol. 69, no. 1, pp. 129–133, 2022.
- [26] H. Urdal, R. Ierna, and A. J. Roscoe, "Stability challenges & solutions for power systems operating close to 100% penetration of power electronic interfaced power sources: exchange of experience between hybrid and major power systems," 3rd International Hybrid Power Systems Workshop, 2018.
- [27] D. Al Kez, A. M. Foley, F. Ahmed, and D. J. Morrow, "Overview of frequency control techniques in power systems with high inverter-based resources: Challenges and mitigation measures," *IET Smart Grid*, vol. 6, no. 5, pp. 447–469, 2023.
- [28] P. Denholm, T. Mai, R. W. Kenyon, B. Kroposki, and M. O. Malley, "Inertia and the Power Grid: A Guide Without the Spin," *National Renewable Energy Laboratory*, no. May, p. 48, 2020.
- [29] G. Xu, F. Liu, J. Hu, and T. Bi, "Coordination of wind turbines and synchronous generators for system frequency control," *Renewable Energy*, vol. 129, pp. 225–236, 2018.

- [30] G. Denis, T. Prevost, M. S. Debry, F. Xavier, X. Guillaud, and A. Menze, "The migrate project: The challenges of operating a transmission grid with only inverter-based generation. A grid-forming control improvement with transient current-limiting control," *IET Renewable Power Generation*, vol. 12, no. 5, pp. 523–529, 2018.
- [31] T. Qoria, F. Gruson, F. Colas, G. Denis, T. Prevost, and X. Guillaud, "Inertia effect and load sharing capability of grid forming converters connected to a transmission grid," *IET Conference Publications*, vol. 2019, no. CP751, 2019.
- [32] Z. Zhou, W. Wang, T. Lan, and G. M. Huang, "Dynamic performance evaluation of grid-following and grid-forming inverters for frequency support in low inertia transmission grids," in *Proceedings of 2021 IEEE PES Innovative Smart Grid Technologies Europe: Smart Grids: Toward a Carbon-Free Future, ISGT Europe 2021*, Institute of Electrical and Electronics Engineers Inc., 2021.
- [33] Q. Hu, R. Han, X. Quan, Z. Wu, C. Tang, W. Li, and W. Wang, "Grid-Forming Inverter Enabled Virtual Power Plants With Inertia Support Capability," *IEEE Transactions on Smart Grid*, vol. 13, pp. 4134–4143, sep 2022.
- [34] R. Alves, P. Jamieson, and A. Egea-Alvarez, "Clustering of electrical generators in a multirotor wind turbine with inertia emulation," in 2021 23rd European Conference on Power Electronics and Applications, EPE 2021 ECCE Europe, 2021.
- [35] O. P. Mahela, N. Gupta, M. Khosravy, and N. Patel, "Comprehensive overview of low voltage ride through methods of grid integrated wind generator," *IEEE Access*, vol. 7, pp. 99299–99326, 2019.

- [36] Y. Ma, L. Tao, X. Zhou, and X. Shi, "Analysis and Control of Fault Ride-Through Capability Improvement for Wind Energy Conversion System Using Linear Active Disturbance Rejection Control with Correction Link," *IEEE Access*, vol. 8, pp. 73816–73827, 2020.
- [37] S. M. Muyeen, R. Takahashi, T. Murata, J. Tamura, M. H. Ali, Y. Matsumura, A. Kuwayama, and T. Matsumoto, "Low voltage ride through capability enhancement of wind turbine generator system during network disturbance," *IET Renewable Power Generation*, vol. 3, no. 1, pp. 65–74, 2009.
- [38] S. Venkateswarlu, M. Janaki, R. Thirumalaivasan, and N. Prabhu, "A review on damping of torsional interactions using VSC based FACTS and subsynchronous damping controller," *Annual Reviews in Control*, vol. 46, pp. 251–264, jan 2018.
- [39] G. Muthuselvi, M. Shanmugasundaram, and B. Saravanan, "Analysis and Mitigation of Subsynchronous Resonance due to Torsional Interaction," *International Journal of Applied Engineering Research*, vol. 9, pp. 5015–5028, 2014.
- [40] V. Telukunta, J. Pradhan, A. Agrawal, M. Singh, and S. G. Srivani, "Protection challenges under bulk penetration of renewable energy resources in power systems: A review," CSEE Journal of Power and Energy Systems, vol. 3, pp. 365–379, dec 2017.
- [41] M. Andreev, A. Suvorov, A. Askarov, A. Kievets, and V. Rudnik, "Impact of renewables on relay protection operation," 2019.
- [42] Z. Guiping, D. Xiaowei, and Z. Chen, "Optimisation of reactive power compensation of HVAC cable in off-shore wind power plant," *IET Renewable Power Generation*, vol. 9, no. 7, pp. 857–863, 2015.

- [43] G. Guidi and O. B. Fosso, "Investment cost of HVAC cable reactive power compensation off-shore," 2012 IEEE International Energy Conference and Exhibition, ENERGYCON 2012, pp. 299–304, 2012.
- [44] A. Rehman, M. A. Koondhar, Z. Ali, M. Jamali, and R. A. El-Sehiemy, "Critical Issues of Optimal Reactive Power Compensation Based on an HVAC Transmission System for an Offshore Wind Farm," Sustainability (Switzerland), vol. 15, no. 19, 2023.
- [45] M. T. Alam, J. Rahaman, F. D. Dhali, and F. D. Dhali, "Technical Comparison of Modern HVAC and HVDC Transmission System Along with Cost Analysis," *Journal of Control and Instrumentation Engineering*, vol. 8, no. 1, 2022.
- [46] S. Xie, X. Wang, C. Qu, X. Wang, and J. Guo, "Impacts of different wind speed simulation methods on conditional reliability indices," *International transactions on electrical energy systems*, vol. 20, no. June 2009, pp. 1–6, 2013.
- [47] J. Dakic, M. Cheah, E. Prieto-Araujo, and O. Gomis-Bellmunt, "Optimal sizing and location of reactive power compensation in offshore HVAC transmission systems for loss minimization," 18th Wind Integration Workshop, no. October, pp. 1–6, 2019.
- [48] J. Dakic, M. Cheah-Mane, O. Gomis-Bellmunt, and E. Prieto-Araujo, "HVAC Transmission System for Offshore Wind Power Plants including Mid-Cable Reactive Power Compensation: Optimal Design and Comparison to VSC-HVDC Transmission," *IEEE Transactions on Power Delivery*, vol. 36, pp. 2814–2824, oct 2021.
- [49] J. Dakic, M. Cheah-Mane, O. Gomis-Bellmunt, and E. Prieto-Araujo, "Low frequency AC transmission systems for offshore wind power plants: Design,

- optimization and comparison to high voltage AC and high voltage DC," *International Journal of Electrical Power and Energy Systems*, vol. 133, no. May, p. 107273, 2021.
- [50] B. M. S. Hodge, H. Jain, C. Brancucci, G. S. Seo, M. Korpås, J. Kiviluoma, H. Holttinen, J. C. Smith, A. Orths, A. Estanqueiro, L. Söder, D. Flynn, T. K. Vrana, R. W. Kenyon, and B. Kroposki, "Addressing technical challenges in 100
- [51] D. Elliott, K. R. Bell, S. J. Finney, R. Adapa, C. Brozio, J. Yu, and K. Hussain, "A Comparison of AC and HVDC Options for the Connection of Offshore Wind Generation in Great Britain," *IEEE Transactions on Power Delivery*, vol. 31, no. 2, pp. 798–809, 2016.
- [52] S. Rahman, I. Khan, H. I. Alkhammash, and M. F. Nadeem, "A comparison review transmission mode for onshore integration of offshore wind farms: HVDC or HVAC," *Electronics (Switzerland)*, vol. 10, no. 12, pp. 1–15, 2021.
- [53] A. Kalair, N. Abas, and N. Khan, "Comparative study of HVAC and HVDC transmission systems," Renewable and Sustainable Energy Reviews, vol. 59, pp. 1653–1675, 2016.
- [54] H. Khalilnezhad, S. Chen, M. Popov, J. A. Bos, J. P. De Jong, and L. Van Der Sluis, "Shunt compensation design of EHV doublecircuit mixed OHLcable connections," *IET Conference Publications*, vol. 2015, no. CP668, 2015.
- [55] J. Song-Manguelle, M. H. Todorovic, S. Chi, S. K. Gunturi, and R. Datta, "Power transfer capability of HVAC cables for subsea transmission and distribution systems," *IEEE Transactions on Industry Applications*, vol. 50, no. 4, pp. 2382–2391, 2014.

- [56] K. Jansen, B. Van Hulst, C. Engelbrecht, P. Hesen, K. Velitsikakis, and C. Lakenbrink, "Resonances due to long HVAC offshore cable connections: Studies to verify the immunity of Dutch transmission network," 2015 IEEE Eindhoven PowerTech, PowerTech 2015, pp. 1–6, 2015.
- [57] V. Mytilinou and A. J. Kolios, "Techno-economic optimisation of offshore wind farms based on life cycle cost analysis on the UK," *Renewable Energy*, vol. 132, pp. 439–454, 2019.
- [58] B. Gustavsen and O. Mo, "Variable transmission voltage for loss minimization in long offshore wind farm AC export cables," *IEEE Transactions on Power Delivery*, vol. 32, no. 3, pp. 1422–1431, 2017.
- [59] X. W. Dui and G. P. Zhu, "Reactive compensation research of HVAC cables for offshore wind farms," Advanced Materials Research, vol. 986-987, pp. 433-438, 2014.
- [60] M. H. Rashid, Power Electronics Handbook. Elsevier Inc., 2011.
- [61] E. Di Bartolomeo, A. Di Giulio, F. Palone, M. Rebolini, and V. Iuliani, "Terminal stations design for submarine HVAC links Capri-Italy and Malta-Sicily interconnections," 2015 AEIT International Annual Conference, AEIT 2015, no. October, 2015.
- [62] S. Lauria and F. Palone, "Optimal operation of long inhomogeneous AC cable lines: The malta-sicily interconnector," *IEEE Transactions on Power Delivery*, vol. 29, no. 3, pp. 1036–1044, 2014.
- [63] V. Mytilinou and A. J. Kolios, "Techno-economic optimisation of offshore wind farms based on life cycle cost analysis on the UK," *Renewable Energy*, vol. 132, pp. 439–454, 2019.

- [64] S. Lauria, M. Schembari, F. Palone, and M. Maccioni, "Very long distance connection of gigawattsize offshore wind farms: Extra high-voltage AC versus high-voltage DC cost comparison," *IET Renewable Power Generation*, vol. 10, no. 5, pp. 713–720, 2016.
- [65] W. Wiechowski and P. B. Eriksen, "Selected studies on offshore wind farm cable connections - challenges and experience of the Danish TSO," IEEE Power and Energy Society 2008 General Meeting: Conversion and Delivery of Electrical Energy in the 21st Century, PES, 2008.
- [66] D. Pagnam, L. H. Kocewiak, J. Hjerrild, F. Blaabjerg, and C. L. Bak, "Overview of Black Start Provision by Offshore Wind Farms," *IECON Proceedings (Industrial Electronics Conference)*, vol. 2020-October, pp. 1892–1898, 2020.
- [67] C. R. (EU), "Establishing a network code on requirements for grid connection of generators."
- [68] National Grid ESO, "Black Start from Non-Traditional Generation Technologies," tech. rep., 2019.
- [69] N. G. ESO, "Gc0156: Facilitating the implementation of the electricity system restoration standard," 2023.
- [70] A. Jain, J. N. Sakamuri, K. Das, Ö. Göksu, and N. A. Cutululis, "Functional Requirements for Blackstart and Power System Restoration from Wind Power Plants," 2nd International Conference on Large-Scale Grid Integration of Renewable Energy in India, 2019.
- [71] J. Su, P. Dehghanian, M. Nazemi, and B. Wang, "Distributed Wind Power Resources for Enhanced Power Grid Resilience," 51st North American Power Symposium, NAPS 2019, pp. 1–6, 2019.

- [72] N. Ganganath, J. V. Wang, X. Xu, C. T. Cheng, and C. K. Tse, "Agglomerative clustering-based network partitioning for parallel power system restoration," *IEEE Transactions on Industrial Informatics*, vol. 14, no. 8, pp. 3325–3333, 2018.
- [73] H. Khoshkhoo, M. Khalilifar, and S. M. Shahrtash, "Survey of Power System Restoration Documents Issued from 2016 to 2021," *International Transactions on Electrical Energy Systems*, vol. 2022, 2022.
- [74] J. W. Feltes and C. Grande-Moran, "Black start studies for system restoration," *IEEE Power and Energy Society 2008 General Meeting: Conversion and Delivery of Electrical Energy in the 21st Century, PES*, pp. 1–8, 2008.
- [75] H. Jain, G. S. Seo, E. Lockhart, V. Gevorgian, and B. Kroposki, "Blackstart of power grids with inverter-based resources," *IEEE Power and Energy* Society General Meeting, vol. 2020-Augus, no. February, 2020.
- [76] Y. O. Udoakah, S. Khalaf, and L. Cipcigan, "Blackout and Black Start Analysis for Improved Power System Resilience: The African Experience," 2020 IEEE PES/IAS PowerAfrica, PowerAfrica 2020, pp. 0–4, 2020.
- [77] Y. Liu, R. Fan, and V. Terzija, "Power system restoration: a literature review from 2006 to 2016," Journal of Modern Power Systems and Clean Energy, vol. 4, no. 3, pp. 332–341, 2016.
- [78] Q. Hassan, P. Viktor, T. J. Al-Musawi, B. Mahmood Ali, S. Algburi, H. M. Alzoubi, A. Khudhair Al-Jiboory, A. Zuhair Sameen, H. M. Salman, and M. Jaszczur, "The renewable energy role in the global energy Transformations," *Renewable Energy Focus*, vol. 48, no. December 2023, p. 100545, 2024.
- [79] T. Letcher, Wind Energy Engineering: A Handbook for Onshore and Offshore Wind Turbines. Elsevier Inc., 2023.

- [80] L. W. Oliveira, E. J. Oliveira, I. C. Silva, F. V. Gomes, T. T. Borges, A. L. Marcato, and A. R. Oliveira, "Optimal restoration of power distribution system through particle swarm optimization," 2015 IEEE Eindhoven PowerTech, PowerTech 2015, no. June, 2015.
- [81] D. Pagnani, F. Blaabjerg, C. L. Bak, F. M. F. Da Silva, L. H. Kocewiak, and J. Hjerrild, "Offshore wind farm black start service integration: Review and outlook of ongoing research," *Energies*, vol. 13, no. 23, 2020.
- [82] S. Golestan, J. M. Guerrero, F. Musavi, and J. C. Vasquez, "Single-phase frequency-locked loops: A comprehensive review," *IEEE Transactions on Power Electronics*, vol. 34, pp. 11791–11812, 12 2019.
- [83] R. Aljarrah, B. B. Fawaz, Q. Salem, M. Karimi, H. Marzooghi, and R. Azizipanah-Abarghooee, "Issues and challenges of grid-following converters interfacing renewable energy sources in low inertia systems: A review," *IEEE Access*, vol. 12, pp. 5534–5561, 2024.
- [84] N. B. Lai, A. Tarraso, G. N. Baltas, L. V. M. Arevalo, and P. Rodriguez, "External inertia emulation controller for grid-following power converter," IEEE Transactions on Industry Applications, vol. 57, pp. 6568–6576, 2021.
- [85] D. W. Sun, H. Liu, P. Song, S. Zhu, and Z. Wei, "Small-signal modelling and stability analysis of current-controlled virtual synchronous generators," in *IOP Conference Series: Earth and Environmental Science*, vol. 192, Institute of Physics Publishing, 11 2018.
- [86] M. Elkhatib, W. Du, and R. Lassester, "Evaluation of inverter-based grid frequency support using frequency-watt and grid-forming pv inverters," in 2018 IEEE Power Energy Society General Meeting (PESGM), IEEE, 12 2018.

- [87] B. K. Poolla, D. Groß, and F. Dörfler, "Placement and implementation of grid-forming and grid-following virtual inertia and fast frequency response," *IEEE Transactions on Power Systems*, vol. 34, pp. 3035–3046, 7 2019.
- [88] J. Zhu, C. D. Booth, G. P. Adam, A. J. Roscoe, and C. G. Bright, "Inertia emulation control strategy for vsc-hvdc transmission systems," *IEEE Transactions on Power Systems*, vol. 28, pp. 1277–1287, 2013.
- [89] J. Fang, H. Li, Y. Tang, and F. Blaabjerg, "Distributed power system virtual inertia implemented by grid-connected power converters," *IEEE Transactions on Power Electronics*, vol. 33, pp. 8488–8499, 10 2018.
- [90] A. Sajadi, J. A. Ranola, R. W. Kenyon, B. M. Hodge, and B. Mather, "Dynamics and stability of power systems with high shares of grid-following inverter-based resources: A tutorial," *IEEE Access*, vol. 11, pp. 29591– 29613, 2023.
- [91] D. Pattabiraman, R. H. Lasseter, and T. M. Jahns, "Comparison of Grid Following and Grid Forming Control for a High Inverter Penetration Power System," *IEEE Power and Energy Society General Meeting*, vol. 2018-Augus, pp. 3–7, 2018.
- [92] S. F. Zarei, H. Mokhtari, M. A. Ghasemi, S. Peyghami, P. Davari, and F. Blaabjerg, "Control of grid-following inverters under unbalanced grid conditions," *IEEE Transactions on Energy Conversion*, vol. 35, pp. 184– 192, 3 2020.
- [93] C. Zhang, X. Dou, L. Wang, Y. Dong, and Y. Ji, "Distributed cooperative voltage control for grid-following and grid-forming distributed generators in islanded microgrids," *IEEE Transactions on Power Systems*, vol. 38, pp. 589–602, 1 2023.

- [94] C. Henderson, "Interactions of grid-forming converters for windfarm applications," 2023.
- [95] B. Fan, T. Liu, F. Zhao, H. Wu, and X. Wang, "A review of current-limiting control of grid-forming inverters under symmetrical disturbances," 2022.
- [96] S. D. Arco and J. A. Suul, "Virtual synchronous machines-classification of implementations and analysis of equivalence to droop controllers for microgrids."
- [97] W. Du, Z. Chen, K. P. Schneider, R. H. Lasseter, S. Pushpak Nandanoori, F. K. Tuffner, and S. Kundu, "A Comparative Study of Two Widely Used Grid-Forming Droop Controls on Microgrid Small-Signal Stability," *IEEE Journal of Emerging and Selected Topics in Power Electronics*, vol. 8, no. 2, pp. 963–975, 2020.
- [98] Q. C. Zhong and G. Weiss, "Synchronverters: Inverters that mimic synchronous generators," *IEEE Transactions on Industrial Electronics*, vol. 58, pp. 1259–1267, 4 2011.
- [99] H. P. Beck and R. Hesse, "Virtual synchronous machine," 2007 9th International Conference on Electrical Power Quality and Utilisation, EPQU, 2007.
- [100] E. Ebinyu, O. Abdel-Rahim, D. E. A. Mansour, M. Shoyama, and S. M. Abdelkader, "Grid-forming control: Advancements towards 100% inverter-based grids—a review," 11 2023.
- [101] H. Zhang, W. Xiang, W. Lin, and J. Wen, "Grid forming converters in renewable energy sources dominated power grid: Control strategy, stability, application, and challenges," *Journal of Modern Power Systems and Clean Energy*, vol. 9, pp. 1239–1256, 11 2021.

- [102] G. Song, B. Cao, and L. Chang, "Review of Grid-forming Inverters in Support of Power System Operation," *Chinese Journal of Electrical Engineering*, vol. 8, no. 1, pp. 1–15, 2022.
- [103] P. Unruh, M. Nuschke, P. Strauß, and F. Welck, "Overview on grid-forming inverter control methods," *Energies*, vol. 13, no. 10, 2020.
- [104] J. Rocabert, A. Luna, F. Blaabjerg, and P. Rodríguez, "Control of power converters in ac microgrids," *IEEE Transactions on Power Electronics*, vol. 27, pp. 4734–4749, 2012.
- [105] M. Paolone, T. Gaunt, X. Guillaud, M. Liserre, S. Meliopoulos, A. Monti, T. V. Cutsem, V. Vittal, and C. Vournas, "Fundamentals of power systems modelling in the presence of converter-interfaced generation," *Electric Power Systems Research*, vol. 189, 12 2020.
- [106] Y. Teng, W. Deng, W. Pei, Y. Li, L. Ding, and H. Ye, "Review on grid-forming converter control methods in high-proportion renewable energy power systems," *Global Energy Interconnection*, vol. 5, pp. 328–342, 6 2022.
- [107] A. Tayyebi, F. Dörfler, F. K. Ait, E. Z. Austria, and E. Z. Switzerland, "Grid-forming converters-inevitability, control strategies and challenges in future grids application," 2018.
- [108] L. Zhang, L. Harnefors, and H. P. Nee, "Power-synchronization control of grid-connected voltage-source converters," *IEEE Transactions on Power Systems*, vol. 25, pp. 809–820, 5 2010.
- [109] D. Remon, A. Cantarellas, E. Rakhshani, I. Candela, and P. Rodriguez, "An active power synchronization control loop for grid-connected converters," in 2014 IEEE PES General Meeting Conference Exposition, [publisher not identified], 10 2014.

- [110] S. Vazquez, J. A. Sanchez, J. M. Carrasco, J. I. Leon, and E. Galvan, "A model-based direct power control for three-phase power converters," *IEEE Transactions on Industrial Electronics*, vol. 55, pp. 1647–1657, 4 2008.
- [111] N. Muangruk and S. Nungam, "Direct power control of three-phase voltage source converters using feedback linearization technique," in *Procedia Computer Science*, vol. 86, pp. 365–368, Elsevier B.V., 2016.
- [112] B. B. Johnson, M. Sinha, N. G. Ainsworth, F. Dorfler, and S. V. Dhople, "Synthesizing virtual oscillators to control islanded inverters," *IEEE Transactions on Power Electronics*, vol. 31, pp. 6002–6015, 8 2016.
- [113] B. Johnson, M. Rodriguez, M. Sinha, and S. Dhople, "Comparison of virtual oscillator and droop control," 2017 IEEE 18th Workshop on Control and Modeling for Power Electronics, COMPEL 2017, 8 2017.
- [114] M. Lu, S. Dutta, V. Purba, S. Dhople, and B. Johnson, "A grid-compatible virtual oscillator controller: Analysis and design," 2019 IEEE Energy Conversion Congress and Exposition, ECCE 2019, pp. 2643–2649, 9 2019.
- [115] D. Raisz, T. T. Thai, and A. Monti, "Power control of virtual oscillator controlled inverters in grid-connected mode," *IEEE Transactions on Power Electronics*, vol. 34, pp. 5916–5926, 6 2019.
- [116] D. Sun, H. Liu, S. Gao, L. Wu, P. Song, and X. Wang, "Comparison of different virtual inertia control methods for inverter-based generators," Journal of Modern Power Systems and Clean Energy, vol. 8, pp. 768–777, 7 2020.
- [117] Y. Chen, R. Hesse, D. Turschner, and H. P. Beck, "Improving the grid power quality using virtual synchronous machines," *International Conference on Power Engineering, Energy and Electrical Drives*, no. May, pp. 1–6, 2011.

- [118] B. Muftau and M. Fazeli, "The Role of Virtual Synchronous Machines in Future Power Systems: A Review and Future Trends," may 2022.
- [119] K. M. Cheema, "A comprehensive review of virtual synchronous generator," International Journal of Electrical Power Energy Systems, vol. 120, p. 106006, sep 2020.
- [120] D. B. Rathnayake, M. Akrami, C. Phurailatpam, S. P. Me, S. Hadavi, G. Jayasinghe, S. Zabihi, and B. Bahrani, "Grid Forming Inverter Modeling, Control, and Applications," *IEEE Access*, vol. 9, pp. 114781–114807, 2021.
- [121] K. Sakimoto, Y. Miura, and T. Ise, "Stabilization of a power system with a distributed generator by a Virtual Synchronous Generator function," 8th International Conference on Power Electronics - ECCE Asia: "Green World with Power Electronics", ICPE 2011-ECCE Asia, no. 2, pp. 1498– 1505, 2011.
- [122] M. Ashabani and J. Jung, "Synchronous voltage controllers: Voltage-based emulation of synchronous machines for the integration of renewable energy sources," *IEEE Access*, vol. 8, pp. 49497–49508, 2020.
- [123] A. Abdelrahim, M. Smailes, K. Ahmed, P. McKeever, and A. Egea-Alvarez, "Modified grid forming converter controller with fault ride through capability without PLL or current loop," 18th Wind Integration Workshop, no. October, pp. 1–8, 2019.
- [124] L. Li, R. Teichmann, C. Wang, and W. Yang, "Method, apparatus and computer program product for wind turbine start-up and operation without grid power," 10 2006.
- [125] T. Edenfeld, "Use of pitch battery power to start wind turbine during grid loss/black start capability," 7 2011.

- [126] C. Damgaard, L. Bede, and A. E. Maarbjerg, "Wind turbine with integrated battery storage," 5 2019.
- [127] R. Burra, R. Delmerico, R. Teichmann, A. Jain, and M. Shu, "Wind turbine energy storage and frequency control," 9 2008.
- [128] L. A. Gomez, A. P. Grilo, M. B. Salles, and A. J. Filho, "Combined control of dfig-based wind turbine and battery energy storage system for frequency response in microgrids," *Energies*, vol. 13, 2020.
- [129] Y. Tang, J. Dai, Q. Wang, and Y. Feng, "Frequency control strategy for black starts via pmsg-based wind power generation," *Energies*, vol. 10, 2017.
- [130] A. Das, A. K. Kar, C. Kumar, Mayur, U. Kumar, A. Verma, S. Pal, A. Joseph, B. Das, P. R. Kasari, A. Chakrabarti, and S. Bhattacharjee, "Tsbc converter with bess for dfig-based wind energy conversion system," *IEEE Transactions on Industry Applications*, vol. 56, pp. 6158–6173, 11 2020.
- [131] B. Hamid, I. Hussain, S. J. Iqbal, B. Singh, S. Das, and N. Kumar, "Optimal mppt and bes control for grid-tied dfig-based wind energy conversion system," *IEEE Transactions on Industry Applications*, vol. 58, pp. 7966–7977, 2022.
- [132] C. L. Nguyen and H. H. Lee, "A novel dual-battery energy storage system for wind power applications," *IEEE Transactions on Industrial Electronics*, vol. 63, pp. 6136–6147, 10 2016.
- [133] A. Yazdani and R. Iravani, Voltage-Sourced Converters in Power Systems: Modeling, Control, and Applications. Wiley-IEEE Press, 2010.

- [134] S. Ebrahimi and J. Jatskevich, "Average-Value Model for Voltage-Source Converters With Direct Interfacing in EMTP-Type Solution," *IEEE Trans*actions on Energy Conversion, vol. 38, pp. 2231–2234, sep 2023.
- [135] G. Amico, "Wind farm high frequency electrical resonances: impedance-based stability analysis and mitigation techniques," 2019.
- [136] L. P. Kunjumuhammed, B. C. Pal, C. Oates, and K. J. Dyke, "The adequacy of the present practice in dynamic aggregated modeling of wind farm systems," *IEEE Transactions on Sustainable Energy*, vol. 8, pp. 23–32, 1 2017.
- [137] P. Kundur, Power Systems Stability and Control. Electric Power Research Institute, 1994.
- [138] J. Song, M. Cheah-Mane, E. Prieto-Araujo, J. Amoros, and O. Gomis-Bellmunt, "Grid Equivalent Representation of Power Systems With Penetration of Power Electronics," *IEEE Transactions on Power Delivery*, vol. 38, no. 4, pp. 2742–2756, 2023.
- [139] "Electricity transmission costing study."
- [140] "National grid msip: 200 mvar shunt reactor benchmark (stocksbridge 400 kv)."
- [141] "100 mvar variable shunt reactor commissioned at mraclin substation."
- [142] "Seagreen offshore substation platform cost assessment (indicative transfer value)."
- [143] "Guide to an offshore wind farm: Cost breakdown."
- [144] T. Van Cutsem and C. Vournas, "Voltage stability of electric power systems," *Voltage Stability of Electric Power Systems*, pp. 1–378, 2008.

- [145] A. Egea-Alvarez, S. Fekriasl, F. Hassan, and O. Gomis-Bellmunt, "Advanced Vector Control for Voltage Source Converters Connected to Weak Grids," *IEEE Transactions on Power Systems*, vol. 30, no. 6, pp. 3072–3081, 2015.
- [146] S.-K. Chung, "A phase tracking system for three phase utility interface inverters," 2000.
- [147] L. Harnefors and H.-P. Nee, "Model-based current control of ac machines using the internal model control method," *IEEE TRANSACTIONS ON INDUSTRY APPLICATIONS*, vol. 34, pp. 133–141, 2 1998.
- [148] A. D. Paquette and D. M. Divan, "Virtual Impedance Current Limiting for Inverters in Microgrids With Synchronous Generators," *IEEE Transactions* on Industry Applications, vol. 51, no. 2, pp. 1630–1638, 2015.
- [149] X. Lu, J. Wang, J. M. Guerrero, and D. Zhao, "Virtual-impedance-based fault current limiters for inverter dominated AC microgrids," *IEEE Trans*actions on Smart Grid, vol. 9, no. 3, pp. 1599–1612, 2018.
- [150] X. Wang, Y. W. Li, F. Blaabjerg, and P. C. Loh, "Virtual-Impedance-Based Control for Voltage-Source and Current-Source Converters," *IEEE Transactions on Power Electronics*, vol. 30, no. 12, pp. 7019–7037, 2015.
- [151] A. Rodriguez-Cabero, J. Roldan-Perez, and M. Prodanovic, "Virtual Impedance Design Considerations for Virtual Synchronous Machines in Weak Grids," *IEEE Journal of Emerging and Selected Topics in Power Electronics*, vol. 8, no. 2, pp. 1477–1489, 2020.
- [152] W. Du, Z. Chen, K. P. Schneider, R. H. Lasseter, S. Pushpak Nandanoori, F. K. Tuffner, and S. Kundu, "A Comparative Study of Two Widely Used Grid-Forming Droop Controls on Microgrid Small-Signal Stability," *IEEE*

- Journal of Emerging and Selected Topics in Power Electronics, vol. 8, no. 2, pp. 963–975, 2020.
- [153] C. Henderson, A. Egea-Alvarez, S. Fekriasl, T. Knueppel, G. Amico, and L. Xu, "The Effect of Grid-Connected Converter Control Topology on the Diagonal Dominance of Converter Output Impedance," *IEEE Open Access Journal of Power and Energy*, vol. 10, no. September, pp. 617–628, 2023.
- [154] C. Henderson, A. Egea-Alvarez, and L. Xu, "Analysis of optimal grid-forming converter penetration in AC connected offshore wind farms," *International Journal of Electrical Power and Energy Systems*, vol. 157, no. August 2023, p. 109851, 2024.
- [155] C. Henderson, A. Egea-Alvarez, and L. Xu, "Analysis of multi-converter network impedance using MIMO stability criterion for multi-loop systems," *Electric Power Systems Research*, vol. 211, p. 108542, oct 2022.
- [156] P. Seiler, A. Packard, and P. Gahinet, "An Introduction to Disk Margins [Lecture Notes]," *IEEE Control Systems*, vol. 40, pp. 78–95, oct 2020.
- [157] R. Alves, A. Egea-Alvarez, and T. Knuppel, "Grid forming and grid following comparison for an offshore wind farm connected via a HVAC cable," 21st Wind Solar Integration Workshop (WIW 2022), pp. 9–16, 2022.
- [158] Y. Zuo, Z. Yuan, F. Sossan, A. Zecchino, R. Cherkaoui, and M. Paolone, "Performance assessment of grid-forming and grid-following converterinterfaced battery energy storage systems on frequency regulation in lowinertia power grids," Sustainable Energy, Grids and Networks, vol. 27, p. 100496, 2021.
- [159] A. Jain, J. Sakamuri, and N. Cutululis, "Grid-forming control strategies for blackstart by offshore wind farms," Wind Energy Science Discussions, no. March, pp. 1–22, 2020.

- [160] Z. Wang, R. Hibberts-Caswell, and L. Oprea, "Comparison of Grid-Following and Grid-Forming Control in Weak AC System," pp. 1–5, feb 2022.
- [161] W. Du, F. K. Tuffner, K. P. Schneider, R. H. Lasseter, J. Xie, Z. Chen, and B. Bhattarai, "Modeling of Grid-Forming and Grid-Following Inverters for Dynamic Simulation of Large-Scale Distribution Systems," *IEEE Transactions on Power Delivery*, vol. 36, pp. 2035–2045, aug 2021.
- [162] R. Rosso, S. Engelken, and M. Liserre, "Robust Stability Investigation of the Interactions among Grid-Forming and Grid-Following Converters," *IEEE Journal of Emerging and Selected Topics in Power Electronics*, vol. 8, pp. 991–1003, jun 2020.
- [163] B. Chatterjee and R. B. Seshadri, Linear Control Theory, vol. 10. 2009.
- [164] J. F. Morris, K. H. Ahmed, and A. Egea, "Standardized Assessment Framework for Design and Operation of Weak AC Grid-Connected VSC Controllers," *IEEE Access*, vol. 9, pp. 95282–95293, 2021.
- [165] W. Teng, H. Wang, and Y. Jia, "Construction and control strategy research of black start unit containing wind farm," *IEEE Region 10 Annual Interna*tional Conference, Proceedings/TENCON, vol. 2016-Janua, no. 51177092, 2016.
- [166] A. Giampieri, J. Ling-Chin, and A. P. Roskilly, "Techno-economic assessment of offshore wind-to-hydrogen scenarios: A UK case study," *International Journal of Hydrogen Energy*, no. xxxx, 2023.
- [167] PROMOTioN Progress on Meshed HVDC Offshore Transmission Networks, "Deliverable 3.7: Compliance evaluation results using simulations," tech. rep., PROMOTioN Progress on Meshed HVDC Offshore Transmission Networks, 2020.

- [168] PROMOTioN Progress on Meshed HVDC Offshore Transmission Networks, "Deliverable 2.4 Requirement recommendations to adapt and extend existing grid codes," tech. rep., 2020.
- [169] Carbon Trust, "Black Start Demonstration from Offshore Wind (SIF BLADE)," 2023.
- [170] O. Göksu, O. Saborío-Romano, N. A. Cutululis, and P. Sørensen, "Black start and island operation capabilities of wind power plants," Proc. 16th Wind Integration Workshop, no. October, pp. 25–27, 2017.
- [171] R. Teichmann, L. Li, C. Wang, and W. Yang, "Method, apparatus and computer program product for wind turbine start-up and operation without grid power, PatentNo.," 2008.
- [172] L. Yu, R. Li, and L. Xu, "Distributed PLL-Based Control of Offshore Wind Turbines Connected with Diode-Rectifier-Based HVDC Systems," *IEEE Transactions on Power Delivery*, vol. 33, no. 3, pp. 1328–1336, 2018.
- [173] P. Egedal, S. Kumar, and K. S. Nielsen, "Black start of wind turbine devices," 2016.
- [174] J. Z. Tee, I. L. H. Lim, K. Zhou, and O. Anaya-Lara, "Transient Stability Analysis of Offshore Wind with OG Platforms and an Energy Storage System," *IEEE Power and Energy Society General Meeting*, vol. 2020-August, pp. 1–5, 2020.
- [175] S. Chapaloglou, D. Varagnolo, and E. Tedeschi, "Techno-Economic Evaluation of the Sizing and Operation of Battery Storage for Isolated Oil and Gas Platforms with High Wind Power Penetration," IECON Proceedings (Industrial Electronics Conference), vol. 2019-October, pp. 4587–4592, 2019.

- [176] J. Z. Tee, I. Li Hong Lim, J. Yang, C. T. Choo, O. Anaya-Lara, and C. K. Chui, "Power system stability of offshore wind with an energy storage to electrify OG platform," *IEEE Region 10 Annual International Conference*, Proceedings/TENCON, vol. 2020-November, pp. 146–151, 2020.
- [177] A. A. Adeyemo and E. Tedeschi, "Technology Suitability Assessment of Battery Energy Storage System for High-Energy Applications on Offshore Oil and Gas Platforms," *Energies*, vol. 16, no. 18, 2023.
- [178] T. Jing Zhong, Development and Analysis of Hybrid Renewable Energy System for Offshore Oil and Gas Rigs. PhD thesis, University of Glasgow, 2022.
- [179] X. Huang and Y. Chen, "Hybrid Auxiliary Power Supply System for Offshore Wind Farm," Journal of Physics: Conference Series, vol. 1102, no. 1, 2018.
- [180] T. K. Chau, S. Shenglong Yu, T. Fernando, H. H. C. Iu, and M. Small, "An investigation of the impact of pv penetration and BESS capacity on islanded microgrids-a small-signal based analytical approach," *Proceedings* of the IEEE International Conference on Industrial Technology, vol. 2019-February, no. i, pp. 1679–1684, 2019.
- [181] D. J. Lee and L. Wang, "Small-signal stability analysis of an autonomous hybrid renewable energy power generation/energy storage system part I: Time-domain simulations," *IEEE Transactions on Energy Conversion*, vol. 23, no. 1, pp. 311–320, 2008.
- [182] R. Alves, A. Egea-Alvarez, and T. Knuppel, "Capabilities and limitations of black start operation for system restoration from offshore wind farms," 4th International Conference on Smart Grid and Renewable Energy, SGRE 2024 - Proceedings, pp. 1–6, 2024.

- [183] "Appendix 1 technical requirements and assessment criteria for the esr wind tender 2022," 2022.
- [184] "Lautec esox run weather downtime simulations."
- [185] F. M. F. da Silva, "Analysis and simulation of electromagnetic transients in HVAC cable transmission grids," *Thesis Aulborg University*, p. 253, 2011.
- [186] L. He, "Effects of pre-insertion resistor on energization of MMC-HVDC stations," IEEE Power and Energy Society General Meeting, vol. 2018-January, pp. 1–5, 2018.
- [187] N. Miller and C. Foote, "Iberdrola Innovation Middle East Distributed ReStart: Non-conventional Black-Start Resources," 2021.
- [188] K. Velitsikakis, C. S. Engelbrecht, K. Jansen, and B. V. Hulst, "Challenges and Mitigations for the Energization of Large Offshore Grids in the Netherlands," *Ipst* 2019, 2019.
- [189] H. Khalilnezhad, Technical Performance of EHV Power Transmission Systems with Long Underground Cables. PhD thesis, TUDelft, 2018.
- [190] A. R. Khatib, T. G. Paul, S. A. Al-Ghamdi, and V. Kumar, "Shunt Reactor Control Performances for HVAC Submarine Cable," *IEEE Transactions on Industry Applications*, vol. 60, no. 3, pp. 5211–5220, 2024.
- [191] G. Abeynayake, L. Cipcigan, and X. Ding, "Black Start Capability from Large Industrial Consumers," *Energies*, vol. 15, no. 19, p. 7262, 2022.
- [192] I. Lafaia, M. T. C. de Barros, J. Mahseredjian, A. Ametani, I. Kocar, and Y. Fillion, "Surge and energization tests and modeling on a 225 kV HVAC cable," *Electric Power Systems Research*, vol. 160, pp. 273–281, 2018.

- [193] K. Velitsikakis, C. S. Engelbrecht, K. Jansen, and B. V. Hulst, "Challenges and Mitigations for the Energization of Large Offshore Grids in the Netherlands," *Ipst 2019*, 2019.
- [194] Y. Pan, X. Yin, Z. Zhang, B. Liu, M. Wang, and X. Yin, "Three-Phase Transformer Inrush Current Reduction Strategy Based on Prefluxing and Controlled Switching," *IEEE Access*, vol. 9, pp. 38961–38978, 2021.
- [195] J. Mitra, X. Xu, and M. Benidris, "Reduction of Three-Phase Transformer Inrush Currents Using Controlled Switching," *IEEE Transactions on Industry Applications*, vol. 56, no. 1, pp. 890–897, 2020.
- [196] A. Alassi, K. H. Ahmed, A. Egea-Alvarez, and C. Foote, "Transformer Inrush Current Mitigation Techniques for Grid-Forming Inverters Dominated Grids," *IEEE Transactions on Power Delivery*, vol. 38, no. 3, pp. 1610–1620, 2023.
- [197] L. He, "Effects of pre-insertion resistor on energization of MMC-HVDC stations," IEEE Power and Energy Society General Meeting, vol. 2018-Janua, pp. 1–5, 2018.
- [198] K. Velitsikakis, C. S. Engelbrecht, K. Jansen, and B. V. Hulst, "Challenges and Mitigations for the Energization of Large Offshore Grids in the Netherlands," *Ipst 2019*, 2019.
- [199] A. Alassi, K. Ahmed, A. Egea-Alvarez, and O. Ellabban, "Performance Evaluation of Four Grid-Forming Control Techniques with Soft Black-Start Capabilities," 9th International Conference on Renewable Energy Research and Applications, ICRERA 2020, pp. 221–226, 2020.
- [200] A. Alassi and C. Foote, "Modified Grid-forming Converter Control for Black-Start and Grid-Synchronization Applications," 2021.

Appendix A

Reference frames

In this study, two reference frame transformations are used: the Clarke transformation and the Park transformation. The Clarke transformation converts three-phase electrical quantities from the standard abc frame into a stationary $\alpha\beta0$ frame. The Park transformation, which is often used in control design and power system analysis, shifts quantities from the ab0 frame to the qd0 frame, also known as the synchronous reference frame.

Details of the Clarke transformation are provided in section A.1, while the Park transformation is discussed in section A.2. Additionally, the theory of instantaneous power in both reference frames is explained.

A.1 Clarke transformation

A.1.1 From abc to $\alpha\beta0$

The Clarke transformation is defined as

$$[x_{\alpha\beta0}] = [T_{\alpha\beta0}][x_{abc}] \tag{A.1}$$

Where $[x_{\alpha\beta0}]$ is the vector of components in the stationary $\alpha\beta0$ reference

Appendix A. Reference frames

frame, $[T_{\alpha\beta0}]$ is the Clarke transformation matrix, which converts the three-phase abc system into the stationary $\alpha\beta0$ reference frame and $[x_{abc}]$ is the vector of components in the three-phase abc system. Expanding equation A.1,

$$\begin{bmatrix} x_{\alpha} \\ x_{\beta} \\ x_{0} \end{bmatrix} = \begin{bmatrix} \frac{2}{3} & -\frac{1}{3} & -\frac{1}{3} \\ 0 & -\frac{1}{\sqrt{3}} & \frac{1}{\sqrt{3}} \\ \frac{1}{3} & \frac{1}{3} & \frac{1}{3} \end{bmatrix} \begin{bmatrix} x_{a} \\ x_{b} \\ x_{c} \end{bmatrix}$$
(A.2)

Where x_{α} , x_{β} , and x_0 are the instantaneous values of each component in the Clarke frame and x_a , x_b and x_c represent the original quantities in the standard reference frame.

The Clarke transformation may be used in converter controllers. However, it needs to be transformed once again to the *abc* frame before being fed to the converter. Thus, the inverse of the Clarke transform is given by

$$[x_{abc}] = [T_{\alpha\beta 0}]^{-1} [x_{\alpha\beta 0}]$$
 (A.3)

And expanding this equation,

$$\begin{bmatrix} x_a \\ x_b \\ x_c \end{bmatrix} = \begin{bmatrix} 1 & 0 & 1 \\ -\frac{1}{2} & -\frac{\sqrt{3}}{2} & 1 \\ -\frac{1}{2} & \frac{\sqrt{3}}{2} & 1 \end{bmatrix} \begin{bmatrix} x_\alpha \\ x_\beta \\ x_0 \end{bmatrix}$$
(A.4)

A.1.2 Clarke transformation instantaneous power theory

For a three-phase balanced voltage system, the instantaneous quantities are defined as

Appendix A. Reference frames

$$x_a(t) = \sqrt{2}X \cos(\omega t + \phi)$$

$$x_b(t) = \sqrt{2}X \cos\left(\omega t + \phi - \frac{2\pi}{3}\right)$$

$$x_c(t) = \sqrt{2}X \cos\left(\omega t + \phi + \frac{2\pi}{3}\right)$$
(A.5)

Using the transformation described in equations A.1 and A.2,

$$x_{\alpha} = \sqrt{2}X \cos(\omega t + \phi)$$

$$x_{\beta} = -\sqrt{2}X \sin(\omega t + \phi)$$

$$x_{0} = 0$$
(A.6)

Assuming now that a voltage signal is represented in the Clarke frame, $\sqrt(2)V^{\alpha\beta} = v_{\alpha} - jv_{\beta}$, and the current $\sqrt(2)I^{\alpha\beta} = i_{\alpha} - ji_{\beta}$, the apparent power in the Clarke frame is defined as

$$S = P + jQ = 3V^{\alpha\beta}I^{\alpha\beta*} = 3\left(\frac{v_{\alpha} - jv_{\beta}}{\sqrt{2}}\right)\left(\frac{i_{\alpha} + ji_{\beta}}{\sqrt{2}}\right) \tag{A.7}$$

Rearranging equation A.7,

$$S = \frac{3}{2} \left(v_{\alpha} i_{\alpha} + v_{\beta} i_{\beta} + j v_{\alpha} i_{\beta} - j v_{\beta} i_{\alpha} \right) \tag{A.8}$$

And separating now into real and imaginary parts, the expressions for both active and reactive power are found in equations A.9 and A.10, respectively.

$$P = \frac{3}{2}(v_{\alpha}i_{\alpha} + v_{\beta}i_{\beta}) \tag{A.9}$$

$$Q = \frac{3}{2}(v_{\alpha}i_{\beta} - v_{\beta}i_{\alpha}) \tag{A.10}$$

A.2 Park transformation

A.2.1 From abc to qd0

The Park transformation is defined as

$$[x_{qd0}] = [T_{qd0}][x_{abc}] \tag{A.11}$$

where $[x_{qd0}]$ is the vector of components in the rotating qd0 reference frame, $[T_{qd0}]$ is the Park transformation matrix, which converts the three-phase abc system into the rotating qd0 reference frame, and $[x_{abc}]$ is the vector of components in the three-phase abc system. Expanding equation A.17,

$$\begin{bmatrix} x_q \\ x_d \\ x_0 \end{bmatrix} = \begin{bmatrix} \cos(\theta) & \cos(\theta - \frac{2\pi}{3}) & \cos(\theta + \frac{2\pi}{3}) \\ \sin(\theta) & \sin(\theta - \frac{2\pi}{3}) & \cos(\theta + \frac{2\pi}{3}) \\ \frac{1}{2} & \frac{1}{2} & \frac{1}{2} \end{bmatrix} \begin{bmatrix} x_a \\ x_b \\ x_c \end{bmatrix}$$
(A.12)

where x_q , x_d , and x_0 are the instantaneous values of each component in the Park frame, and x_a , x_b , and x_c represent the original quantities in the standard reference frame.

The inverse Park transformation is given by

$$[x_{abc}] = [T_{qd0}]^{-1}[x_{qd0}] (A.13)$$

And expanding this equation,

$$\begin{bmatrix} x_a \\ x_b \\ x_c \end{bmatrix} = \begin{bmatrix} \cos(\theta) & \sin(\theta) & 0 \\ \cos(\theta - \frac{2\pi}{3}) & \sin(\theta - \frac{2\pi}{3}) & 1 \\ \cos(\theta + \frac{2\pi}{3}) & \sin(\theta + \frac{2\pi}{3}) & 1 \end{bmatrix} \begin{bmatrix} x_q \\ x_d \\ x_0 \end{bmatrix}$$
(A.14)

A.2.2 Park transformation instantaneous power theory

Similar to the Clarke transformation introduced previously, the current and voltage quantities may be defined as

$$V^{qd} = \frac{v_q - jv_d}{\sqrt{2}} \tag{A.15}$$

$$I^{qd} = \frac{i_q - ji_d}{\sqrt{2}} \tag{A.16}$$

Hence, the apparent power in the synchronous frame is defined as

$$S = 3V^{qd}I^{qd*} = 3\left(\frac{v_q - jv_d}{\sqrt{2}}\right)\left(\frac{i_q - ji_d}{\sqrt{2}}\right) \tag{A.17}$$

Manipulating equation A.17 and separating the real (active power) and imaginary (reactive power) components,

$$P = \frac{3}{2}(v_q i_q + v_d i_d)$$
 (A.18)

$$Q = \frac{3}{2}(v_q i_d - v_d i_q)$$
 (A.19)

Appendix B

System And Controller

Parameters

B.1 System parameters

The parameters listed in table B.1 were used across all the system configurations. The only variation was in the SCR and X/R, which were reduced to account for the impact of a weaker grid on system stability.

Parameter	Value	Unit
S_{base}	350	MVA
U_n	230	kV
SCR	1.5/3	-
X/R	1.5/5/10	-
L_g	0.096	Η
R_g	0.302	Ω
L_c	0.048	H
R_c	1.511	Ω
C_f	3.160	μF
R_{hv}	0.2620	Ω/km
L_{hv}	0.0018	H/km
C_{hv}	11.11	$\mu F/km$

Table B.1: System parameters

B.2 Converter controller parameters

The converter controller parameters were adjusted based on the length of each HVAC submarine cable and configuration. The parameters presented in this appendix are specific to arrangement A2 and cable length of 80 km.

Parameter	Value
m_p	$1.73 \cdot 10^{-8}$
m_i	$0.91 \cdot 10^{-7}$
$k_{p,VCC}$	1.28
$k_{i,VCC}$	22.73
R_v	0.38
L_v	$1\cdot 10^{-3}$

Table B.2: GFM converter parameters for A2, 80 km

Parameters	Value
$k_{p,PLL}$	0.0024
$k_{i,PLL}$	0.53
$ au_{il}$	$2\cdot 10^{-3}$
$k_{p,il}$	1.58
$k_{i,il}$	62.23
$k_{p,PC}$	$8.02 \cdot 10^{-7}$
$k_{i,PC}$	$2.86 \cdot 10^{-4}$
$k_{p,QC}$	$6.42 \cdot 10^{-6}$
$k_{i,QC}$	$9.54 \cdot 10^{-4}$

Table B.3: GFL converter parameters for A2, 80 km

B.3 Designing shunt compensations

This section presents the shunt reactors designed for the specified cable lengths, and for the three different configurations.

The table provides, for each cable length, the amount of reactive power compensated, followed by the corresponding inductance values required to achieve that compensation.

Appendix B. System And Controller Parameters

		Cable length (km))
	80	120	150
Q (MVAr)	138	210	240
A1 (H)	0.49 + 0.73	0.32 + 0.48	0.28 + 0.42
A2 (H)	2.53 + 2.43 + 3.37	1.26 + 1.26 + 1.68	0.84 + 0.84 + 1.22
A3 (H)	0.48	0.43	0.16

Table B.4: Reactive power measured and shunt reactors values in (H) for the three cable lengths, for SCR = 3 and X/R = 5

Appendix C

State-Space Matrices For The Power System

Appendix C. State-Space Matrices For The Power System

$$\dot{x}_{sys} = \begin{bmatrix} i_{cq} & i_{cd} & u_{fq} & u_{fd} & i_{bq} & i_{bd} & i_{hvq} & i_{hvd} & u_{hvq} & u_{hvd} & i_{dq} & i_{dd} \\ i_{gq} & i_{gd} \end{bmatrix}$$

$$u_{sys} = \left[\begin{array}{ccc} v_q & v_d & e_q & e_d \end{array} \right]$$

Appendix D

Parameters for PSR Studies

Table D.1: Power system parameters

Parameter	Value	Unit
S_{base}	350	MVA
Z_{base}	151	Ω
$E_1,\!E_2$	66	kV
R_c	0.1245	Ω
L_c	3.1693	mH
C_f	1.2788	mF
$ {R_g}$	0.2489	Ω
L_g°	7.9232	mH/km
R_{hv}°	0.0216	Ω/km
L_{hv}	0.44	mH/km
C_{hv}	1.3518	$\mu F/km$
R_o	0.02	Ω
L_o	0.2	mH/km
R_p	0.02	$\dot{\Omega}$
L_p	0.2	mH/km
$\dot{L_i}$	0.2495	mH
L_{j}	0.3742	mH

Appendix D. Parameters for PSR Studies

Table D.2: (P,Q) pairs, R_{LD} and C_{LD} for local network studies

Step	P (MW)	Q (MVAr)	$R_{LD} (\Omega)$	$C_{LD} (\mu F)$
(P_1, Q_1)	70	0.40	745	0.0241
(P_2, Q_2)	156	8	339	0.4814
(P_3, Q_3)	206	21	257	1.2636
(P_4, Q_4)	241	31	220	1.8653

Table D.3: Offshore transformer parameters

Parameter	Value	Unit
Apparent power	2.3	MVA
Frequency	50	${ m Hz}$
V_1	6.6	kV
V_2	230	kV
R_1	0.002	pu
L_1	0.08	pu
R_2	0.002	pu
L_2	0.08	pu
R_m	500	pu
Saturation pairs (i, ϕ)	$[0\ 0,\ 0\ 0.9,\ 0.0024\ 1.2,\ 1$	pu
	1.52]	
Initial flux (a, b, c)	[0.8, 0, -0.8]	pu

Table D.4: Grid forming converter controller parameters

Parameter	Value
m_p	$1.5 \cdot 10^{-8} \\ 0.9 \cdot 10^{-7}$
m_i	$0.9 \cdot 10^{-7}$
$k_{p,VCC}$	1.2
$k_{i,VCC}$	10
$k_{p,VCC} \ k_{i,VCC} \ \mathrm{R}_v$	0.38
L_v	0.38 $1 \cdot 10^{-3}$

Table D.5: Grid following converter controller parameters

Parameter	Value
$-{k_{p,PLL}}$	0.0024
$k_{i,PLL}$	0.5256
$ au_{il}$	$2\cdot 10^{-3}$
$k_{p,il}$	1.5846
$\vec{k_{i,il}}$	62.2286
$k_{p,PC}$	$8.02 \cdot 10^{-7}$
$k_{i,PC}$	$2.862 \cdot 10^{-4}$
$k_{p,QC}$	$6.416 \cdot 10^{-6}$
$k_{i,PC} \ k_{p,QC} \ k_{i,QC}$	$9.54 \cdot 10^{-4}$

D.1

This appendix includes the matrices, state space vectors and inputs that were used for both the aggregated wind farm and power system for the linear time invariant model developed to study small signal stability. A_{WF} , B_{WF} , \dot{x}_{WF} and u_{WF} form the state space representation of the aggregated wind farms with both grid forming with grid forming converters. A_{PS} , B_{PS} , \dot{x}_{PS} and u_{PS} form the state space representation of the power system, from the offshore PCC to the electrical grid and RL load.

Appendix D. Parameters for PSR Studies

Appendix D. Parameters for PSR Studies

$$u_{WF} = \left[\begin{array}{ccccc} v_{1q} & v_{1d} & v_{2q} & v_{2d} & v_{4q} & v_{4d} \end{array} \right]$$

	0	$-\omega$	$rac{1}{L_i}$	0	0	0	0	0	0	0	
	0	0	0	0	0	0					
	ω	0	0	$\frac{1}{L_i}$	0	0	0	0	0	0	
	0	0	0	0	0	0					
	$-\frac{1}{C_{HV}}$	0	0	$-\omega$	$-rac{1}{C_{HV}}$	0	0	0	0	0	
	0	0	0	0	0	0					
	0	$-\frac{1}{C_{HV}}$	ω	0	0	$-\frac{1}{C_{HV}}$	0	0	0	0	
	0	0	0	0	0	0					
	0	0	$rac{1}{L_{HV}}$	0	$-\frac{R_{HV}}{L_{HV}}$	$-\omega$	$-\frac{1}{L_{HV}}$	0	0	0	
	0	0	0	0	0	0					
	0	0	0	$\frac{1}{L_{HV}}$	ω	$-rac{R_{HV}}{L_{HV}}$	0	$-rac{1}{L_{HV}}$	0	0	
	0	0	0	0	0	0					
	0	0	0	0	$\frac{1}{C_{HV}}$	0	0	$-\omega$	$-\frac{1}{C_{HV}}$	0	
	$-\frac{1}{C_{HV}}$	0	0	0	0	0					
	0	0	0	0	0	$\frac{1}{C_{HV}}$	ω	0	0	$-\frac{1}{C_{HV}}$	
$A_{PS} =$	0	$-\frac{1}{C_{HV}}$	0	0	0	0					
T_{PS} —	0	0	0	0	0	0	$\frac{1}{L_j}$	0	0	$-\omega$	
	0	0	0	0	0	0					
	0	0	0	0	0	0	0	$\frac{1}{L_j}$	ω	0	
	0	0	0	0	0	0					
	0	0	0		0		$\frac{1}{L_g}$	0	0	0	
	$-\frac{R_g}{L_g}$	$-\omega$	$-rac{1}{L_g}$	0	0	0					
	0	0	$-\frac{1}{L_g}$ 0 0 0	0	0	0	0	$\frac{1}{L_g}$	0	0	
	ω	$-\frac{R_g}{L_g}$	0	$-\frac{1}{L_g}$	0	0					
	0	0	0	0	0	0	0	0	0	0	
	$\frac{1}{C_{ld}}$	0	$-\frac{1}{C_{ld} \cdot R_{ld}}$		$-\frac{1}{C_{ld}}$						
	0	0 $\frac{1}{C_{ld}}$	0	0	0	0	0	0	0	0	
	0	$\frac{1}{C_{ld}}$	$-\frac{1}{C_{ld} \cdot R_{ld}}$	ω	0	$-rac{1}{C_{ld}}$					
	0	0	0	0 2	21	0	0	0	0	0	
			$\frac{1}{L_p}$	0	$-\frac{R_p}{L_p}$	C_{ld} 0 $-\omega$					
	0	0	0	0	0	0	0	0	0	0	
	0	0	0	$\frac{1}{L_p}$	ω	$-\frac{R_p}{L_p}$					

Appendix D. Parameters for PSR Studies

$$\dot{x}_{PS} = \begin{bmatrix} i_{\alpha,q} & i_{\alpha,d} & v_{4q} & v_{4d} & i_{2q} & i_{2d} & v_{5q} & v_{5d} & i_{\gamma,q} & i_{\gamma,d} & i_{4q} & i_{4d} \\ v_{7q} & v_{7d} & i_{gq} & i_{gd} \end{bmatrix}$$

$$u_{PS} = \left[\begin{array}{cccc} i_{o1q} & i_{o1d} & i_{o2q} & i_{o2d} & v_{gq} & v_{gd} \end{array}\right]$$

Appendix E

State Space Matrices for Controller Models

This appendix presents the linearised state-space matrices and transfer functions used for the small signal model analysis of both grid-forming and grid-following converter controllers. For each controller, the state-space and transfer functions are linearised individually and subsequently interconnected through their inputs and outputs. This appendix provides a description of the different linearised control loops.

E.1 Filters, Park and Park Inverse Transformations

E.1.1 Low Pass Filter

Low pass filters are used for currents, voltages and active and reactive power. Hence, need to be linearised to be used in the small signal model.

The state-space representation of the low pass filters is the following.

$$\dot{x}_{lpf} = A_{lpf} x_{lpf} + B_{lpf} u_{lpf} \tag{E.1}$$

$$y_{lpf} = C_{lpf} x_{lpf} + D_{lpf} u_{lpf} \tag{E.2}$$

where

$$A_{lpf} = \begin{bmatrix} -\frac{1}{\tau} & -\omega \\ \omega & -\frac{1}{\tau} \end{bmatrix}$$

$$B_{lpf} = \begin{bmatrix} \frac{1}{\tau} & 0\\ 0 & \frac{1}{\tau} \end{bmatrix}$$

$$C_{lpf} = \begin{bmatrix} 1 & 0 \\ 0 & 1 \end{bmatrix}$$

$$D_{lpf} = 0$$

The described state-space representation may be used for both q and d components of a specific signal, might that be a current, a voltage or active and reactive power. Thus, it receives as inputs both components of a signal in the synchrous frame, and outputs these quantities filtered. Let z represent the variable to be filtered, then

$$u_{lpf} = \begin{bmatrix} z_{qp} & z_{dq} \end{bmatrix} \tag{E.3}$$

$$y_{lpf} = \begin{bmatrix} z_{qpf} & z_{dpf} \end{bmatrix}$$
 (E.4)

E.1.2 Park Transformation

As it was seen in Chapter 4, the signals used in the abc frame are transformed, using the Park transformation, or Clarke transformation, into the qd0 or $\alpha\beta0$

frames. These transformations also need to be linearized to be used in the small signal model

The state-space representation of the Park transformation is given by:

$$\dot{x}_l = A_l x_l + B_l u_l \tag{E.5}$$

$$y_l = C_l x_l + D_l u_l \tag{E.6}$$

The matrices A_l, B_l, C_l and D_l are as follows:

$$A_l = B_l = C_l = 0$$

$$D_{l} = \begin{bmatrix} \cos(\theta_{u0}) & -\sin(\theta_{u0}) & -z_{q}\sin(\theta_{u0}) - z_{d}\cos(\theta_{u0}) \\ \sin(\theta_{u0}) & \cos(\theta_{u0}) & z_{q}\cos(\theta_{u0}) - z_{d}\sin(\theta_{u0}) \end{bmatrix}$$

where z_q and z_d are generic variables representing the components of the input, which may be currents or voltages. This module receives as inputs the filtered signals and outputs the signals in the synchrnous frame. The inputs are

$$u_l = \begin{bmatrix} z_{qf} & z_{df} \end{bmatrix} \tag{E.7}$$

$$y_l = \begin{bmatrix} z_{fqp} & z_{fdp} \end{bmatrix} \tag{E.8}$$

E.1.3 Inverse Park Transformation

The same exercise described in E.1.2 may be done for the inverse Park transformation, which is only required for the voltage, as the voltages need to be in the *abc* frame for the PWM modulation and fed back to the converter.

The state-space representation of the inverse Park transformation is given by:

$$\dot{x}_{li} = A_{li}x_{li} + B_{li}u_{li} \tag{E.9}$$

$$y_{li} = C_{li}x_{li} + D_{li}u_{li} \tag{E.10}$$

$$A_{li} = B_{li} = C_{li} = 0$$

$$D_{li} = \begin{bmatrix} \cos(\theta_{u0}) & \sin(\theta_{u0}) & -v_q \sin(\theta_{u0}) + v_d \cos(\theta_{u0}) \\ -\sin(\theta_{u0}) & \cos(\theta_{u0}) & -v_q \cos(\theta_{u0}) - v_d \sin(\theta_{u0}) \end{bmatrix}$$

$$u_l = \begin{bmatrix} v_{qp} & v_{dp} \end{bmatrix}$$
(E.11)

$$y_l = \begin{bmatrix} v_q & v_d \end{bmatrix} \tag{E.12}$$

E.2 Grid-Following Controller

E.2.1 Phase Locked Loop

The PLL is linearised as a transfer function with the d component of the voltage computed at the PCC, $u_{f,d}$, as the input, and the angle, θ , as the output. The PLL controller is detailed in Section 4.2.1, where its equations and controller gains are presented.

$$\mathrm{PLL}(s) = \frac{-k_{p,pll}\cos(\theta_0)s - k_{i,pll}\cos(\theta_0)}{s^2 + \left(k_{p,pll}\cos(\theta_0)u_{f,q0} + k_{p,pll}\sin(\theta_0)u_{f,d0}\right)s + \left(k_{i,pll}\cos(\theta_0)u_{f,q0} + k_{i,pll}\sin(\theta_0)u_{f,d0}\right)}$$

E.2.2 Outer Loop Controller

The equations related to the outer loop controller are detailed in Section 4.2.3. This section outlines two potential configurations for the outer loop controller: one that uses active power and voltage as inputs, and another that uses active and

reactive power as inputs. In both scenarios, however, the active power, reactive power, and voltage must be calculated. This calculation is performed according to the equations presented in Appendix A for active and reactive power in the synchronous frame, which are Equations A.18 and A.19, respectively.

$$\dot{x}_{ol} = A_{ol}x_{ol} + B_{ol}u_{ol} \tag{E.13}$$

$$y_{ol} = C_{ol}x_{ol} + D_{ol}u_{ol} \tag{E.14}$$

Outer Loop Case 1

$$A_{ol} = 0$$

$$B_{ol} = \begin{bmatrix} 1 & 0 & -1 & 0 \\ 0 & 1 & 0 & -1 \end{bmatrix}$$

$$C_{ol} = \begin{bmatrix} -k_{i,vc} & 0\\ 0 & k_{i,pc} \end{bmatrix}$$

$$D_{ol} = \begin{bmatrix} -k_{p,vc} & 0 & k_{p,vc} & 0\\ 0 & k_{p,pc} & 0 & -k_{p,pc} \end{bmatrix}$$

The inputs, u_{ol} and outputs, y_{ol} of the outer loop controller are the following:

$$u_{ol} = \begin{bmatrix} U_{ref} & P_{ref} & V_{mod} & P_{conv} \end{bmatrix}$$
 (E.15)

$$y_{ol} = \begin{bmatrix} i_{c,dr} & i_{c,qr} \end{bmatrix}$$
 (E.16)

$$\dot{x} = P_{c,A}x + P_{c,B}u \tag{E.17}$$

$$y = P_{c,C}x + P_{c,D}u \tag{E.18}$$

Where the matrices are defined as:

$$P_{c,A} = P_{c,B} = P_{c,C} = 0$$

$$P_{c,D} = \begin{bmatrix} \frac{u_{f,q0}}{u_m} & \frac{u_{f,d0}}{u_m} & 0 & 0\\ \frac{3}{2}i_{c,q0} & \frac{3}{2}i_{c,d0} & \frac{3}{2}u_{f,q0} & \frac{3}{2}u_{f,d0} \end{bmatrix}$$

where u_m referes to the magnitude of the voltage as $\sqrt{u_{fq0}^2 + u_{fd0}^2}$. The inputs, u_c , and outputs, y_c , for the active power and voltage computations are the following:

$$u_c = \begin{bmatrix} u_{f,qf} & u_{f,df} & i_{c,qf} & i_{c,df} \end{bmatrix}$$
 (E.19)

$$y_c = \begin{bmatrix} V_{mod} & P_{conv} \end{bmatrix}$$
 (E.20)

Outer Loop Case 2

The state-space for the outer loop case 2 is similar to that of case one, however, instead of using the voltage magnitude as an reference, the reactive power is used instead.

$$A_{ol} = 0$$

$$B_{ol} = \begin{bmatrix} 1 & 0 & -1 & 0 \\ 0 & 1 & 0 & -1 \end{bmatrix}$$

$$C_{ol} = \begin{bmatrix} k_{i,qc} & 0\\ 0 & k_{i,pc} \end{bmatrix}$$

$$D_{ol} = \begin{bmatrix} k_{p,qc} & 0 & -k_{p,qc} & 0\\ 0 & k_{p,pc} & 0 & -k_{p,pc} \end{bmatrix}$$

The inputs, u_{ol} , and outputs, y_{ol} , of the outer loop (with active and reactive power references) are the following:

$$u_{ol} = \begin{bmatrix} Q_{ref} & P_{ref} & Q_{conv} & P_{conv} \end{bmatrix}$$
 (E.21)

$$y_{ol} = \begin{bmatrix} i_{c,dr} & i_{c,qr} \end{bmatrix}$$
 (E.22)

For this specific scenario, the power calculations detailed in Appendix A, equations A.18 and A.19, are utilised to determine both active and reactive power respectively. Similar to the outerloop described previously, the state-space for the power computations is:

$$\dot{x} = P_{c,A}x + P_{c,B}u \tag{E.23}$$

$$y = P_{c,C}x + P_{c,D}u \tag{E.24}$$

Where the matrices are defined as:

$$P_{c,A} = P_{c,B} = P_{c,C} = 0$$

$$P_{c,D} = \begin{bmatrix} \frac{3}{2}i_{c2d0} & -\frac{3}{2}i_{c2q0} & -\frac{3}{2}u_{f2d0} & \frac{3}{2}u_{f2q0} \\ \frac{3}{2}i_{c2q0} & \frac{3}{2}i_{c2d0} & \frac{3}{2}u_{f2q0} & \frac{3}{2}u_{f2d0} \end{bmatrix}$$

The inputs u_c and outputs, y_c are:

$$u_c = \begin{bmatrix} u_{f2qf} & u_{f2df} & i_{c2qf} & i_{c2df} \end{bmatrix}$$
 (E.25)

$$y_c = \begin{bmatrix} Q_{conv} & P_{conv} \end{bmatrix}$$
 (E.26)

E.3 Grid-Forming Controller

This section concerns the small signal state-space matrices developed for the GFm converter controller. This controller includes the P/f loop, the voltage loop which also factors the virtual impedance considered and several power and voltage calculations.

E.3.1 Power loop

A state-space representation is firstly used to output the angular frequency, ω , and afterwards a transfer function, consisting of an integrator was developed to get the angle. The angular frequency is then found via the following state-space representation:

$$\dot{x}_{pl} = A_{pl}x_{pl} + B_{pl}u_{pl} \tag{E.27}$$

$$y_{pl} = C_{pl}x_{pl} + D_{pl}u_{pl} \tag{E.28}$$

$$A_{pl} = C_{pl} = 0$$

$$B_{pl} = \begin{bmatrix} -1 & 1 \end{bmatrix}$$

$$D_{pl} = \begin{bmatrix} mp & -mp \end{bmatrix}$$

The inputs, u_{pl} and outputs, y_{pl} of the outer loop controller are the following:

$$u_{pl} = \begin{bmatrix} P_{ref} & P_f \end{bmatrix} \tag{E.29}$$

$$y_{pl} = \omega$$

Where P_f is the active power computed after being filtered via a low pass filter.

Having the angular frequency, ω , computed, a transfer function is required to obtain the angle:

$$\theta(s) = \frac{\omega}{s} \tag{E.30}$$

E.3.2 Voltage loop

The voltage loop encapsulated both the PI voltage regulator and the virtual impedance considered. Its state-space model is:

$$\dot{x}_{vl} = A_{vl}x_{vl} + B_{vl}u_{vl} \tag{E.31}$$

$$y_{vl} = C_{vl}x_{vl} + D_{vl}u_{vl} \tag{E.32}$$

Where

$$A_{vl} = 0$$

$$B_{vl} = \begin{bmatrix} 1 & 0 & 0 & 0 & -1 & 0 \\ 0 & 0 & 0 & 0 & 0 & -1 \end{bmatrix}$$

$$C_{vl} = k_{i,vc}$$

$$D_{vl} = \begin{bmatrix} k_{p,vc} & 0 & -R_v & -L_v\omega & -k_{p,vc} & 0\\ 0 & 0 & 0 & -R_v & 0 & -L_v\omega \end{bmatrix}$$

The inputs, u_{vl} and outputs, y_{vl} of the voltage loop are the following:

$$u_{vl} = \begin{bmatrix} U_{ref} & U_f & i_{cq,f} & i_{cd,f} & u_{cq,f} & u_{cd,f} \end{bmatrix}$$
 (E.33)

$$y_{vl} = \begin{bmatrix} v_q & v_d \end{bmatrix} \tag{E.34}$$

E.3.3 Power and Voltage Calculations

To compute both active power and voltage magnitude which are required in the formerly introduced state-space models of both active power and voltage loops, the following state-state model was designed:

The state-space matrices for the power calculations using the grid-forming converter (GFM) are defined as follows:

The state-space equations for the GFM power calculation model are:

$$\dot{x} = A_{pvc}x + P_{pvc}u$$

$$y = P_{pvc}x + P_{pvc}u$$

Where

$$A_{pvc} = B_{pvc} = C_{pvc} = 0$$

$$D_{c,D} = \begin{bmatrix} \frac{u_{fq0}}{u_m} & \frac{u_{fd0}}{u_m} & 0 & 0\\ \frac{3}{2}i_{cq0} & \frac{3}{2}i_{cd0} & \frac{3}{2}u_{fq0} & \frac{3}{2}u_{fd0} \end{bmatrix}$$

The inputs and outputs for the state-space representation of the GFM system are defined as:

$$u_{pvc} = \begin{bmatrix} u_{fqf} & u_{fdf} & i_{cqf} & i_{cdf} \end{bmatrix}$$

$$y_{pvc} = \begin{bmatrix} U_f & P_f \end{bmatrix}$$

Appendix F

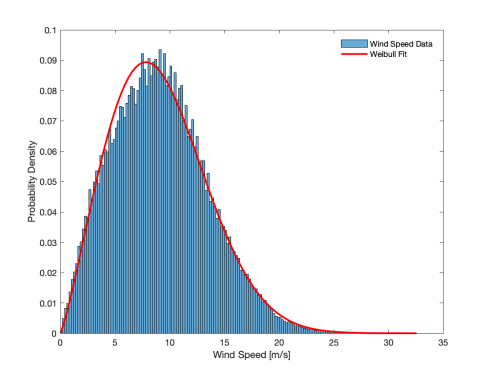
Wind Speed and Power Curves

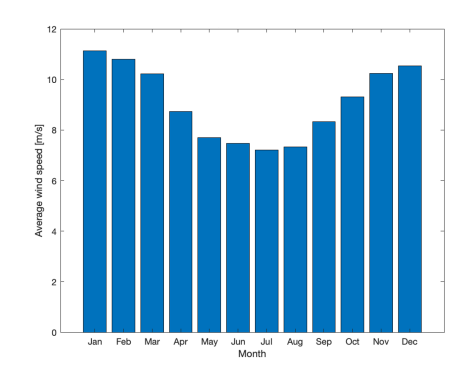
This chapter presents how the wind speed and power curves were computed for the studies of Section 6.3.

F.1 OWPP Case 1

F.1.1 Wind Speed

Using the 30-year wind speed data available for the NNG OWPP, the Weibull distribution for the yearly wind speed was plotted and may be seen in Figure F.1a. This data was used to compute the average daily power which can be produced by one wind turbine and by the OWPP. Figure F.1b displays the average wind speed for each month of the year and this data is used to compute the average power produced daily, and weekly, for each month.





- (a) OWPP Case 1 wind speed Weibull distribution
- (b) Monthly average wind speed for OWPP Case 1

Figure F.1: Weibull distribution for OWPP Case 1 and monthly average wind speed

F.1.2 Power Curve For the NNG Wind Turbines

The OWPP Case 1 has 54 8MW Siemens Gamesa SG 8.0 -167 DD wind turbines. To compute how much power the wind farm is able to extract, it was firstly necessary to compute the power produced by each turbine. To do so, it was necessary to compute the power curve of said turbine and then, with wind speed data retrieved from the location of the wind farm, compute the active power which can be taken from the wind. Table F.1 contains the parameters that were used to compute the power curve.

Table F.1: Wind Turbine Properties for OWPP Case 1

Property	Value	Unit
Cut-in wind speed	3	m/s
Rated wind speed	12	m/s
Cut-out wind speed	25	m/s
Wind turbine radius	83.5	\mathbf{m}
Swept area (A)	21904	m^2
Rated power	8	MW
Air density (ρ)	1.225	${ m kg/m^3}$
Power coefficient (C_P)	0.345	-

Appendix F. Wind Speed and Power Curves

With the information provided in Table F.1 and knowing that the power produced below the rated wind speed is given by F.1, the power curve was computed and may be seen in Figure F.4.

$$P = \frac{1}{2}C_P \rho A U^3 \tag{F.1}$$

Where U is the wind speed range, varying between the cut-in and cut-out wind speeds previously defined.

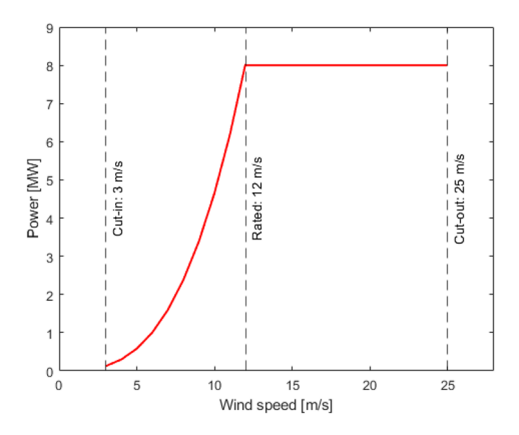


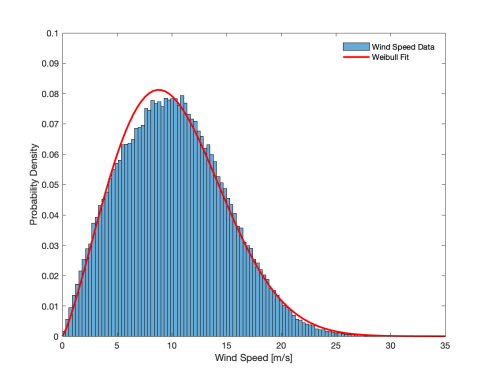
Figure F.2: OWPP Case 1 wind turbine computed power curve

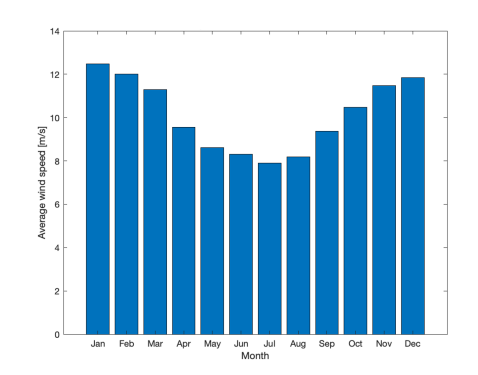
F.2 OWPP Case 2

F.2.1 Wind Speed

The same methodology was followed for the second offshore wind farm considered. However, as this is a different wind farm site, new wind data was considered. The Weibull distribution for OWPP Case 2 was also plotted and may be seen in Figure F.3a and the average wind speed histogram with respect to this wind farm in Figure F.3b.

Appendix F. Wind Speed and Power Curves





- (a) OWPP Case 2 wind speed Weibull distribution
- (b) Monthly average wind speed for OWPP Case 2

Figure F.3: Weibull distribution for OWPP Case 2 and monthly average wind speed

F.2.2 Power Curve

The second OWPP under study is still in the early stages of development and thus, there is no information with regards to the wind turbines that will be employed. However, it is said that the nominal power of the OWPP is of 4.1 GW with up to 307 wind turbines, thus the power generated by each wind turbine will be approximately of 13 MW. It is also mentioned that the rotor is to be no more than 310 m. With this information, and for the purpose of this study, a wind turbine with a nominal active power of 13 MW was used. With the information from Table F.2, the power curve for the 13 MW wind turbine was plotted and may be seen in Figure F.4.

Appendix F. Wind Speed and Power Curves

Table F.2: Wind Turbine Properties for OWPP Case $2\,$

Property	Value	Unit
Cut-in wind speed	3	m/s
Rated wind speed	15	m/s
Cut-out wind speed	25	m/s
Wind turbine radius	107	\mathbf{m}
Swept area (A)	35968.09	m^2
Rated power	13	MW
Air density (ρ)	1.225	${ m kg/m^3}$
Power coefficient (C_P)	0.345	-

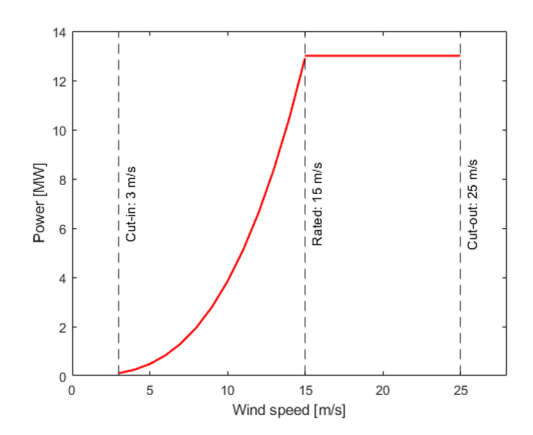


Figure F.4: BwB OWPP wind turbine computed power curve